Coupling of electron spectroscopies for high resolution elemental depth distribution profiles in complex architectures of functional materials

Paul Risterucci

▶ To cite this version:

Paul Risterucci. Coupling of electron spectroscopies for high resolution elemental depth distribution profiles in complex architectures of functional materials. Other. Ecole Centrale de Lyon; Syddansk Universitet (Danemark), 2015. English. NNT : 2015ECDL0047 . tel-01355424

HAL Id: tel-01355424
https://theses.hal.science/tel-01355424v1

Submitted on 23 Aug 2016

ÉCOLE CENTRALE LYON

Thèse de l'Université de Lyon

délivrée par l'Ecole Centrale de Lyon

Spécialité: **Matériaux**

Soutenue publiquement le 23 Avril 2015 à l'University of Southern Denmark

par

Paul RISTERUCCI

Préparée au Laboratoire d'Électronique et de Technologie de l'Information (LETI)
et à l'University of Southern Denmark (USD)

Coupling of electron spectroscopies for high resolution elemental depth profiles in complex architectures of functional materials

---

Ecole Doctorale Matériaux de Lyon

Devant le jury composé de:
Mr A. C. Simonsen en qualité de Président
Mme A. Taleb en qualité de Rapporteur
Mr. F. Yubero en qualité de Rapporteur
Mme G. Grenet en qualité de co-encadrant de thèse
Mr. S. Tougaard en qualité de co-encadrant de thèse
Mr. O. Renault en qualité de co-encadrant de thèse

UNIVERSITÉ DE LYON

"J'aime l'humain quand il fait l'effort

D'être beau et magique malgré les autres

Quand il accepte ses fautes, mais surtout les comprend

Devient le changement donc devient l'enseignant"

Rockin' Squat

Contents

List of publications:

“Probing deeper by hard x-ray photoelectron spectroscopy” P. Risterucci, O. Renault, E. Martinez, B. Detlefs, V. Delaye, J. Zegenhagen, C. Gaumer, G. Grenet, S. Tougaard, Applied Physics Letters, 104, 051608 (2014).

“Inelastic background analysis of HAXPES spectra: towards enhanced bulk sensitivity in photoemission” P. Risterucci, O. Renault, E. Martinez, B. Detlefs, J. Zegenhagen, G. Grenet, S. Tougaard, Surface and Interface Analysis, 46, 906-910, (2014).

“Complementarity of inelastic background and high resolution core level in HAXPES” P. Risterucci, O. Renault, E. Martinez, C. Zborowski, D. Céolin, J.-P. Rueff, G. Grenet, S. Tougaard, in preparation.

List of abbreviations:

AOS: amount of substance
APT: atom probe tomography
CCD: charge coupled device
CMOS: complementary metal oxide semiconductor
CVD: chemical vapor deposition
DPN: decoupled plasma nitridation
DRF: depth resolution function
EELS: electron energy loss spectroscopy
EOT: equivalent oxide thickness
FWHM: full width at half maximum
HEMT: high electron mobility transistor
HAXPEEM: hard x-ray photoelectron emission microscopy
HAXPES: hard x-ray photoelectron spectroscopy
ITRS: International technology roadmap for semiconductors
ISSG: in-situ steam generation
MCP: Multi channel plate
MOSFET: metal oxide semiconductor field effect transistor
NMOS: n-doped metal oxide semiconductor
PEEM: photoelectron emission microscopy
PMOS: p-doped metal oxide semiconductor
PNA: post nitridation annealing
PVD: physical vapor deposition
RMS: root mean square
TEM: transmission electron microscope
XPEEM: x-ray photoelectron emission microscopy
XPS: x-ray photoelectron spectroscopy

Remerciements

Je tiens à remercier Jean-Claude Royer ainsi que Olivier Renault pour m'avoir permis de venir effectuer ma thèse au seins du service de caractérisation. J'espère leur avoir rendu la confiance qu'ils m'ont accordée.

Je tiens également à remercier Geneviève Grenet et la patience qu'elle a eut avec moi. Son aide dans les difficultés scientifiques et administratives m'ont été d'un grand secours.

Parmi les personnes importantes je voudrais également remercier Sven Tougaard pour l'écoute qu'il m'a donné tout au long de la thèse et les échanges que nous avons eus dès que nous pouvions nous voir.

Tout ce travail n'aurait pas pus voir le jours si je n'avais pas été formidablement accueilli par mes collègues de la PFNC. Que ce soit l'aide constante d'Eugénie, l'aide à la préparation des échantillons de Jean-Marc, l'aide ponctuelle de Vincent et Dominique, l'aide de dernière minute de Nicolas ou tout simplement pour les bons moments passés à la pause café.

Beaucoup de gens m'ont soutenu et encouragé durant mes années d'études; la première personne à l'avoir fait est Mme Assens du collège Sonia Delaunay. Je tiens particulièrement à la remercier pour avoir réussi à éveiller ma curiosité, pour m'avoir montré combien la connaissance était importante. La confiance que vous m'avez porté ne m'a jamais quitté et elle m'a souvent servi dans le reste de mon parcours.

Bien évidement d'autres personnes m'ont aidés par la suite, notamment M. Rochet qui m'a trouvé mon premier stage au synchrotron SOLEIL. Ce stage à été déterminant dans ma poursuite en thèse. C'est grâce à Fausto que j'ai réellement découvert ce qu'était un scientifique, dans l'anticipation mais aussi la réactivité face aux expériences. Je tiens aussi à remercier Matthieu pour sa disponibilité et les échanges que nous avons pus avoir. Je remercie aussi Azzedine pour toute son implication et les nuits passés à travailler sur la ligne. Je remercie également Mario pour m'avoir initié à “l'art” du peak fitting et Christian pour toute son aide.

Je souhaite également remercier toute ma famille. En premier lieu mes parents qui m'ont toujours fais ressentir leur amour et leur soutiens. Je remercie mes grands parents de m'avoir accueilli toutes les vacances, pour nous avoir tous aimé et réussit à créer cette joie à chaque fois que l'on se retrouve. Merci à ma sœur d'avoir supporté mon attitude durant toute ma jeunesse. Merci à mes tantes et oncles, mes cousins et cousines pour les bons moments passés ensemble.

Et merci à tous ceux qui m'ont accueillis à Grenoble. Merci à Stéphanie de m'avoir accepté en collocation du jour au lendemain. Merci à Amandine et Ludovic pour ces presque deux années de vie ensemble. Merci également à toute l'équipe de foot de l'AS, sans vous mon séjour à Grenoble aurait été beaucoup plus calme !

Preface

The present thesis was conducted in the Commissariat à l'Energie Atomique et aux Energies Alternatives (CEA) in the Laboratoire d'Electronique et de technologie de l'Information (LETI) from January 2012 to February 2015. The research has evolved around the analysis of inelastic background in photoelectron spectroscopy, mainly at high photon energy. The experiments were performed in synchotron facilities in Grenoble (ESRF) and in Saclay (SOLEIL). The thesis is made in collaboration with the University of Southern Denmark, the Ecole centrale and Institut des Nanotechnologies de Lyon (INL) and the CEA-LETI.

Résumé:

Ce travail de thèse est focalisé sur la détermination, de manière non-destructive, d'interfaces profondément enterrées dans des empilements multi-couches utilisés dans les conditions de technologie réelles au travers d'une méthode innovante basée sur la photoémission avec utilisation de rayons-x de haute énergie (HAXPES) et l'analyse du fond continu inélastique.

Au cours de cette thèse, une procédure numérique à été développée pour quantifier la correspondance entre la mesure du fond continu faite par HAXPES et la simulation du fond continu représentative d'une distribution en profondeur donnée. Cette méthode permet de trouver la distribution en profondeur d'un élément grâce à une procédure semi automatisée.

Dans un premier temps cette méthode à été testée en étudiant une couche ultra fine de lanthane enterrée à une profondeur >50 nm dans un dispositif de grille métallique high-$\varkappa$. L'influence des paramètres utilisés lors de l'analyse y est étudié et révèle l'importance principale d'un paramètre en particulier, la section efficace de diffusion inélastique. La combinaison de mesures HAXPES avec l'analyse du fond continu inélastique utilisant cette nouvelle méthode permet d'augmenter la profondeur de sonde jusqu'à un niveau sans précédent. Ainsi l'échantillon peut être sondé jusqu'à 65 nm sous la surface avec une haute sensibilité à une couche nanométrique.

Dans un second temps, la méthode précédemment validée d'analyse de fond continu inélastique est combinée avec une étude haute résolution des niveaux de cœur dans un échantillon servant de source dans un transistor à haute mobilité. Les deux analyses sont complémentaires puisqu'elles permettent d'obtenir la distribution en profondeur des éléments ainsi que leur environnement chimique. Le résultat donne une description complète des diffusions élémentaires dans l'échantillon suivant les différentes conditions de recuit.

Abstract:

This thesis tackles the challenge of probing in a non-destructive way deeply buried interfaces in multilayer stacks used in technologically-relevant devices with an innovative photoemission method based on Hard X-ray PhotoElectron Spectroscopy (HAXPES) and inelastic background analysis.

In this thesis, a numerical procedure has been implemented to quantify the matching between a HAXPES measured inelastic background and a simulated inelastic background that is representative of a given depth distribution of the chemical elements. The method allows retrieving depth distributions at large depths via a semi-automated procedure.

First, this method has been tested by studying an ultra-thin layer of lanthanum buried at depth $>$50 nm in a high-$\varkappa$ metal gate sample. The influence of the parameters involved in the analysis is studied unraveling the primary importance of the inelastic scattering cross section. The combination of HAXPES with inelastic background analysis using this novel method maximizes the probing depth to an unprecedented level, allowing to probe the sample up to 65 nm below the surface with a high sensitivity to a nm-thick layer.

Second, the previously-checked inelastic background analysis is combined with that of high resolution core-level spectra in the case of the source part of a high electron mobility transistor. The two analyses are complementary as they allow retrieving the elemental depth distribution and the chemical state, respectively. The result gives a complete picture of the elemental intermixing within the sample when it is annealed at various temperatures.

Dansk resumé (Abstract in Danish):

Denne afhandling omhandler problemet med at probe dybt begravede grænseflader i multilags stacks, som bruges i teknologisk relevante devices, med en innovativ fotoemissions metode, der er baseret på Hard X-ray PhotoElectron Spectroscopy (HAXPES) og analyse af den uelastiske baggrund. I afhandlingen er en numerisk procedure blevet implementeret til at kvantificere forskellen mellem en HAXPES målt uelastisk baggrund og en modelleret baggrund, som svarer til en given dybdefordeling af atomerne. Metoden muliggør, med en halv-automatisk procedure, at bestemme dybdefordelingen i store dybder.

Metoden er først blevet testet ved at studere et ultra-tyndt lag af lanthan, som er begravet i en dybde $>$ 50 nm i en high-$\varkappa$-metal-gate prøve. Indflydelsen af parametrene der ingår i analysen er blevet studeret for at opklare den primære betydning af det anvendte uelastiske spredningstværsnit. Kombinationen af HAXPES med analyse af den uelastiske baggrund og brug af den nye numeriske metode giver en hidtil uset probe-dybde, som giver mulighed for at probe den atomare sammensætning i op til 65 nm dybde under overfladen og med høj følsomhed af et kun nm tykt lag.

Dernæst er den uelastiske baggrundsanalyse blevet kombineret med højopløst core-level spektroskopi for at studere de aktive dele i en høj-elektronmobilitets transistor. De to analyser er komplementære, idet de henholdsvis bestemmer den atomare fordeling og atomernes kemiske bindingstilstand. Resultatet giver et fuldstændigt billede af atomernes omfordeling i prøven når denne opvarmes til forskellige temperaturer.

Introduction

Nowadays electronic devices surround our environment. An electronic device is meant to shape and manage electrical signal, to emit, stock or receive an information. This general description shows the multiple purposes of electronic devices, even though the major parts are made for computer components. Those devices are composed differently upon their application field and require a large number of complex operations to be made. The increasing demands for optimized device performances come from both consumers (as the life quality increases with technology) and from industries as electronics enables to perform automated accurate tasks with almost infinite repeatability. Finally, advanced devices must be efficient in many aspects as power consumption, transportability, strength or execution speed. This is reached only because of the ever increasing integration devices such as Complementary Metal Oxide Semiconductor (CMOS) following Moore's law on the one hand and a diversification of the chip's functionality on the other hand. The key ingredient in this revolution comes from the novel active materials introduced over the past decade to replace silicon derived materials.

The need for new ultra-thin active material is still ongoing and requires a need for innovative characterization techniques. The work materials presented here is related to two of the main challenges expressed by the International Technology Roadmap for Semiconductors (ITRS) in 2013:

- Non-destructive characterization method for interface characterization: at extreme miniaturization size where the materials are of nm-thickness, the *"characterization and metrology methods are needed for control of interfacial layers"* and *"require a thorough understanding of nano-scale materials properties and of the physics involved in making the measurement"*.
- Probing the material in integration like conditions. In the real device, the active materials are coated with a nm-thick electrode. The measurement of a technological sample must be performed for the fully deposited structure to account for the real device. Non-destructive characterization techniques must be made to ensure that the derived physical properties are relevant for the real conditions.

This thesis tackles the challenge of probing deeply buried interfaces in multilayer stacks used in real devices with a non-destructive technique. Additionally the ultra-thin active layers composing the transistor are difficult to produce and must be controlled between steps of fabrication, implying the use of non-destructive techniques for *in-line* characterization.

Among the potential non-destructive techniques, x-ray photoelectron spectroscopy (XPS) has an important place as it is a surface sensitive technique perfectly suited for the study of nm-thick materials and interfaces. The limited probing depth of XPS, typically < 10 nm, can be increased with recent use of hard x-rays (HAXPES) delivered by synchrotron radiations as excitation sources. However HAXPES remains limited so far to the analysis of core-level spectra.

The aim of the thesis is to investigate how inelastic background analysis (IBA) can be applied to HAXPES spectra. Combining HAXPES and IBA would indeed enable much larger probing depth. This work will show that such a method allows to obtain elemental depth distribution up to 65 nm below the surface, making possible to probe a deeply buried active layer in a real device structure.

This thesis was conducted at the Platform For NanoCharacterization (PFNC) of CEA-Minatec (Atomic and Alternative Energy Authority), which is a major actor of French research and innovation. The mission of the PFNC is to provide support for off-line characterization at the nanometric scale for internal or academic purposes and for associated companies of the CEA.

Thanks to the diversity of public and industrial research, the CEA has a great asset for development of characterization techniques, through the large range of technological samples available. As a result, the CEA is the 3rd French institute for patents (33th European) and the 2nd for publications. The PFNC has state-of-the-art equipment covering the most used characterization techniques and expert researchers to ensure their exploitation.

The first Chapter of the thesis describes the principles of photoemission spectroscopy. The physical processes involved in photoelectron energy loss are described as they form the inelastic background which will be analyzed in the following. The last paragraphs explain the effects that need to be taken into account when employing hard x-rays and measuring high velocity photoelectrons of HAXPES measurements.

The second Chapter provides a description of the characterization techniques allowing to obtain elemental depth distribution. Among them, photoemission is widely used for its high surface sensitivity in the first nanometers; depth distribution can be obtained either with varying the photoelectron collection angle or by varying the photon energy. Two inelastic background analysis methods which increase the probing depth of XPS are detailed in this section.

The third Chapter will present the first results of inelastic background analysis applied to HAXPES spectra of high-k metal gate samples. The investigation of input parameters describing the physical processes in the sample which are influencing the inelastic background shape are analyzed with extensive analysis of a nanometric La layer buried at depth >50 nm. An original method to obtain the depth distribution with an empirical formula for computing the matching between the measurement and the modeling is shown. A first application dealing with the annealing of the samples investigated is presented in the last Section.

The last Chapter is dedicated to application cases, based on the results obtained previously. A series of samples reserved for high Electron Mobility Transistor (HEMT) structures with different thermal treatment is analyzed by combining analysis of high resolution core-level spectra and inelastic background analysis. The results give a global description of the samples allowing to propose a reaction scheme for the formation of an ohmic contact according to the annealing temperature.

1 Relevant aspects of photoelectron spectroscopy

Photoelectron spectroscopy is a non-destructive surface chemical characterization technique whose fundamental principles were discovered by Hertz in 1887 [1]. Theoretical explanations of the photoelectric effect were given in 1905 by Einstein [2] for which he received the Nobel Prize in 1921. The first practical results by Siegbahn [3] were also rewarded by a Nobel Prize in 1981.

This work presents innovative aspects of photoemission with use of a recent advanced high energy light source and analysis of inelastically scattered photoelectron. To ensure a good understanding of such advanced experiments, one must firstly recall the main physical processes involved (section 1.1).

Because this thesis addresses the quantitative treatment of the inelastic loss signal in a photoemission spectrum, a specific emphasis is made in this Chapter on the photoelectron energy loss in section 1.2.

When laboratory X-ray source is used as excitation, only the first nanometers below the surface are probed. The technique is now commonly referred to X-ray Photoelectron Spectroscopy (XPS). Photoelectron spectroscopy can also be performed with x-ray synchrotron radiation which offers many alternative experiments exploiting energy and/or polarization tunability of the beam [4]. The specificity of HArd X-rays PhotoElectron Spectroscopy (HAXPES) is described in section 1.3.

1.1 General aspects

1.1.1 Principles of photoemission experiment

A photoemission experiment relies on the photoelectric effect, an interaction between a monochromatic light of energy hν and matter, from which results an electron emission . The so-called *photoelectron* can be emitted from the atom if the photon energy hν is higher than the electron binding energy $\mathrm{E_B}(> 0)$. Because of the energy conservation law, the photon energy is equal to the binding energy of the core-level plus the kinetic energy of the photoelectron $\mathrm{E_K}$. Practically the binding energy is measured with respect to the Fermi level of the sample grounded to the metallic sample holder and the electron spectrometer as depicted in Fig. 1. In the experiment, the measured quantity is $E_{K,m} = E_K + (\phi_s - \phi_m)$, where the analyzer work function Φ_m is determined by calibration, usually measuring $\mathrm{E_F}(\mathrm{E_B}=0)$ of a clean silver surface. The energy conservation equation is:

$$h\nu = E_{K,m} + E_B + \phi_m \tag{1}$$

The photoelectron spectrum is obtained by plotting the photoelectron intensity as a function of the measured kinetic energy.

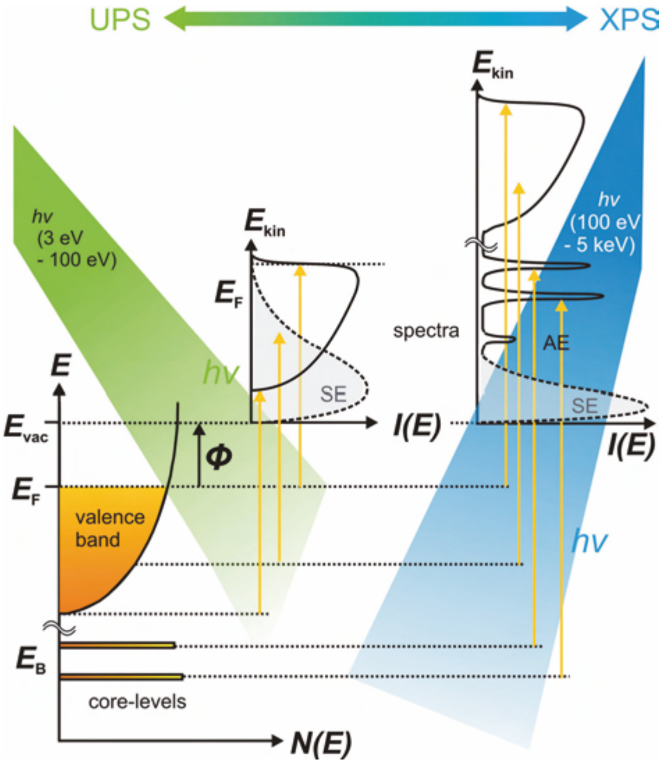

Figure 1: *Scheme of the relevant energy levels in the sample (left) and measured spectra in a photoemission experiment (right).*

1.1.2 Core-level chemical shift

Photoemission is widely used for surface characterization of chemical states [5] thanks to core-level photoemission at high energy resolution ($\Delta E < 0.5$ eV). The atoms bonded to the element of interest have an effect on the valence and core level electrons, dominated by their difference in electronegativity χ. If the element A is bonded to an element B of higher χ (i.e. $\chi_A < \chi_B$), there is a charge transfer of valence electrons from the atoms A to the atom B. The electrons of atom A tighten and decrease their energy of $-\Delta\varepsilon$ (with $-\Delta\varepsilon > 0$ by convention) which is called *chemical shift* [6, 7]*:*

$$\Delta\varepsilon = ke + qV \tag{2}$$

where k is a constant, e is the charge of the atom and V is the potential of neighboring atoms. The chemical energy shift is independent of the subshell of the atom. The reported chemical shift in literature for a given compound can be used to assign a chemical environment to the studied chemical element. The energy conservation of eq.1 can be written, considering the chemical shift as:

$$h\nu = E_{K,m} + E_\varepsilon + \Delta\varepsilon + \phi \tag{3}$$

where E_ε represents the binding energy of the free atom, which can be computed by Koopman's equations.

1.1.3 The three step model

The practical description of the photoemission process is usually performed within the so-called *three step model* [8]: (1) the atom is photoionized, (2) the photoelectron is transported in the medium toward the surface, (3) the photoelectron crosses the surface and travels inside vacuum toward the analyzer as shown in Fig. 2.

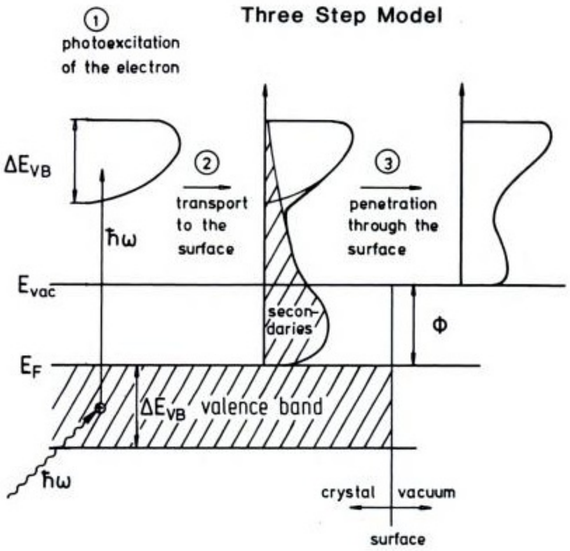

Figure 2: *Three step model of valence-band photoemission. (1) photoionization; (2) the photoelectron is transported toward the surface; (3) the photoelectron crosses the surface, travels into vacuum and is detected. Adapted from [9].*

The core-level binding energy can be deduced from Eq.1. It enables to determine the elemental composition of the surface, and more importantly the bonding state of the elements from the so-called chemical shift (see section 1.1.3). During the transport to the surface, photoelectrons suffer energy losses (see Fig. 2) within a nm-long distance, making XPS very surface sensitive.

The following section addresses in more details some relevant aspects of the first step, the second and the last steps are detailed in Sec.1.2.

Photoionization cross-section When considering the photoelectron angular distribution within the dipole approximation (see Appendix I) the differential photoionization cross section of a core level i under a polarized light can be written as:

$$\frac{d\sigma_i}{d\Omega} = \frac{\sigma_i}{4\pi}[1 + \beta P_2(cos\theta)] \tag{4}$$

with β the energy- and subshell-dependent asymmetry parameter of the photoelectron angular distribution, $\sigma_i$the photoionization of the ith atomic subshell and $P_2(cos\theta)$ the second order Legendre

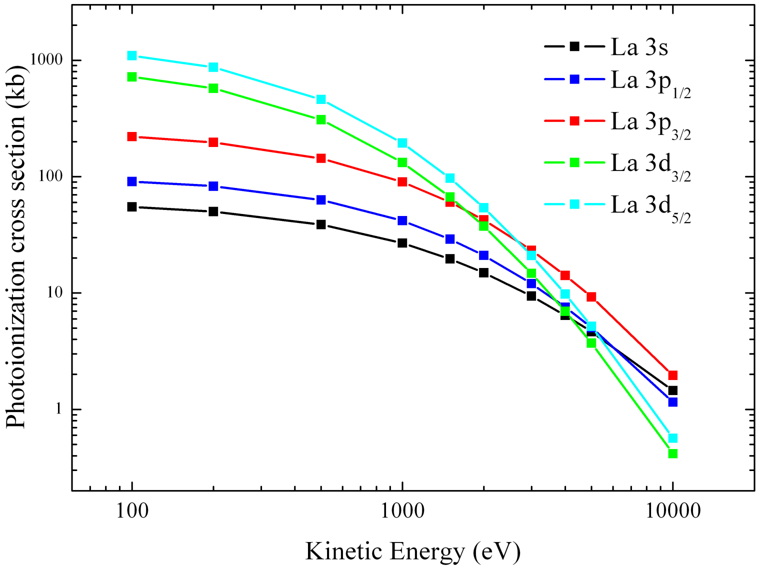

Figure 3: *Photoionization cross section of La 3s, La 3p and La 3d, calculated from [12, 13].*

polynomial. In case of unpolarized light the differential photoionization is:

$$\frac{d\sigma_i}{d\Omega} = \frac{\sigma_i(1 - [\beta(3cos^2\psi - 1)]/4)}{4\pi} \tag{5}$$

with ψ the angle between the direction of X-rays and the mean direction toward the analyzer.

When refinement of this value is needed, two non-dipolar parameters γ and δ can be added to eq.4 to obtain [10]:

$$\frac{d\sigma_i}{d\Omega} = \frac{\sigma_i}{4\pi}[1 + \beta P_2(cos\theta) + \left[\delta + \gamma cos^2\theta\right] sin\theta cos\phi] \tag{6}$$

The photoionization cross-section decreases with increasing photon energy [11, 12] as can be seen in Fig. 3 . The asymmetry of the β parameter is of high importance for comparing measurements taken at various angles.

1.1.4 Photoelectron transport inside the material

As x-ray photons get into a few micrometers inside the sample, the probed depth is limited by the distance over which an electron can travel inside the medium. Only electrons that have not suffered inelastic scattering have the expected binding energy, they form the photoelectric peak or *no-loss peak*. The others are detected with less kinetic energy due to inelastic losses. Therefore they appear shifted towards higher binding energies, forming the inelastic background. The various phenomena giving rise to photoelectrons energy loss and their study will be detailed in Chapter II.

Inelastic mean free path The *Inelastic Mean Free Path* λ (IMFP) is the average distance that an electron with a given energy E (eV) travels between successive inelastic collisions [14]. The IMFP is a calculated quantity and depends on the material. A predictive value can be determined by the Tanuma-Penn-Powell (TPP-2M) formula [15] as presented in Fig. 4 and which neglects elastic scattering:

$$\lambda = \frac{E}{E_p^2[\beta ln(\gamma E) - (C/E) + (D/E^2)]} \tag{7}$$

with

$$\beta = -0.10 + 0.944(E_p^2 + E_g^2)^{-1/2} + 0.069\rho^{0.1} \tag{8}$$

$$\gamma = 0.101\rho^{-1/2} \tag{9}$$

$$C = 1.97 - 0.91U \tag{10}$$

$$D = 52.4 - 20.8U \tag{11}$$

$$U = N_v\rho/M = E_p^2/829.4 \tag{12}$$

where $E_p=28.8(N_v\rho/M)^{1/2}$ is the free electron plasmon energy (in eV), N_v is the number of valence electrons per atom (for elemental solid) or molecule (for compounds), ρ is the density (in g.cm^{-3}), M is the atomic or molecular weight and E_g is the bandgap energy (in eV).

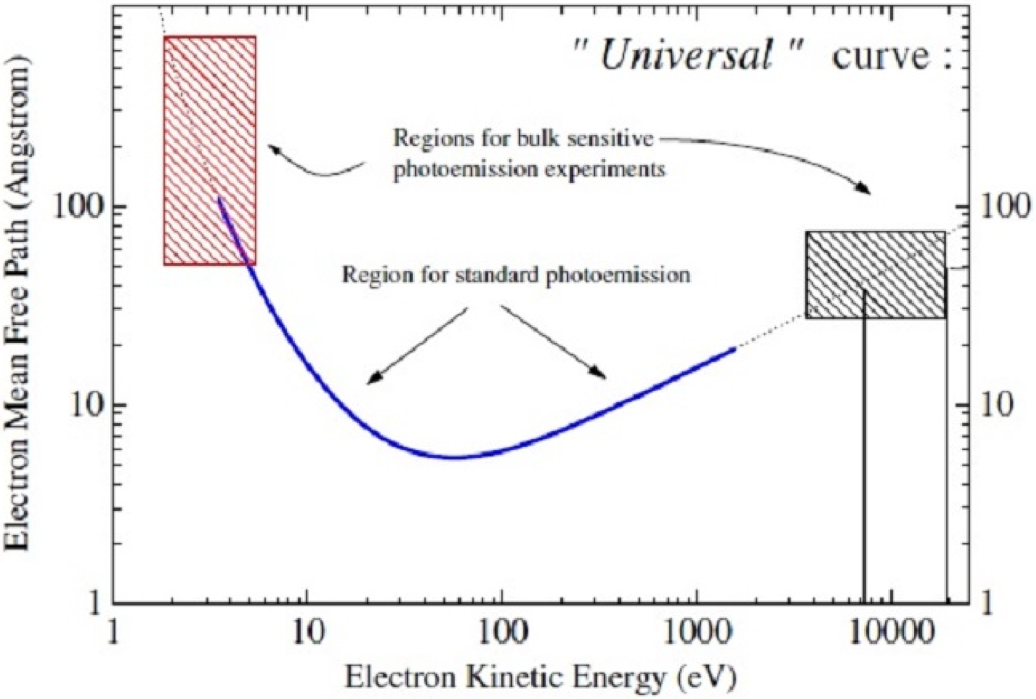

Figure 4: *Trend curve of inelastic mean free path, taken from [16].*

The uncertainties on the results of the predictive TPP-2M formula mainly come from the choice

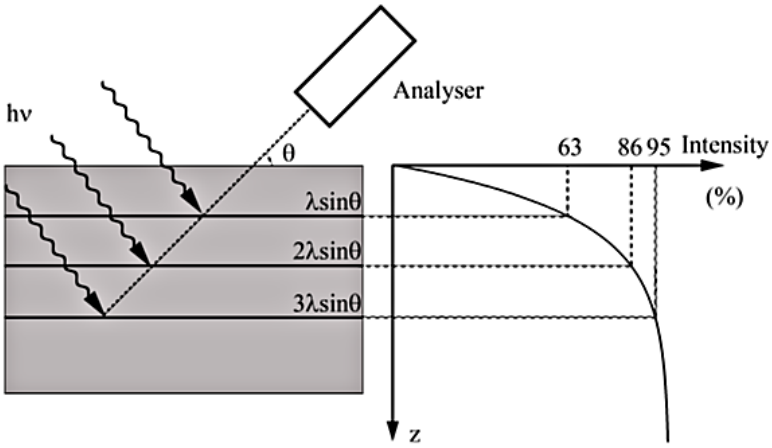

Figure 5: *Relative intensity contribution of layers with thickness $\lambda sin\vartheta$ from [9].*

of N_v. For elemental solids N_v is directly the number of valence band electrons but an ambiguity on the choice of N_v arises for certain elemental solids in the Periodic Table placed after an element in which an atomic subshell is totally filled. In this case the electrons that were formally in the valence band then occupy a subshell with small binding energy. There are a few recommended N_v values given by *Tanuma et al.* and *Seah et al.* Although the results vary with material, a change in the value of N_v by 50% from the known values will typically lead to a change of <15% in the derived IMFPs results.

For electrons with kinetic energy higher than 70 eV, increasing the kinetic energy of the photoelectron increases the IMFP. Thus the low kinetic energy photoelectrons are representative of the surface whereas high kinetic energy photoelectrons are more representative of the bulk.

Information depth As seen from Monte-Carlo simulations [17] the intensity of photoelectrons elastically scattered (giving rise to the core-level no-loss peak) follow an exponential decay law [18, 19]. The intensity of the no-loss peak as a function of the *probing depth* d can thus be written as a Beer-Lambert law:

$$I(d) = I_0 e^{(-\frac{d}{\lambda sin\theta})} \tag{13}$$

where I_0 is the peak intensity, λ is the inelastic scattering mean free path and ϑ is the detection angle from the surface. Therefore 63% of the signal of the no-loss peak arises from $\lambda sin\theta$, 86% from $2\lambda sin\theta$ and 95% of the no-loss peak signal from $3\lambda sin\theta$ as can be seen in Fig. 5. It is possible to experimentally change the angle θ and then obtain information on the depth distribution of elements. This method called Angle Resolved X-rays Photoemission Spectroscopy (ARXPS) will be described later in details.

The *effective attenuation length* (EAL) is also used in XPS (or AES). If the EAL is introduced instead of the IMFP in an expression derived for XPS (or AES), this expression will be corrected for elastic scattering [14]. Even though the experimental value is very much sample dependent, a large database given by NIST can be used to perform analysis [20]. The elastic scattering modulates the exponential attenuation of eq.13, mainly for diffraction effects. These effects are anisotropic and depend mainly on the nearest neighbors of the photoionized atom.

Elastic scattering The elastic collisions change the direction of the emitted photoelectron. The intensity measured is affected by this phenomenon.

The effects of elastic scattering of photoelectrons in amorphous and polycrystalline materials can be accounted for by the introduction of two corrections parameters in Eq.6: Q describes the reduction in photoelectron intensity due to elastic scattering and β_{eff} an effective anisotropy parameter defining the modified angular distribution of photoelectrons. The resulting expression of the photoionization cross section becomes:

$$\frac{d\sigma_i}{d\Omega} = \frac{\sigma_i Q(1 - \left[\beta_{eff}(3cos^2\psi - 1)\right]/4)}{4\pi}$$

From extensive series of Monte Carlo simulations, *Jablonski* found the following equations, fitted to the derived values of$Q$ andβ_{eff} :

$$\beta_{eff} = a_1 cos^2\alpha + a_2 cos\alpha + a_3 \tag{14}$$

$$Q = b_1 cos^2\alpha + b_2 cos\alpha + b_3 \tag{15}$$

where $a_1, a_2, a_3, b_1, b_2\, and\, b_3$ are fitted coefficients listed in an extensive tabulations [21]. The effect of elastic scattering is used in MC simulation to obtain the depth distribution function [19].

1.1.5 Experimental aspects

There are two kinds of x-rays sources, the laboratory sources with fixed photon energy and synchrotron radiation sources which deliver photons of tunable energy.

X-ray laboratory sources The specificity of laboratory sources for photoemission are due to the material used as a source. The choice of photon source must be determined by two criteria: the photon flux which should be high to decrease the time measurement and the monochromatic energy of the emitted photons to achieve high resolution. The photon emitted by the source are not monochromatic and must be selected in energy via an optical apparatus called monochromator. This energy selection decreases the photon flux.

Two sources correspond to these criteria and are usually employed in laboratory experiments, the aluminum with photon emission ray Al K_α of 1486.6 eV or magnesium Mg K_α which produces photons of 1253.6 eV. This energy regime, called soft x-ray ensures to measure low kinetic energy

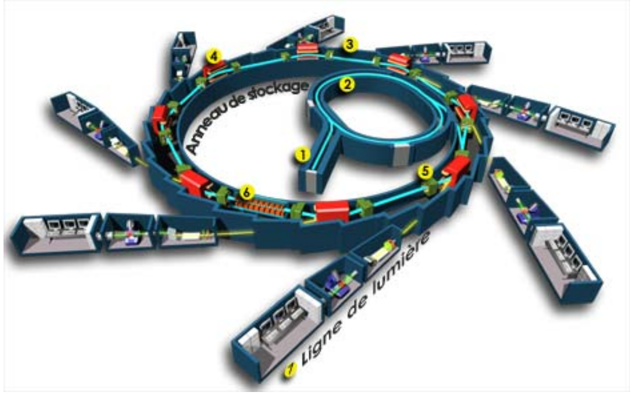

Figure 6: *Scheme of a synchrotron facility. (1) LINAC, (2) Booster, (3) storage ring, (4-5) wiggler, (6) insertion device, (7) beamline.*

photoelectrons. The IMFP is then lower than 3 nm, providing the surface sensitivity of XPS experiments. It is interesting to note that first photoemission experiments carried out by *K. Siegbahn et al.* were using a copper anode delivering photons of 5.4 keV. The use of hard x-ray increases the IMFP giving to HAXPES a higher bulk sensitivity than XPS. They quickly gave up this source as they needed days of measurement due to very low photon flux and low photoionization cross-section. Recent advances allow to use silver to emit photon from Ag L_α radiation of energy 2984.2 eV, but its emission flux is also rather low.

Synchrotron sources Synchrotron radiation is the electromagnetic field emitted from a relativistic electron. A synchrotron machine consists of three parts: the linear accelerator which produces the electrons and accelerates them; a booster, where electrons become relativistic and a storage ring where electrons are maintained at constant velocity and orbit as can be seen in Fig. 84. Detailed setup of SOLEIL synchrotron where injection in the storage ring is continuous (top-up mode), on opposite of the ESRF where injection is non-continuous with time can be seen in Appendix II. The main interests of using synchrotron radiation for XPS are the tunability of the photons produced, the high photon flux and the high energy resolution that can be achieved. The energy range can be between infrared to hard x-rays, allowing to produce low or high kinetic energy photoelectron. Various properties of synchrotron radiation can be used as its coherence for diffraction experiments, the polarization can be tuned for absorbance or dichroism experiments.

Electron analyzer Most of the analyzers in XPS are electrostatic hemispherical analyzers (HSA) which scheme is represented in Fig. 7: photoelectrons are retarded with electrostatic lenses, then selected in energy inside the hemispheres and can reach the detector, a table summarizing some of the commercial electron analyzers performances is presented in Appendix III.

The aperture of the analyzer is composed of a thin entrance slit with acceptance angle of a few degrees, which can be changed by the operator. A higher entrance slit increases the number of collected photoelectrons but decreases the resolution, this mode is called high flux.

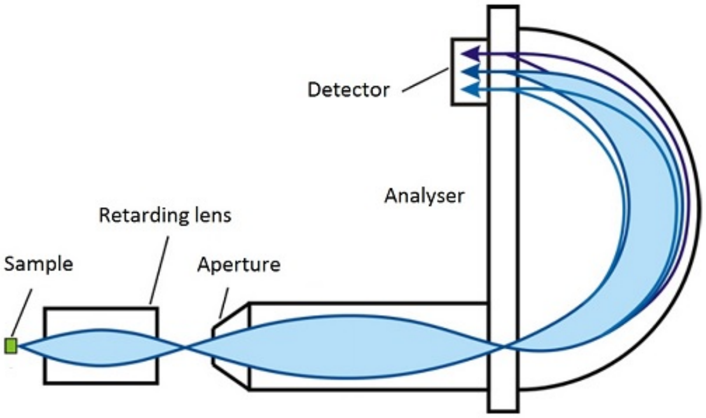

Figure 7: *Schematic of an hemispherical analyzer with retarding lens, Adapted from [22].*

To measure the kinetic energy of the photoelectrons, the analyzer is composed of electrostatic lenses which select the desired kinetic energy by applying a tension reducing the energy to the selected *pass energy* at which electrons will travel into the analyzer. For example if the selected kinetic energy acquisition is between 100 and 200 eV with a pass energy of 50 eV, the lenses will apply a potential difference of 50 eV to 150 eV during the measurement. This function is very important as the resolution depends on the pass energy, which must stay constant to operate with constant resolution.

The photoelectron is then selected in energy in by application of a potential difference ΔV between the two hemispheres of the analyzer. Only photoelectrons of selected energy E can reach the detector, photoelectrons of higher or lower kinetic energy do not reach the detector. The overall resolution ΔE is given by :

$$\frac{\Delta E}{E_p} = \frac{s}{2R} + \frac{\alpha}{4} \tag{16}$$

With $\mathrm{E_p} \propto \Delta \mathrm{V}$ the pass energy of the analyzer, s the entrance slit size, R the mean radius of the hemispheres and α the photoelectron angle from the optical axes of the retarding lenses.

The photoelectrons reach the detector, usually a system based on charge coupled device (CCD) camera and Multi-Channel Plate (MCP) detector. MCP is used to increase the number of photoelectrons with a cascade effect along very-small glass capillaries and convert them into photons. The photons are detected by the CCD camera. This system is used as it yields high speed recording and very high spacial resolution.

1.2 Energy loss phenomena in photoemission

1.2.1 Two step Vs three step model

Section 1.1 described the three step model in photoemission (photoionization; photoelectron traveling inside the medium; photoelectron crossing the surface and traveling into vacuum) but a simplification in a two step model where the third step is neglected can be used. This approximation can be significant when surface physics is predominant in the experiment but this approximation is valid for HAXPES experiments.

The processes that take place as the photoelectron is traveling inside vacuum toward the analyzer is almost always neglected, as the ultra-high vacuum regime must be maintained in the experimental environment at a pressure lower than 10^{-9} mbar, which corresponds to the highest pressure at which the analyzer can work.

Two phenomena can happen at the surface that can change the detected photoelectron kinetic energy:

- Band bending can be important. This phenomenon appears when surface atoms are ionized. To compensate the positive (or negative) charge appearing on the surface atoms, a small negative (or positive) space charge must appear. This zone is usually of a few nanometers [23].
- Surface photovoltage, which corresponds to surface potential modification due to radiation on the sample [24]. The intense beam (especially from synchrotron radiation) can create electron-hole pairs by interband transition or by liberation of carriers trapped inside bands. In this zone, electric field leads to diffusion toward the bulk for majority carriers whereas minority carriers are trapped on the surface.

1.2.2 Type of excitations inducing photoelectron energy loss

The excitations accompanying photoionization in solids can be roughly classified in four types: the **intrinsic** energy losses which are due to the hole created after photoionization, the **extrinsic** energy losses due to electron transport in the sample, the **multiple** excitations and **interferences** between intrinsic and extrinsic contributions. They influence the spectral shape and decrease the measured photoelectron kinetic energy. It results a tail of the elastic peak (or no-loss peak) toward lower kinetic energy, called inelastic background.

The extrinsic contributions The electric field created by the photoelectron during its transport in the sample cause excitations, this energy loss processes are referred as **extrinsic** contributions. They are mainly dominated by plasmons loss. The plasmons are collective excitations of electrons. The plasmon energy ω_0 depends on the energy of the photoelectrons and on the

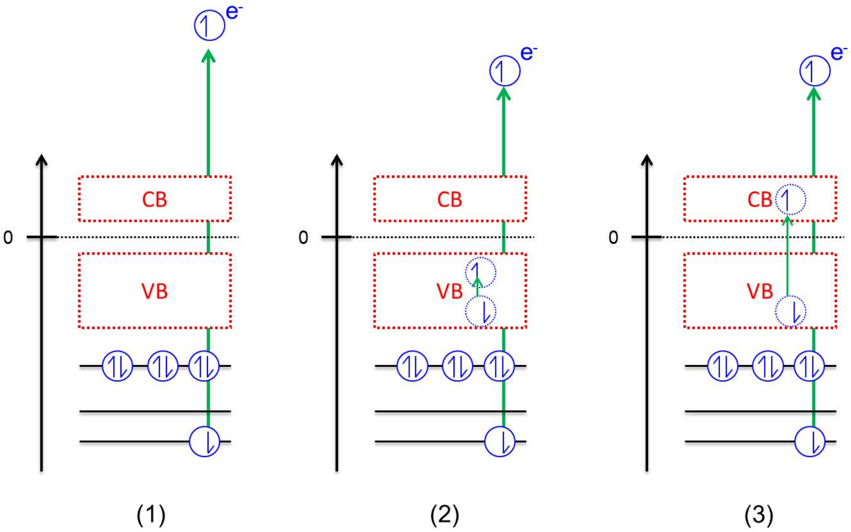

Figure 8: *Schemes of (1) photoionization; (2) shake up process, (3) shake off process.*

density of free electrons. The plasmon resonances are multiple of ω_0 and their intensity increases with increasing photoelectron energy. They can be classified in two categories depending on their origins: the bulk plasmons and surface plasmons. Both of them are considered in the three step model whereas the surface plasmons are considered as bulk plasmons with an attenuation factor in the two step model. The extrinsic contribution run over a 10-20 eV range and are clearly distinguishable in an XPS spectrum, they contain information about the depth distribution of the atoms as will be explained later.

The intrinsic contributions The core-hole created by the photoemission process produces an electric field which excites the valence electrons and decreases the photoelectron energy. This processes are named **intrinsic** contributions and account for 20-50% of the measured intensity in an energy range $\sim 15-25$ eV [25] and extend to ~ 50 eV below the no-loss peak [26]. They can give rise to satellite peaks as described in Fig. 8:

- The "shake-up" effect is when the photoelectron interacts with the valence band. In this process a valence band electron is promoted to a higher orbital of the valence band. The resulting measured kinetic energy of the photoelectron is then lower and forms a distinguishable satellite peak.
- The "shake-off" effect also arises when the photoelectron interacts with the valence band, but in this process a valence band electron is promoted to the conduction band. The resulting measured kinetic energy of the photoelectron is then lower and contributes to the inelastic background.

Multiple excitations Multiples excitations are possible in photoemission but their influence is negligible both for energy determination and intensity contribution in the usual experiments. The energy loss due to phonon-electron interaction is also negligible [27].

Interferences between extrinsic and intrinsic excitations. Interferences between extrinsic and intrinsic contributions are considered to be very weak in energy loss (< 20 eV) and have a small effect on the measured intensity [28]. The Begrenzungs effect is the decreasing of the bulk inelastic scattering cross-section close to the surface. This effect which comes from the orthogonal coupling between the volume and surface modes [29] is very weak. *Fujikawa et al.* showed that interference term in bulk plasmon losses is much smaller than that from the surface plasmon losses [28] and therefore is of negligible contribution to the spectrum measured.

1.3 Hard x-ray photoemission (HAXPES)

The first x-ray photoemission experiment was performed in the 60's by *K. Siegbahn et al.* using of hard x-rays [30] produced by Cu K_α and Cu K_β radiation. Due to very low photoemission intensity, Cu sources were quickly dropped. For 40 years, HAXPES was only performed in synchrotron facility and devolved to fundamental aspects: *Lindau et al.[31]* measured the intrinsic linewidth of the Au 4f core-level. At his point HAXPES studies were performed with low resolution. It is only since major technical improvements from the early 2000's that high resolution HAXPES beamlines are available to user experimentation. Since then, HAXPES experiments started to increase and beamlines were created at synchrotron facilities. The number of workshops, congresses and publications is also increasing, K. Siegbahn even went out of retirement to publish an historical article in the special issue of NIMA in 2005 [32]. A table of main HAXPES beamlines and their capabilities are summarized in Appendix II.

The main interest of using hard x-rays is to increase the probing depth which allows studying deeply buried interfaces. The decreasing photoionization cross section and the low efficiency of photoelectron analyzer for high energy photoelectrons had been experimental difficulties for a long time. Only recent advances in high brilliance X-ray undulator sources at 3rd generation synchrotrons and commercially available high voltage electron analyzers had broadened the community [33]. The details of these technological advances can be found in ref [34]. The effects of high energy regime (for photons and photoelectrons) on the three steps describing the photoemission are detailed hereafter.

1.3.1 Photoionization in HAXPES

Photoionization cross-section The main difference compared to soft x-rays photoemission is the drastic decrease in photoionization cross-section, which is in general two orders of magnitude lower than the one obtained with classical laboratory sources. Theoretical calculations by *Trzhaskovskaya et al.* [11, 12, 13] provide values for photoelectron of 5 and 10 keV. Interpolation between these two values is commonly admitted. Extrapolation for higher kinetic energies is possible with the use of a fit made by two exponential decays but without any theoretical justification at present. Furthermore, for the same element, a high principal quantum number and a low angular momentum are promoted (i.e. s shells are easier to be seen than p shells) at high energy as can be seen in Fig. 9.

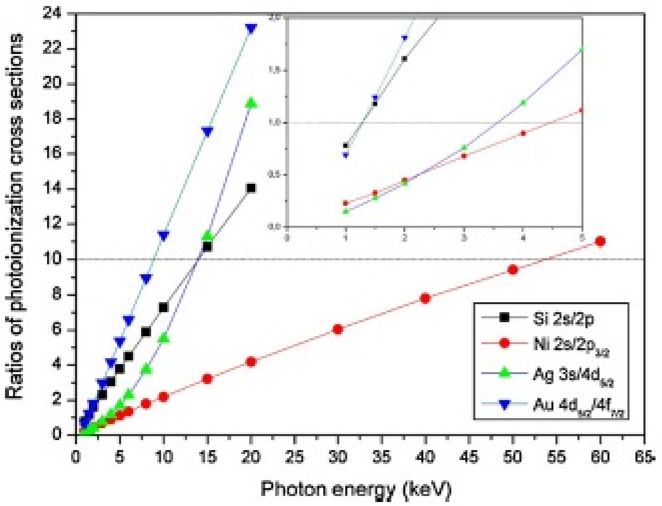

Figure 9: *Photon energy dependence of ratios of subshell photoionization cross-sections for selected atoms from [35].*

Recoil energy The photoelectrons produced during HAXPES experiments are emitted with such high energy that a term called recoil energy and noted E_R is not negligible anymore [36, 37, 38]:

$$E_R = -\frac{Q}{2M} \tag{17}$$

where

$$Q = q - k \approx \sqrt{2(\hbar\omega - E_B)} \tag{18}$$

and M is the mass of the emitter atom, q is the photon momentum and k the momentum of the photoelectron. This term induces a broadening of the spectrum [36]:

$$\left\langle (E_R)^2 \right\rangle = \frac{Q^2 k_B T}{M} \tag{19}$$

The recoil energy is neglected in classical XPS analysis where the momentum transfer is very

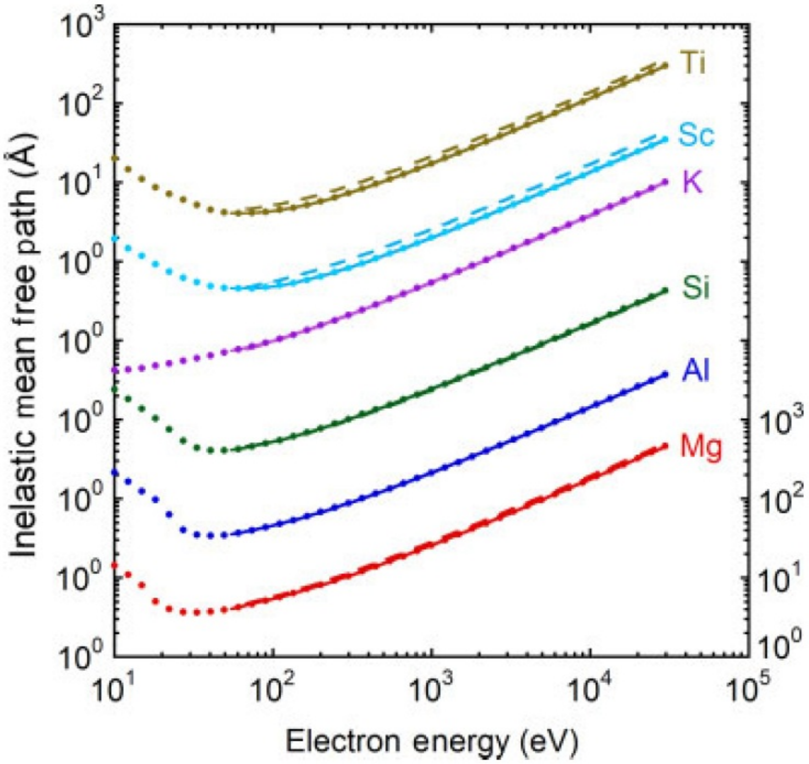

Figure 10: *Inelastic mean free path as a function of the photoelectron kinetic energy for Ti, Sc, K, Si, Al and Mg. The solid circles show calculated IMFPs from the Penn algorithm. The solid lines show fits to these IMFPs with modified Bethe equation and the long-dashed lines indicate the IMFPs calculated from TPP-2M equation. Successive plot have been displaced vertically for clarity. From [39].*

low, but becomes non negligible in HAXPES, where it can induce energy shift comparable to the chemical shift. Equation 3 becomes at high energy:

$$h\nu = E_{K,m} + E_{\varepsilon} + \Delta\varepsilon + \phi + E_R \tag{20}$$

1.3.2 Photoelectron transport inside the material in HAXPES

It has been shown that usual TPP-2M formula with simple pole approximation leads to good results with Bethe equation when employed for high kinetic energy photoelectrons with an estimated error about 12.3% [39]. As seen in eq.7 and in Fig. 4, increasing the kinetic energy of the photoelectron increases the IMFP (thus the EAL) and therefore the probed depth. The difference between the IMFP and EAL can be studied by defining the single scattering albedo ω as [35]:

$$\omega = \frac{\lambda}{\lambda + \lambda_{tr}} \tag{21}$$

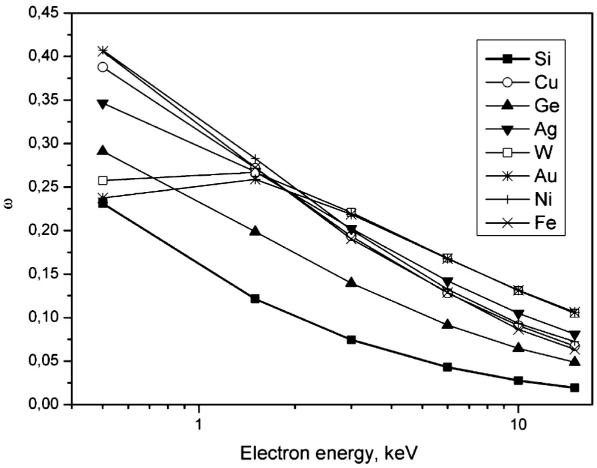

Figure 11: *Single scattering albedo ω as a function of the kinetic energy of the photoelectron for elemental solids Si, Fe, Ni, Cu, Ge, Ag, W and Au. From [35].*

where λ_{tr} is the transport mean free path defined as:

$$\lambda_{tr} = \frac{1}{M\sigma_{tr}} \tag{22}$$

with M the atomic density and σ_{tr} the transport cross-section defined as:

$$\sigma_{tr} = \int 4\pi(1-\cos\theta)({}^{d\sigma}/{}_{d\Omega})d\Omega \tag{23}$$

with $d\sigma/d\Omega$ the differential cross-section for elastic electron scattering. The data are easily accessible via a NIST software [40, 20] and calculations of ω allow estimating the importance of the elastic scattering compared to inelastic scattering. This dependence is shown in Fig. 11 for Si, Fe, Ni, Cu, Ge, Ag, W and Au. The linear decreasing after 1.5 keV kinetic energy indicates the decreasing strength of elastic scattering at higher energy [19]. It has been shown by *Jablonski and Powell* [41] that average EALs L_{ave} of 16 photoelectron lines and 9 Auger lines of elemental solid Si, Cu, Ag, W, Au and inorganic compounds ZrO_2, $ZrSiO_4$, HfO_2 and $HfSiO_4$ varied linearly with the single scattering albedo ω as:

$$L_{ave} = \lambda(1-0.735\omega) \tag{24}$$

Eq.24 shows that when elastic scattering tends to 0, which is the case in HAXPES, the average EAL is equal to the IMFP. Thus for analyzing HAXPES spectra, the approximation of replacing the EAL by the IMFP is correct, which simplifies the quantification as the IMFP is a computed value whereas the EAL is a measured value.

1.3.3 Crossing the surface and traveling toward the analyzer

Electron transport in materials leads to two extrinsic excitations: surface plasmons which are largely considered in classical theory and bulk plasmons which are neglected for low energy photoemission. For high energy photoemission, it's the opposite: a major part of the signal comes from the bulk instead of from the surface [42] as the probed depth is increasing with increasing photoelectron kinetic energy. Another effects of increasing the photoelectron kinetic energy is the decreasing of surface losses relatively to bulk losses [43].

Photoelectron angular distributions depend strongly on the kinetic energy. For energies higher than a few keV, non-dipolar effects (first and second order) have a strong influence on spectra distortion [44]. The elastic scattering diffusion coefficient is also strongly modified by higher order non-dipolar effects and must be amended for use of ARXPS at high energy.

1.3.4 Experimental

There are two major experimental difficulties in HAXPES experiments:

- Hard x-rays laboratory sources have a much lower photon flux than the soft ones (a few orders of magnitude). Although the technique started in laboratory, acquisition time was very long to obtain a satisfactory signal/noise ratio. Furthermore, it is necessary to have a monochromator in order to achieve high resolution and Bragg reflections decrease drastically the photon flux. For this reason, a highly brilliant source in 3rd generation synchrotron must be used. Furthermore, the tunable energy from synchrotron radiation will allow to select the probed depth. Only two HAXPES laboratory machines exist: one can only perform qualitative measurement to our knowledge [45, 46] and the other was just developed [47].
- High kinetic energy photoelectrons are difficult to measure precisely. In order to achieve high energy resolution, the high kinetic energy photoelectrons must be decelerated [48]. This can be achieved by placing retarding lens between the sample and the analyzer entrance [22]. This was the case for ID-32 beamline at ESRF where experiments were conducted. The difficulty relies in the stability of the current delivered in the kV range by the power supply for which the noise must be < 200 µV.

1.4 Conclusion of Chapter I

X-ray Photoelectron Spectroscopy is a widely used experiment allowing to obtain **chemical** information from the surface of a sample by analyzing the **photoelectric peak** (or no loss peak). In this case the probing depth, which is **up to 9 nm** in soft x-rays XPS, is limited by the kinetic energy of the photoelectron.

When **increasing the photon energy** to hard x-rays (HAXPES), the **probing depth can increase up to 20 nm** but the **photoionization cross section decreases**. The **recoil energy** in the energy conservation law becomes **non negligible** at these high energy and non-dipolar effects affect several parameters, promoting the forward scattering and the **bulk predominant** information at the expense of the surface.

The energy loss phenomena have been described and the next Chapter will show that analysis of inelastically scattered photoelectrons can increase the probing depth in photoemission and thus allow characterization of deeply buried layer.

2 Inelastic background analysis and other depth profiling methods

Here are presented the most commonly used techniques in photoelectron spectroscopy to obtain depth distribution of deeply buried elements. The principal other experiments that allow to obtain such information are presented in Appendix IV. Among them, the photoelectron spectroscopy is used for its non-destructive character and its ability to obtain the elemental composition in the surface and near-surface region.

In classical XPS, the measurement of a high resolution core-level spectrum allows to obtain depth distribution within the 3 first IMFP below the surface. The maximum probed depth when analyzing core-level is up to 9 nm with use of soft x-rays and 50 nm with hard x-rays (the deepest layer analyzed with hard x-ray published so far is buried at 25 nm [16]). This probing depth remains too low to analyze deeply buried interfaces in a stack of technological interest. Therefore the analysis of the inelastically scattered photoelectrons which ensure a probed depth up to 8 IMFP may be a solution to solve this issue [49].

This Chapter describes the main XPS experiments to obtain depth profile using core-level analysis and inelastic background analysis.

2.1 Usual depth-profiling methods in core-level photoemission

There are three widely used types of core-level analysis to obtain depth profile: the depth profiling with sputtering, the Angle Resolved X-ray Photoemission Spectroscopy (ARXPS) which employs the $\sin\vartheta$ dependence of eq.13 to obtain depth profile (i.e. angle of measurement) and the Variable Kinetic Energy X-ray Photoemission Spectroscopy (VKE-XPS) which exploits the energy dependence of eq.13.

They possess the advantage of high sensitivity to chemical states and other characteristics of surfaces but are **limited in probed depth to 3 IMFP** (i.e. ~9 nm below the surface) as they are based on the study of the no-loss peak, except for the depth profiling with sputtering which is explained hereafter.

2.1.1 Depth profiling with sputtering

In a sputtering surface sensitive technique, a monoatomic ion source sputters the surface to remove a few layers off the surface and a surface sensitive experiment is done. By cycles of sputtering and/or analysis, depth distribution of elements as a function of the sputtering time is obtained. The ion bombardment can induce variations of the chemical composition and morphology of the surface, changing the obtained depth profile.

The measurement can be performed either during sputtering (continuous mode) or with cycles of sputtering/measurement (alternate mode). The continuous mode enables fast data acquisition and limits surface contamination if the pressure in the system is not sufficiently low. The disadvantages are the lower signal-to-noise ratio and the ion beam induced Auger electrons from the crater rim which may distort the profile, especially for low energy peak (Al, Si and Mg for example). If the study is focused on thin layers or possesses a concentration gradient near detection limit, further complications can arise from continuous mode. To overcome this difficulty, the alternate sputtering is performed. This mode can be employed only if the residual background pressure is sufficiently low to avoid surface contamination.

Sputtering Sputtering is a process where primary ions are accelerated to a few keV onto the sample. As the ions impinge the sample, they transfer energy and momentum to the sample, as a function of the mass of the incident ions and targeted atoms. The collision parameters are described by binary Rutherford scattering. The cross section for elastic energy transfer is high [50], resulting in a collision cascade. Most of the incident particles are consumed in generating damage and heat within the collision cascade. Sputtering will occur if a struck target atom near the surface is accelerated in a direction toward the vacuum with sufficient energy to overcome the surface energy barrier. The process of sputtering can be described by a random ejection of surface atoms during ion bombardment: the roughening of the surface is counteracted by surface diffusion [51]. The relocation of the atoms results in interdiffusion, resulting in an atomic mixing zone [52, 53]. Also the variation of sputtering combined with variation of crystalline orientation and inhomogeneities of the chemical composition result in a larger-scale roughening. The etching rates are generally given by the manufacturer of the ion gun as it depends on its specificity. For specific samples (with overdensity, voids, exotic alloys etc.) the sputtering rate must be measured with a reference sample.

If the ions impinge the surface at an angle, the sample must rotate during the sputtering to get an uniform crater as seen in Fig. 12(b). The so-called Zalar rotation improves depth resolution [54]. Recent advance allows to employ ions formed by cluster of hundreds of atoms, decreasing the amount of substance removed and the defects on the sample [55].

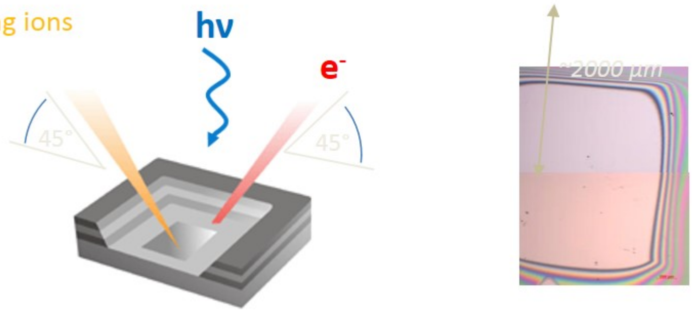

Figure 12: *Scheme of an XPS experimental sputtering (a), optical image of a formed crater (b).*

Depth profile The depth profile is typically obtained by (1) calibration of the intensity scale in unit of instantaneous concentration, (2) converting the sputtering time to a sputter depth, (3) deconvolution of the measured profile with the aid of a depth resolution function. For many applications, it is sufficient to assume that the intensity I measured and the depth profile can be treated separately [56].

The calibration of the intensity scale in unit of instantaneous concentration can be done when knowing the sputtering yield Y_m, from literature or measurement of a reference sample. As the sputtering induces changes on the surface of the sample, a practical way for obtaining depth profile concentration is to measure the total core-level peak area, losing the chemical information. The sputter depth can be written as:

$$z(t) = \int_{0}^{\infty} \dot{z}(t)dt \tag{25}$$

with

$$\dot{z} = dz/dt = j_p Y_m / eN \tag{26}$$

where j_p is the ion-current density of the primary ions, e the elementary charge and N is the atomic density. The error in depth calibration mainly comes from variations in the sputtering rate and surface contamination layer and can change the thicknesses up to 5 nm. Another source of error is the shift of 50% intensity at interfaces toward lower depths, caused by the photoelectron escape depth. The atomic mixing can also gives an error on the estimated thickness up to 5 nm [57]. Under favorable conditions, these errors can be minimized, but but better results can generally be obtained by using a depth resolution function (DRF).

The experimentally-determined normalized in-depth intensity is given by a convolution of the mole fraction $X(z)$ of an element at depth z, and the DRF $g(z)$ as [58]:

$$\frac{I(z)}{I(0)} = \int_{-\infty}^{+\infty} X(z')g(z-z')dz' \tag{27}$$

where z' is the running depth parameter for which the composition is defined. The shape of g(z) depends on the material and sputtering process. X(z) can be determined by deconvolution of Eq.27, the difficulties are arising if the data precision and the signal to noise ratio are low.

DRF can be approximated by an error function, assuming that the sputter depth profile obtained is representative of a sharp interface. In this case g(z) is a Gaussian function and the depth resolution Δz is given by 2σ, with σ the standard deviation of the Gaussian function. In a general way, the depth resolution is given by several factors and can be written as [59]:

$$\Delta z = (\Delta z_0^2 + \Delta z_s^2 + \Delta z_m^2 + \Delta z_\lambda^2 + \Delta z_r^2 + ...)^{1/2} \tag{28}$$

where 0 stand for the intrinsic surface roughness, s for surface roughening by sputtering statistics, m for the atomic mixing and preferential sputtering, λ for the information depth and r for the ion sputtering induced roughening.

2.1.2 Angle Resolved X-ray photoelectron spectroscopy (ARXPS)

ARXPS is widely used for its ability to retrieve depth profiling and quantification of thin layers. The method is more precise than depth profiling with sputtering but is strictly limited to the first three IMFPs. Despite very good absolute depth resolution, without prior knowledge on the sample, atomic resolution cannot be achieved. It is possible to obtain information of samples with lateral inhomogeneities, roughened surfaces, island covered surfaces with additional assumptions. For clarity purposes, the next two paragraphs illustrate the simpler cases of a flat surface covered with a thin homogeneous layer and the multiple-layeres structure respectively.

The method relies on intensities of no-loss photoelectron peaks. By changing the angular detection, the probed depth is changed as can be seen in the Fig. 13.This figure illustrates the following situation: the sample consists of a top overlayer on a substrate with a broad interface between them. If photoelectrons are collected at low take-off angle (in red), the measured spectrum is representative of the surface overlayer. If the take-off angle increases (in blue), the experiments becomes more bulk sensitive and the measured spectrum is representative of the overlayer, the substrate and the interface. With measurements at various angles, the depth profile can be reconstructed.

Generalities for core-level analysis The analysis of the core-level photoemission spectra possesses several degrees of sophistication for the analysis, and even if cookbooks exist, the methodology is chosen by the operator according to his/her experience [60]. In most cases, the core-level high resolution spectrum is corrected for inelastically scattered photoelectron by subtraction of a background. The resulting curve is the fitted, generally using a convolution of Gaussian and a Lorentzian. The Lorentzian Full Width at Half Maximum (FWHM) depends on the core-hole lifetime whereas the Gaussian FWHM is dominated by the overall resolution. For metals, the peak

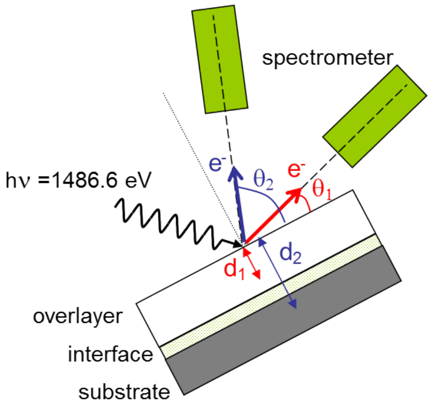

Figure 13: *Scheme of the principle of ARXPS.*

can be asymmetric, either by introducing an asymmetry parameter or using a Doniach-Sunjic lineshape [61]. The center of the corresponding curve is representative of the chemical shift of the element and is used for attribution of the chemical environment of the considered atom.

Single layer analysis of ARXPS measurement Determination of uniform film thickness is by far the most used system treated by ARXPS.

If S_s and S_o are the sensitivity factors for the element present in the substrate and the overlayer respectively, and the spectrum is acquired at take-off angle ϑ, the measured corresponding peak intensities I_s and I_o are defined by:

$$\frac{I_s}{s_s} = e^{-\lambda_s \cos\theta} \tag{29}$$

$$\frac{I_o}{s_o} = e^{-t/\lambda_0 \cos\theta} \tag{30}$$

where t is the overlayer thickness, λ_o and λ_s are the EALs of the photoelectrons from the overlayer and the substrate when passing through the overlayer material. If the substrate and the overlayer are composed by different elements, the EALs are very different and resolving the two previous equations involves solving a nonlinear transcendental equation. In the simpler case where the same element is present in the substrate and in a different chemical state, i.e. sufficiently shifted in measured kinetic energy to be resolvable, the two EALS can be approximated and the Eq.29 and 30 can be rearranged to obtain the so-called Hill equation:

$$t = \lambda \cos\theta ln \left(1 + \frac{I_o/s_o}{I_s/s_s}\right) \tag{31}$$

The curve represented by Eq.31 is plotted in Fig. 14. Two areas are shaded, corresponding to the limit of the model:

- When the layer thickness is below the thickness of a single atomic layer, it is more accurate to describe the overlayer with a covering factor.

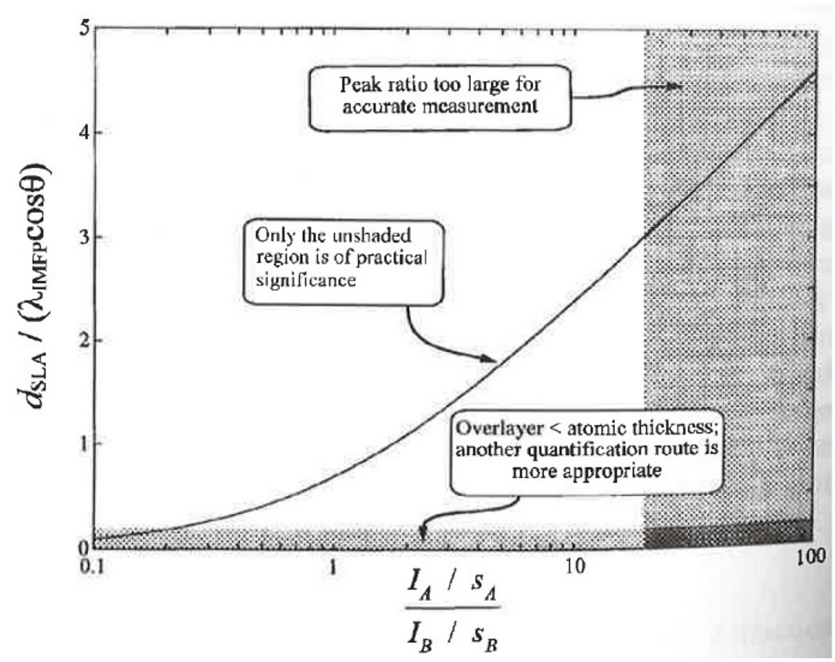

Figure 14: *Layer thickness measurement using the Hill equation (Eq.31). Extracted from [48].*

- When the overlayer thickness is greater than 3 IMFP (right part of the figure), the substrate peak is too small to be measure accurately.

This method excels at determining surface oxide thickness, typically silicon or aluminum.

Multilayered structures analysis of ARXPS measurement In the case of a multilayered structure, it is possible to obtain the depth distribution of several layers, if they are in the 3 IMFP range from the surface. In the case of a stratified sample (where the chemical states of the layers do not interfere in the XPS spectrum) with n layers, the Eq.29 and 30 can be generalized to:

$$\frac{I_n(\theta)}{I_n(0)} = k(\theta)\left[\frac{1 - e^{\frac{t_n}{\lambda_n \cos\theta}}}{1 - e^{-\frac{t_n}{\lambda_n}}}\right]\frac{e^{-\frac{d_n}{\lambda_n \cos\theta}}}{e^{-\frac{d_n}{\lambda_n}}} \tag{32}$$

where $I_n(\theta)/I_n(0)$ is the ratio of the peak area at angle ϑ and normal emission, $\mathrm{t_n}$, λ_n and $\mathrm{d_n}$ are the thickness, the EAL and the mean depth of the n^{th} layer. $k(\theta)$ is an instrumental function that can be estimated by the intensity ratio of the background $\mathrm{I_b}$ at the angle ϑ and at normal emission as:

$$k(\theta) = \frac{I_b(\theta)}{I_b(0)} \tag{33}$$

It is then possible to obtain a value close to the average depth of the layer called characteristic depth parameter $\mathrm{Z_n}$, representing a depth approximately 35% of the distance between the top and bottom interface of the nth layer defined as:

$$Z_n = \frac{ln\left[\frac{I_i(\theta)I_b(0)}{I_i(0)I_b(\theta)}\right] - ln(\sec\theta)}{1-\sec\theta} \tag{34}$$

Another useful quantity, the relative amount of material in the nth layer, A_n, can be obtained:

$$A_n = \frac{I_n(0)}{S_n} e^{Z_n}$$

The theoretical depth resolution Δz at depth z is given by [62]:

$$\frac{\Delta z}{z} = 2sinh\left\{\frac{\pi^2}{2cosh^{-1}\left[\pi(n-1)(\frac{I}{\sigma_i})^2\right]}\right\} \tag{35}$$

with (σ_I/I) the fractional precision of the peak intensities and n the number of layers. For example, if the measurement of the peak intensity is 2% over 5 emission angles for a depth z of 2 nm, the depth resolution $\Delta z \simeq 1.8\,nm$. From this observation, *P.J. Cumpson* showed the need of prior knowledge on the sample [63].

The stratification method is very powerful for quantification of ARXPS data because of the combination between the depth and relative amount in each layer. However the method cannot distinguish two or more distinct layers having similar composition (where the peak shift is below the resolution of the experiment).

The case of a stratified sample is however not the most common situation encountered. To analyze continuous depth profile (often encountered in diffusion process), stepped interface or layers with different composition (in this case the approximation of equal EAL cannot be retained), additional assumptions on the sample composition and/or depth model profile must be employed. The next paragraph illustrates one of the most used numerical method, the Maximum Entropy.

Regularization method - Maximum entropy ARXPS method relies on the determination of the intensity and energy of the no-loss peak. This quantity is not trivial to quantify as the no-loss peak is dependent on the structure of the sample (concentration and location) and on many physical parameters such as the chemical shift, the core-hole lifetime, the photoionization cross-section, the photon beam (size and energy resolution) and the analyzer efficiency. To increase the reliability and the consistency of the quantification, the operator can use of a regularization method [63].

A regularization procedure quantifies a matching between a measurement and a predictive formula by means of two quantities, the residual norm χ and the solution norm α. The residual norm is the standard deviation root mean square χ and is expressed as the formula:

$$\chi = 100 \times \sqrt{\sum_i \frac{(y_i^m - y_i^b)^2}{n_i}} \tag{36}$$

with y_i^m the measured intensity at energy i, y_i^b the modelled intensity at energy i and n_i the number of points considered. A smaller value of χ indicates a better match between measurement and modeling. The solution norm is a measure of the complexity of the proposed depth profile. It can be of different forms, depending on the prior knowledge of the sample structure. *Paynter et al.* showed that the results obtained for an exponential profile with various regularization schemes depends more on the prior input parameters (concentration, slopes or curvature in depth profile) than on the regulator which calculates the profile entropy [60]. However the specific method of Maximum Entropy is widely used in ARXPS and VKE-XPS analysis, which will be explained in the next section.

In both statistical thermodynamics and information theory, the entropy is a measure of disorder (negative quantity). In information theory, the entropy S is the opposite of information content defined as [64]:

$$S = -\sum_i p_i \ln(p_i) \tag{37}$$

with p_i the probability of finding the system in a state i. The Maximum Entropy (MaxEnt) designates a regularization method which minimizes the information content or maximizes the entropy. If extended to include all positive additive terms, then eq.37 is developed as [65]:

$$S = \sum_i \sum_j n_{j,i} - m_{j,i} - n \log(\frac{n_{j,i}}{m_{j,i}}) \tag{38}$$

with $n_{j,i}$ the proportion of element j at depth i and $m_{j,i}$ the initial estimate for the proportion of element j at depth i. The MaxEnt solution is then obtained by maximizing S. It is done by calculation of chi-squared χ^2 (not to be confused with χ of eq.36) misfit statistic C defined as:

$$C = \chi^2 = \sum_k \frac{I_k^{calc} - I_k^{obs}}{\sigma_k^2} \leq N \tag{39}$$

whereI_k^{calc} and I_k^{calc} are the calculated and observed intensity at the k$^{\text{th}}$ measurement (angle for ARXPS or energy for VKE-XPS), σ_k^2 is the variance of the k$^{\text{th}}$ measurement and N is the number of independent observations in the data. The MaxEnt then maximize the joint logarithmic probability function Q defined as:

$$Q = \alpha S - \frac{C}{2} \tag{40}$$

where α is a regularizing parameter. A probability distribution of α can be determined by Bayesian statistical analysis [66], but if the data present sharp peaks, the determination of α can be performed by the operator as a large value of α will result in an over-smooth solution while a small value will lead to overfitting the data [67].

Active background method The regularization method previously described details the no-loss peak fitting procedure. However the spectra must be **previously** corrected from background subtraction of secondary photoelectrons (which will be detailed in the next Section). This *static* approach implying operator decision upon the background type and energy range (defined as (E_{left}, I_{left}) and (E_{right}, I_{right})) can lead to deviations on quantification results [68]. In the *active background* approach, the shape and intensity of the background is assessed **during** the peak fitting and can be a combination of background types [69]. The measurement of intensities depending on the take-off angle is fitted with a model for depth distribution of all elements.

The peaks of interest for retrieving the depth profile are treated in parallel, which maximizes the consistency of the procedure. This is illustrated in the Fig. 15(a) showing the intensity versus take off angle for all the elements present in a sample of TiN/Al_2O_3/InGaAs [70] and fitted with the theoretical behavior of the model in Fig. 15(b). This example also shows the robustness of the active approach which can treat simultaneously two overlapping peaks and the accuracy of the profile obtained [71].

This new method has the interest of increasing the independence of the results upon operator background choice. The method is implemented in a commercial software AAnalyzer® [72] and therefore not widely used, in spite of its high accuracy which can shows sub-nanometric diffusion [70].

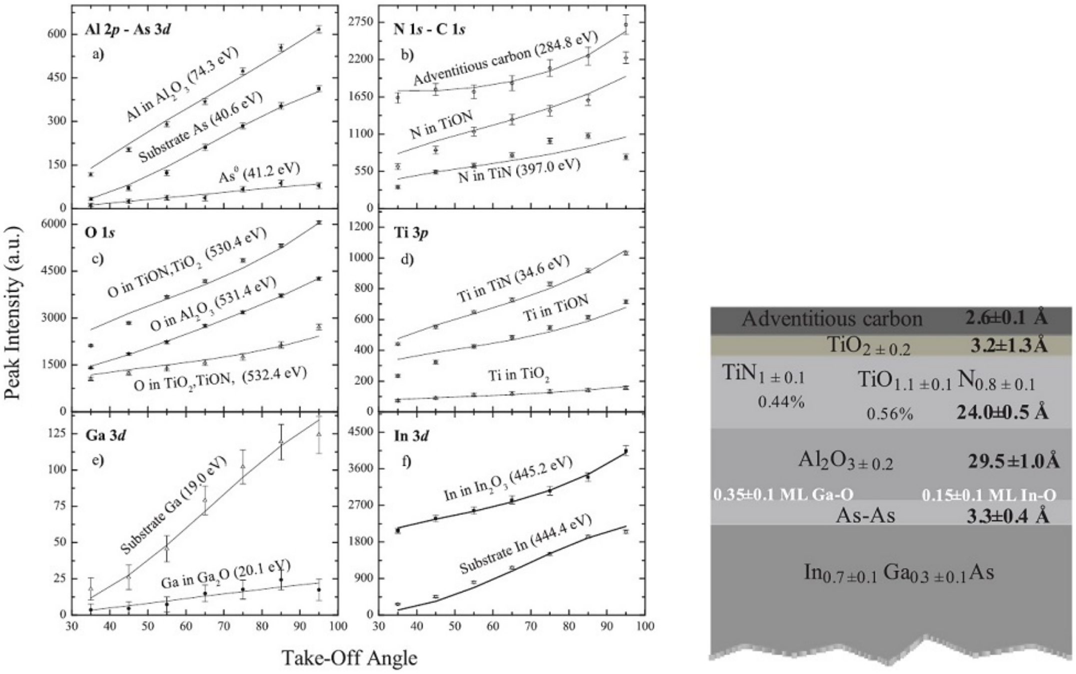

(a) (b)

Figure 15: *(a) Take off angle dependence of the peak areas for a TiN/Al_2O_3/InGaAs sample. The solid lines correspond to theoretical behaviour generated according to the physical model in (b). Extracted from [70].*

2.1.3 Variable kinetic energy

The method also relies on intensity determination of no-loss peaks. By increasing the photon energy, the IMFP (or EAL) of a given core-level photoelectron, thus the probed depth, increases. It allows to probe several interfaces [73] but requires the use of a reference sample to be quantitative. To probe the sample with various photon energies, different laboratory sources can be employed but the tunability of the photon energy delivered by synchrotron radiation is more adapted to the situation. This paragraph illustrates the simpler case of an overlayer thickness determination with illustration taken from *Rubio-Suazo et al.* [74] of determination of a Ge overlayer on Si semi-infinite substrate.

The peak intensity I, depending on the kinetic energy E_{kin} of the photoelectron of an element located between depth Z_A and Z_B, referenced to the bulk signal I^∞ is defined as:

$$I(E_{kin}) = \frac{I^\infty}{N_A^\infty \lambda(E_{kin}) \cos\theta} \int_{Z_A}^{Z_B} n_A(z) \exp\left(-\frac{z}{\lambda(E_{kin}) \cos\theta}\right) dz \qquad (41)$$

with $\lambda(E_{\mathrm{kin}})$ the EAL depending on the kinetic energy, $n_A(z)$ is the atomic density profile as a function of depth, N_A^∞ is the density of the bulk and ϑ is the angle between the surface normal and the emitted photoelectrons.

In the case of an overlayer A of thickness Z_A deposited on semi-infinite substrate B, the integral

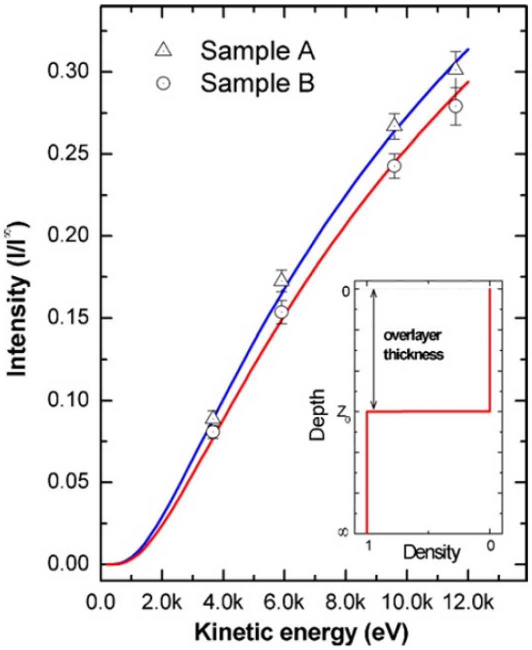

Figure 16: *Intensities of the Ge 1s and 2s photoelectron peaks normalized to the corresponding Ge-bulk signals, for sample A (triangles and sample B (circles). The fit (solid line) to the experimental data indicates the presence of a sharp interface between Si and Ge, without the formation of Ge oxide, for both samples. Extracted from [74].*

is evaluated between 0 and $\mathrm{Z_A}$ for the overlayer and between $\mathrm{Z_A}$ and infinite for the substrate, thus:

$$I_A = I_A^{\infty}\left[1 - \exp\left(-\frac{Z_A}{\lambda(E_{kin})\cos\theta}\right)\right] \tag{42}$$

and

$$I_B = I_B^{\infty}\exp\left(-\frac{Z_A}{\lambda(E_{kin})\cos\theta}\right) \tag{43}$$

By fitting the I_n/I_n^{∞} measurements as a function of the kinetic energy of the photoelectron as presented in Fig. 16, the thickness $\mathrm{Z_A}$ is obtained, corresponding in this case of to 8.9 nm-thick overlayer. The I_n^{∞} is the intensity of a pure semi-infinite sample measured in the same condition, hence is the requirement of a reference sample.

Many physical parameters such as the photoionization cross-section, the EAL and the plasmons intensity change with variation of the photon energy, complicating the retrieving of the depth profile and appearance of Auger peak can overlap with the measurement. However the method allows to obtain relative depth profile or simple overlayer model [75, 76, 77, 74], the concentrations of the elements depending upon depth profile have not been calculated yet. Similarly to ARXPS, specific data treatment is required in VKE-XPS to retrieve an accurate profile, such as MaxEnt presented previously.

2.1.4 Summary

The main limitation of core-level analysis is the probing depth of 3 IMFP. The choice between the three types of experiments for core-level depth profiling is up to the operator. This choice is mainly determined by the location of the point of interest and the in-depth precision needed:

- The sputtering depth profile technique can overcome the 3 IMFP probing depth limitation, but the use of the ion gun for sputtering induces surface modification and decreases the depth resolution. However with the use of depth resolution function a precision < 1 nm can be reached.
- The ARXPS is strictly limited to 3 IMFP. This experiment, with additional use of a regularization method gives the best accuracy possible, near atomic resolution, but is very sensitive to surface roughness and needs acquisitions of high resolution spectra, which can be rather long.
- The VKE-XPS can only be performed with use of several photon sources or in a synchrotron facility. It is difficult to extract the concentration versus depth profile, and to date VKE-XPS has mainly be used for qualitative depth profile or simple overlayer model.

2.2 Tougaard method for analysis of inelastic background

The two non-destructive methods to obtain depth profile presented in the previous Section are limited to the first 3 IMFP in probing depth, because they rely on determination of intensity of the no-loss peak. This Section exposes the inelastic background analysis, which is improving the probing depth up to 8 IMFPs with analysis of a single spectrum.

2.2.1 Principles

This method can be illustrated by spectra of Cu 2p depending on the Cu depth profile in a gold matrix as depicted in Fig. 17. The total amount of Au atoms in the near surface region varies in the four distributions but because of peak attenuation due to inelastic scattering, the observed peak intensities are identical. The inelastic loss shape at lower energy changes from one depth distribution to the other. This method is a modeling of energy loss distribution generated by the photoelectron during its transport in the material. The evaluation of the spectra is based on inelastic scattering cross-sections which may be calculated by a dielectric model. In contrast to the three step model described in sec.1.3.1 the phenomenological description used within Tougaard inelastic background analysis method uses the two step model described in sec.2.1.1.

Modeling of inelastic background is performed by computing the energy loss spectrum and subtracting it from the measured spectrum $J(E)$ to obtain only the spectrum $F(E)$ from photoionization of the element. If $F(E_0,\Omega)d^2\Omega dE_0$ is the photoelectron flux emitted from dE_0 around E_0 from the solid angle Ω, then $J(E,\Omega)$ the number of electrons emitted by second and energy unit in

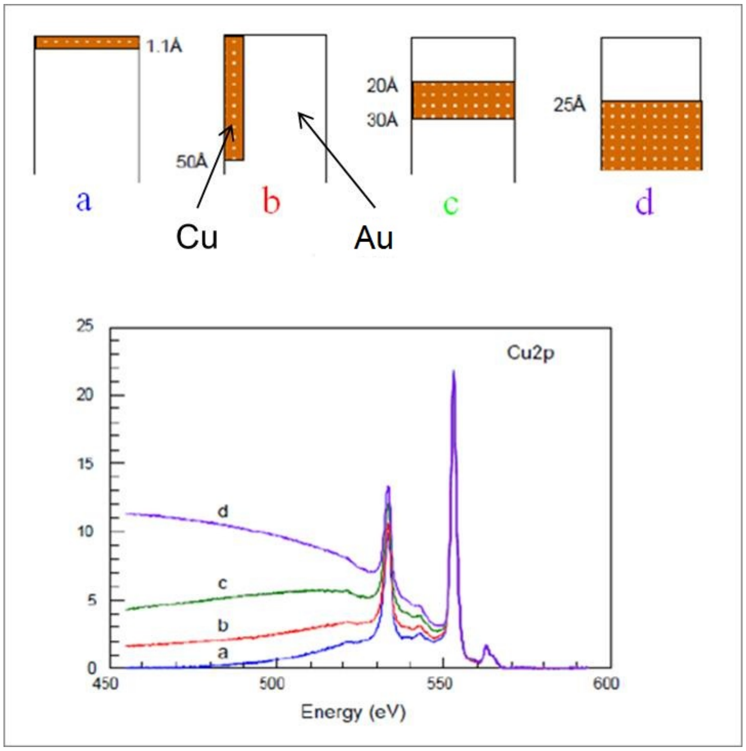

Figure 17: *First observation of influence of various depth distribution of copper (orange) inside a gold matrix (white) on inelastic background, from [78].*

solid angle Ω is [79]:

$$J(E,\Omega) = \int dE_0 F(E,\Omega) \int f(z) G(E_0, \frac{z}{\cos\theta}; E) dz \tag{44}$$

where f(z) is the depth distribution profile from the surface as a function of depth z of the considered element, *G(E)* is the probability that an electron with initial energy E_0 has an energy in the interval E,E+dE after having traveled a path $R = z/cos\theta$. If the energy loss is small compared to the energy of no-loss peak, then Landau showed [80]:

$$G(E_0, R; E) = \frac{1}{2\pi} \int\limits_{-\infty}^{\infty} e^{is(E_0 - E)} e^{-R\sum(s)} ds \tag{45}$$

with

$$\sum(s) = \frac{1}{\lambda_i} - \int_0^{\infty} K(T) e^{-isT} dT$$

where s is an integration variable without any physical meaning and K(T)dT is the probability for an electron of energy E_0 to lose energy between T and T+dT per unit path length traveled. To determine the intrinsic spectrum *F(E,Ω)*, a rigorous solution of eq.44 has been found [81]:

$$F(E,\Omega) = \frac{1}{P_1} \left[J(E,\Omega) - \frac{1}{2\pi} \int dE' J(E',\Omega) \int ds e^{-is(E-E')} (1 - \frac{P_1}{P(s)}) \right] \tag{46}$$

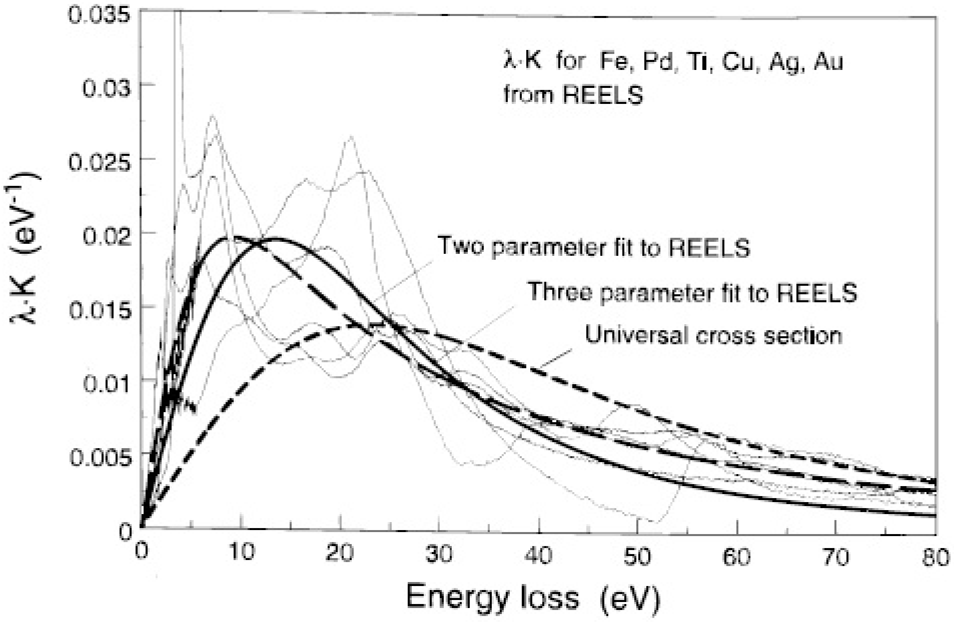

Figure 18: *Cross-sections for Fe, Pd, Ti, Cu, Ag and Au determined from REELS analysis and best least-square fits of the Two- and Three-parameters universal cross-sections of eq.49 and eq.50 respectively. Extracted from [85].*

with

$$P(s) = \int f(z)e^{(-z/\cos\theta)\sum(s)} \tag{47}$$

and

$$P_1 = \lim_{s\to\pm\infty} P(s) = \int_0^\infty f(z)e^{(-z/\lambda\cos\theta)}dz \tag{48}$$

This function can be evaluated by Fourier transform.

The inelastic scattering cross-section *K(T)* is the main parameter. These experimental curves which may be obtained by analysis of REELS experiments [82, 83] depend strongly on the material as can be seen in Fig. 18, but at energy > 30 eV, the individual inelastic scattering cross section have the same trend. The inelastic scattering cross section can also be expressed by mean of an universal curve obtained from least square-fitting of several samples, which is a good approximation for transition metals and their oxides[84] :

$$\lambda(E)K(E,T) = \frac{BT}{(C+T^2)^2} \tag{49}$$

with $C = 1643$ eV^2 and $B \simeq 3000$ eV^2. The cross-section is normalized to unit area with B=2C=3286 eV^2. For solids with sharp plasmon structure (like silicon, aluminum, germanium ...etc.) [85]:

$$\lambda(E)K(E,T) = \frac{BT}{(C+T^2)^2 + DT^2} \tag{50}$$

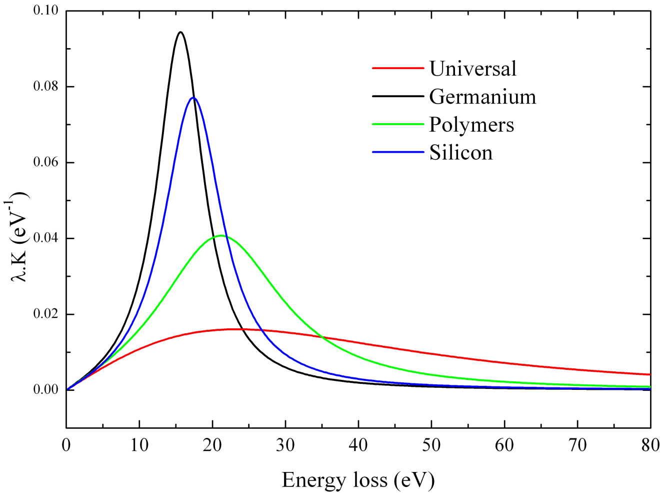

Figure 19: *Two parameter Universal cross-sections (red). Three parameters universal cross-section valid for Germanium (black), polymers (green) and silicon (blue) implemented in QUASES-Analyze.*

Modeling consists in varying f(z) in eq.46 until $F(E) \simeq 0$ beyond 30-40 eV below the no-loss peak.

The analysis takes into account the effects of inelastic scattering. However in cases where all detected photoelectrons arise from far in depth, the elastic effects can be of importance for the analysis [49]. From extensive Monte-Carlo simulation, it was found that this correction can be expressed as a simple parameterization factor *CF(z,ϑ,E)* accounting for the effects of elastic scattering. For the experimental geometry where $\theta < 30°$ (near normal emission) a simple expression was found [86]:

$$CF(z) = \exp(-0.157764\tau - 1.25132) + \exp(-0.0562417\tau^2 + 0.00698849\tau - 0.201962) \qquad (51)$$

where

$$\tau = \frac{z}{\lambda_{tr}\omega} = \frac{z(\lambda + \lambda_{tr})}{\lambda\lambda_{tr}} \qquad (52)$$

with z the burying depth of the element, λ_{tr} the transport mean free path, λ the inelastic mean free path and ω the single scattering albedo from eq.11.

2.2.2 Practical approach

The rigorous and general expression for *F(E,Ω)* in eq.46 has analytical solutions for some morphologies of depth distribution f(z) [87] shown in Fig. 20.

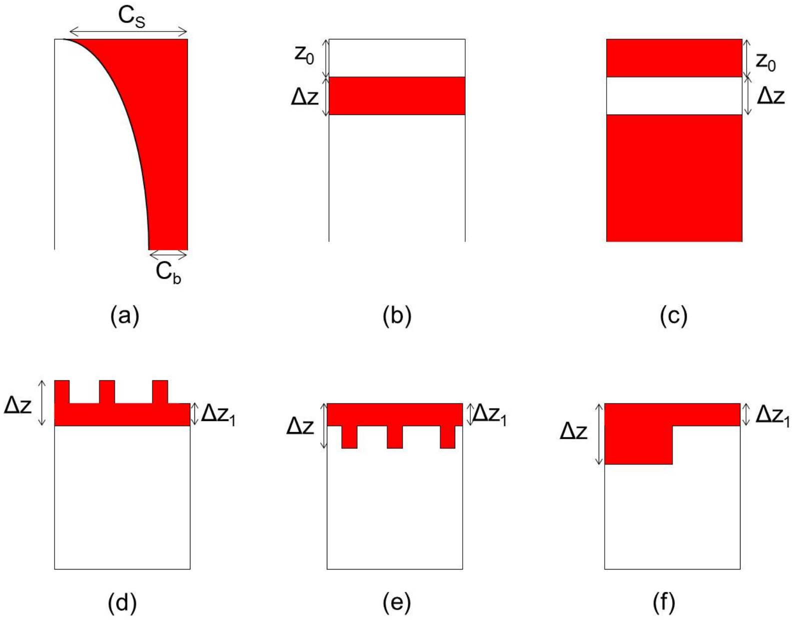

Figure 20: *Various depth profile morphology that can be analyzed with QUASES-Analyze: (a) exponential profile; (b) single layer; (c) Multilayer; (d) island with active substrate; (e) island with passive substrate; (f) islands. The structures (d), (e) and (f) give identical spectra. Adapted from [87].*

Homogeneous and exponential depth profile If the sample has an exponential profile in the form of

$$f(z) = Ce^{-z/L} \tag{53}$$

the exact solution of eq.46 becomes[88]:

$$F(E,\Omega) = \frac{L + \lambda\cos\theta}{C\lambda L\cos\theta}\left[J(E,\Omega) - \frac{\lambda L}{L + \lambda\cos\theta}\int_E^\infty dE' J(E',\Omega)K(E'-E\right] \tag{54}$$

and then for an infinite sample where L→∞ then

$$F(E,\Omega) = \frac{1}{C\lambda\cos\theta}\left[J(E,\Omega) - \lambda\int_E^\infty dE' J(E',\Omega)K(E'-E)\right] \tag{55}$$

if one assumes that the sample is homogeneous, i.e. the concentration is constant in the bulk then eq.53 becomes

$$f(z) = (C_s - C_b)e^{-z/L} + C_b \tag{56}$$

and analytical expression of 48 can be found

$$P_1 = C_b\lambda\cos\theta + (C_s - C_b)\frac{L\lambda\cos\theta}{L + \lambda\cos\theta} \tag{57}$$

and

$$P(s) = C_b \frac{\cos\theta}{\sum(s)} + (C_s - C_b) \frac{L\cos\theta}{L\sum(s) + \cos\theta} \tag{58}$$

Layered profile If one consider a delta layer profile where N atoms are located at depth z_0

$$f(z) = N\delta(z - z_0) \tag{59}$$

and the exact expression of eq.48 becomes

$$P_1 = Ne^{-z_0/(\lambda\cos\theta)} \tag{60}$$

and eq.47 is

$$P(s) = Ne^{-z_0\sum(s)/\cos\theta} \tag{61}$$

This case is very uncommon in real devices. Instead the atoms are mostly localized between z_0 and $z_0+\Delta z$, thus eq.60 and 61 can be written with

$$f(z) = \begin{cases} 0 & for\; 0 < z < z_0 \\ C_A & for\; z_0 < z < z_0 + \Delta z \\ 0 & for\; z_0 + \Delta z < z \end{cases} \tag{62}$$

and then

$$P_1 = C_A \lambda \cos\theta e^{-z_0/(\lambda\cos\theta)} \left[1 - e^{-\Delta z/(\lambda\cos\theta)}\right] \tag{63}$$

and

$$P(s) = C_A \frac{\cos\theta}{\sum(s)} e^{-z_0\sum(s)/\cos\theta} \left[1 - e^{-\Delta z\sum(s)/\cos\theta}\right] \tag{64}$$

These equations can also be used to represent a surface overlayer with thickness Δz (where z_0=0) or for a substrate located at depth z_0 (where $\Delta z \rightarrow \infty$).

Equations for modeling island structure have also been found [87] but as they will not be used in the following they are not be described here.

Equations of 2.4.2 are implemented in a commercial software, QUASES-Analyze® [89]. This software is very user friendly, as can be seen in Fig. 21, only the geometry of the experiment (Angle of emission) and the IMFP value have to be input by the user. There is a possibility to change the inelastic scattering cross section, choosing between the two parameter universal cross section valid for transition metals and their oxides and the computed cross sections for specific elements (polymer, SiO_2, Si, Ge, Al). The user also has the possibility of performing modeling with its own inelastic scattering cross section (X-Sect, determined for example from a REELS experiment). The software can perform simple manipulation of the data, as noise reduction, correcting it for analyzer transmission and subtracting linear background. The user can choose between several morphology classes to perform modeling. By clicking on "Buried Layer", the buttons "Start Depth" and "End Depth" opens, and the user can click step by step to increase or decrease the interface locations until a good match between the modeling and the measurement is found. The resulting subtracted spectrum is also plotted (in Fig. 21, the top interface position is set to be 7 nm below the surface and the bottom interface is out of the probed depth).

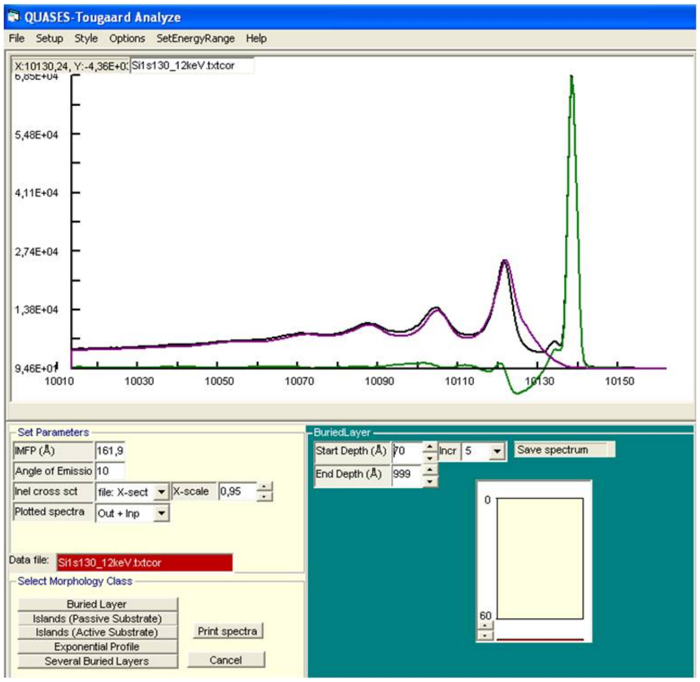

X:10130,24, Y:-4,36E+0: Si1s130_12keV.txtcor

IMFP (Å) 161,9

Angle of Emissio 10

Inel cross sct file: X-sect X-scale 0,95

Plotted spectra Out + Inp

Data file: Si1s130_12keV.txtcor

Start Depth (Å) 70 Incr 5

End Depth (Å) 999

Figure 21: *Print screen of the QUASES-Analyze ® software. The measurement is in black, the modelled inelastic background is in purple and the subtracted spectrum is in green.*

2.2.3 Comparison with the Shirley background

The so called Shirley background [90] is used to correct spectra from inelastic scattering in the vicinity of the no-loss peak. The background due to inelastic collision is the exact equivalent of [79]:

$$S_T(E) = \int_E^{+\infty} K(E' - E) j'(E) dE' \tag{65}$$

where *j'(E)* is the measured spectrum at energy E and *K(T)* is the inelastic energy loss cross-section function. Assuming that *K(T)* is constant, the Shirley background correction *S_S(E)* can be expressed as [91]:

$$S_S(E) = k \int_E^{+\infty} dE' (j(E') - S_{S,0}(E')) \tag{66}$$

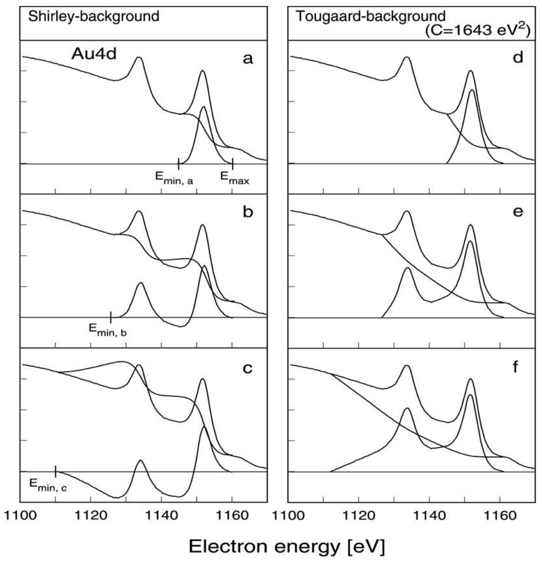

Figure 22: *Comparison between Shirley and Tougaard backgrounds on Au 4d: (a) Shirley background for Au $4d_{5/2}$; (b) Shirley background for Au $4d_{3/2}$; (c) Shirley background for Au $4d_{3/2,5/2}$; (d) Tougaard background for Au $4d_{5/2}$; (e) Tougaard background for Au $4d_{3/2}$; (f) Tougaard background for Au $4d_{3/2,5/2}$.*

where $S_{S,0}(E')$ is a constant background taken at energy E' defined by the operator. The Shirley background is then iteratively computed as:

$$S_{S,i}(E) = k \int_{E}^{+\infty} dE'(j(E') - S_{S,i-1}(E')) \tag{67}$$

it was shown [92] that a specific $K_S(T)$ applied to 65 can reproduce the behaviour of the iterated Shirley background if $K_S(T)$ is expressed as:

$$K_S(T) = \frac{B_S}{C_S + T^2} \tag{68}$$

where T is the energy loss, B and T are parameters.

In practice the Shirley background is set to correct for inelastic scattering of photoelectrons in the vicinity of the no-loss peak and results as a step-like background as can be seen in the left panels of Fig. 22.

The expression of the energy loss depicted in the Shirley background (eq.66) can be seen as the kernel function in eq.68 of the Tougaard background (eq.68 and 49-49). The Tougaard Universal cross-section (eq.49-50) is a functional form fit to the average of several materials. It can be widely used but as it uses the energy loss T as a multiplier it enforces a linear behaviour of the cross-section at low energy loss (i.e. in the vicinity of the no-loss peak). In practice the Shirley background is calculated for a precise energy range and not to infinity as it should be (see eq.67). The resulting shape of the Shirley background depends on the selected energy range. This is less important in the case of the Tougaard background as can be seen in Fig. 22 where Au 4d of a pure gold sample is measured and the effects of applying Shirley background or Tougaard background over different energy ranges are compared. The Tougaard background shape does not depend on

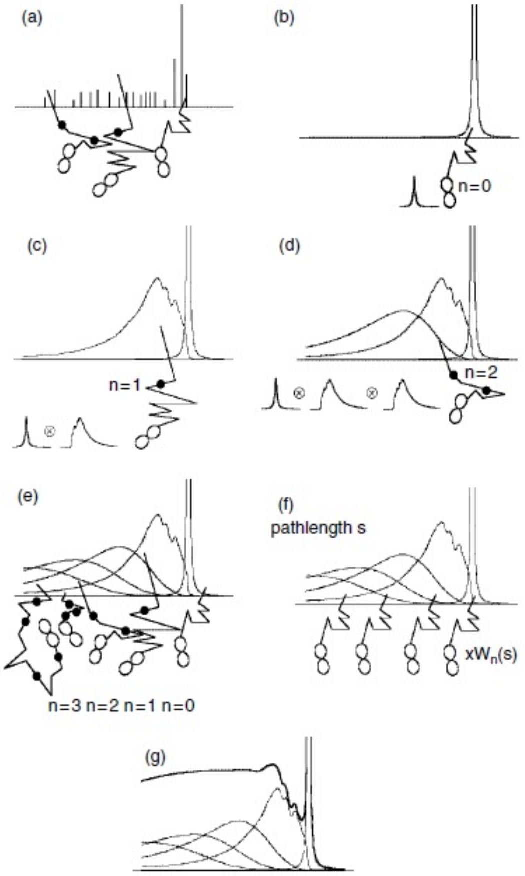

Figure 23: *Illustration of the method used. (a) direct simulation approach, (b-e) contribution of scattered electrons. The sum of all these scattered electrons gives (e) and (f) is the sum affected by coefficients. The resulting spectrum (g) is obtained. From [96].*

the selected energy range and thus provides a more robust solution for subtracting the effects of inelastic scattering of the photoelectrons. For an expert user, this limitation is well known and the obtained result with Shirley or Tougaard background are consistent if specific ranges were used for Shirley background [93].

2.2.4 Comparison with the Partial intensity approach (PIA)

This particular method has the advantage to be potentially the fastest in terms of computing time (it has been developed for simulation program SESSA [94, 95]). The method uses a mathematical decomposition of the signal where the sample is referred as a multilayer; and every layer has a contribution to the no-loss peak and inelastic background [96]. In a simple picture depicted in Fig. 23, it is possible to see that the inelastic background is composed of electrons that suffer quantified inelastic losses and the sum of these contributions, affected by coefficients, forms the overall inelastic background.

Principles The method uses an equivalent of the quasi-elastic (QE) approximation or constant cross-section approximation, where the electron-solid interaction is independent of the value of the energy loss [97]. It is justified as the energy lost in a scattering event is small compared to the initial energy of the photoelectron. This approximation is strengthened when using hard x-rays. It also assumes that the energy $f_0(E)$, the angular distribution $g_0(\vec{\Omega})$ and depth distribution $c_0(z)$ are uncorrelated. Then the source function $S_0(E, \vec{\Omega}, z)$ can be written as:

$$S_0(E, \vec{\Omega}, z) = f_0(E) \times g_0(\vec{\Omega}) \times c_0(z) \tag{69}$$

The measured spectrum Υ can be expressed with a term $G(s,T,\mu)$ representative of the energy loss T [96], assuming a plane symmetry:

$$\Upsilon(E, \mu) = \int_0^\infty \int_0^\infty \int_{4\pi} G(z, T, \mu) \times S_0(z, E + T, \mu) dz dT d\Omega \tag{70}$$

with Ω the solid angle and μ the polar deflection.

This formula describes the physical dependence of the measured spectrum. The principle of the partial intensity is to express the energy distribution of Υ as the sum of photoelectrons who suffer n times an inelastic scattering event. These photoelectrons are affected with a coefficient C_n corresponding to the number of particles participating to a loss process. The eq.70 can be written in a more convenient form as [98]:

$$\Upsilon(E, \mu) = \sum_{n_1=0}^{\infty} \sum_{n_2=0}^{\infty} \sum_{n_3=0}^{\infty} C_n(\mu) \Gamma_n(T) \otimes f_0(E + T) \tag{71}$$

with Γ_n the distribution of energy loss after n scattering event, f_0 the source energy distribution and $\otimes$ denotes a convolution over the energy. If the inelastic events are considered as uncorrelated then :

$$C_{n_1,n_2,n_3\dots}(\mu) \backsim C_{n_1 n_2 n_3\dots}(\mu) = \int\limits_0^\infty Q(s, \mu) W_{n_i}(s) ds \tag{72}$$

with Q(s) the pathlength distribution and $W_{n_i}(s)$ is the Poisson stochastic process. In the straight line approximation (SLA), the deflections are neglected and any two points in space are connected by a unique straight line path, thus Q(s) is expressed as a delta function and:

$$C_n(\mu) = \int\limits_0^\infty \left(\frac{z}{\lambda\mu}\right)^n \frac{\exp(-z/\lambda\mu)}{n!} c_0(z) dz \tag{73}$$

where z represents the depth of the element, λ is the inelastic mean free path and c0(z) is the compositional depth profile.

The surface excitation can be taken into account using the Tung model where the surface scattering zone is approximated by a straight line [99], the surface and volume scattering are uncorrelated, then:

$$C_{n_b,n_s} = C_{n_b} \times C_{n_s} \tag{74}$$

where C_{n_b} is the n-fold inelastically scattered bulk coefficient and C_{n_s} is the n-fold inelastically scattered surface coefficient. This approximation is not strictly adequate but has been shown to be effective [100]. The equation 71 can be written when taking surface effects into account as:

$$\Upsilon(E) = \sum_{n_b=0}^{\infty} \sum_{n_s=0}^{\infty} C_{n_b} C_{n_s} \Gamma_{n_b}(T') \otimes \Gamma_{n_s}(T) \otimes f_0(E+T+T') \tag{75}$$

The contribution of the various loss processes can be subtracted to the measured spectrum if the sequence of partial intensities $\mathrm{C_n}$ and the loss function $\mathrm{L_n}$ are known using [101]:

$$\Upsilon_{k+1}(E) = \Upsilon_k(E) - q_k \int \Upsilon_k(E+T) L_k(T) dT \tag{76}$$

where $q_k = q_k(C_n/C_0)$. This operation is applied to the measured spectrum until convergence over the considered energy range. It ultimately yields to $\mathrm{f_0}$. If the solid is homogeneous with isotropic emitters then $C_k = q_1 C_{k-1}$and

$$f_0(E) = \Upsilon(E) - q_1 \int \Upsilon(E+T) \omega(T) dT \tag{77}$$

Practical approach The Partial Intensity Approach is implemented in the SESSA software which uses the symmetry property of the linearized Boltzmann equation (the source and the detector are inverted in the algorithm) [102, 103]. The software can compute the distortions of the inelastic background, relevant to depth profiling, but is mostly used for analysis of the no-loss peak by resolution of the Eq.76 with n=0. It has the great advantage to use the large NIST database [20, 40, 104] as can be seen in Fig. 24. The software has been recently implemented with possibility of analysis of surface nanostructures and specific HAXPES experiments [105].

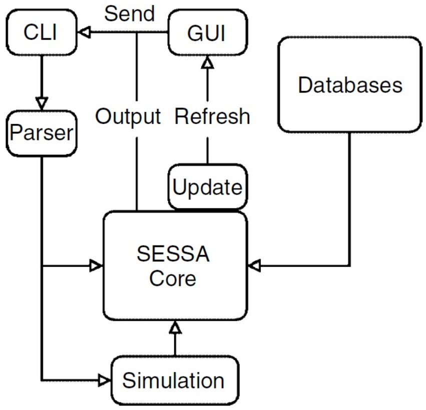

Figure 24: *Schematic illustration of the internal structure of SESSA. User interacts with the software through CLI (command line Interface) or GUI (Graphical User Interface), from [94].*

2.3 Conclusion of Chapter II

The characterization techniques presented in this Chapter allows to analyze deeply buried layers. The analysis relying on the no-loss peak such as ARXPS or VKE-XPS are limited in probing depth up to 3 IMFP. The VKE-XPS allows to obtain relative depth profile and overlayer thickness whereas the ARXPS can retrieve depth distribution at nanometric scale. The sputtering depth profile can overcome the 3 IMFP limitation with accuracy up to the nanometer resolution but destroys the sample. All these methods present various degrees of sophistication and require modeling for ultimate accuracy.

During the photoemission process, the photoelectron can suffer various physical excitations: the **intrinsic** excitations due to the core-hole creation; the **extrinsic** excitations corresponding to the energy loss during the transport of the photoelectron, the **multiple** excitations and **interferences** between intrinsic and extrinsic excitations. The multiple excitations in a single scattering event are negligible regarding their intensity contribution to the no-loss peak and the inelastic background. The interference terms can be evaluated only if the intrinsic and extrinsic contributions are known. The intrinsic and extrinsic excitations give rise to a *tail* of lower energetic photoelectrons, the influence of intrinsic excitation being lower in intensity and in energy loss than the extrinsic contributions.

The main advantage over the no-loss peak analysis which unravels the chemical environment of the element over the first 3 IMFP is the **increasing of the probing depth up to 8 IMFP for the analysis relying on the inelastic background** [49] as illustrated in Tab.1. Three different kinds of inelastic background modeling have been shown:

The **Shirley background** is usually employed when analyzing the no-loss peak, as it corrects the spectrum for inelastically scattered electrons **in the vicinity of the no loss peak**. It is used

	Soft x-ray (hν = 1487 eV)	Hard x-ray (hν = 10000 eV)
Kinetic energy (eV)	1387.4	9900.4
IMFP (nm)	3.1	16.4
no-loss peak probing depth (3xIMFP) (nm)	9.3	49.2
inelastic background analysis probing depth (8xIMFP) (nm)	24.8	131.2

Table 1: *Theoretical maximum probed depth for Si 2p of 99.6 eV. The IMFP calculated from TPP-2M formula.*

for almost every analysis of core-level, but its intensity depends on the selected energy range on which it is applied. As emphasized by *Shirley*, it is an empirical formula depending on the density of states of the sample.

The **PIA** has the advantage to treat the no-loss peak and the inelastic background with the same theory frame, but relies on a mathematical deconvolution depending on the sample. The practical application for the PIA is done by SESSA and can properly function with help of the NIST database.

The **Tougaard method** corrects the measured spectrum from **extrinsic excitations**, leading to the intrinsic spectrum of the element. By measuring a reference sample (pure and homogeneous), the intrinsic spectrum can be obtained, and this can be used to perform inelastic background modeling with great accuracy. The Tougaard method is very efficient to analyze the observed **changes** in the inelastic background and from this to determine the corresponding changes in atom depth distributions. The two step model (in which thesurface effects are neglected) is well adapted to HAXPES (in which bulk contributions dominate). The next Chapter will illustrate the implementations made in this work to successfully perform inelastic background analysis in HAXPES spectra with good accuracy.

3 Implementations and limits of background analysis in HAXPES

This Chapter is dedicated to the setting up of background analysis of HAXPES spectra. One of the main advantages of the inelastic background analysis is that the depth distribution of a buried layer can be extracted from a single spectrum recorded at a fix experimental geometry. The background analysis was originally developed for soft x-ray experiments.The photon energy has a great influence on the photoionization, the inelastic mean free path and the signal/noise ratio affecting the measurement.

This Chapter presents the implementations of the method for specific applications to HAXPES spectra. The accuracy and the sensitivity of the method will be discussed by focusing on two different situations encountered when studying the same type of MOSFET samples using Hard X-Ray PhotoEmission:

- A deeply buried monolayer of lanthanum will be analyzed to demonstrate the sensitivity and accuracy of the method. This study is of high importance as the lanthanum depth distribution is critical for device performance. The study of La 3d and La 4f are rather complex in XPS due to shakeup and charge transfer processes. The burying depth $>$50 nm below the surface is limit, even with use of hard x-rays photons (due to the large peak intensity attenuation, analysis of the no-loss peak almost impossible).
- Multiple layers of silicon, with various chemical environment and depths, which is a difficulty in background analysis to illustrate the accuracy of the depth distribution obtained.

The results obtained by inelastic background analysis will be compared with results from other characterization techniques. Effects of experimental and methodological parameters will be discussed as well as the advantage of using a reference sample in the analysis.

3.1 Experimental methods

3.1.1 High-k MOSFET

Metal Oxide Semiconductor Field Effect Transistor or MOSFET is the principal component of integrated circuits. Its success comes from the ability to be easily made as type P or type N (PMOS or NMOS). The association of two types of transistors is called Complementary MOS (CMOS). It allows to perform complex logical functions and limits the energy consumption of the device.

The first MOS device with silicon substrate fully operational was made by *D. Kahng and M. Atalla* in 1962 [106]. It operates on the transport modulation of charge density in a semi-conductor

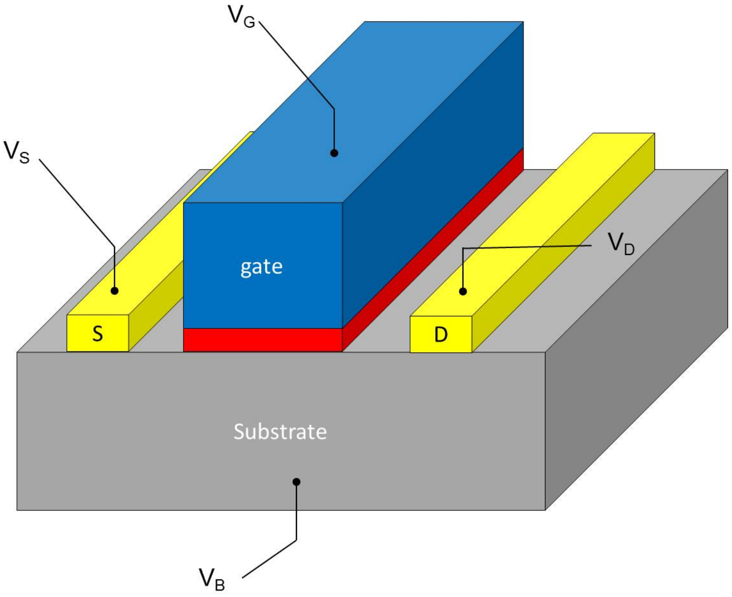

Figure 25: *Scheme of a MOS transistor. (S) is the source; (D) is the drain; the red layer corresponds to the conduction canal.*

layer (*conduction canal*) by ways of a perpendicularly applied electrical field. Creation of carriers by field effect is ruled by the polarization V_G of the electrode called *grid* through an insulating layer called *dielectric*. Transport of the carriers in the canal is done by pulse of a differential potential V_D between two charge reservoirs, the *source* and the *drain*.

The transistor goes from a blocked state where $V_G = 0$ V (the drain current I_D is then equal to the leakage current I_{OFF}) to an operating state where grid polarization is equal to drain polarization ($V_G = V_D$) allowing the drain current I_{ON} to flow. The effective switching from these two states is only possible when the applied grid tension V_G is superior to a minimum value V_{th} specific to the device.

From this stage, the architecture of the MOSFET has not changed. The component size reduction down to a few nanometers has made the initial dielectric layer of SiO_2 downscale to 5 nm in MOS devices. At this thickness the leakage current can be significant [107]. Therefore to further decrease the dielectric layer thickness, the replacement of the SiO_2layer by new material is compulsory. Amongst other candidates, Hf and La oxides appeared to be promising as they present a high oxide capacity and a reduced leakage current [108]. They are isolated from the silicon substrate by an interfacial layer (IL) of SiON to reduce the lattice parameter [109]. The gate had also been improved by substituting a metal to the usual silicon because of depletion in silicon and Fermi level pinning [110]. TiN metal is used both for its compatibility with CMOS technology and its ability to be easily p- or n-doped (for NMOS or CMOS components).To control

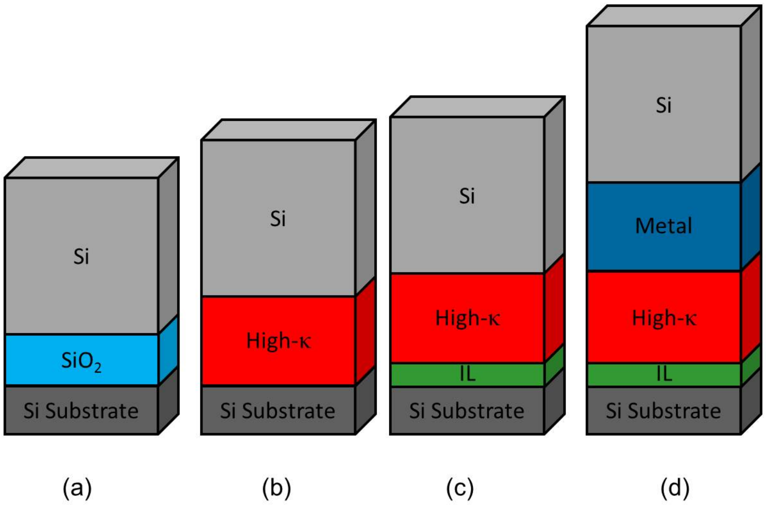

Figure 26: *Scheme of evolution of the structure of the gate for a MOSFET structure. (a) original design; (b) after introduction of a high-κ; (c) introduction of an Interfacial Layer (IL); (d) integration of a metal gate.*

the threshold voltage V_{th} precisely, insertion of a thin lanthanum oxide has been integrated in the device in form of a LaO_x layer between the TiN and the HfSiON layers. Addition of LaO results in a decreasing of V_{th} and is then used for NMOS components. The obtained improvement is measured as the Equivalent Oxide Thickness (EOT), expressed as a function of the thickness t and dielectric constant K of the considered high-k oxide as:

$$EOT = t_{eq} = \frac{\kappa_{SiO_2}}{\kappa_{high-k}} t_{high-k} \tag{78}$$

When the dielectric layer is formed by two layers of thickness T and relative permittivity ε then the EOT is expressed as the sum of the contributions:

$$EOT = \varepsilon_{SiO_2}(\frac{T_1}{\varepsilon_1} + \frac{T_2}{\varepsilon_2}) \tag{79}$$

3.1.2 Samples description

The samples used in this experiment were manufactured by STMicroelectronics. They are made to be integrated in CMOS industrial technology manufacturing as gate part of the device. They were prepared in a *gate-first* integration process on 300 nm Si(100) wafers; this *gate-first* process is used when dopants are activated through annealing after the deposition. This annealing induces diffusion in the already-made stack, which can decrease the device performances if not well controlled. Thicknesses of deposited layers and their depth distribution before and after annealing must be characterized for the final composition of the stack to assess diffusion process.

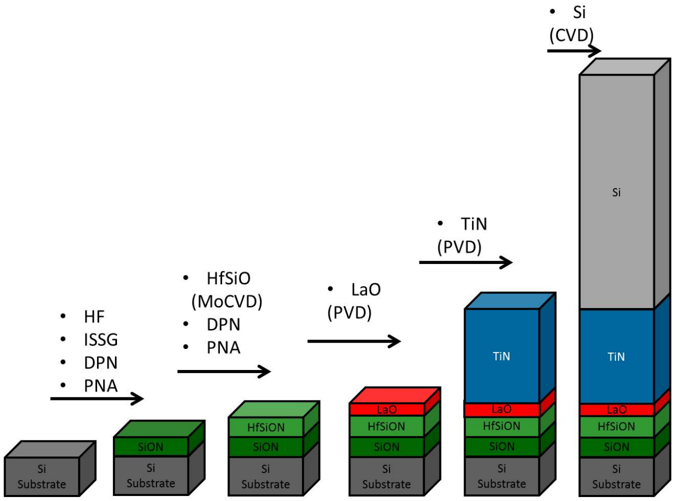

Figure 27: *Sample production scheme.*

The sample growth is schemed in Fig. 27. The first step is to get rid of the native oxide on the silicon wafer, this is done with a HF-SC1 cleaning operation. The amount of silicon oxide after this chemical cleaning is 0.8 nm and is used to grow a thin SiON interfacial layer (IL) in three steps: oxidation of the silicon substrate with in-situ steam generation (ISSG) at 1025°C; decoupled plasma nitridation (DPN) and post nitridation annealing (PNA); the resulting thickness of the SiON layer is 1.5 nm.

The high-k dielectric HfSiO film is deposited by Metal-Organic Chemical Vapor Deposition (MOCVD) of HfSiO followed by DPN and PNA which nitrides the film (nitride dose of 10^{15} at.cm^{-2}) to obtain a HfSiON layer of 1.7 nm.

La layer is deposited by Physical Vapor Deposition (PVD), to avoid any carbon contamination. The thickness of the layer is of 0.4 nm.

The metal gate stack is composed of a 6.5 nm TiN film deposited by PVD. This specific choice of metal has been motivated by its work function which can be tuned close to the conduction band or the valence band of silicon, depending on the doping element (between 4.1 and 4.3 eV for N-type and between 5 and 5.2 eV for P-type) and its thermal stability compatible with a *gate-first* process. Two samples were then prepared to investigate the effect of burying depth in HAXPES analysis, a 20 nm-thick, a 30 nm-thick and a 50-nm thick amorphous Si (a- Si) films were deposited using Chemical Vapor Deposition (CVD) with a maximum thermal budget of 600°C, the sample will thereafter be named by their silicon thickness, namely *20 nm sample*, *30 nm sample* and *50 nm sample.*

The same stack was realized with an increasing active layer thickness of 1.5 nm-thick HfSiON and 1 nm-thick La layer. This sample with a 20 nm thick amorphous Si presents the same TiN thickness of 6.5 nm as the *20 nm sample.* This sample will be referred as *high-k sample.*

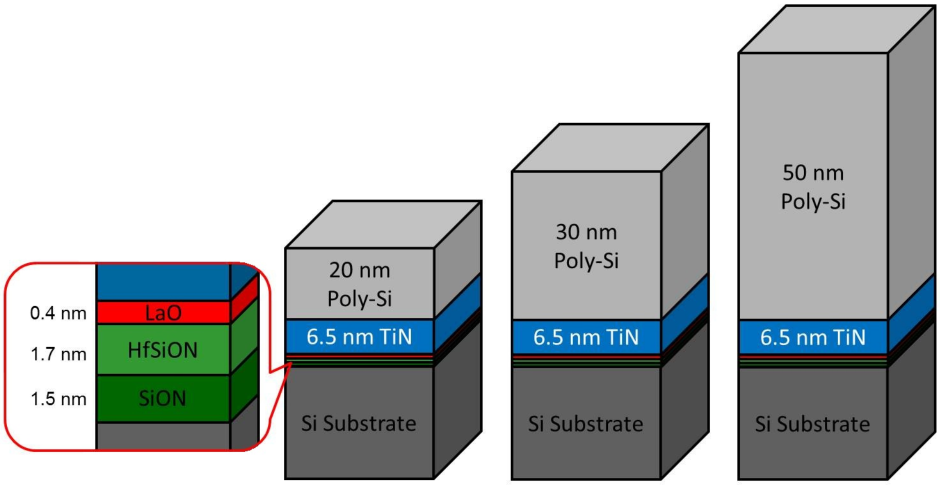

Figure 28: *Sample scheme of the metal gate architecture typically used in CMOS technology. The thicknesses are at scale with respectively 20 nm, 30 nm and 50 nm top electrode composed of polysilicon.*

The samples were studied using many techniques. The primordial control step in such devices is to perform very thin active layer to decrease the EOT.

As a result, the active layer of the device is composed (from top to bottom) of a $\mathrm{LaO_x}$ monolayer, a HfSiON layer of a few nanometres and a very thin SiON layer. Lanthanum and Hafnium have such a close atomic number that differencing the two layers is not possible in TEM. La and Hf present well separated peaks in photoemission but these active layers are located 50 nm below the surface for the real device. Such a depth is not accessible with classical XPS and this kind of samples has to be studied by XPS at each of the step, but not on the final device. This Chapter will show how combining HAXPES and inelastic background analysis ensure to probe the entire device. The schemes of the samples presented in Fig. 28 are at scale and illustrate the difficulty of such an analysis when the total active layer composed of three nanometric layers with different elemental composition is buried under two different layers (the poly-Si top electrode and the TiN metal barrier). The actual technological device is composed of a 50 nm top amorphous Si (a-Si) electrode but to investigate the effect of the burying depth for HAXPES analysis, a 30 nm-thick a- Si top electrode will also be investigated.

The deepest buried layer presently published is for a layer located at 20 nm below the surface. A method is presented here that enables to obtain the depth distribution deeper than this value.

3.1.3 Beamlines description

Three different beamlines were used in this work, their experimental stations are shown in Fig. 29. The ID32 beamline from ESRF [111] was used to measure the sample at very high photon energies up to 18 keV; BM25 from ESRF [112] was used to compare the data; GALAXIES from SOLEIL [113] was used to have the highest resolution and constant flux.

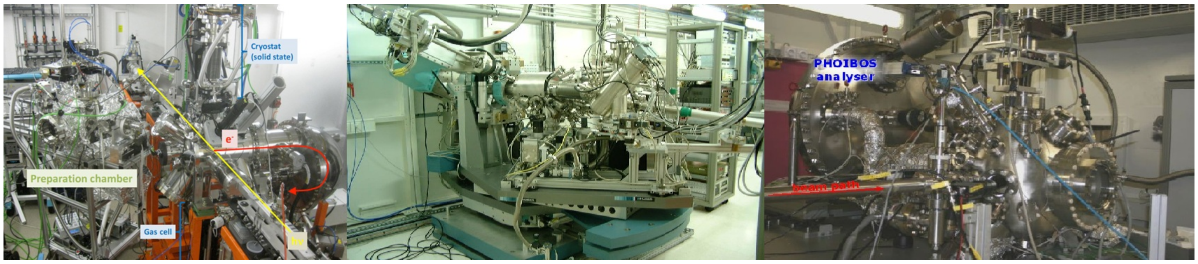

Figure 29: *Pictures of the used beamlines, (a) GALAXIES from SOLEIL synchrotron; (b) BM25 from ESRF; (c) ID32 from ESRF.*

High energy beamline: ID 32, ESRF. The ID32 beamline of the European Synchrotron Radiation Facility (ESRF, Grenoble, France) was a high energy beamline with photon range delivery between 2.5 and 25 keV. This beamline supplied the highest photon energy available among the three beamlines used, successfully measuring photoelectrons with photon energy as high 18 keV. Due to high energy storage ring of 6 GeV, the peak flux measured at 25 m was 7.10^{14}ph s^{-1} mm^{-2}, 0.1% bw, 0.2 A. In order to achieve maximum bulk sensitivity and to optimize for signal intensity, the incident photons impinged on the sample at an angle of 10° and photoelectrons were detected at an angle of 80° both with respect to the surface sample. To reduce data acquisition time, the most relaxed incident beam energy resolution of 1.6 eV available at the given energy with a Si(111) monochromator was used in order to maximize the photon flux. Further signal intensity optimization was achieved by a choice of the largest entrance slit on the electron energy analyzer. The SPECS PHOIBOS 225 high resolution spectrometer fitted with entrance optics enabled the analysis of high kinetic energy photoelectrons up to 15 keV. This experimental setup led to the overall energy resolution of 4.7 eV at 15 keV when fitting the Fermi level of gold sample inside the analysis chamber. ID32 was closed for user experiments on 5 December 2011.

Intermediate beamline: BM25, ESRF. BM25 beamline of the European Synchrotron Radiation Facility (ESRF, Grenoble, France) is also designed to deliver high energy photons but has the particularity of having a bending magnet as insertion device. This ensures a wide photon energy accessibility but a lower photon flux, estimated to be 1.10^{14} ph s^{-1} mm^{-2} 0.2 A on the sample. The experimental station is designed to perform high energy photoemission experiments with an electrostatic cylinder-sector FOCUS HV CSA capable of measuring high kinetic energy photoelectrons up to 15 keV. As the method does not imply high energy resolution, the beamline was setup to deliver the maximum photon flux possible by decreasing the resolution. As for ID32 beamline the photon flux is measured through a gold grid and the associated current I_0 is used to normalize the measurements intensity. Unlike other experiments, the geometry of the experiment had to be changed, with photons impinging the surface from 75° from surface normal and emergent photoelectrons were detected with an angle of 15° from the surface normal due to the beam size.

However this slight change doesn't modify strongly the measurement as the signal is only decreased by the cosine of the emission angle from the surface normal.

High flux beamline: GALAXIES, SOLEIL. GALAXIES beamline from SOLEIL synchrotron (Saclay, France) is one of the most recent HAXPES beamlines available for user experiments. This specific synchrotron works in a so-called top-up mode. In this particular mode, electrons are continuously injected from the booster to the storage ring in order to maintain the current constant, and so a constant photon flux in the beamline. For this reason, the photon flux doesn't need to be measured at every acquisition, the spectra can be easily compared in intensity. The beamline is designed to provide a monochromatic focused beam with the highest flux possible in the 2.4-12 keV ($1.5\text{x}10^{12}$ ph s^{-1}) spectral range and an adaptable photon energy bandwidth between 100 meV and 1 eV. The estimated X-rays spot at the focusing point onto the sample is 30 x 100 um [VxH] FWHM. The HAXPES chamber is equipped with a EW4000VGScienta hemispherical photoelectron analyzer with a 60° angle. In the experimental geometry used for the study, photons impinge the surface with an angle of 10° and the analyzer is located at 80° with respect to the surface sample.

3.1.4 Characterization with other techniques

Depth distribution profiles of lanthanum obtained for TEM measurements, Atom probe Tomography, Auger depth profiling and Inelastic Background Analysis are summarized in Tab.2.

Method	Top interface (nm)		Bottom interface (nm)		Thickness (nm)	
	Nominal	Measured	Nominal	Measured	Nominal	Measured
Background Analysis	56.5	57.3	56.9	61.8	0.4	4.5
Auger Depth Profiling		60.0		70.0		10.0
TEM (La + Hf)		55.7		57.1		1.4
Atom Probe Tomography						1.0

Table 2: *Depth distribution of lanthanum for 50 nm sample.*

TEM and EELS Because La and Hf have an atomic number too close one from each other (^{57}La and ^{72}Hf) and the 1ML La layer is located just next to the Hf-containing layer, TEM experiment cannot give a straightforward result for this type of stack. The result for *50 nm sample* from TEM experiment can only give the combined thickness of the La and Hf layers. The a-Si and TiN thicknesses obtained are very accurate so that the burying depth of the active layer can be estimated at 51.1 nm below the surface. Fig 30 shows a high-resolution TEM image measured using a JEOL 2010FEF operated at 200 kV with an overall lateral resolution better than 0.2 nm. The image shows the 1.4 nm-thick SiON layer, below an intermixed HfSiON and LaO_x layer; the

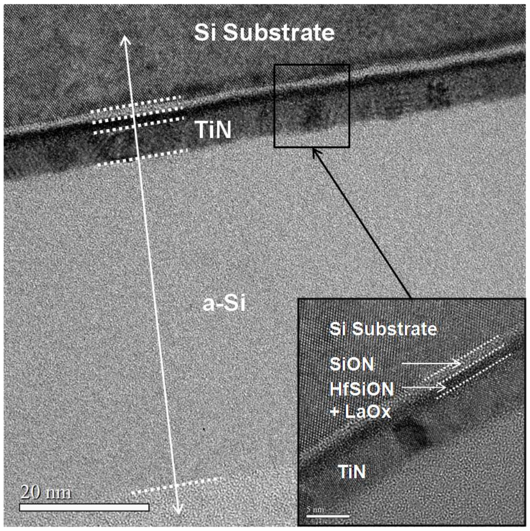

Figure 30: *TEM cross-section image of the 50 nm sample.*

overlayer thicknesses are 4.6 nm (TiN) and 51.1 nm (a-Si). The depth of the top La interface is thus determined at 55.7 nm according to the measured thicknesses of TiN and a-Si.

STEM-EELS measurements in Fig. 31 are obtained at 80 kV using the quantification tools made by Gatan which allows to obtain the relative concentration of each element. The resulting depth profile obtained confirms the complete intermixing of the LaO_x and the HfSiON layers; the overall thickness is found to be 1.4 nm. The active layer shows a very high concentration of oxygen which is not present in the TiN layer. The interface between the substrate and the active layer is rather sharp as the decrease of silicon from 90% (the substrate) to 10% (contained in the HfSiON layer) is seen in a 1 nm range. The interface between the active layer and the TiN barrier is wide and progressive (about 2.5 nm).

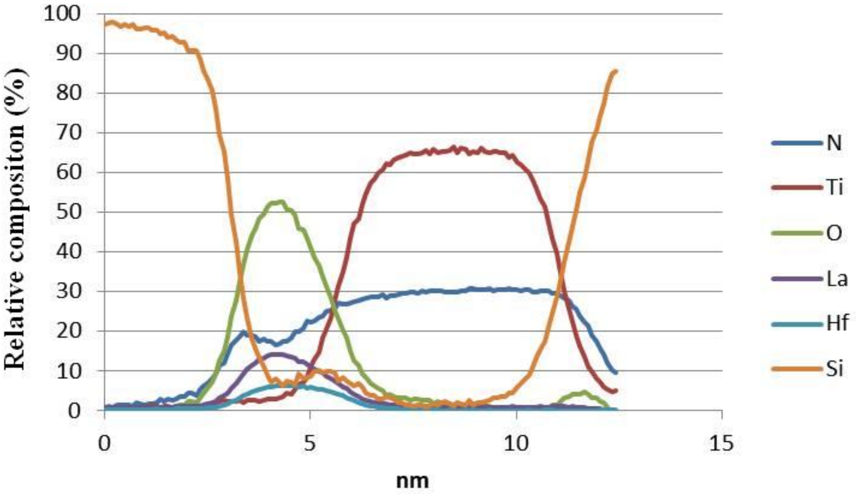

Figure 31: *EELS profile of the active layer containing HfSiON and LaO layers and the TiN barrier of the 50 nm sample.*

Auger depth profiling Fig 32 shows low-energy destructive Auger depth profiling of the 50 nm sample. The depth profile was obtained by sputtering the surface by monoatomic Ar^+ ions of 500 eV kinetic energy impinging on the sample surface at 28° from the surface. The sample was rotated about the normal axis during analysis in order to optimize the depth resolution, which was not better than 2 nm [54]. Sputtering cycles of 1 min were done between measuring the N(KLL), O(KLL), Ti(MNN), Si(KLL), La(MNN) and Hf(MNN) Auger transitions. The depth profile presented in Fig. 32 is obtained from the peak to peak height of the derivative spectra weighted by the corresponding sensitivity factor. The depth scale is determined according to a sputter rate at 500 eV measured under the same conditions on a calibration sample of silicon dioxide on Si of known thickness. Deviations from this calibration are expected on our measurement due to slight differences of the sputtering rate for pure Si compared to SiO_2. The different layers are distributed according to the expected depth below the 50 nm-thick a-Si capping layer. The TiN layer is composed of 55% titanium, 40% nitride and 5% of oxygen. The fact that oxygen is present in this layer and is absent in the a-Si layer indicates that this oxygen is not due to residual gases in the analysis chamber but is contained in the TiN layer. The residual signal of silicon is attributed to ion implantation while performing the experiment. Oxygen concentration increases in the active layers as both La and Hf layers are present in their partially oxidized state. The thicknesses of these layers are overestimated due to differences in sputtering yield. The depth profiles obtained for La and Hf are asymmetric and present a tail due to ion implantation during sputtering. The observed concentrations in the La and Hf layers are very low ($<3\%$). They are much lower than the expected stoechiometry from deposition rate for La and Hf respectively. This is due to the very low amount of substance and the ion implantation which flattens the signal.

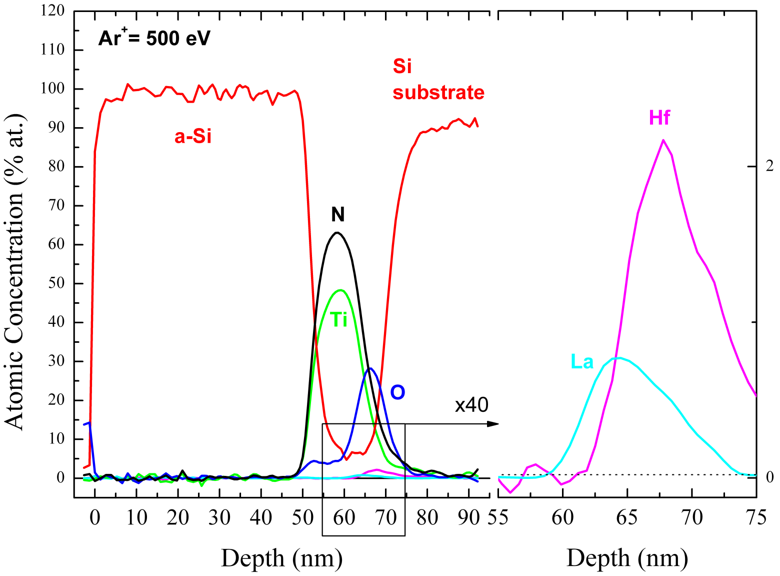

Figure 32: *Auger depth profiling of the 50 nm sample, highlighting the thickness of the a-Si cap and the depth distribution of the La layer in between the TiN and HfSiON layers. The broadening of the TiN layer is due to different sputter rates for TiN and Si.*

Atom probe tomography Fig. 33 shows the 3D spatial distribution of atoms for the 50 nm sample which has been obtained from atom probe tomography. Each dot corresponds to one atom. As defined previously, all chemical species are identified by the time-of-flight measurement leading to a mass spectrum of atoms and/or molecules within the analyzed volume. Hence, the La elemental contribution was detected at m/n = 77 corresponding to LaO^{2+} ion compound. Since no other peaks for La contribution were detected during the experiment, the conclusion is that La is mainly present in the oxidized form in the sample. Hf contribution was also only detected in the oxide ion form at m/n = 98. The difference in evaporation fields between chemical species can slightly curved interfaces between layers. This is a well-known phenomenon which is intrinsic to the evaporated phases [114]. To overcome this bias that can be introduced in the concentration profiles, a proximity histogram has been used [115]. This has the added advantage of correcting any surface roughness due to the polycrystalline nature of the materials. For the calculation a 37% TiN iso-surface was chosen as the plot reference (0 on the depth scale). The depth profile shows that La and Hf layers are located between the TiN layer and the silicon substrate. Pink and blue dots in TiN layer and Si substrate are due to a small signal at the noise level and so are not defined as La and Hf ions, respectively. Since the intensity of La is non-negligible at Hf maximum intensity, the experiment shows a partial intermixing between the La and the Hf layers induced by the thermal budget during the deposition process. The obtained thicknesses are of 1 nm for the La layer and 1.3 nm for the Hf layer and the resulting layer has an overall thickness of 1.5 nm. The TiN layer was found to be stoechiometric (not shown here).

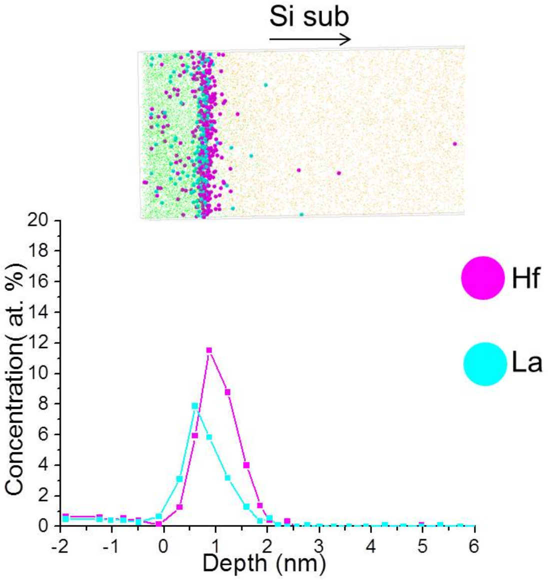

Figure 33: *(a) 3D Atom Probe Tomography of the 50 nm sample. (b) Corresponding proximity histogram of La and Hf calculated from 37% TiN iso-surface. The top panel shows the reconstruction of the La and Hf layers and the depth profile of these elements are presented in the bottom panel.*

3.1.5 Implementation for practical use of QUASES Analyze®

There are difficulties in the practical use of the software. Firstly the variation of f(z) is made either by typing the interface values or by clicking a button in the software which changes the interface with steps of 0.1, 0.2, 0.5, 1, 2, 5, 10 or 50 Å. Then finding good match between the modeling and the measurement for an element with no prior knowledge on its location can be time consuming.

The second problem arises from the "eye control" of the matching between the modeling and the measurement. There are possibilities to use computed formula inside the QUASES Analyze software but they are not consistent as the final result depends on the first guessed input top and bottom interface positions.

These two difficulties have been overcome by computing a *bot* and by finding an empirical method of computing the matching between modeling and measurement. The resulting error is then plotted as a colour map. All scripts were coded using Python. This specific language has been chosen as it is a free language and thus can be implemented on any computer. Python language is object-oriented and works efficiently for treating the large number of files created by the bot. Python has a math-like syntax with indented structure which makes it easy to read and quick to understand.

bot A *bot* is a software application that runs automated tasks. Bots perform tasks that are both simple and structurally repetitive, at a much higher rate than would be possible for a human.

In our case, the bot performs a cycle of clicks where the top and bottom interface are changed with a tunable step (which can be different for the top interface and the bottom interface); it then saves the obtained background modelled and the subtracted spectrum (difference between the measurement and the modeling) with a name corresponding to the depth distribution.

Computed error As assumed by theory the matching between the modelled background and the measured background must be taking into account only for energy loss larger than ~30 eV and up to 120 eV below the no loss peak. For these reasons, the error is computed only for this energy range for background analysis without reference sample. If the analysis applies a reference sample then the shape and intensity can be compared over the full energy of the measurement, χ (see eq.36) is evaluated for all points in the spectrum.

Small variation in top interface location varies strongly the modelled background in the 40-70 eV lower kinetic energy range of the no-loss peak whereas modifying the bottom interface location changes only the far energy loss region (around 100 eV below the no-loss peak). The computed error from eq.36 can lead to erroneous results in which the far from no-loss peak energy region is not well reproduced and the near no-loss peak region is better accounted for. Several empirical calculations for computing an error value have been tried, the best formula (which leads to a good reproduction of the background over the considered energy range) was found when cutting the energy region in three regions of 30 eV each. The first region α is located between 120 and 90 eV below the no-loss peak, the second region β is located between 90 and 60 eV below the no-loss peak and the third region γ from 60 to 30 eV below the no-loss peak. To each of these regions is applied the error calculation of eq.36 and the total error χ_{eff} is computed as the sum of an increasing power law:

$$\chi_{eff} = \alpha + \beta^2 + \gamma^4 \tag{80}$$

As eq.80 has no physical meaning, it is not possible to extract much information from it. However the matching between the modelled and the measured background is always very good for the minimum χ_{eff} value. Assuming that only the matching between the measurement and the modeling accounts for the depth distribution of the element, with this calculation very small variation of χ_{eff} corresponding to small depth distribution variation can be emphasized.

In order to have a visualization, χ_{eff} values are normalized by the lowest value and is plotted as a colour map with the x-axis the top interface position and the y-axis the bottom interface position. To obtain the final map, a linear interpolation is done between two points and lines corresponding to 1% changes from the minimum x_{eff} value are drawn.

3.2 Qualitative results

Even though the background analysis has proven its efficiency during the past decade, the application of the method to the hard x-ray regime (and thus high velocity photoelectrons) deserves careful attention. In this section the qualitative effects of high velocity photoelectrons on the background shape will be studied.

3.2.1 Effects of the photon energy

The selected photon energy has two effects on the inelastic background of HAXPES spectra: the photoionization cross section : when the photon energy increases, the IMFP and thereby the escape depth increases but at the same time the photoionization cross-section decreases drastically [13]. These two factors influence the intensity of both the no-loss peak and the inelastic signal to lower kinetic energy. The IMFP depends on the material the photoelectron passes through when traveling inside the medium and on its kinetic energy.

The effective IMFP used in the study is an average of individual IMFP weighted by the nominal thickness of the crossed layer. Tab.3 presents the parameters used to compute the IMFP of La2p$_{3/2}$ photoelectrons for the 50 nm sample. Values of the IMFP for high energy electrons have been published for pure elements [39] but not for compounds and alloys. Therefore the corresponding IMFPs are computed from the TPP-2M formula [15]. The weighted average is dominated by the 50 (or 30-20) nm a-Si. A source of uncertainty comes from the density of the layers. The samples are technologically advanced and their density may not be corresponding to tabulated values, especially after annealing; this is another source of uncertainty in the evaluated effective IMFP.

	Layer	thickness (nm)	IMFP (nm)
	a-Si	50	15.9
	TiN	6.5	12.4
	LaO	0.4	11.9
Effective IMFP			15.4

Table 3: *Effective IMFP for La 2p$_{3/2}$ at photon energy of 15 keV in nm for the 50 nm sample.*

Silicon samples A Silicon wafer substrate was treated by HF for surface cleaning before immediately transferring into an ultra-high vacuum transfer box via a glove box, then transferred into the experimental chamber of the BM25 beamline with less than 2 min air exposure, the resulting spectra measured at 8, 10, 12 and 15 keV are presented in Fig. 34 where no oxide peak is detected. The inelastic background shape is seen for each energy with oscillations which correspond to 1, 2, 3, 4 and 5 multiple excitation plasmons separated by ~16 eV. The insert of Fig. 34 shows the intensity for the five first plasmon losses relative to the no-loss peak intensity. The intensity for each plasmon loss increases when increasing photon energy and their behaviour is similar. This means that in this high energy regime >8 keV, the intensity of plasmon loss relative to the no-loss peak intensity is directly connected with the probed depth inside the sample.

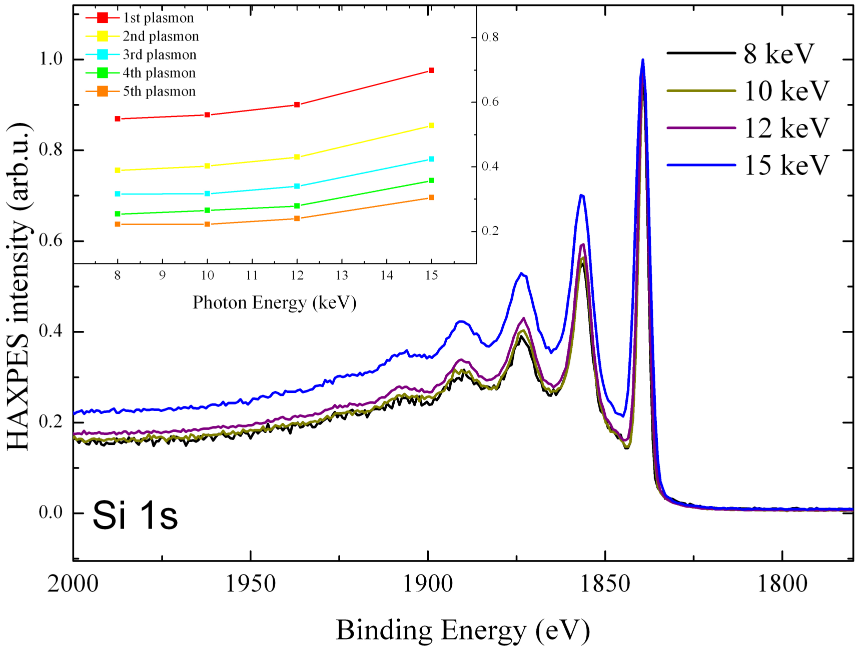

Figure 34: *Si 1s spectra measured at 8 (black), 10 (brown), 12 (purple) and 15 keV (blue) photon energy. Spectra are normalized to the same intensity at the no-loss peak maximum.*

Another sample was studied at GALAXIES beamline. It was prepared in the same way but followed by a few days of air exposure. It was measured at 10 and 12 keV and additionally at lower photon energies of 6, 4, 3 and 2.5 keV. The air exposed sample present a peak located 4 eV below the Si 1s no-loss peak as can be seen in Fig. 35. This is attributed to an oxide layer SiO_2 as the chemical shift of 4 eV corresponds to the shift observed for the SiO_2 component in Si 2p at low energy [116]. To compare relative intensities, the spectra have been normalized at the no-loss peak maximum. The inset of the figure shows the oxide peak and plasmon maximum intensities as a function of the photon energy. The oxide peak intensity decreases with increasing photon energy, which means that a layer of oxidized silicon is at the surface as expected from air exposure. The plasmon intensity increases with the photon energy as seen in Fig. 34. The similarity of the SiO_2 peak from Si 1s between the 6, 10 and 12 keV measurements shows the low surface sensitivity of HAXPES when performed with very high photon energy. The difference between the lowest energy of 2.5 keV in black and the highest energy of 12 keV in purple is representative of the change in surface sensitivity of the experiment. The inelastic background does not present the oscillations seen at 12 keV because the photoelectrons have an IMFP of 16.9 nm for the 12 keV measurement whereas of 1.79 nm for the 2.5 keV measurement. When photon energy is lower than 6 keV, the

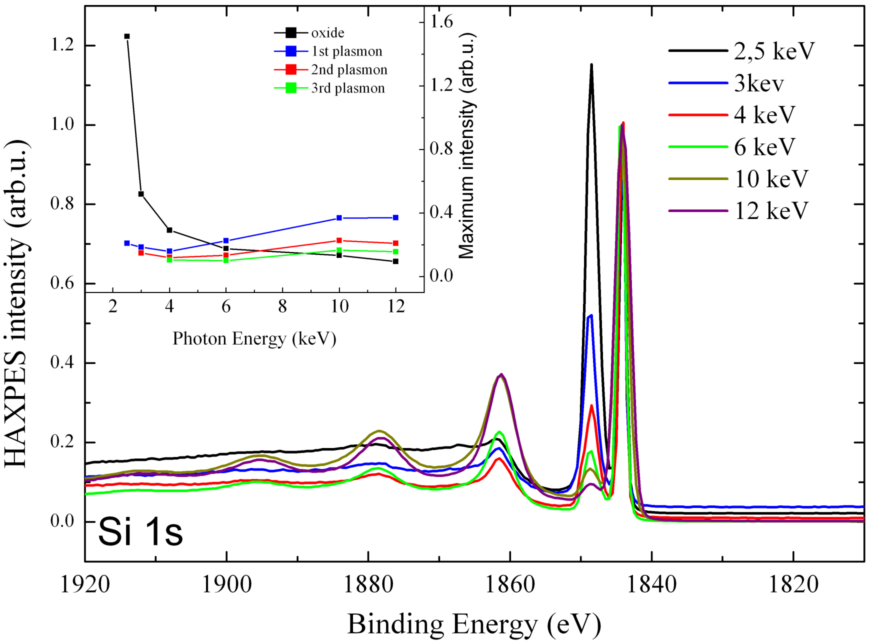

Figure 35: *Si 1s spectra of oxidized silicon measured at 2.5 keV (black), 3 keV (blue), 4 keV (red), 6 keV (green), 10 keV (brown) and 12 keV (purple). The inset of the figure shows maximum intensity for the oxide peak located at 4 eV below the Si1s no-loss peak and plasmon losses.*

oxide peak has a higher intensity than the first plasmon peak. When increasing photon energy, the first plasmon becomes more intense than the oxide peak. In the lowest energy experiment, the detected photoelectrons originate mainly from the oxidized silicon layer whereas at the highest energy the detected photoelectrons come from deeper in the layer of pure Si. The resulting energy losses are therefore pure silicon-like at high energy whereas they are a mixture of oxidized silicon and pure silicon at lower energy.

The two samples measured at 10 and 12 keV are shown in brown and purple respectively in Fig. 34 and Fig. 35. The difference between the two samples can be seen for the oxide peak which is still visible for the oxidized sample but also for maximum intensity of plasmon losses. The pure silicon sample presents higher intensity for plasmon losses and more visible plasmons (the five first are plotted in the insert of Fig. 34) as electron scattering is dominated by pure silicon bulk plasmon losses in the sample.

3.2.2 Effects on technological sample

As shown in the previous section, using hard x-rays has an impact on the inelastic background for pure samples. This section will study the behavior of the spectra from the *50 nm sample*, *30 nm sample*, *20 nm sample* and *high-k sample* using HAXPES at varying photon energy.

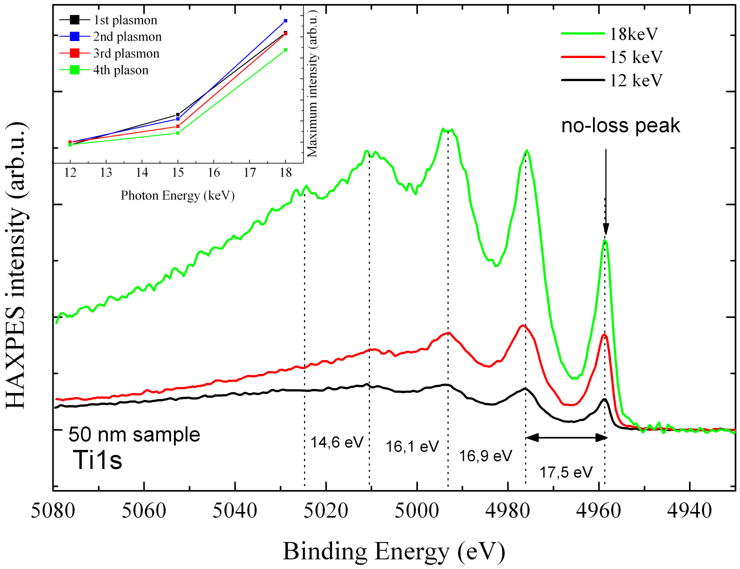

Figure 36: *Spectra of Ti 1s measured with photons of 12 keV (black), 15 keV (red) and 18 keV (green) with a detection angle of 10° from surface normal.*

Ti 1s The influence of varying the photon energy can be seen in Fig. 36 which shows Ti 1s peak for the *50 nm sample* at 12, 15 and 18 keV. This peak is much more intense than La $2p_{3/2}$ measured for the same three energies (see Fig. 38). Clear oscillations are seen below the no-loss peak which correspond to the bulk plasmons excitations as the photoelectrons passe through the Si capping layer. The first oscillation is located 17.5 eV below the no-loss peak and has a higher intensity than the no-loss peak. It can be seen for the three selected photon energies and corresponds to the highest probability of energy loss in silicon. The second plasmon loss is shifted by 16.9 eV toward lower kinetic energy. The energy shift between successive plasmon losses are decreasing with increasing scattering events (16.1 eV for the third and 14.6 eV for the fourth plasmon loss).

Ti 1s photoelectrons suffer inelastic losses inside the Si capping layer, dominated by the sharp plasmon losses but also inelastic scattering events inside the TiN layer. In the TiN layer, energy losses are represented by the smooth two-parameters universal cross section valid for metals and their oxides (see eq.49 and Fig. 19). The mixing between these two different inelastic scattering events induces a broadening in the inelastic background. Moreover the Ti 1s peak is wider than the Si 1s peak, thus the intensity attenuation of the succesive plasmons makes the number of observed plasmons of Ti 1s inelastic background lower than the one observable from Si 1s. These two reasons give an interpretation of the observed changes in the plasmon peaks seen in Fig. 36.

La 2p Similar observations can also be made for the ultra thin and deeply buried layer of La. Fig. 37 shows the La$2p_{3/2}$ HAXPES spectra of the 50 nm sample measured at 12, 15 and 18 keV photon energy. The spectra consists in the no-loss peak located at 5523 eV binding energy, and

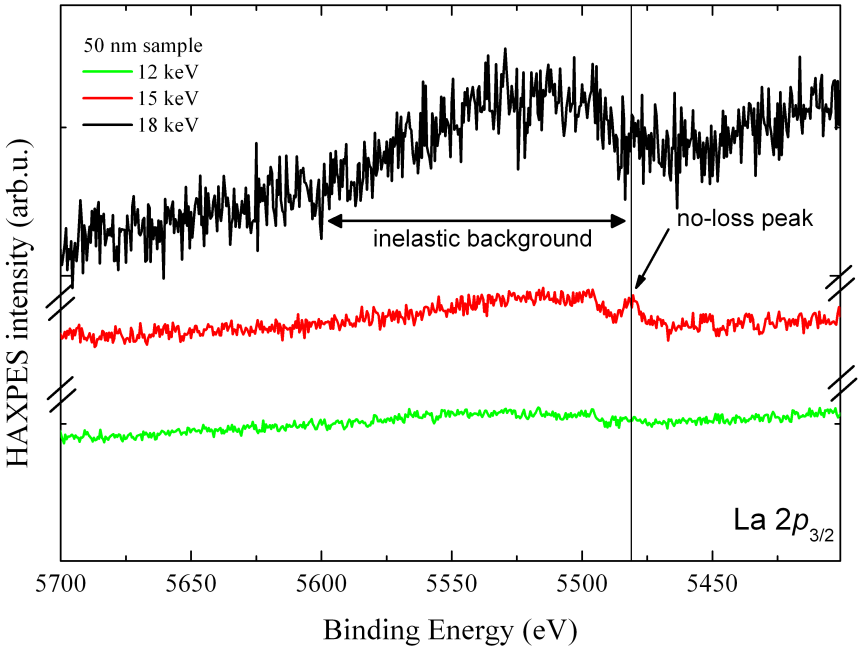

Figure 37: *La $2p_{3/2}$ threshold of 50 nm sample measured at 12 keV (green), 15 keV (red) and 18 keV (black) with detection angle of 10° from surface normal. The line points to the no-loss peak binding energy of 5523 eV.*

of inelastic loss features extending over typically 120 eV to lower kinetic energy. At 12 keV, the no-loss peak is not detected because, with a calculated IMFP of 10.3 nm, the escape depth is a factor ∼5 smaller than the thickness of the Si overlayer. A closer look at 17 eV below the position of the no-loss La peak reveals another peak due to a bulk plasmon loss in the silicon overlayer [85]. Theoretically, with background analysis it could be possible to probe the location of the La buried layer but the poor signal-to-noise ratio makes the inelastic background analysis difficult. In the spectrum at 15 keV, the corresponding IMFP is 15.5 nm and the no-loss peak can be clearly seen since the escape depth now ∼3 smaller than the overlayer thickness. As a result, the inelastic background signal-to-noise ratio is now better although the photoionization cross-section is smaller at 15 keV. At 18 keV, the very low intensity of the no-loss peak is due to the decrease of the photoionization cross-section despite an escape depth of nearly 60 nm (IMFP of 19.6 nm). In conclusion, the best signal/noise and probing depth combination to analyze the ML-thick La buried layer is therefore at the intermediate energy of hν=15 keV. At this energy the probing depth when analyzing the core-level is representative for ∼45 nm below the surface but the inelastic losses can be used to extract the in-depth distribution at larger depths (see sect.2.4.1) under good conditions.

The optimum photon energy must be a compromise between the increasing escape depth and the decreasing photoionization cross section when increasing the photon energy in HAXPES. In conclusion, the 15 keV photon energy has to be selected for the experiments presented in the following since it has the **best signal/noise ratio**, the **photoionization** is sufficient to see all elements of interest and the **IMFP** values ensure to probe the entire stack. At this photon energy, the experiment is very low surface sensitive and with a take-off angle of 80°, the bulk sensitivity is enhanced.

3.2.3 La2p$_{3/2}$ inelastic background for 20, 30 and 50 nm samples

The 15 keV HAXPES survey spectra of the samples in the spectral regions of the K subshell of Ti (Ti1s peak) and of the L subshells of La and Hf (2s and 2p$_{3/2,1/2}$ peaks) are shown in Fig. 38. The inset shows La 2p$_{3/2}$ peak for the three samples. All elements of interest are deeply buried underneath the a-Si overlayer (see Fig. 28). They are detected by their characteristic photoelectron emissions. In particular, the detection of the LaO$_x$ deeply buried below the surface in the 50 nm-sample demonstrates the extreme depth sensitivity of HAXPES. The issue is now to retrieve the in-depth distribution of this element. In the inset of Fig. 38, the La 2p$_{3/2}$ core level peak is located at 9524 eV kinetic energy. It is separated from the first energy loss peak by ∼17 eV, which corresponds to the bulk plasmon excitation energy of silicon (measured from Fig. 34 at 17.5 eV). The loss structure is due mostly to inelastic scattering events of photoelectrons traveling through the a-Si overlayer. The contribution to the inelastic background of much thinner layers located below a-Si can be neglected in a first approximation. It is also noticeable that the

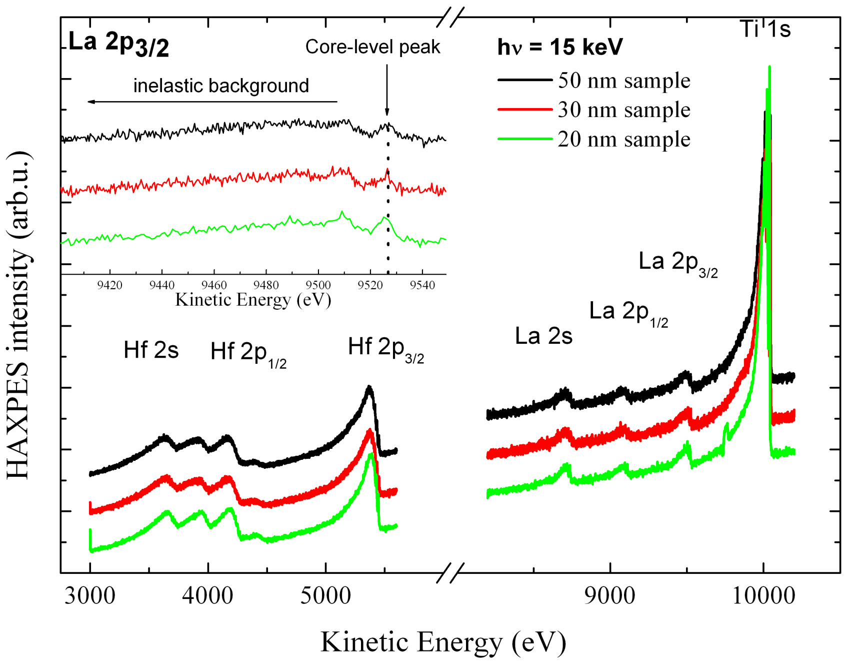

Figure 38: *HAXPES survey spectra measured at hν = 15 keV on the 50 nm (red) and 30 nm (black) samples. The inset shows the La 2p$_{3/2}$ transition along with its energy loss structure. Right: structure of the gate stack samples for the thickest a-Si capping layer (50 nm-sample).*

first plasmon loss peak has a higher intensity than the main peak. This is true also for the Ti 1s in Fig. 36 and La peaks in Fig. 38 where the plasmon features actually dominate. The inelastic background signal is thus higher than the no-loss peak which is due to the large burying depth of the overlayer.

3.3 Quantitative results - Analysis without reference sample

The previous section showed the qualitative impact of high velocity photoelectrons on the inelastic background. These observations were used to determine the best experimental conditions for good background analysis. This section shows the depth distribution obtained without the use of reference sample as it is sometimes difficult to find a good reference sample.

3.3.1 Input parameters

The calculations for modeling inelastic background need some input parameters: the IMFP, the detection angle and the inelastic scattering cross-section. The IMFP value is calculated from formula (see eq7); the detection angle is an experimental parameter; the inelastic scattering cross-section is both energy and material dependent. Their influence will be studied in this section.

Inelastic mean free path As previously mentioned, the IMFP for high energy photoelectrons is not perfectly known yet. Tabulations with modified TPP-2M formula are given by *Tanuma et al.* [15, 39, 117] for various elements, but for compounds, the IMFP must be estimated from individual IMFP. The complexity of the presently studied samples increases the difficulty of choosing a correct inelastic mean free path. An effective IMFP was used for all elements, which corresponds to a weighted average of individual IMFPs calculated with TPP-2M formula according to the nominal thicknesses of the crossed layers as seen in table 4. Assuming an error on the individual IMFPs of 10% [39], the resulting error for the effective IMFP are lower than 20% (see also Tab.4).

$h\nu$	λ_{eff} Ti1s (nm)	λ_{eff} La2p$_{3/2}$(nm)	λ_{eff} Hf2p$_{3/2}$(nm)
12 keV	11.9 (12%)	11.4 (11%)	
15 keV	16.2 (16%)	15.4 (15%)	9.5 (9%)
18 keV	20.3 (21%)	19.6 (19%)	13.8 (14%)

Table 4: *Table of effective IMFP λ in nm and their associated estimation of uncertainty for 12, 15 and 18 keV for 50 nm sample.*

The effective IMFP is mainly dependent on the IMFP inside the silicon layer because this latter is the thickest one. It was observed that the IMFP choice influences the background modeling especially in the 60 eV region below the no-loss peak but not that much at the lowest kinetic energy range of the spectrum. To explore more clearly the effect of the IMFP choice, modeling

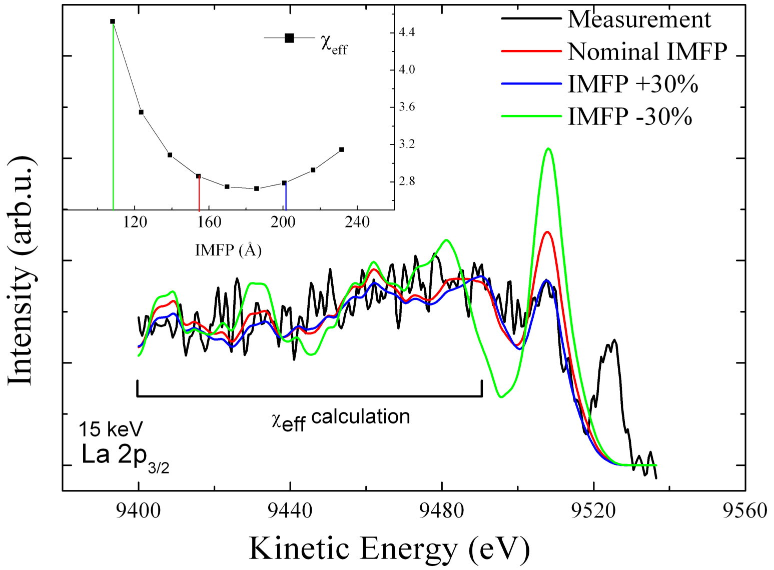

Figure 39: *La $2p_{3/2}$ threshold of 50 nm sample measured at 15 keV photon energy with detection angle of 10° from surface normal (black) and modeling for depth distribution of top interface located at 56 nm below the surface and bottom interface at 61 nm. The modeling corresponding to the computed IMFP (15.54 nm) is plotted in red, the green modeling is computed for an increasing value of the IMFP of 30% (20.07 nm) and the blue to a decrease of 30% (10.91 nm). The inset shows the χ_{eff} value computed for the energy range between 9400 and 9490 eV.*

for various IMFP values but same depth distribution (corresponding to the nominal interface positions) were performed for La $2p_{3/2}$ peak measured at 15 keV photon energy. The χ_{eff} (from eq.80) obtained are plotted in the inset of Fig. 39 as function of the IMFP value. The χ_{eff} curve has a minimum corresponding to an IMFP value of 18.6 nm. The computed effective IMFP of 15.4 nm gives almost the same χ_{eff} value (difference of 2.8 nm) and the IMFP difference is within the 19% error on the calculated effective IMFP. This difference can arise from the data used to compute the IMFP previously discussed, but the resulting χ_{eff} are very close and ensure an acceptable analysis. The modeled inelastic backgrounds corresponding to the correct IMFP value (red), an IMFP increased by 30% (green) and IMFP decreased by 30% (blue) for modeling the La $2p_{3/2}$ spectrum from the 50 nm sample are presented in Fig. 39. Increasing the IMFP does not change very much the background simulation but lowering the IMFP value gives a great mismatch between the measurement and the modeling. This is also seen in the inset of Fig. 39 where the normalized χ_{eff} varies slowly when increasing the IMFP but decreasing the IMFP value increases drastically χ_{eff} and affects the general shape of the background with highly pronounced oscillations. The use of the computed effective IMFP from TPP-2M formula which error is lower than 20% is then a reasonable approximation.

Detection angle The detection angle for photoelectrons is known with an accuracy of around 5°. Fig. 40 shows results of modeling for a detection angle of 0°, 10° (the angle corresponding to our

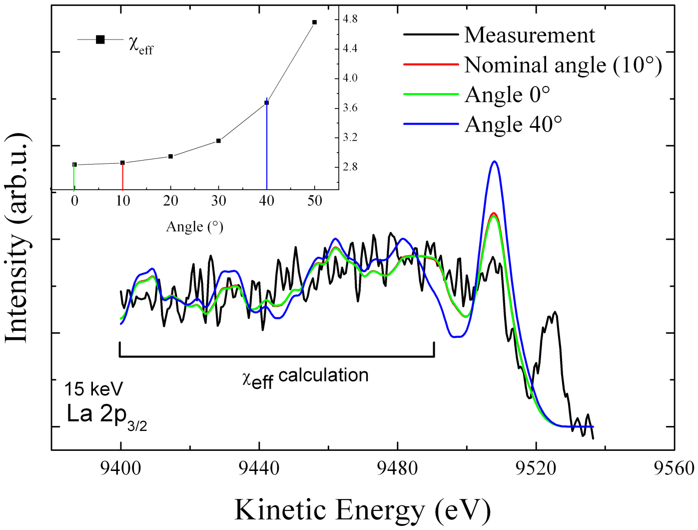

Figure 40: *La $2p_{3/2}$ threshold of 50 nm sample measured at 15 keV photon energy with detection angle of 10° from surface normal (black) and modeling for depth distribution of top interface located at 56 nm below the surface and bottom interface at 61 nm. The modeling corresponding to the correct detection angle (10° from surface normal) is plotted in red, the green modeling is computed for an angle of 0° from surface normal and the blue to an angle of 40° from surface normal. The inset shows the χ_{eff} value computed for the energy range between 9400 and 9490 eV.*

experimental setup) and 40° from surface normal. For angles ±5°from the actual value one leads to a negligible variation of the normalized χ_{eff} as can be seen in the inset of Fig. 40. This is due to the sine dependent variation for the probed depth as discussed in §2 since the analyzer acceptance angle is usually $\sim 5°$ the effect on the angle is negligible. At larger photoelectron collection angle like 40°, strong variations all along the chosen energy range of the inelastic background can be clearly see .

3.3.2 Choice of the inelastic scattering cross-section K(T)

This section considers the **critical influence** of the choice of K(T). As previously pointed out, K(T) varies with the energy and the material [85, 118]. In contrast to most materials, silicon has a sharp plasmon loss feature. In this particular case a three-parameter cross-section is more accurate than the two-parameter universal cross-section. But at the high photoelectron kinetic energies accessible in HAXPES, we found that it is more accurate to apply a cross-section derived from REELS measurements at 10 keV using the QUASES-REELS software.

The bottom panel of Fig. 41 illustrates the result of using three different K(T) functions for background analysis of the loss structure in the La $2p_{3/2}$ spectrum. In bottom-left panel of Fig. 41 is presented the use of the two parameter universal cross-section which does not reproduce at all the fine structure in the background. The bottom-middle panel of Fig. 41 shows the result of the analysis performed with the three-parameter universal cross section valid for Si [85]. The modeled spectrum reproduces well the first plasmon loss, but the second one is overestimated and the third loss is underestimated. Furthermore, there is an energy shift of 2.5 eV between modeling and measurement for the first plasmon energy, whereas the agreement is perfect for the second plasmon. In the bottom-right panel of Fig. 41, is plotted the result of the analysis performed with a silicon inelastic cross section derived from REELS measurements at 10 keV i.e, close to the La2p$_{3/2}$ photoelectron kinetic energy at 15 keV. Clearly, such a cross section enables a much better account for the fine structures present in the inelastic background and reproduces quite well the plasmon peaks, including the first one. This is expected because photoexcitation of the La2p$_{3/2}$ peak takes place in the La layer and therefore it does not have contributions from intrinsic Si plasmon excitation. The full intensity at the Si plasmon loss peak is therefore extrinsic, i.e. it is entirely caused by the transport of the La2p$_{3/2}$ spectrum through the a-Si overlayer. Theory predicts a matching between measurement and modeling only between 120 and 40 eV below the no-loss peak [87], therefore only this region of interest (as sketched in Fig. 38) must be taken into account in the modeling.

The top panel of Fig. 41 shows the inelastic scattering cross section used for the modeling. The two parameter universal cross section has a lower maximum probability than the two others but is much wider. This *K(T)* is very different from the *K(T)* for silicon. It reasonably accounts for the background $\geq$ 40 eV from the no-loss peak. As an example of behavior of free electron like materials the inelastic scattering cross section for Si has a sharper distribution corresponding to plasmon excitation. Moreover *K(T)* at high energy (measured at 10 keV) has sharper distribution centered at 17.5 eV than the one determined for soft x-ray energies centered at 18 eV [85]. The interpretation of this behavior is attributed to the probed depth: at high energy, the information is considered as bulk information whereas at the low energy, as surface information.

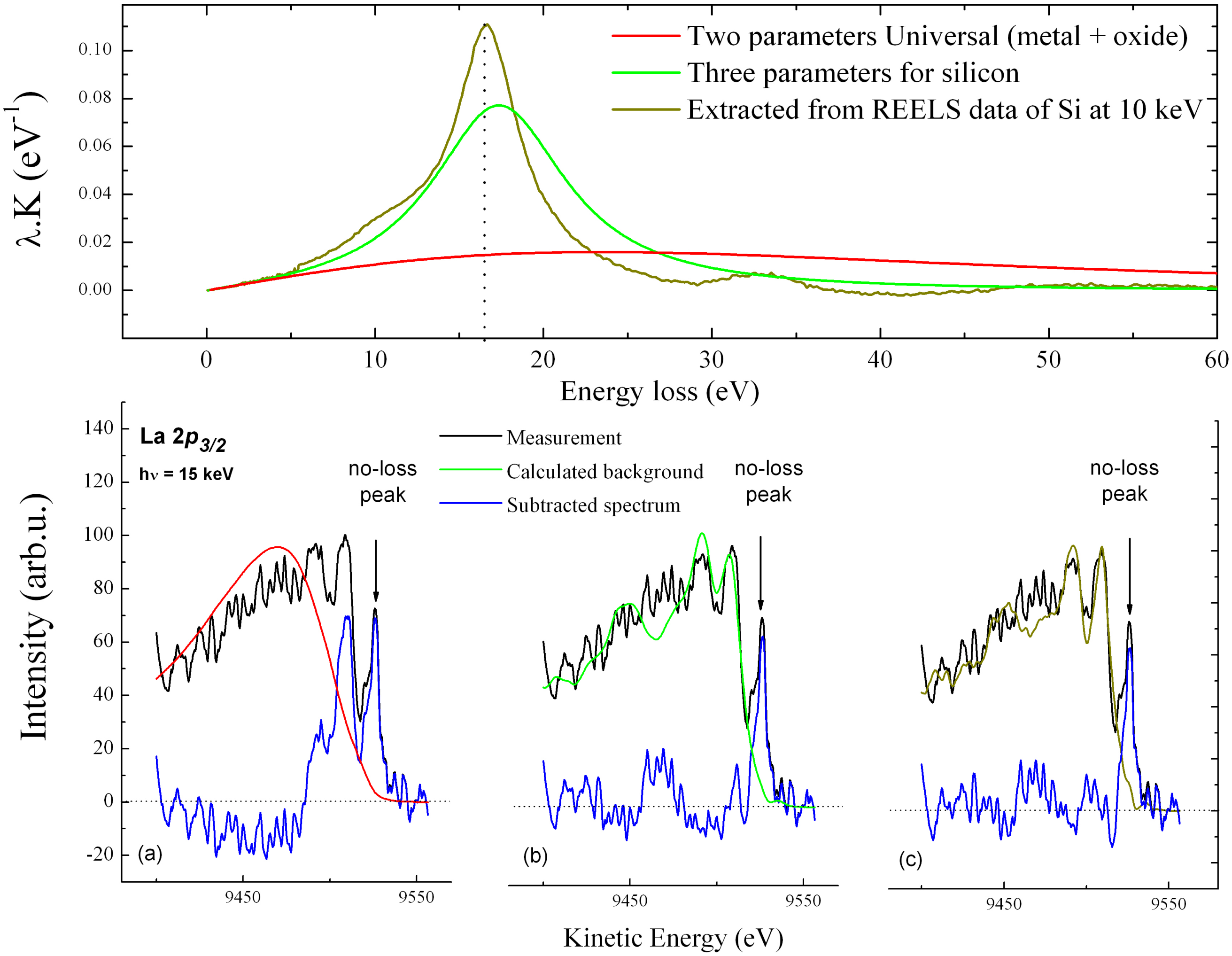

Figure 41: *The top panel presents various inelastic scattering cross-sections: three parameter universal cross section in red, three parameter cross section of Silicon (in green) and cross-section calculated from REELS measurements at 10 keV (brown). The corresponding modeling for nominal depth distribution of lanthanum of the 50 nm sample is plotted on the bottom panel with (a) the three parameter cross section, (b) the three parameters silicon cross section and (c) the cross section derived from REELS measurements at 10 keV.*

3.3.3 Effect of the Si overlayer thickness

This Section focuses on the depth at which the La layer is buried on the determination of the depth distribution. The background analysis is performed on the La2p$_{3/2}$ HAXPES spectra with photon energy of 15 keV for samples capped with 20, 30 and 50 nm-thick a-Si overlayers.

The results from the bot operation and the χ_{eff} calculation from eq.80 are plotted as colormap in Fig. 42 where the lowest χ_{eff} value is used for normalization and increasing χ_{eff} value of 0.1% are drawn as lines. The center of the first line (in red) corresponds to the determined depth distribution profile. The best background reproductions are representative of depth distribution of 57.3 nm to 61.8 nm below the surface for the *50 nm sample*, 41 to 43 nm for the *30 nm sample* and 35.0 nm to 36.0 nm for the *20 nm sample* as summarized in Tab.5.

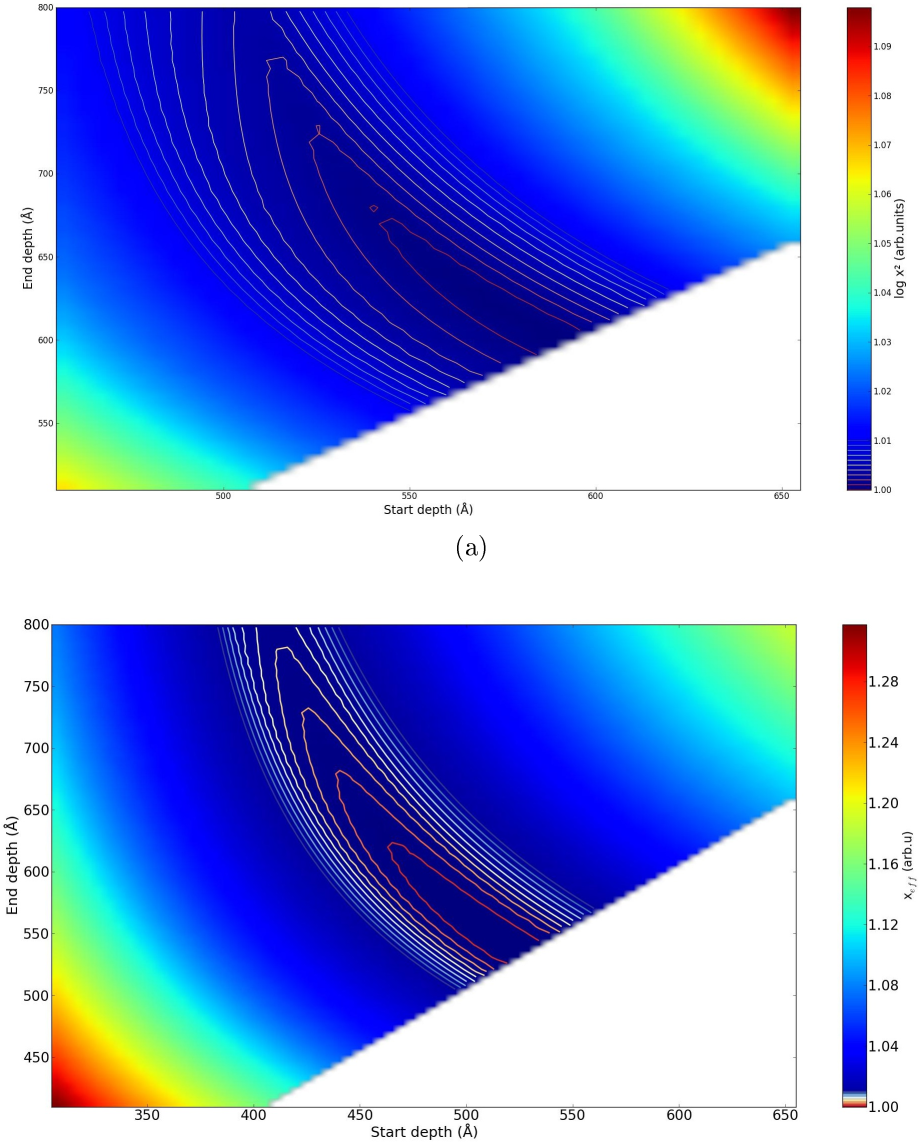

(a)

(b)

Figure 42: *Maps of χ_{eff} as function of the top interface (x-axis) and bottom interface (y-axis) for (a) 50 nm sample and (b) 30 nm sample . The lines drawn represent an increase of 0.1% in the normalized χ_{eff}.*

The measured spectra and their associated inelastic backgrounds are shown in Fig. 43. In comparison to the nominal structure, a strong influence of the overlayer thickness is observed: the determined La **depth distribution is more accurate, when the overlayer is thinner**. The top and bottom interface positions are overestimated compared to the expected ones for all samples presented. The discrepancy can be due to uncertainties in the IMFP values used for the analysis, but can also be influenced by elastic electron scattering effects which are neglected in this analysis. Moreover, even if inelastic scattering cross section, derived here from REELS measurements of

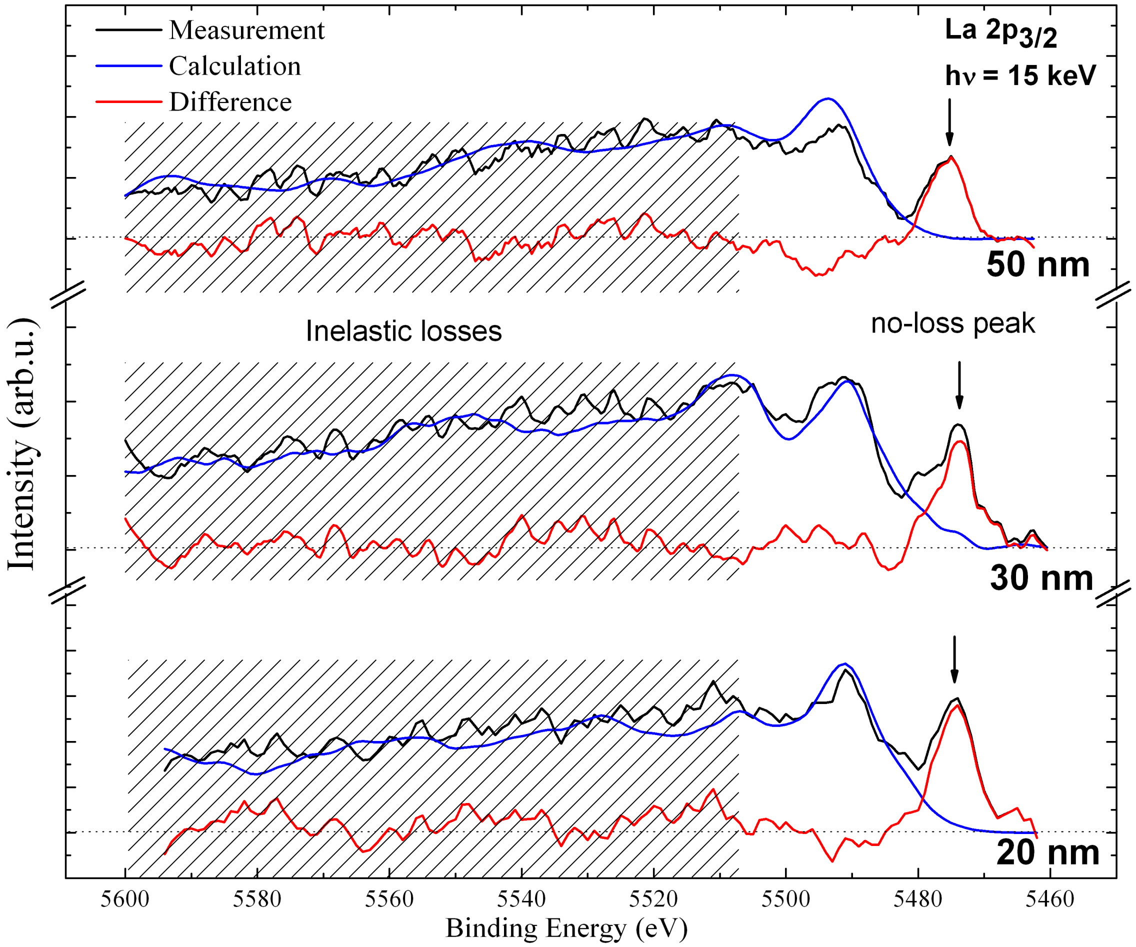

Figure 43: *Background analysis of the La2*$p_{3/2}$ *HAXPES spectrum of the 50, 30 and 20 nm samples. The blue curves are the calculated backgrounds corresponding to a depth distribution of La extending over 1 nm from 35.0 nm below the surface for the 20 nm sample; 2 nm-thick from 41 nm below the surface for the 30 nm sample; 4 nm from 57 nm below the surface for the 50 nm sample. The hatched part represent the reproducible part of the measurement by inelastic background analysis and the arrow points to the core-level no-loss peak.*

pure Si is suitable, it does not correspond exactly to the real composition of the overlayer which contains a TiN layer of 6.5 nm. When the top a-Si layer is very thick compared to the rest of the sample, the approximation of using inelastic scattering cross-section of pure Si is reasonable.

The results of the inelastic background modeling summarized in Tab.5 show that **the error on the absolute interface position decreases when increasing the overlayer thickness**. On the reverse, **the error on the thickness decreases with decreasing overlayer thickness**. While performing background analysis, the supposed 0.4 nm-thick lanthanum layer is found to be 4.5, 2 and 1 nm-thick for the 50, 30 and 20 nm samples respectively as summarized in Tab.5. Note first that the low statistics of the spectra have made the modelling difficult, and second the error on the bottom interface depth determination is not without influence on the thickness determination. However for all three samples, **a 0.4 nm-thick layer is compatible within the estimated error bars** of the analysis.

Sample	Top interface (nm)		Bottom interface (nm)		Thickness (nm)	
	Nominal	Modeled	Nominal	Modeled	Nominal	Modeled
50 nm sample	56.5	57.3	56.9	61.8	0.4	4.5
30 nm sample	36.5	41.0	36.9	43.0	0.4	2
20 nm sample	26.5	35.0	26.9	36.0	0.4	1

Table 5: *Positions of top and bottom interfaces of lanthanum obtained by background analysis.*

3.3.4 Effect of the amount of substance

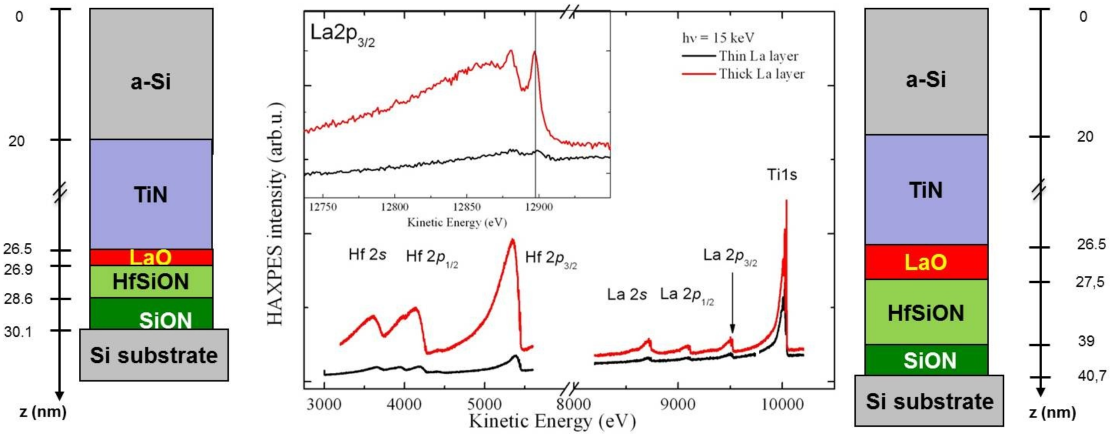

Figure 44: *HAXPES spectra measured for 20 nm samples at 10° from surface normal for 0.4 nm-thin La layer (left and black) and for the 1 nm-thick one (right and red). The inset focuses on La $2p_{3/2}$ peaks where the line corresponds to the kinetic energy of La $2p_{3/2}$ of 12897 eV.*

	top interface (nm)		bottom interface (nm)		Thickness (nm)	
	Expected	Modeled	Expected	Modeled	Expected	Modeled
20 nm sample	26.5	35.0	26.9	36.0	0.4	1.0
high-k sample	26.5	43.2	27.5	45.4	1.0	2.2

Table 6: ***Positions of top and bottom interfaces obtained by background analysis for the 20 nm sample and the high-k sample.***

The Fig. 44 displays HAXPES spectra for two samples, the *high-k sample* (sketched on the right and in red in Fig. 44) and the *20 nm sample* (sketched on the left and in black in Fig. 44). The two spectra are different due to the amount of substance (AOS), the two samples differ only by their thicknesses of the LaO_x (0.4 and 1.0 nm) and HfSiON layers (1.7 and 11.5 nm). At 15 keV the HfSiON layer is detected by very intense Hf 2s,2p no-loss peaks. The HfSiON layer is more visible, despite its location under the LaO_x layer, because Hf 2s,p peaks have higher photoionization cross-section than the La peaks. Moreover, the HfSiON layer has a higher Hf AOS than the LaO_x layer has a La AOS. The inset in Fig. 44 shows the La $2p_{3/2}$ region. One can see that increasing the thickness increases the intensity of the no-loss peak and therefore gives a much better signal-to-noise of the inelastic background. Modeling of La depth distribution gives the lowest χ_{eff} value for the *high-k sample* with a top interface located at 43.2 nm and a bottom interface at 45.4 nm below the surface, whereas the 20 nm sample results locate the top interface at 35 nm and the bottom interface at 36 nm as summarized in Tab.6. The overestimation of interfaces positions from the surface is attributed to the uncertainty on the IMFP, on theelastic electron scattering and on the inelastic scattering cross section. The lanthanum thicknesses estimations are now closer to the expected value, for the *high-k sample* where a 2.2 nm-thick lanthanum layer is found with an expected thickness of 1 nm and for the *20 nm sample* where the analysis gives a 1 nm thick La layer (expected value of 0.4 nm) as summarized in Tab.6. The AOS has a strong effect: both the top and bottom interface position error is decreasing with increasing AOS.Background analysis is **reliable for measuring the thickness** of the layer, but the absolute positions of the interface need to be taken with caution.

3.3.5 Results for all elements

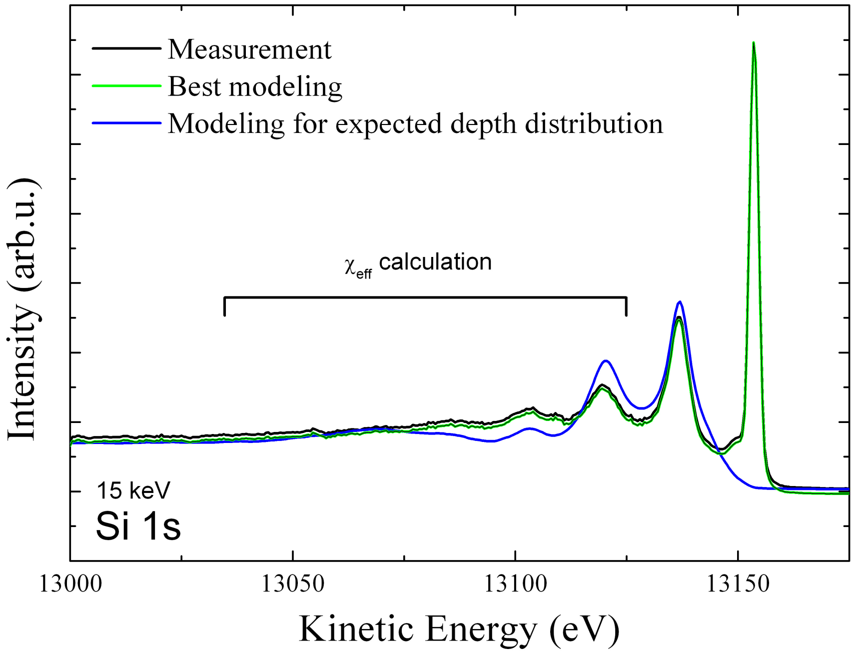

Figure 45: *Si 1s measurement (in black) with modeling of the expected depth distribution of two layers (in blue) and the best modeling (in green).*

Silicon Background analysis of silicon is very difficult as silicon is present everywhere in the sample except in the TiN and LaO_x layers. Fig. 45 shows a small shoulder located at 5 eV lower kinetic energy from the Si 1s no-loss peak corresponding to a small oxidization of the top part of the silicon capping layer as it was conserved at atmospheric pressure. There is a possibility in QUASES-Analyze ® to model two distinct layers in a sample, but no quantitative information can be extracted from such analysis without reference samples in its depth distribution configuration. The differences when modeling inelastic background distortions for various depth distributions close to the nominal values are too weak to be truly reproduced or analyzed. The best modeling obtained by the bot procedure is found for a pure infinite homogeneous silicon layer with top interface located at 8 nm below the surface. This result does not agree with results from TEM, Auger depth profile or Atom Probe Tomography.

Titanium and Hafnium Modeling has been performed on ID32 experiment with IMFP values from Tab.3 and detection angle of 10° from surface normal. As for La $2p_{3/2}$, the first plasmon loss is overestimated and cannot be taken into account while performing background analysis as it is in the 30-40 eV region below the no-loss peak.

The colormap of χ_{eff} presented in top panel of Fig. 46 presents two distinct minima. One is centered around the values of 49 nm and 60 nm below the surface for top and bottom interface

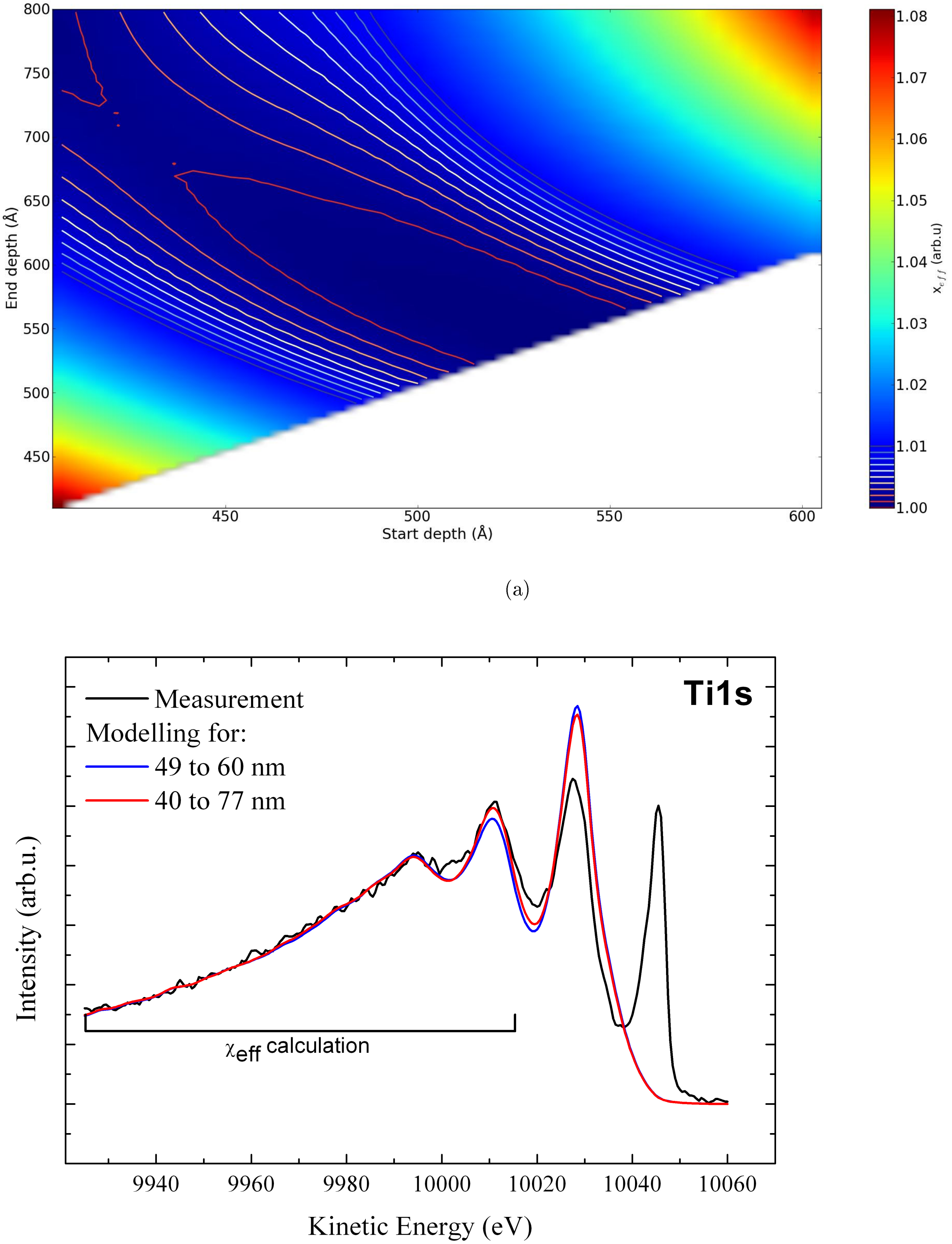

(a)

(b)

Figure 46: *(a) colormap of χ_{eff} for Ti 1s of 50 nm sample; (b)modeling for depth distribution of 49 nm to 60 nm below the surface (blue) and 40 to 77 nm below the surface (in red).*

positions respectively and the other for 40 to 77 nm below the surface. The two backgrounds associated with these depth distributions are presented in bottom panel of Fig. 46. The reproduction of the background is the same for the far energy below the no-loss peak region , the main difference arises from the reproduction of the second plasmon loss. The 40-77 nm distribution leads to a better reproduction of this plasmon. The third plasmon loss is reproduced in the same way for the two modelings. From TEM experiment in Fig. 30 and Auger depth profile in Fig. 32, Ti is located between the top Si layer and the La-containing layer. The EELS profile of Fig. 31 shows a Ti thickness of 4.6 nm. The nominal top interface is located at 50 nm below the surface and the bottom interface at 56.5 nm below the surface. Photoelectrons of Ti 1s measured at 15 keV photon energy are of kinetic energy around 10 keV, thus leading to a better reproduction of the inelastic background. In conclusion, the correct depth distribution is obtained for the top interface position of 49 nm and a bottom interface position of 60 nm below the surface. The top interface position is in good agreement with the nominal value of 50 nm and other characterization methods but the bottom interface is overestimated as summarized in Tab.7.

Technique	Titanium	
	Top interface (nm)	Bottom interface (nm)
Background Analysis	49	60
Auger	52	65
TEM	51.1	55.7
Nominal value	50	56.5

Table 7: *Depth distributions of titanium obtained for 50 nm sample with inelastic background analysis, Auger depth profile and TEM.*

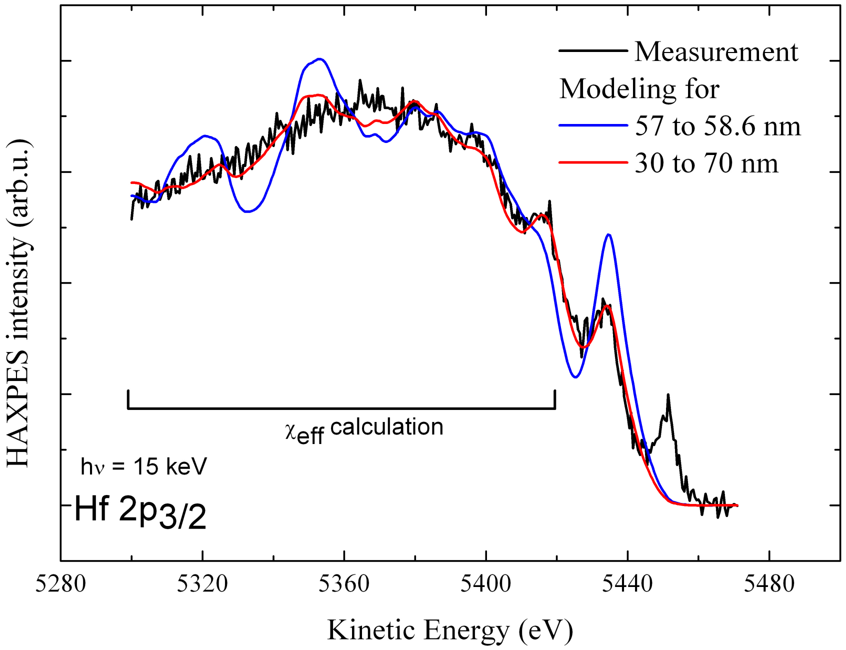

Figure 47: *Spectrum of Hf $2p_{3/2}$ for the 50 nm sample measured at 15 keV (in black) with background for a layer with top and bottom interface at 57 and 58.6 nm respectively (blue) and the background with lowest χ_{eff} value with top interface at 30 nm and bottom interface at 70 nm below the surface (red).*

The Fig. 47 shows the background modeling performed on Hf $2p_{3/2}$ spectra measured at 15 keV. The depth distribution presented here is for the nominal values of top interface located at 57 nm and a bottom interface at 58.6 nm below the surface. As for all the other peaks, the inelastic background has a higher intensity than the no-loss peak. The modeled background presents oscillations between 5300 and 5380 eV kinetic energy (as for any other modeling around this depth distribution) which are not present in the measurement. The lowest χ_{eff} value is obtained for a depth distribution of 30 to 70 nm below the surface which is not in agreement with previous results of TEM, EELS or Auger depth profile. The error is attributed both to the kinetic energy of the photoelectrons of 5450 eV as the inelastic scattering cross section is taken from 10 keV measurements and to the IMFP value of 9.47 nm which can be different from the EAL, due to the calculation method or intrinsic error in the original IMFP calculation. A modeling with too low IMFP leads to a background modeling with too high oscillations (see Fig. 39).

To overcome this difficulty, the photon energy was increased to 18 keV which leads to photoelectrons of Hf $2p_{3/2}$ with kinetic energy of 8429 eV. At this photoelectron energy, the IMFP is of 14.8 nm. Calculation of χ_{eff} leads to the result showed in Fig. 48(a) where the depth distribution is explored from the thinnest one of 59 to 61 nm below the surface to the thickest one from 50 to 75 nm. These two background modelings are presented in Fig. 48(b) and are almost the same.

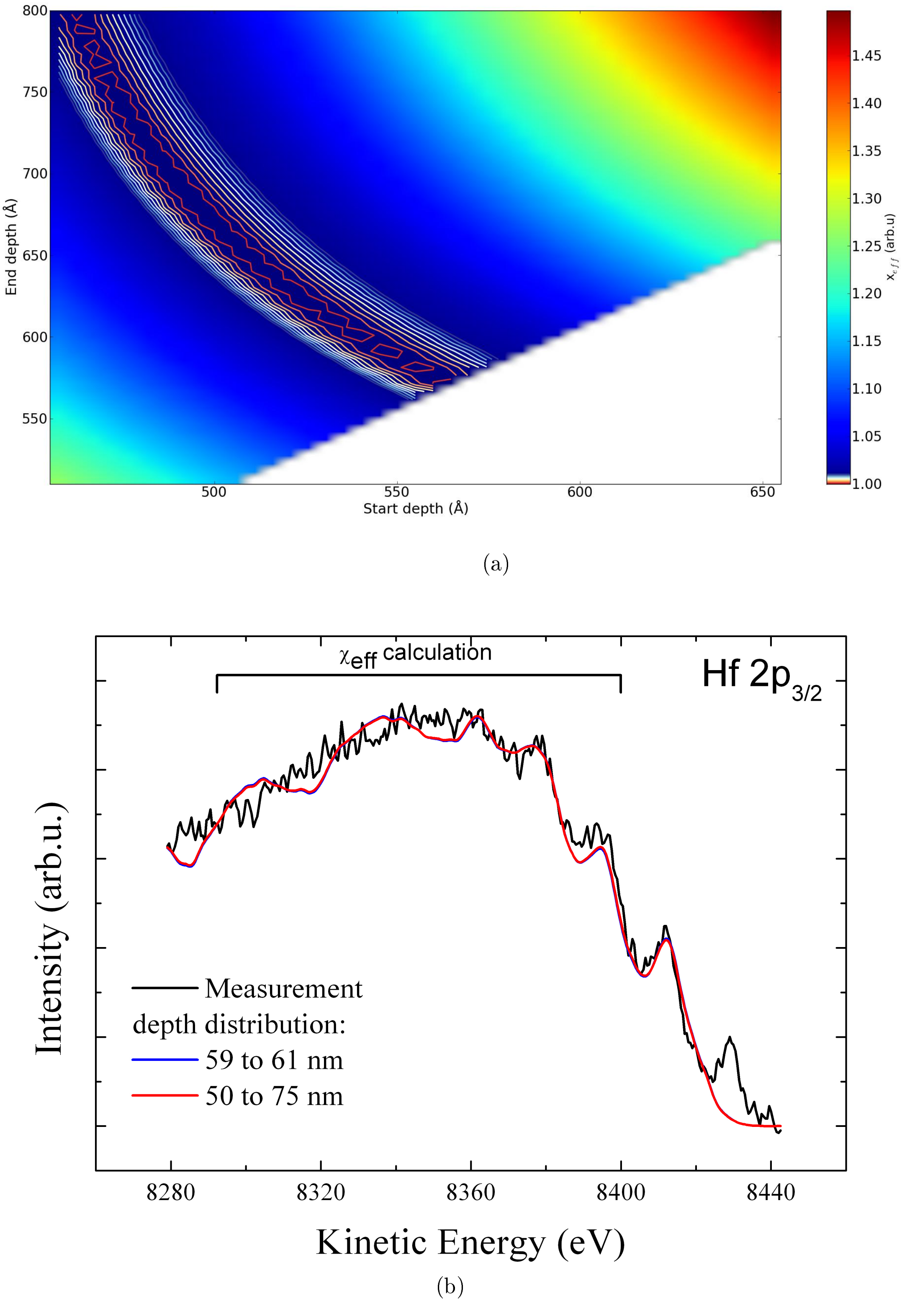

(a)

(b)

Figure 48: *(a) colormap of χ_{eff} for Hf $2p_{3/2}$ of 50 nm sample; (b) modeling for depth distribution of 59 nm to 61 nm below the surface (blue) and 50 to 75 nm below the surface (in red).*

3.4 Use of reference samples

The results from the background analysis without reference samples are in good agreement with deposition rate and compared with other characterization techniques. As described in Sec.2.3, the method is good at emphasizing *changes* in the depth distribution; thus analysis with a reference sample should give more precise results. This section describes background analysis using Tougaard method with use of reference samples.

3.4.1 Experimental conditions

Titanium reference and Hafnium reference were measured at ID32 beamline whereas lanthanum reference was measured at GALAXIES beamline. In theory, background analysis must be done from measurements for all the reference samples using the same apparatus than the one that had been used for the sample of interest. However, in this section, the spectra for Ti and Hf are from another measurement than the one for La.

The TiN reference sample consists of a 150 nm-thick layer of TiN deposited on the same condition as the TiN in the gate stack on silicon. The effective IMFP for Ti 1s in TiN at kinetic energy of 10045 eV is 12.68 nm. Therefore, 8 IMFP overcome the bottom interface of TiN layer located at 56.5 nm below the surface.

The hafnium reference is obtained by deposition of a thin film of HfSiO by MOCVD followed by DPN and PNA as the it has been done for the layer in the studied stack. The resulting thickness of the HfSiON layer in the reference sample is 15 nm.

The lanthanum reference consists of a commercial sample LA000200 from goodfellow. It is a 25x25 mm lanthanum foil of 0.025 mm-thick with La concentration of 99.9%. The sample has been directly transferred from the packaging of sample provider to the experimental chamber within a minute of air exposure. Even if this La reference sample can be seen as a pure infinite sample from an XPS point of view, its fabrication process does not correspond to the technological sample deposition condition. The studied stack is composed of oxidized lanthanum of unknown oxidation state whereas the reference sample is composed of pure lanthanum.

The pure silicon sample is the one presented in sec.3.2.1 and in Fig. 34.

3.4.2 Results and discussion

The Sec.3.3.5 showed the difficulty of the silicon background analysis as silicon is present in various layers in the stack. This Section will study such analysis with use of a reference sample.

Multilayer modeling of silicon Possibilities are available in QUASES-Analyze ® for performing background analysis of our samples with use of the reference samples. The Fig. 49 presents the differences between the modeling and the measurement for various options implemented in QUASES-Analyze. The black curve is the result found by our method, it corresponds to a depth distribution of silicon as a single monolayer with a top interface located at 9 nm below the surface and a bottom interface located below detection limit. The two blue curves show results obtained by use of either the "Optimized Area" (dark blue) or "Optimized RMS" options in QUASES-Analyze®. If the optimized RMS results are clearly not reproducing the background (oscillations are seen in the subtracted spectrum), the area optimized spectrum can be considered as a good qualitative reproduction of the background (there are no remaining oscillation in the subtracted spectrum) even if the intensity of the subtracted spectrum is always higher than the 0 value. The depth distribution obtained by this method is a single silicon layer located at 17.2 nm below the surface and a bottom interface beyond detection limit. Modeling with a distribution of the expected depth distribution of two layers, the first as a top layer of 50 nm and the second with top interface located at 55 nm below the surface with a bottom interface located beyond detection limits is plotted in red: it does not reproduce the oscillations in the lower energy loss region. In conclusion, the best background reproduction is found by our error estimation method but the depth distribution is not corresponding to the real depth distribution of silicon.

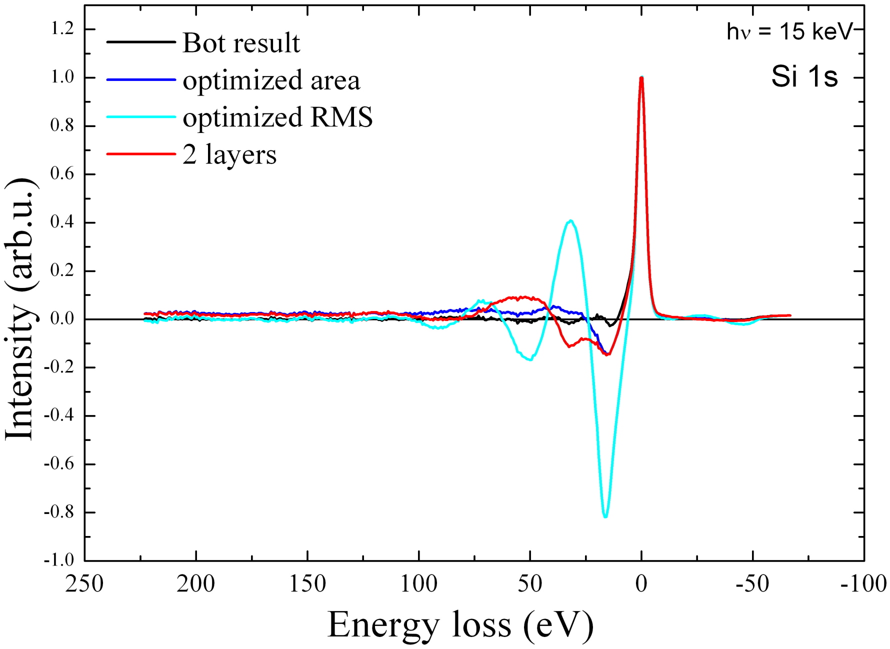

Figure 49: *Difference between the modelled spectrum and the measurement for the Si 1s spectra of the 50 nm samples with various error calculation: the "set homogeneous layer" from QUASES-Analyze software (red), our error computing method (green), the "optimized AREA" from QUASES-Analyze software (dark blue), the "optimized RMS" from QUASES-Analyze software (light blue), results for two homogeneous layers (black), results for "set homogeneous layer" from QUASES-Analyze software with Universal cross-section (yellow) and an infinite layer with top interface located at 9 nm below the surface with the universal cross-section (pink).*

Thin monolayer of lanthanum Lanthanum presents a very weak signal as can be seen in Fig. 38 due to the very small amount of La in the sample and its high burying depth. GALAXIES beamline presents a high photon flux. The measurements at 12 keV gives best analytical conditions. This energy has been chosen as it allows a good resolution and maximum photon flux. Analysis for depth distribution was performed, resulting in a top interface located at 56 nm and a bottom interface at 61 nm below the surface. The resulting background modeling can be seen in Fig. 50: analysis has been performed with or without the modified inelastic scattering cross-section and with or without use of reference sample. For presentation purposes, spectra have been normalized to maximum no-loss peak and have been shifted in intensity. Comparison of the subtracted spectra without use of reference sample shows the increases in background reproduction, the proper inelastic scattering cross section corresponding to a weighted average of the pure silicon cross-section measured at 10 keV and the universal one gives a flatten spectra in the energy loss region (in red).

Additional use of reference sample increases the flattening of this part of the spectrum, especially around kinetic energy of 5660 eV. The purple subtracted spectrum corresponding to an analysis with three parameters universal cross-section clearly does not reproduce these oscillations. The gain in using the modified cross-section is interesting but not spectacular. It is surprising to see the oscillations very well reproduced at this kinetic energy of 5710 eV from the inelastic scattering cross section measured at 10 keV. Oscillations are mainly dominated by bulk plasmon losses. At 5 or 10 keV, the surface information is very poor compared to the bulk information (see Fig. 35). The various options as "optimized RMS" and "optimized AREA" are not presented as they led both to a poor background reproduction and unrealistic depth distributions. The option "homogeneous layer" also gave unrealistic results and did not even match the specificity of the sample (La is only present in a monolayer).

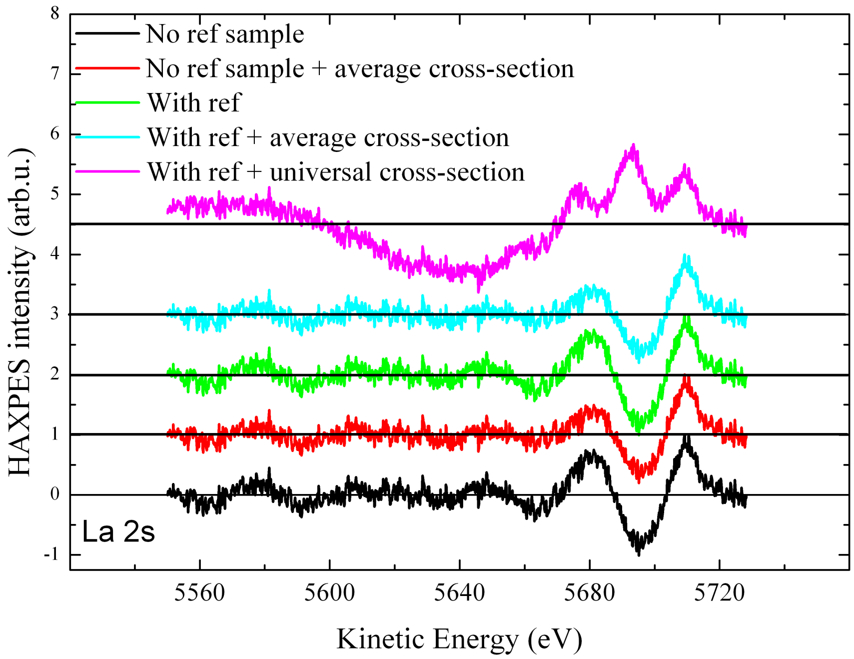

Figure 50: *La 2s subtracted spectra modeling for 50 nm sample corresponding to a depth distribution La of 56 nm to 61 nm, with the pure silicon cross section measured at 10 keV without reference sample (black), with average cross-section without reference sample (red), with the pure silicon cross section measured at 10 keV and reference sample (green), with average cross-section and reference sample (blue) and with universal cross-section and reference sample (pink).*

The Fig. 51 shows the colormap of χ_{eff} for depth distribution of La in the 50 nm sample with use of reference samples. The lowest χ_{eff} value is found for a top interface located at 59.5 nm below the surface and a bottom interface at 61.8 nm. The obtained thickness of 2.3 nm is in good agreement with results from other experiments and compared to the 4.5 nm obtained without reference. It is closer to the expected 0.7 nm from deposition tools. The bottom interface position does not change with use of reference sample but the top interface position does change. The obtained top position with reference samples is however in the error bar of the analysis without reference. The

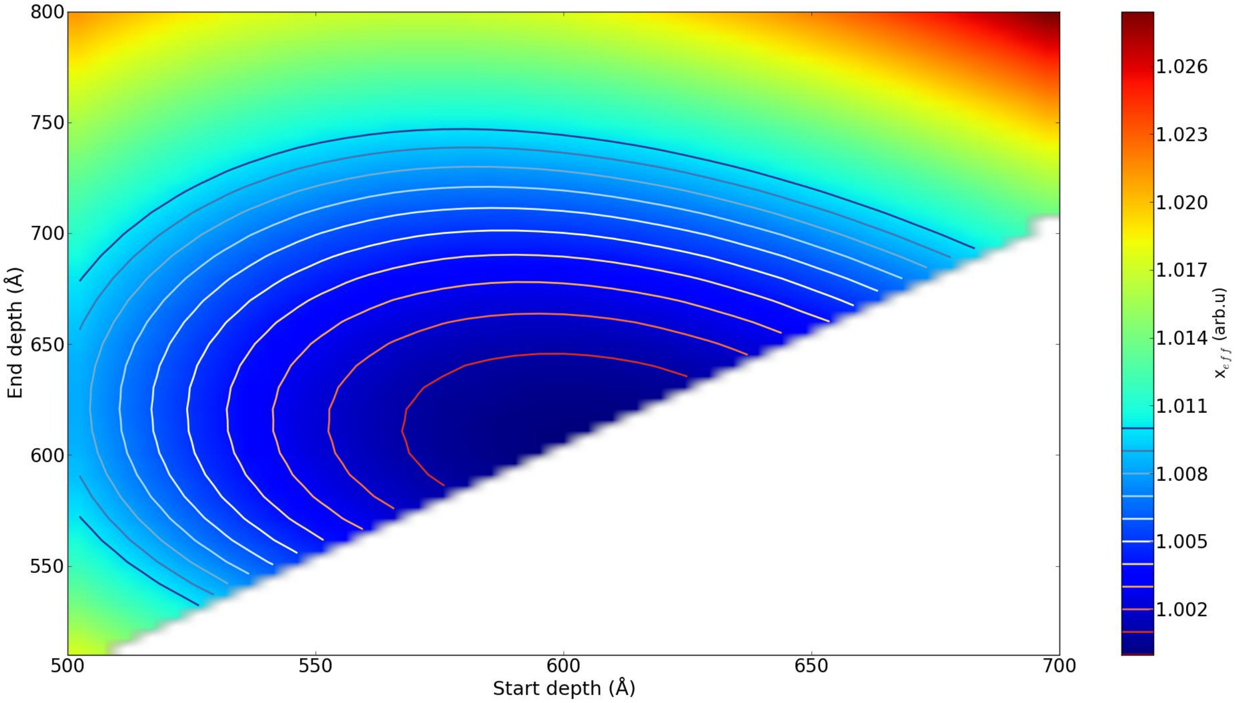

Figure 51: *Colormap of χ_{eff} of La in the 50 nm sample with use of reference sample.*

subtracted spectrum is presented in Fig. 50 along with the subtracted spectrum obtained without reference sample.

Thick buried layer of Titanium The case of Ti modeling will illustrate how the procedure could be at its best to analyze inelastic background. When treating the measurement with only the use of parameters, the result could be ambiguous as different depth distributions can lead to the same background reproduction (see sect.3.3.5). Use of reference samples reduces the number of possible depth distributions as can be seen in Fig. 52 where the domain of the lowest χ_{eff} is narrowed when compared to that of Fig. 46. However two distinct types of depth distributions are equally reproducing the inelastic background and the result remains ambiguous. An additional procedure consists in multiplying the obtained thicknesses by the "scale factor" of QUASES-software which corrects the signal from the reference sample no-loss peak and the CF factor which takes into account elastic scattering (see sect.2.4.1) as summarized in Tab.8. The two distinct cases for a 10 nm-thick layer (ddp1) and for a 37 nm-thick (ddp2) give thicknesses of 4.5 and 4.1 nm, respectively after correction (close to the 4.6 nm obtained by TEM). The discrepancy between the two obtained thicknesses comes from the uncertainty of the scale factor and of the CF function. In the case of La, the amount of substance is so low in the sample that the scale factor is 0 and thus this procedure cannot be applied.

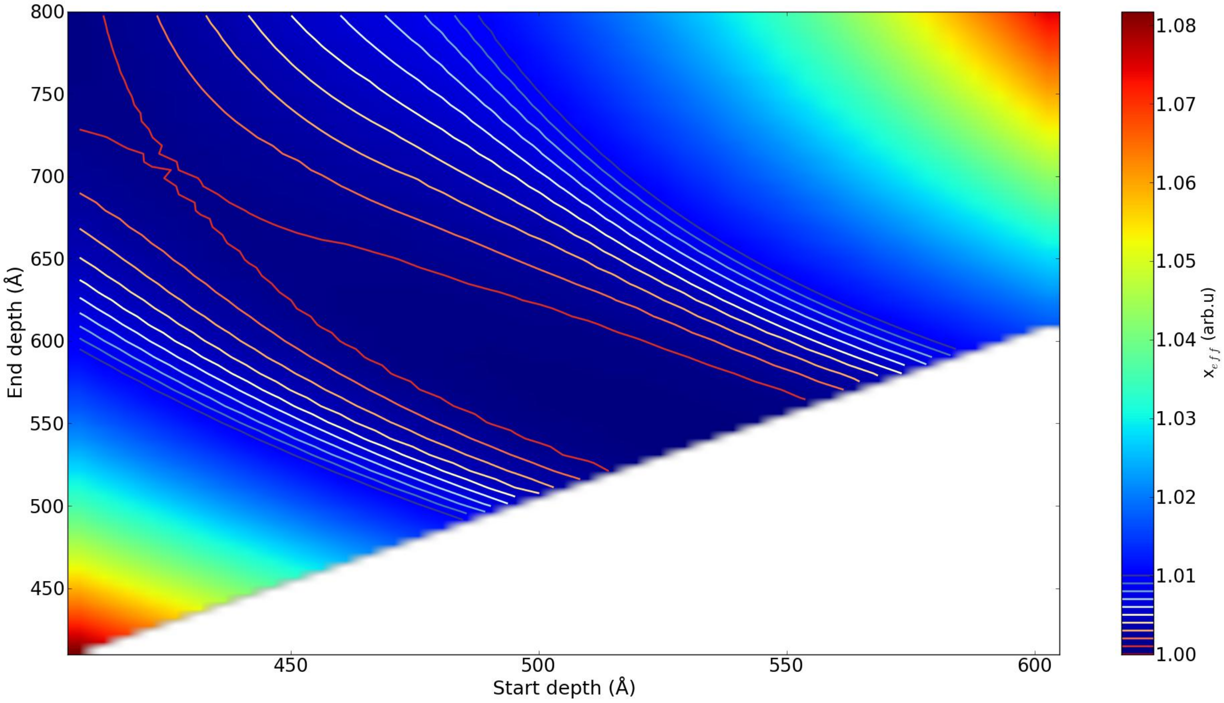

Figure 52: *Colormap of χ_{eff} of Ti in the 50 nm sample with use of reference sample.*

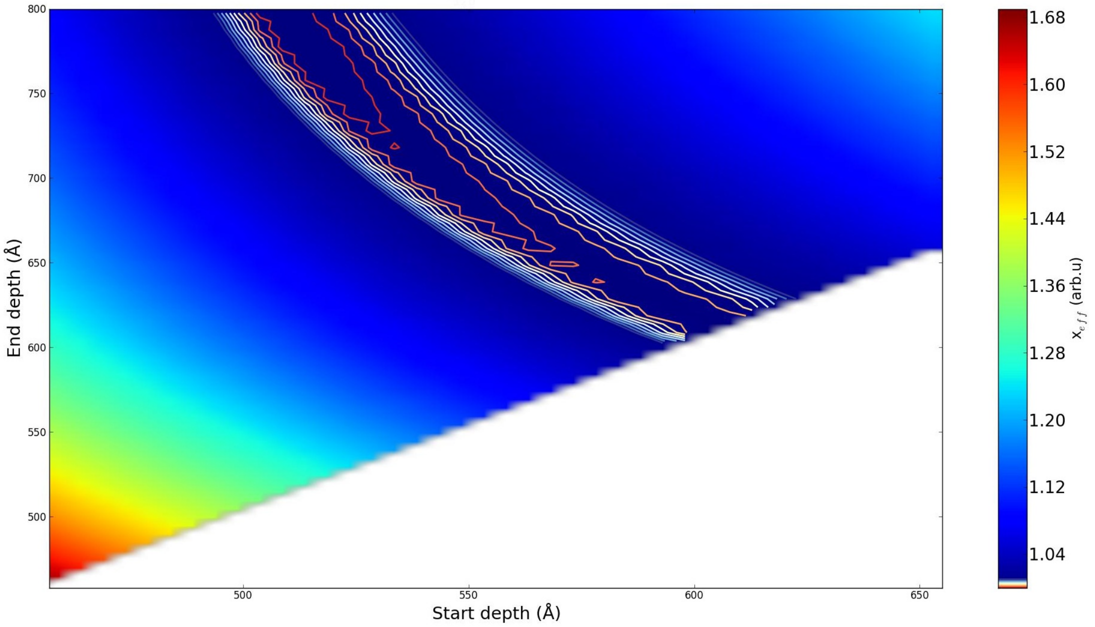

Figure 53: *plot of χ_{eff} calculation for Hf depth distribution profile with help of reference sample in the 50 nm sample.*

	Obtained thickness (nm)	Scale factor	CF	Corrected thickness (nm)	Nominal thickness (nm)
Ti ddp1	10	0.30	0.665	4.5	6.5
Ti ddp2	37	0.091	0.819	4.1	
Hf	26	0.045	0.478	2.4	1.7

Table 8: *Parameters influencing the obtained thickness of a layer when performing inelastic background analysis with reference sample.*

Thick buried layer of Hafnium The previous case of Hf study is completed by an analysis with reference samples. The reference sample is a 15 nm thick HfSiON layer and not a pure homogeneous sample. As the difference in the no-loss peak area between the reference and the sample is expected to be small, the total amount of substance are close in the two samples. The result of the *bot* operation and χ_{eff} calculation is presented in Fig. 53. The lowest χ_{eff} value is obtained for a layer with top interface located at 51 nm below the surface and the bottom interface at 77 nm. The resulting thickness of 26 nm is absolutely incompatible with nominal thickness or the results obtained by other characterization techniques. However, use of the scale factor of 0.045 (output of the software) and correction function of 0.478 (computed from the Eq. 51), the resulting thickness is of 2.4 nm, which is very close to the 1.7 nm nominal thickness.

3.5 Annealing of gate stacks

The background analysis of HAXPES spectra has been successfully applied to the previous samples, which were used to explore depth resolution limits. In technological devices designed in *gate last* process, the samples undergo annealing for the activation of dopants after deposition of the complete structure. This annealing is typically of a few seconds at high temperature (>1000°C) and can potentially induce interdiffusion of elements in the sample. The diffusion can be either required (as for the samples studied in the next Chapter) or undesirable (because it decreases the device performance in the case of a high-k metal gate sample).

In this Chapter the previous observations are applied to the study of high-k metal gate samples after annealing at 1200°C.

The *50 nm sample, 30 nm sample, 20 nm sample* and *high-k sample* were annealed at 1200°C for 10 s. In device production this step is meant to activate dopants in the sample and force intermixing of the active layers (LaO, HfSiON and SiON layers).

3.5.1 Results of inelastic background analysis of La

50 nm sample The 50 nm sample annealed was measured at ID 32 beamline with hv = 15 keV Inelastic background analysis was performed with the inelastic scattering cross-section derived from REELS measurement at 10 keV of pure silicon sample and IMFP = 15.4 nm for La $2p_{3/2}$. The result of the automated procedure is shown in Fig. 54(a) where the lowest χ_{eff} is centered around a top interface located at 49.9 nm and bottom interface at 56.2 nm below the surface. The corresponding modeling for inelastic background is shown in Fig. 54(b) where the background is quite well reproduced. The measured spectrum (in black) is very different from the unannealed sample where after the first plasmon loss the inelastic background is smooth (see Fig. 43). The La $2p_{3/2}$ spectrum of the annealed sample presents a second plasmon loss clearly distinguishable (located at 9470 eV kinetic energy) with higher intensity than the first plasmon loss. Then the inelastic background increases between 9420 and 9460 eV corresponding to a third plasmon loss and finally decreases from 9420 eV. All these qualitative observations are well reproduced in the modeled background. The inelastic background shape difference is mostly due to the low intensity of the no-loss peak for the annealed sample. This intensity of the La $2p_{3/2}$ peak is too low to perform core-level analysis. The background analysis overcomes this difficulty and allows quantification of depth distribution of such a sample. The resulting thickness of the La layer is of 7.4 nm. There is a thickness increase with respect to the unannealed sample (of 4.5 nm without reference sample).

The same procedure with use of reference samples is showed in Fig. 55(a). The automated procedure gives almost the same results. The top interface is located at 49.4 nm below the surface

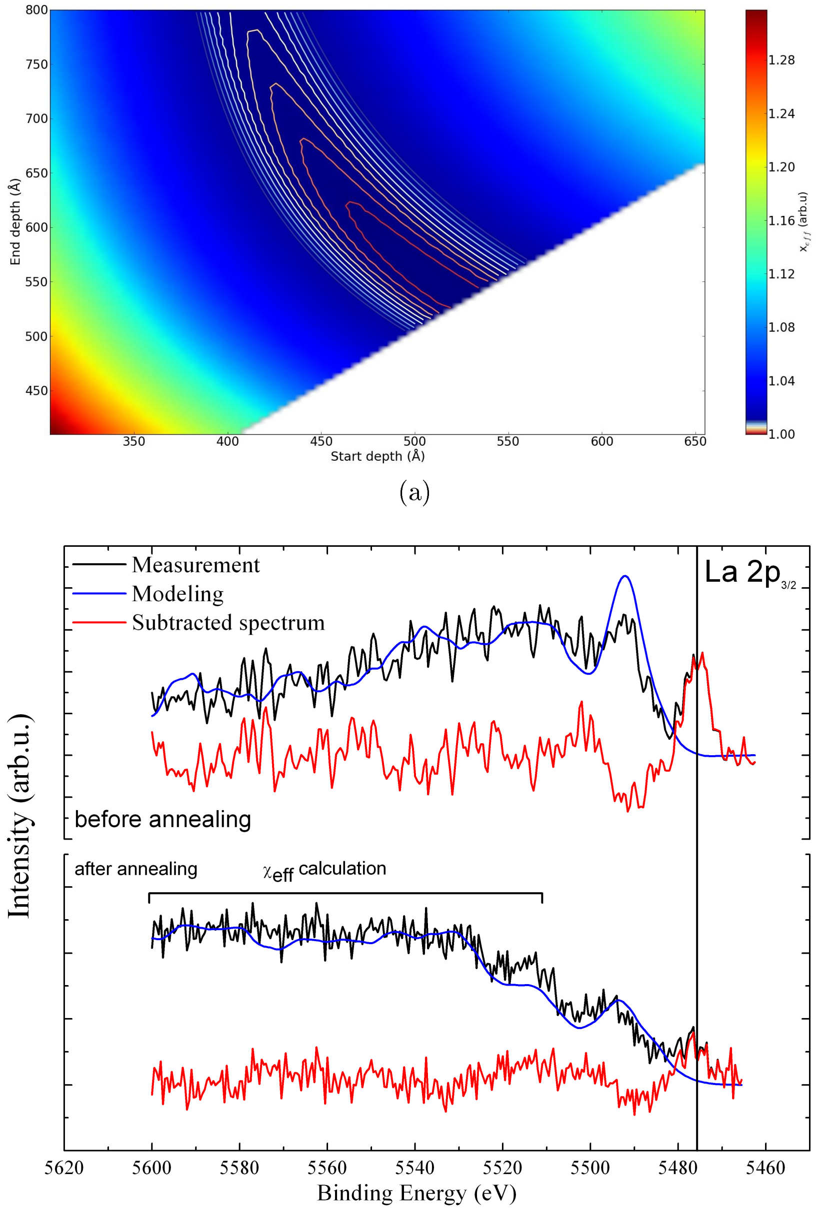

(a)

(b)

Figure 54: *(a) Result from automated treatment of the 50 nm sample annealed on La2p$_{3/2}$ spectrum, showing a depth distribution with top interface located at 49.5 nm and a bottom interface located at 56.2 nm below the surface. (b) Measured spectrum (in black) and corresponding modeled background (in blue) are presented with the subtracted spectrum (in red).*

and the bottom interface at 57.4 nm (instead of 49.5 and 56.2 nm without use of reference sample). If the difference in top interface of 0.1 nm between the analysis with and without reference sample is too low to be significant, the bottom interface changes by 1.2 nm. The resulting thickness of the La layer of 8.0 nm shows the diffusion of La during annealing when compared to the 2.3 nm obtained (with reference sample) for the unannealed sample.

The Fig. 55(b) shows the two subtracted spectra obtained with (red) and without (blue) use of the reference sample, the difference between the two spectra is plotted in the top panel. The two spectra correspond to two close depth distributions but the spectrum with use of reference samples is closer to the baseline over the full energy loss region. As this spectrum presents a better match to the measurement, the corresponding depth distribution of top interface located at 49.4 nm below the surface and bottom interface at 57.4 nm is more trustworthy.

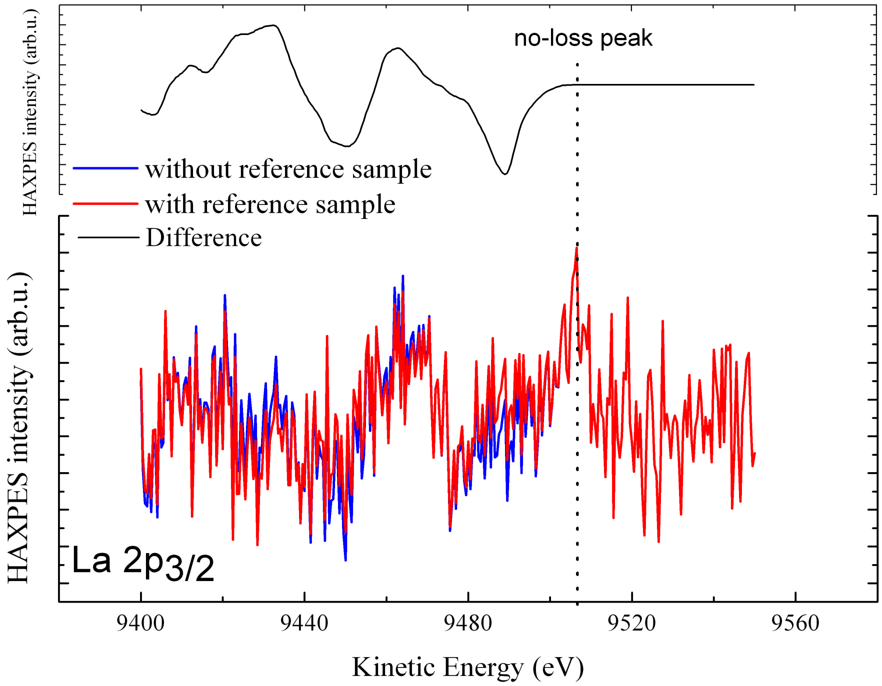

Figure 55: *The two subtracted spectra with (in red) and without (in blue) reference sample, the top layer shows the difference between these two spectra.*

30 nm sample The inelastic background analysis of the annealed 30 nm sample was performed on the La 2s measurement taken at GALAXIES beamline. The better stability and brilliance of the beam give a better recording the La energy loss signals. The result of the automated procedure is shown in Fig. 56(a) where the lowest χ_{eff} is obtained for a La layer with a top interface located at 35.8 nm below the surface and a bottom interface at 42.3 nm below the surface. The associated modeled inelastic background is shown in Fig. 56(b). The second plasmon loss is well reproduced (around 5670 eV) as well as the rest of the inelastic background over a wide energy range, except for the energy region around 5650 eV which is underestimated in the calculation as for the unannealed sample (see Fig. 43). The comparison of the thicknesses of the annealed (6.5nm) and of the unannealed (2nm) 30 nm sample suggests an intermixing of La during the annealing.

The use of reference sample using the same procedure analysis gives very similar results as the obtained top interface is found to be located at 35.5 nm below the surface and the bottom interface at 42.2 nm (instead of 35.8 and 42.3 without reference sample) as can be seen in Fig. 57(a). The difference in location of the top interface with and without reference sample is of 0.3 nm whereas of the bottom interface of 0.1 nm. For the 50 nm sample, the use of reference sample had only a small influence on the top interface but a non negligible one in the bottom interface. For the 30 nm sample it is the opposite. In other words, the use of reference sample does not impact the absolute position of interfaces in a systematic way. The resulting thickness obtained is of 6.7 nm and shows an intermixing when compared to the previously obtained 2 nm (without reference sample).

Fig. 57(b) shows the subtracted spectra with use of reference sample (in red) and without (in blue). The difference between the two spectra in the top panel shows the almost perfect superposition of the two spectra in the top panel is representative of two very close depth distributions (the scale is multiplied by 100). It is impossible to decide which one of the two spectra is a better reproduction of the measurement. As the analysis with use of reference sample could be more accurate, the corresponding depth distribution of the top interface located at 35.5 nm and bottom interface at 42.2 nm below the surface will be retained in the following.

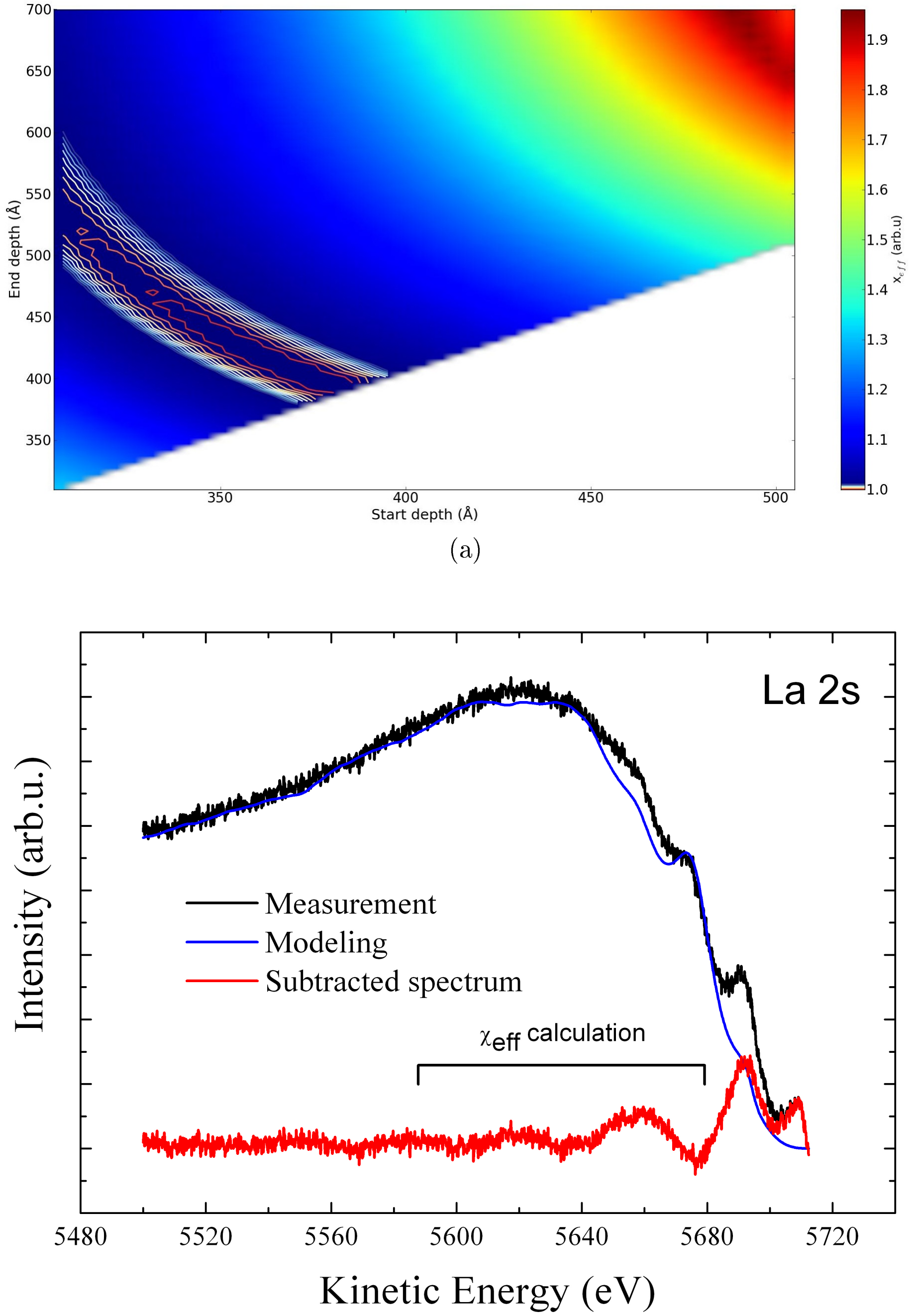

(a)

(b)

Figure 56: *(a) Result from automated treatment of the 30 nm sample annealed without use of reference sample on La 2s spectrum, showing a depth distribution with top interface located at 35.8 nm and a bottom interface located at 42.3 nm below the surface. The measured spectrum (in black) and the corresponding modeled background (in blue) are presented in (c) with the subtracted spectrum (in red).*

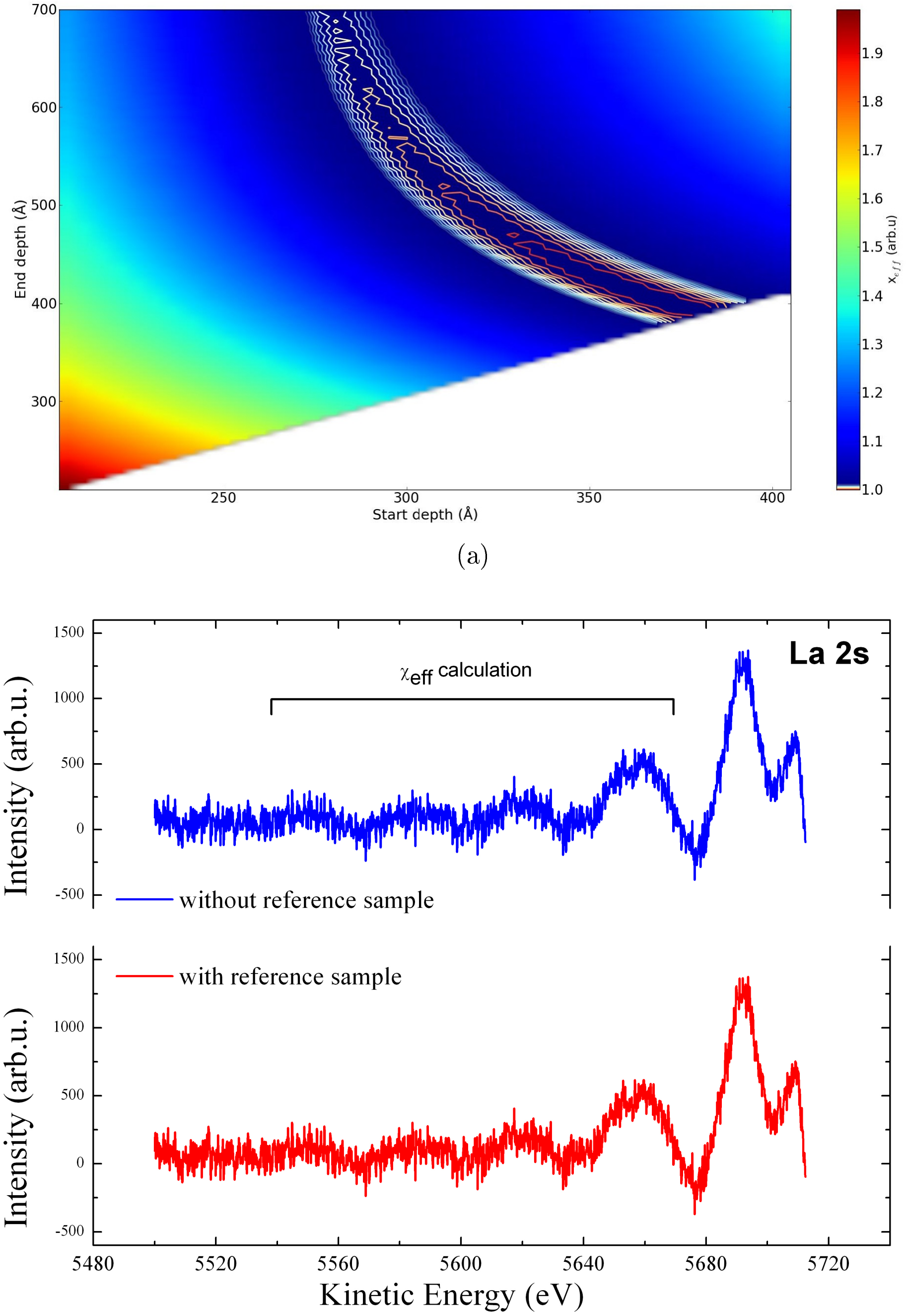

(a)

(b)

Figure 57: *(a) Result from automated treatment of the 30 nm sample annealed on La 2s spectrum with use of reference sample, showing a depth distribution with top interface located at 35.5 nm and a bottom interface located at 42.2 nm below the surface. (b) The two subtracted spectra with (in red) and without (in blue) reference sample.*

20 nm sample Inelastic background analysis was performed on measurements done at 12 keV in Fig. 58, as it is more surface sensitive than the 15 keV measurements, the corresponding IMFP of 11.2 nm ensures a sufficient depth analysis. The inelastic cross-section used is a weighted average of the pure silicon at 10 keV and of the three parameter universal cross-section according to the nominal thickness of 20 nm for silicon and 6.5 nm for Ti. The result of the automated procedure is shown in Fig. 58(a) where the lowest χ_{eff} points to a La layer located at 30.9 nm below the surface and a bottom interface located at 35.0 nm. The associated modeled background is shown in Fig. 58(b): the first plasmon loss is underestimated in the modeling, but the second is fairly well reproduced. The measured intensity of the tail of the inelastic background decreases at low kinetic energy (<6480 eV).

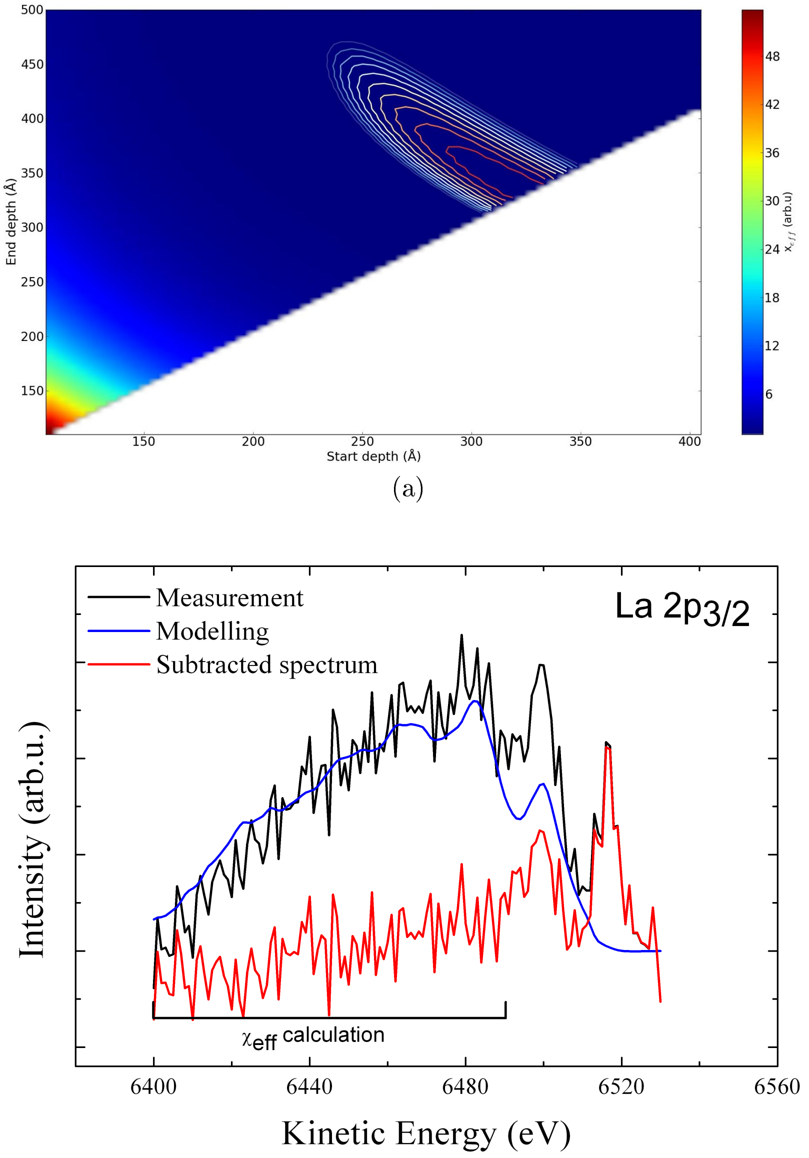

(a)

(b)

Figure 58: *(a) Result from automated treatment of the 20 nm sample annealed without use of reference sample on La* $2p_{3/2}$ *spectrum, showing a depth distribution with top interface located at 30.9 nm and a bottom interface located at 35.0 nm below the surface. The measured spectrum (in black) and the corresponding modeled background (in blue) are presented in (c) with the subtracted spectrum (in red).*

The use of a reference sample modifies slightly the previous results as showed in Fig. 59(a) where the lowest χ_{eff} points to a top interface located at 30.8 nm below the surface and a bottom interface at 35.5 nm (instead of 30.9 and 35.0 nm without reference). The change of the top interface location is very small (0.1 nm) whereasthat of the bottom interface is of 0.5 nm. The resulting thickness of 4.7 nm when compared to the 1 nm found for the unannealed sample (without reference) shows the intermixing.

Fig. 59(b) shows the two subtracted spectra with (in red) and without use of reference sample (in blue). The difference between the two spectra is plotted in the top panel. It shows that the major deviation is located directly below the no-loss peak and extends to 70 eV energy loss (6440 eV kinetic energy). The spectrum with use of reference samples presents a better matching with the baseline. The corresponding depth distribution with top interface at 30.8 and bottom interface at 35.5 nm below the surface is much trustworthy.

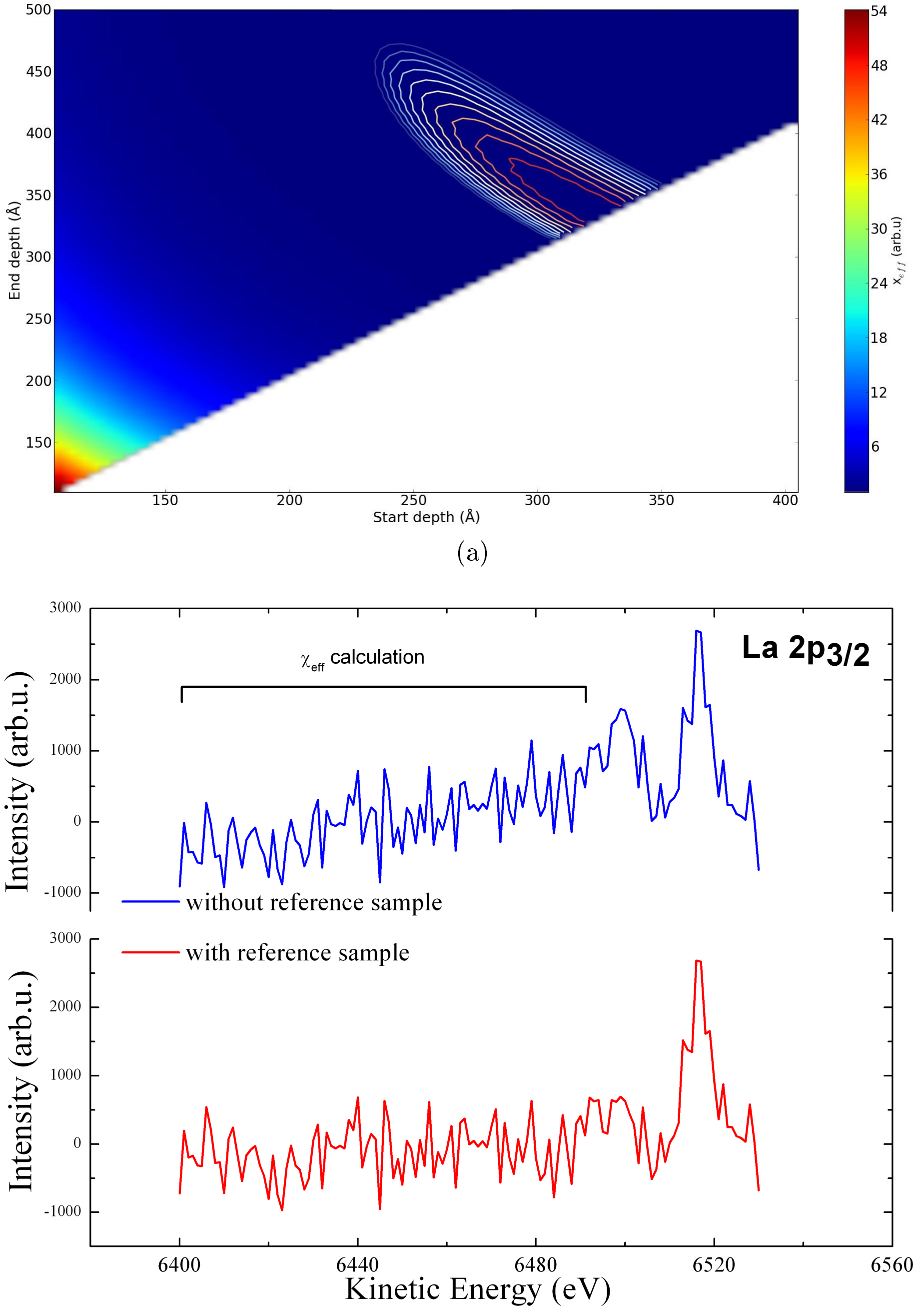

(a)

(b)

Figure 59: *(a) Result from automated treatment of the 30 nm sample annealed on La2*$p_{3/2}$ *spectrum with use of reference sample, showing a depth distribution with top interface located at 30.8 nm and a bottom interface located at 35.5 nm below the surface. (b) The two subtracted spectra with (in red) and without (in blue) reference sample, the top layer shows the difference between these two spectra.*

high-k sample As the high-k sample has the same top structure as the 20 nm sample (20 nm of Si and 6.5 nm of Ti) the inelastic background modeling was performed under the same conditions. However the use of a reference sample does not change the obtained depth distribution, neither the corresponding modeled inelastic background (not shown here). The result of the automated procedure is shown in Fig. 60(a) where the lowest χ_{eff} points to a top interface located at 29.4 nm below the surface and a bottom interface located at 35.0 nm below the surface. The corresponding measurement (in black) and modeled background (in blue) are presented in Fig. 60(b) with the subtracted spectrum (in red). The first plasmon loss is underestimated by the modeling but the second plasmon is nicely taken into account. The further energy loss region ($<$6480 eV kinetic energy) is very well reproduced, even when the measurement matches the baseline. The thickness of the La layer (5.6 nm) shows a thickiness increased when compared to the unannealed sample (2.2 nm).

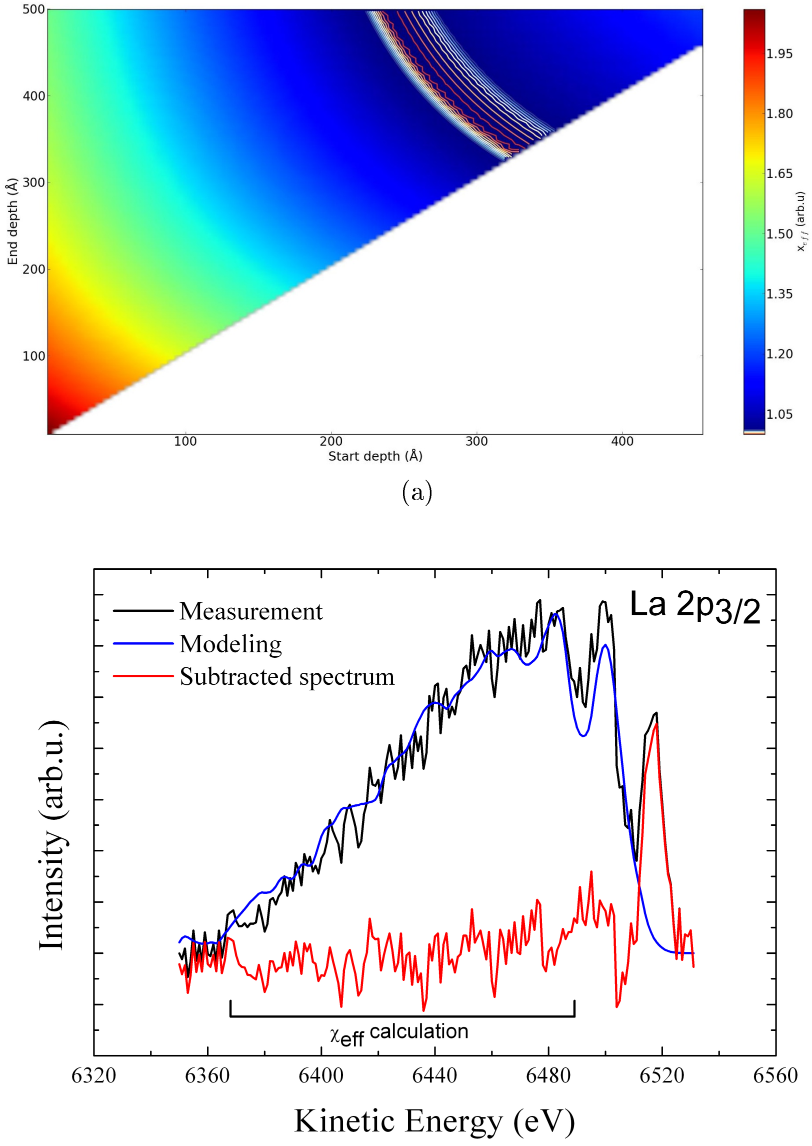

(a)

(b)

Figure 60: *(a) Result from automated treatment of the high-k sample annealed without use of reference sample on La* $2p_{3/2}$ *spectrum measured at 12 keV, showing a depth distribution with top interface located at 29.8 nm and a bottom interface located at 35.0 nm below the surface. The measured spectrum (in black) and the corresponding modeled background (in blue) are presented in (c) with the subtracted spectrum (in red).*

3.5.2 Summary

The determined depth distribution for the annealed samples are summarized in Tab.9. As was the case for the unannealed sample (see Tab.5), the obtained thicknesses for the 50 nm, 30 nm and 20 nm decrease with the decrease of the capping layer thickness, confirming that the accuracy is better when the studied layer is closer to the surface. The top interface positions of 49.5, 35.8 and 30.9 nm below the surface (without reference sample) are very close to the nominal values of 56.5, 36.5 and 26.5 nm given by deposition tools.

	50 nm		30 nm		20 nm		high-k
	no ref	with ref	no ref	with ref	no ref	with ref	no ref
Top La interface (nm)	49.5	49.4	35.8	35.5	30.9	30.8	29.4
Bottom La interface (nm)	56.2	57.4	42.3	42.2	35.0	35.5	35.0
La thickness (nm)	6.7	8.0	6.5	6.7	4.1	4.7	5.6
As received La thickness (nm)	4	2.3	2		1		2.2

Table 9: *Results of inelastic background analysis for annealed samples.*

Both annealed 20 nm sample and high-k sample present almost the same depth distribution: the top interface is located at 30.9 nm for the 20 nm sample and at 29.4 nm below the surface for the high-k sample. However the estimated thickness is larger for the high-k sample than for the 20 nm sample. This result is expected because in this latter case, the active layer thickness has been intentionally increased..

In overall, as seen in Tab.9, the use of a reference sample does not change very much the interface positions for both the top and the bottom La interface locations. The layer thickness however, is always found to be thicker with the use of a reference sample. As the inelastic background analysis is expected to be more reliable with the use of reference samples, as confirmed by the better background reproduction, the thus-obtained thickness results are expected to be also more reliable. The differences between the results with and without use of reference samples are small due to the optimization of the inelastic scattering cross-section used, which is always representative of the sample composition as it is defined as a weighted average of the individual cross sections according to their nominal thicknesses.

3.5.3 Comparison with other techniques

Atom probe Tomography Fig. 61 shows the 3D spatial distribution of atoms for the 50 nm annealed sample, which has been obtained from the atom probe reconstruction. Each dot corresponds to one atom. As for the unannealed sample of Fig. 33, La elemental contribution was detected at m/n = 77 corresponding to LaO^{2+} ion compound and Hf contribution was only detected in the oxide ion form at m/n = 98. The maximum intensity for La and Hf are located at the same depth and follows the same trend. From comparison with the unannealed sample presented in Fig. 33, the La has diffused toward the substrate: the result is a complete intermixing of La and Hf. The oxide layer has a thickness estimated at 1.5 nm, as for the unannealed sample. The small shoulder of La located at 2.3 nm cannot be considered as relevant because its intensity is very low.

Auger depth profile Fig. 62 is obtained from the peak to peak height of the derivative spectra weighted by the corresponding sensitivity factor under the same experimental conditions as for

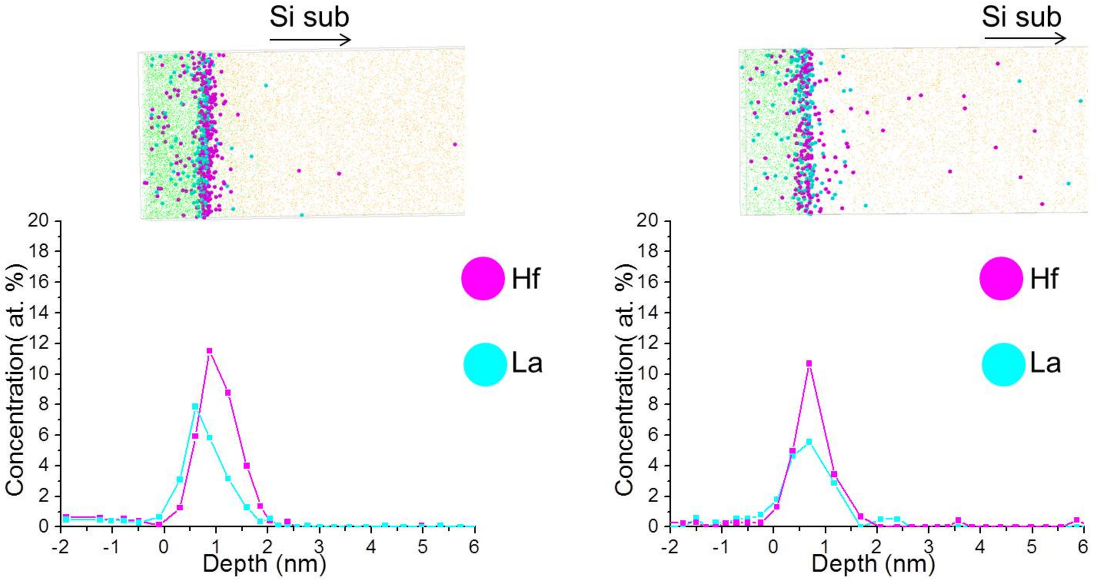

(a) (b)

Figure 61: *3D Atom Probe Tomography of the 50 nm sample unannealed (a) and annealed (b) with corresponding proximity histogram of La and Hf calculated from the 37% TiN iso-surface. The top panels show the reconstruction of the La and Hf layers and the depth profile of these elements are presented in the bottom panels.*

Fig. 32. The right panel shows a zoom on the the concentration profile between 60 nm and 70 nm below the surface. It confirmes that the oxided state of both La and Hf as seen in APT. The overall thickness of the layer containing La and Hf is ∼ 6 times wider than the thickness obtained by APT. This is due to ion implantation during sputtering while performing the Auger depth profile (specially for Hf which presents a large tail at >70 nm depth).

Comparison with the as-received samples The La layer thicknesses obtained before and after annealing are summarized in Tab.10. The atom probe tomography, Auger depth profiling and the inelastic background analysis show an increase in thickness of the La layer after annealing. The APT shows an increas in thickness of 50% from 1 to 1.5 nm during annealing. The Auger depth profile can only show a qualitative increase in thickness because the strong ion implantation prevents to conclude in a more quantitative way.

The inelastic background analysis shows an increase in thickness after annealing for all the samples. Without use of reference sample, the increase is 64%, 225% and 310% for the 50 nm, 30 nm and 20 nm samples respectively.

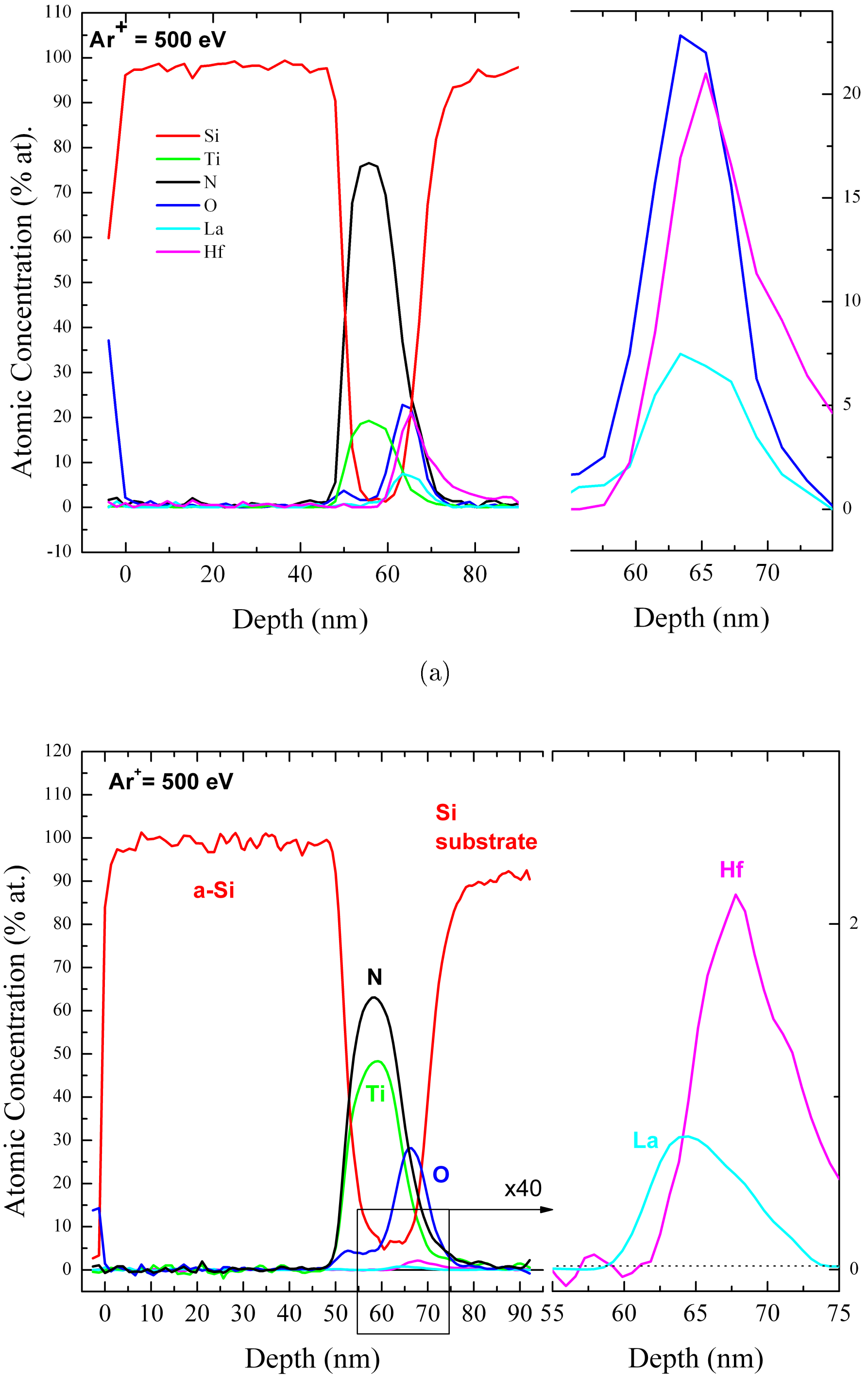

(a)

(b)

Figure 62: *Auger depth profiling of the annealed 50 nm sample annealed (a) and unannealed (b), highlighting the thickness of the a-Si cap and the depth distribution of the La layer in between the TiN and HfSiON layers. The broadening of the TiN layer is due to different sputter rates for TiN and Si.*

Sample	50 nm	50 nm annealed	30 nm	30 nm annealed	20 nm	20 nm annealed	high-k	high-k annealed
APT	1.0	1.5						
Auger	10	>10						
IBA	4.5	7.4	2	6.5	1	4.1	2.2	5.6
IBA with reference	2.3	8.0	✖	6.7	✖	4.7	✖	

Table 10: *Thicknesses of La layer in nm obtained with various methods. IBA stands for inelastic background analysis.*

3.6 Conclusion of Chapter III

Thicknesses obtained by background analysis of HAXPES spectra using Tougaard's implemented method are summarized in Tab.11.

		20 nm sample	30 nm sample	50 nm sample	
	Nominal (nm)	No ref (nm)	No ref (nm)	No ref (nm)	With Ref (nm)
Ti	6.5			11	4.1-4.5
La	0.4	1	2	4	2.3
Hf	1.7	✖	✖	✖	2.4

Table 11: *Layer thicknesses obtained for 20 nm, 30 nm, and 50 nm samples with photon energy of 15 keV.*

As seen in this Chapter, the HAXPES experiment is sensitive to deeply buried layer. A deeply buried layer gives an inelastic background intensity higher than the no-loss peak. The shape of this background is determined by the depth distribution of the element, which can be directly analyzed using proper input parameters. The main observations of this Chapter are:

- The photon energy must be chosen as a compromise between the photoionisation ratio which decreases with increasing photon energy and the probed depth which increases with increasing photon energy.

- Modification of the IMFP parameter in the studied cases does not change a lot the error value (10%). However, if the material is very exotic the difference between the calculated IMFP and the EAL could be large.

- If the sample presents a thick component with plasmon loss as Si, then the inelastic scattering cross section must be carefully chosen to match the physical phenomenon while photoelectrons travel inside the medium. The obtained absolute depth distribution depends on this parameter: the more precise it matches the sample, the more accurate is the absolute position of the modeled interface positions. The obtained thicknesses depend on the location of the layer, a more deeply buried layer gives an overestimated layer thickness whereas a layer located near the surface gives almost perfect match between the expected thickness and the obtained one. The best absolute positions of the layer are then obtained for the *50 nm sample* whereas the best thickness modeling is obtained for the *20 nm sample.*

- Use of reference samples increases the reliability of the background analysis and additional use of corrections for elastic scattering gives a thickness closer to the nominal values.
- The original method set up for computing error between the modeling and the measurement gives better reproduction of the background than the methods available in QUASES-Analyze®, but is more time consuming due to the external treatment of the data.

4 Application to High Electron Mobility Transistor (HEMT) materials

This Chapter highlights the **combination of inelastic background analysis and high resolution core-level analysis** by the study of the HEMT sample series (as a function of the annealing temperature). The high-resolution core-level analysis gives the chemical environment of the considered atom in the first 3 IMFP. From these observations, an inelastic scattering cross-section representative of the scattering events suffered by the photoelectrons is determined, as an input of the calculation. This ongoing experiment on technological sample still in development exposes a new methodology to obtain depth distribution and the elemental chemical environment and to depict the structure of the sample and the effects of the annealing.

Among various types of transistors, the need for RF power electronics is increasing. GaN based compounds conveniently correspond to the requirements of wide bandgap materials due to their potential in high output power density, high operation voltage and high input impedance. GaN also presents a high electron saturation velocity, which allows high frequency operation. The combination of these features results in a high current density and low channel resistance, giving GaN based transistors good predisposition to be a candidate for high frequency operation and power switching application. To ensure a sustainable high power and high frequency transistors require to be based on semiconductor material with both large breakdown voltage and high electron mobility. The wide bandgap of GaN and its ability to form heterojunctions makes it a good candidate to perform High Electron Mobility Transistor (HEMT).

Transistor are based on GaN/AlGaN heterostructures as the annealing forms a thin AlN layer which conducts electricity between AlGaN and GaN layers like as a Two-dimensional Electron Gas (2DEG) [119]. At first the saturation drain current of 40 mA/mm was observed [120] and the first demonstration of RF power data of 1.1W/mm at 2 GHz for an AlGaN/GaN HEMT was demonstrated [121]. The increasing performances have been ensured by technological improvements, firstly with use of a SiN_x passivation layer [122] to reduce the DC-to-RF dispersion caused by surface trap states, the output power was then measured to 9 and 11 W/mm [123]. Then the addition of a *field plate* (FP) in the transistor architecture decreased the peak value of the electric field, reducing trapping effect and increasing breakdown voltage. As a result a 10 W/mm was demonstrated [124] and optimization of the FP led to a 30 W/mm GaN based HEMT [125]. It is also possible to connect the source to the FP, then the FP-to-channel capacitance becomes the drain-source capacitance, both possibilities are illustrated in Fig. 63.

The studied samples are designed to be the source electrodes in the global HEMT structure and are based on Ti/Al alloys (labeled S in Fig. 63). As previously stated, a 2DEG of AlN is formed at

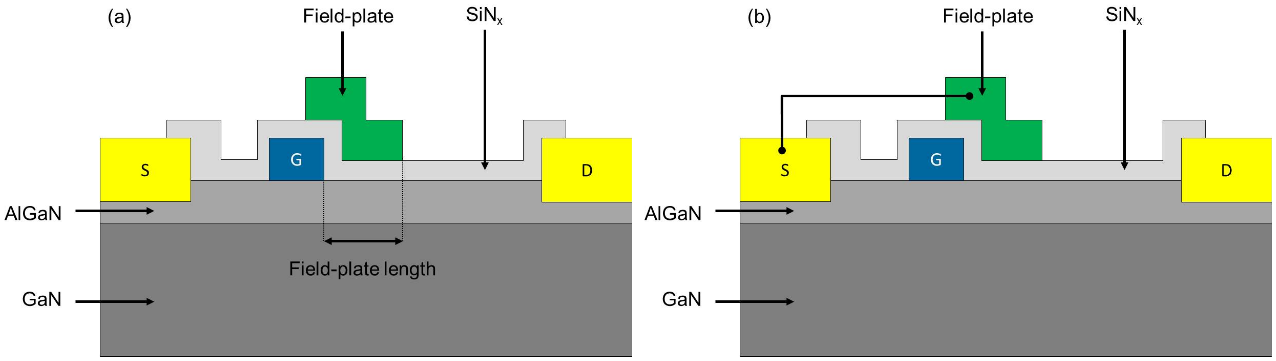

Figure 63: *Scheme of GaN based HEMT with (a) gate-connected field plate and (b) source-connected field plate; (S) is the source and (D) is the drain.*

the interface of the GaN and AlGaN layers. In order to not deteriorate the device performances, the bottom interface of the AlGaN layer must remain unaltered during contact formation in the source, thus the elements forming the source must not diffuse toward the substrate down to the GaN layer. The present study is not focused on the 2DEG gas, as this was pinpointed in other studies [126, 127], but on reactions occurring in the top layers containing Al and Ti which form the source in the device. After the 2DEG is formed, a junction must appear with the rest of the source (i.e. the Ti and the Al layers) to form an ohmic contact (see Fig. 63).

4.1 Experimental

4.1.1 Samples description

Samples processed for this study are based on an $Al_{0.25}Ga_{0.75}N/GaN$ (24/1000 nm) epitaxial stack grown by MOCVD on Si (111) substrate as schemed in Fig. 64.

A 15 nm-thick Ti layer was deposited by electron-beam evaporation; then a 10 nm-thick Al layer was deposited in the same chamber, also by electron beam evaporation; then the sample was cut in three pieces. One is conserved without further treatment whereas the two others were annealed in a Rapid Thermal Annealing (RTA) system under N_2 atmosphere. The result is three different samples:

- The unannealed sample.
- A sample annealed at 600°C for 300 s. This sample is referred to as *600°C sample* in the following.
- A sample annealed at 600°C for 300 s and then 900°C for 60 s. This sample is referred to as *900°C sample* in the following. It presents an ohmic behavior as presented in Appendix V.

The samples are deposited over a large area to avoid any edge effects. They cannot be used to measure DC characteristics, neither I-V curves, but are representative of the physical processes

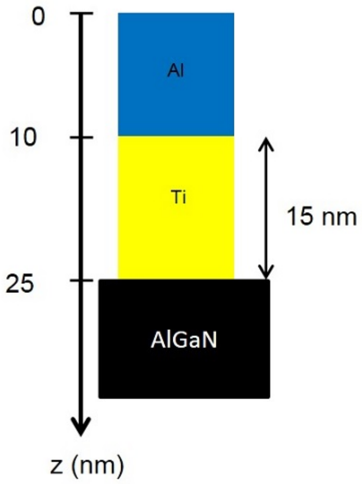

Figure 64: *Scheme of the sample used as source in HEMT structure. The thicknesses are nominal values given by deposition tools.*

which are occurring in the real device. The thicknesses of the metal layers are reduced compared to the thicknesses in the functional devices but are the same as the ones used to measure DC characteristics presented in Appendix V.

4.1.2 HAXPES measurements

The measurements were performed on GALAXIES beamline at SOLEIL synchrotron using 8 keV photon energy without any specific surface preparation. The experimental geometry was chosen with x-rays impinging the sample at 10° from the surface and with photoelectrons being detected at 10° from surface normal. High resolution core-level spectra were measured to obtain information on the chemical environment of Ti and Al and high-photon flux measurements were performed for inelastic background analysis of Ti, Al and Ga. At such a high photon energy (8 keV), the corresponding effective IMFPs tabulated in Tab.12 ensure to probe the complete stack with inelastic background analysis. When studying the no-loss peak, 95% of the signal (3 IMFP) comes from 32.4 nm and 14.4 nm below the surface for Al 1s and Ti 1s respectively. The low kinetic energy of Ti 1s photoelectrons of 3011 eV is not sufficient to probe the full Ti layer (assuming a bottom interface location at 25 nm below the surface according to deposition tools), but increasing the photon energy (i.e. increasing the IMFP) would lower the energy resolution of the spectrometer and affect the high resolution spectra; for this reason the photon energy was kept at 8 keV. Information given by analysis of the Ti 1s no-loss peak will therefore be representative mainly of the top of the Ti layer, while the interface between Ti and AlGaN layer could be analyzed with background analysis.

Element	Kinetic energy (eV)	Nominal Thickness (nm)	Individual IMFP (nm)	Effective IMFP (nm)	3 x IMFP (nm)	8 x IMFP (nm)
Al 1s	6425	10	10.8	10.8	32.4	86.4
Ti 1s	3011	15	4.2	4.8	14.4	38.4
Ga 2s	6750	∞	10.8	9.5	28.5	76

Table 12: *Effective IMFP for Al, Ti and Ga according to Eq.7 with photon energy of 8 keV.*

4.1.3 Core-level fitting procedure

The energy calibration is achieved by measuring the Au $4f_{5/2}$ peak located at 7906.9 eV kinetic energy. The recoil energy shift has been considered using Eq.17, the binding energy has been defined according to Eq.20, thus the photon energy is calculated to be 7994.6 eV. All high resolution spectra have been fitted with a Voigt function except for metallic Ti and metallic Al which have been fitted with Doniach-Sunjic line shape. The used Voigt functions are products of Gaussian and Lorentzian with ratio of 80% and 20% respectively. These parameter are kept constant during the fitting procedure, thus an increase of the Full Width at Half Maximum of the peak is interpreted as an increasing structural and/or chemical disorder in the compound. This Voigt function has been chosen as it is found to be the best shape for the peaks in the spectra under consideration.

4.2 Results overview

Fig. 65 shows the high-flux measurements of the Ti 1s used for the inelastic background analysis, corrected to match the baseline, and the insert shows the high-resolution spectra used for the peak fitting.

For the unannealed sample, the Ti 1s core-level signal is weak, as Ti is expected to be deeply buried. The strong oscillations seen in the high flux measurements show the metallic character of both the Ti and the Al layers. The inelastic background is of same intensity as the no-loss peak.

The first annealing at 600°C leads to a new peak located at higher binding energy in the high resolution spectrum and an overall intensity increases. Furthermore only one plasmon loss is seen and slightly shifted toward the lower kinetic energy than the first plasmon seen for the unannealed sample: it corresponds to a change in the metallic character of Ti and Al. The intensity decrease of the inelastic background indicates a diffusion of the Ti toward the surface.

Further annealing at 900°C leads to components located between the two peaks seen at 600°C and to an intensity increase compared to the one observed for the 600°C sample. These observations indicate the formation of alloys of Ti with different compositions. The intensity decreasing of the inelastic background indicates the diffusion of Ti toward the surface.

The Fig. 66 shows the high photon flux measurements of the Al 1s used for the inelastic

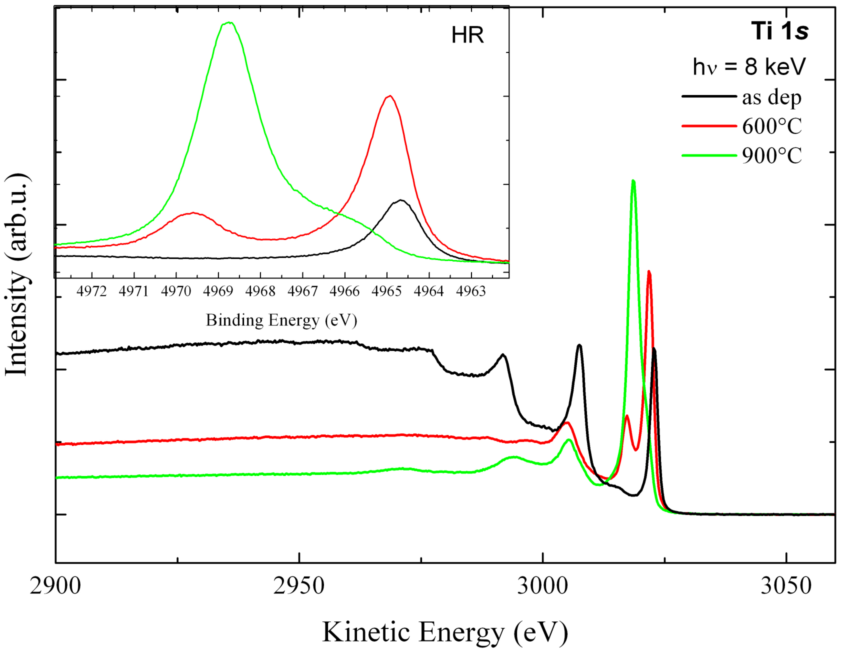

Figure 65: *Measurements of Ti 1s with high photon flux of 8 keV, the insert shows the high-resolution spectra of Ti 1s for the various annealing.*

background analysis, corrected to match the baseline and the insert shows the high-resolution spectra used for the peak fitting.

The Al 1s high resolution spectrum of the unannealed sample presents two distinct peaks: the one located at low binding energy is asymmetric and representative of metallic Al while the other is representative of an oxidized aluminum. The inelastic background presents a strong feature near the no-loss peak, representative of the metallic character of aluminum.

The annealing at 600°C gives rise to a wide peak located at higher binding energy than the oxide peak and an energy shift for the metallic Al peak. The decrease of the intensity near the no-loss peak indicates a change in the bonding of the Al.

The annealing at 900°C gives rise to a large peak located at intermediate position between the two previously observed peaks. The inelastic background is low at the vicinity of the no-loss peak, indicating the loss of metallic character of Al.

The chemical shift toward higher binding energy indicates the bonding with more electronegative elements. With incorporation of high electronegativity element, the energy shift is higher. For these reasons and as detailed further in the next sections, the highest shift observed is more likely to be due to incorporation of oxygen (for the 600°C sample) whereas the intermediate shift is due to incorporation of nitrogen (for the 900°C sample). For all the samples, the Al 1s inelastic background decreases rapidly, showing a location of Al close to the surface.

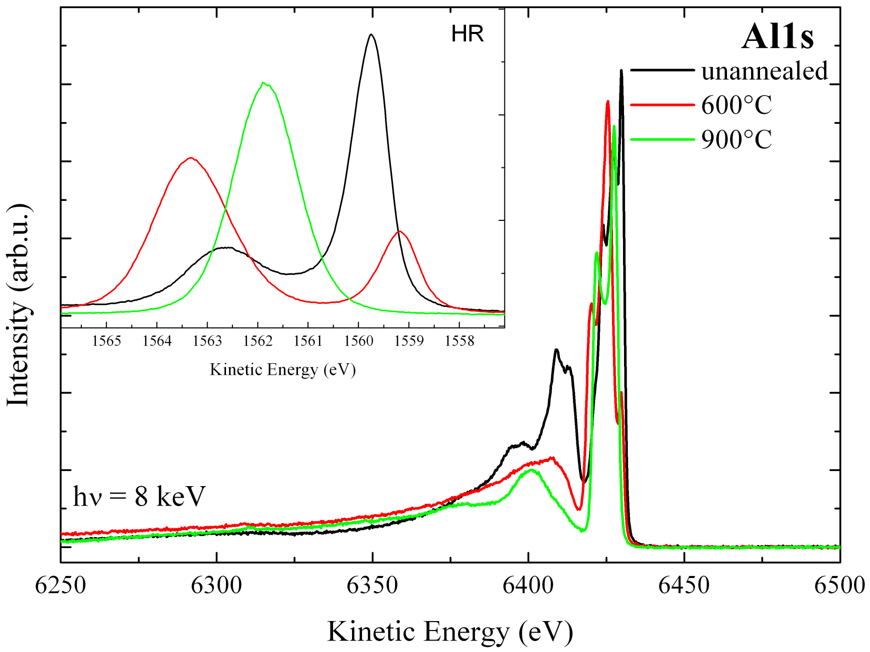

Figure 66: *Measurements of Al 1s with high photon flux of 8 keV, the insert shows the high-resolution spectra of Ti 1s for the various annealing.*

4.3 Results for the unannealed sample

4.3.1 Aluminum 1s core-level analysis

The Al 1s high-resolution core level spectrum normalized to unit area is shown in Fig. 67(a) along with its peak fitting. The majority of the signal, 88%, is attributed to metallic Al located at 1559.8 eV binding energy. The peak is fitted with a Doniach-Sunjic line shape with an asymmetry parameter of 0.12 and a Full Width at Half Maximum (FWHM) of 0.70 eV. The binding energy of 1559.8 eV is in perfect agreement with *K. Yates et al.* [128] and is very close to the literature value of 1559.6 eV for the element in its natural form [129]. The second peak located at 1562.7 eV binding energy is attributed to surface Al oxide due to air exposure [130] and corresponds to 12% of the total peak area. The chemical shift of 2.9 eV is in concordance with the Al 1s chemical shift found by *J.E. Castle et al.* [131]. The fitting curve is a product between a Gaussian function (80%) and Lorentzian function (20%) with a FWHM of 1.4 eV. The top layer of aluminum is therefore composed of metallic Al and a layer of oxidized Al on the surface. The peaks characteristics are summarized in Tab.13(a).

4.3.2 Titanium 1s core-level analysis

The Ti 1s high-resolution core level spectrum normalized to unit area is presented in Fig. 67(b) along with its peak fitting. This spectrum is fitted with a Doniach-Sunjic line shape representative of the metallic Ti at 4964.7 eV binding energy with a smaller asymmetry parameter than for Al 1s of 0.05 and a higher FWHM of 1.1 eV. A second peak located at 4965.6 eV binding energy is representative of TiN states [132, 133, 134, 135]. This peak is fitted with a product between a Gaussian function (80%) and Lorentzian function (20%) with a FWHM of 1.0 eV. The fitting with one component characteristic of the metal (97.3% of the signal) and only one other component (2.7 % of the signal) shows the good quality of the deposed Ti layer. There is no presence of N during the deposition of the Ti layer so the TiN found in the measurement is most likely arising from the AlGaN layer on which the Ti is deposited. The peak characteristics are summarized in Tab.13(b).

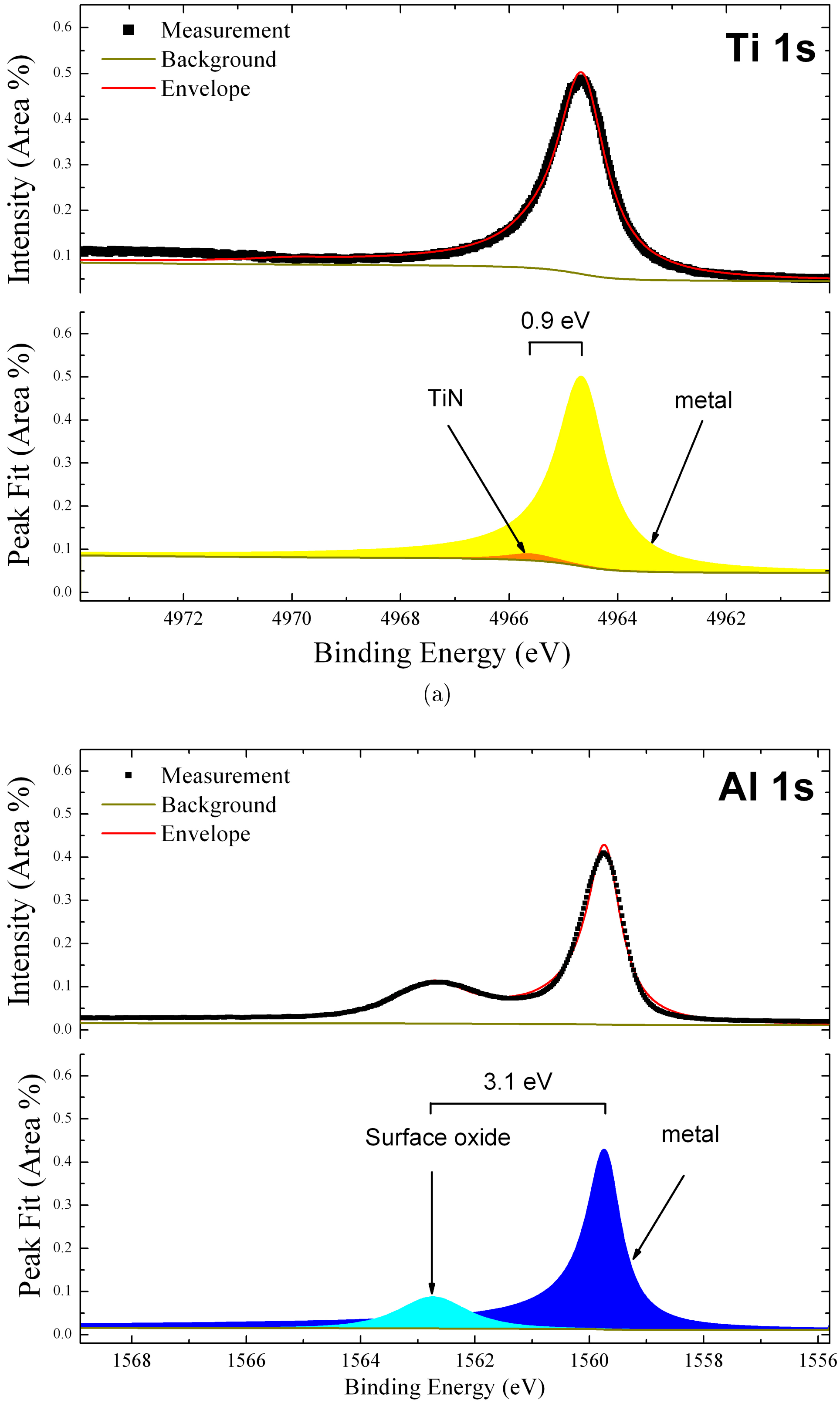

(a)

(b)

Figure 67: *High resolution spectra of (a): Ti 1s; (b): Al 1s measured at 8 keV photon energy for the unannealed sample. The spectra are normalized to unit area.*

4.3.3 Consequences for the inelastic scattering cross-section

The high resolution spectra show the metallic character of Ti and Al for the unannealed sample. Therefore to describe the inelastic losses for TiAl alloying, the inelastic scattering cross sections could be a pondered average of metallic Al inelastic scattering cross section (dominated by a plasmon loss at 15.1 eV) and metallic Ti inelastic scattering cross section. However, the Ti inelastic scattering cross section is not implemented in QUASES analyze, so the TiO inelastic cross-section, which is very close to the Ti one, has been used. Thus the background analysis was performed with use of a weighted averaging of Al and TiO inelastic cross sections.

As emphasized in the previous Chapter, the effective inelastic cross-section used in the background analysis should take into account the effect of photoelectron high kinetic energy. This energy-dependent cross-section must be measured in REELS from a pure sample. As the photoelectron kinetic energy of Ti 1s is of 3020 eV, such refinement is not needed. Thus the inelastic scattering cross-sections used in the following are taken from low energy regime.

For the analysis of the Ga, present in the AlGaN layer and in the thick (micrometric) GaN substrate, the difficulty is the deep location of the Ga and its very low photoionization cross section. The signal was too low to measure a high resolution spectrum for gallium, Ga is located so deep that the energy loss part of the Ga 2s and Ga 2p spectra are more intense than the no-loss peaks themselves as can be seen in Fig. 69(b). The two components are separated by 156 eV (with binding energies of 1299 eV for Ga 2s, 1143.2 eV for Ga $2p_{1/2}$ and 1116.4 eV for Ga $2p_{3/2}$). The fitting of the gallium spectra was performed on the whole energy range using the two parameters universal scattering cross section.

4.3.4 Inelastic background analysis of Ti 1s and Ga 2s,2p

Fig. 68(a) shows the results of inelastic background analysis for Ti 1s unannealed sample. The lowest χ_{eff} obtained by the automated procedure points to a titanium layer with a top interface at 17.9 nm below the surface and a bottom interface at 32.2 nm below the surface. The resulting thickness of 14.3 nm is very close to the 15 nm given by the nominal thickness. The spectrum corresponding to this depth distribution is presented in Fig. 68(b) and gives good account for the inelastic background at high energy loss (2880 eV kinetic energy). However, the low energy loss (<40 eV) region is not so well reproduced in intensity even if the general shape of the measurement, dominated by plasmon loss from the Al layer is well accounted for.

Inelastic background analysis was also performed for the gallium spectrum. Fig. 69(b) shows the result of the automated procedure previously described. The lowest χ_{eff} is not very well defined as can be seen in Fig. 69(a), most of the depth distributions with lowest χ_{eff} point to a top interface around 25 nm below the surface, but the bottom interface can be from 70 to 90 nm below the surface. As the Ga is present in the micron-thick GaN substrate, well beyond the detection limit

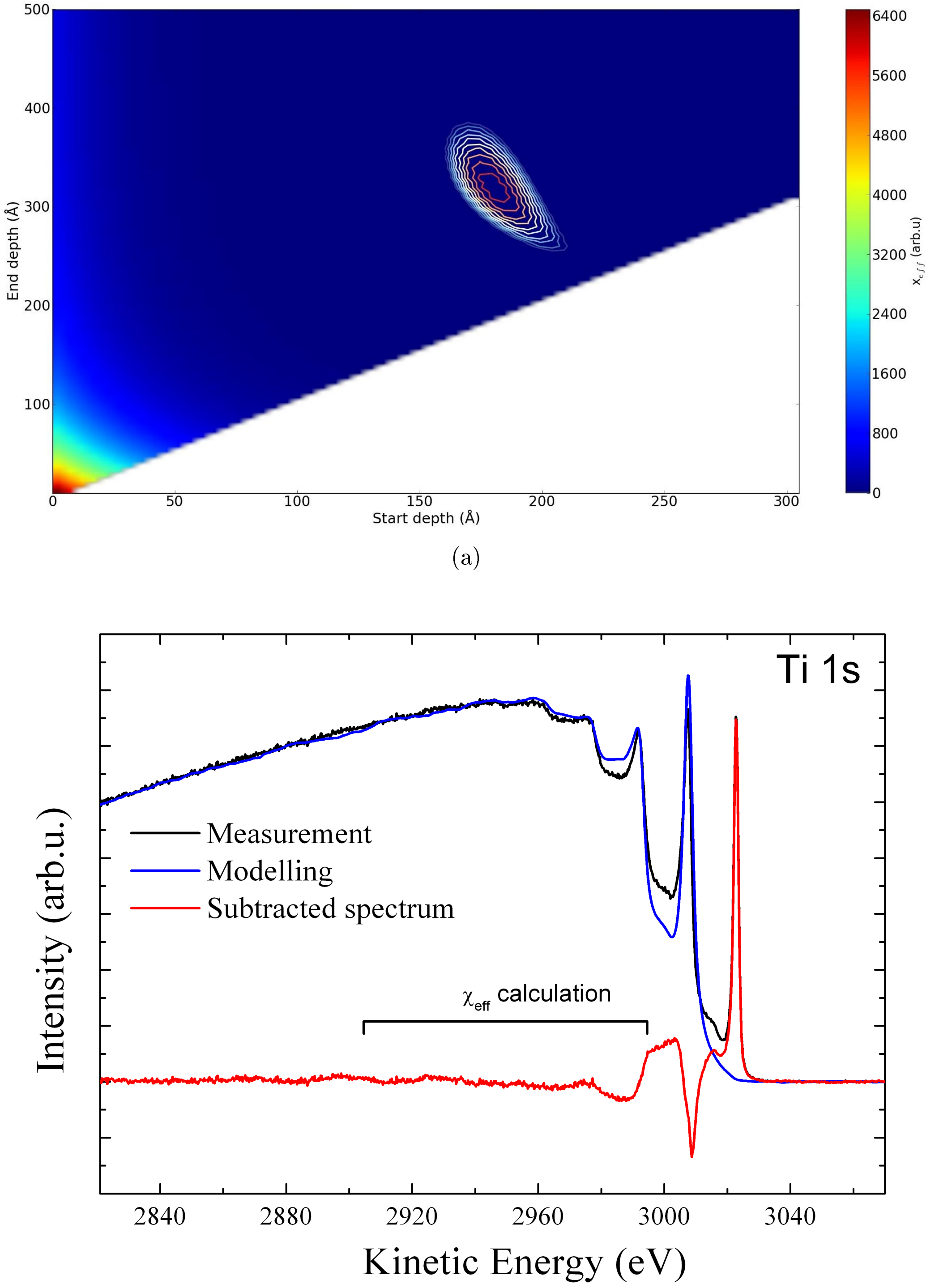

(a)

(b)

Figure 68: *(a) Result from the automated treatment of the unannealed Ti 1s spectrum, showing a depth distribution with top interface located at 17.9 nm and a bottom interface located at 32.2 nm below the surface. The corresponding measurement (in black) and the corresponding modelled background (in blue) also with the subtracted spectrum (in red) are presented in (b) with the energy range used for calculation of* χ_{eff}.

of inelastic background analysis (the IMFP used for calculation is of 9.5 nm), the best inelastic background modeling is obtained with a bottom interface at infinity and a top interface at 25 nm below the surface: this range of depth corresponds to the GaN substrate.

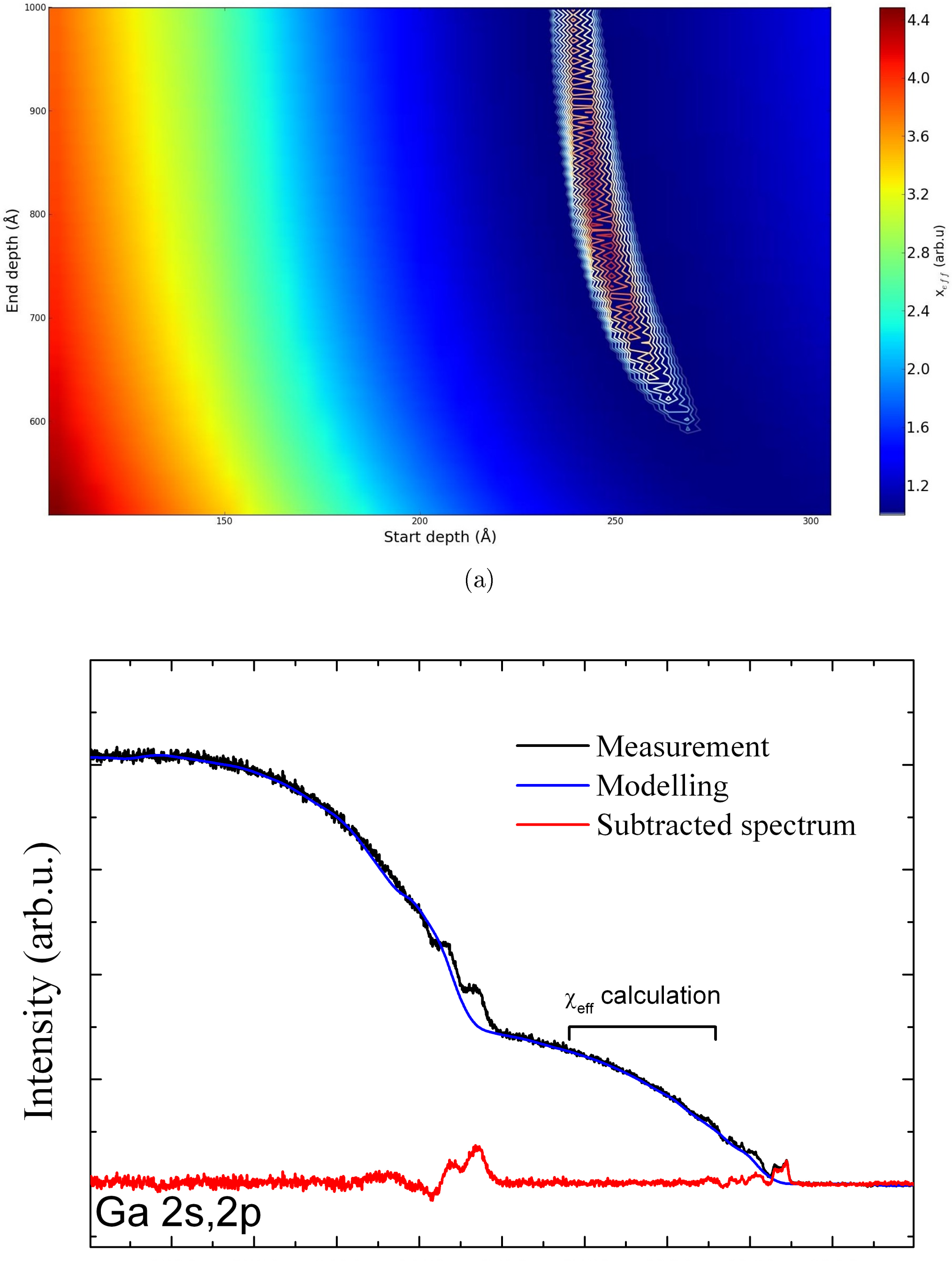

(a)

(b)

Figure 69: *(a) Result from the automated treatment of the unannealed Ga 2s,2p spectrum, showing a depth distribution with top interface located at 25.0 nm and a bottom interface beyond detection limit. The corresponding measurement (in black) and the corresponding modelled background (in blue) also with the subtracted spectrum (in red) are presented in (b) with the energy range used for calculation of* χ_{eff}.

Assignment	Binding energy (eV)	Peak shape	FWHM (eV)	Area (%)
Ti metal	4964.7	Doniach-Sunjic α=0.05	1.1	96.5
TiN	4965.6	Gaussian 80% - Lorentzian 20%	1.3	3.5
Al metal	1559.8	Doniach-Sunjic α=0.12	0.7	87.9
Al surface oxide	1562.7	Gaussian 80% - Lorentzian 20%	1.4	12.1

Table 13: *Components used in the peak fitting procedure for Al 1s and Ti 1s of the unannealed sample.*

4.3.5 Structure of the sample deduced from the analysis

The high resolution spectra unravel the predominantly metallic character of Ti and Al in the unannealed sample in the topmost 3 IMFP and a surface oxidation of the Al layer. These results were used for the choice of the inelastic scattering cross-section used in the background analysis: for Ti 1s an average of pure Al cross section and the universal cross-section for Ti 1s and the two parameters universal cross section for Ga.

The top interface of the AlGaN layer is located at 25 nm below the surface whereas the bottom interface of the titanium is located at 32.2 nm. The 7.5 nm difference between the two interfaces comes from the roughness of the AlGaN layer: as the photoemission experiment is averaging the signal, the step between two AlGaN terraces induces an uppershift of the top interface of AlGaN layer and an lowershift of the bottom interface of the Ti layer. The result of inelastic background analysis is seen as the mean location of the interface. The TiN component seen in the high resolution spectrum is representative of this roughness. The inelastic background analysis defined a depth distribution of Ti with a thickness of 14.3 nm with a top interface located at 17.9 nm below the surface. This value shows that Ti is covered by a larger layer than the expected 10 nm of Al layer. As a surface oxide component has been seen in the Al 1s spectra, the top layer consists of metallic Al and oxidized Al. The depth distribution of Al could not be retrieved as Al is present in the top layer and in the substrate. The real Al thickness may not be of 17.9 nm as the deposition tools forecast a layer of 10 nm. As the sample was kept at air exposure and no surface preparation was made, the discrepancy between the nominal Al layer thickness and the result of inelastic background analysis can be explained by surface contamination. Fig. 70 only shows the results of the present analysis which omits the contamination layer.

4.4 Results for the 600°C sample

4.4.1 Titanium 1s core-level analysis

For the sample annealed at 600°C for 300 s, new components appear in the Ti 1s high resolution spectrum normalized to unit area presented in Fig. 71(a): the Ti metallic component located at 4964.9 eV has decreased in relative intensity to 73.7% of the total peak area and is shifted

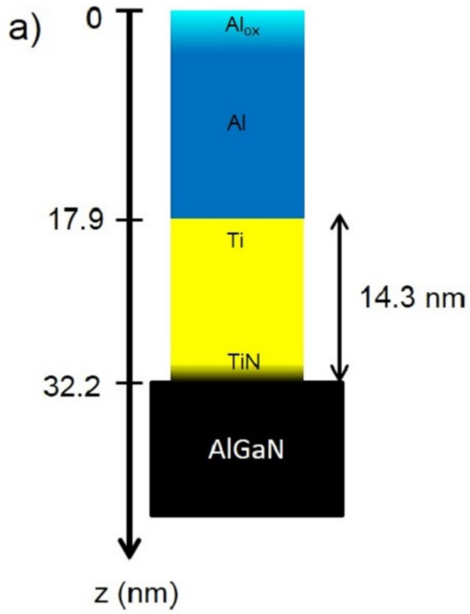

Figure 70: *Structure of the unannealed HEMT sample. The depths of the layer are extracted from the inelastic background analysis and the different layers from the core-level analysis.*

by 0.2 eV compared to the unannealed sample. This peak is fitted with the same lineshape as for the unannealed sample, the energy shift will be explained by the formation of a Ti-Al alloy. The corresponding energy shift compared to the metallic peak is very small, the two peaks are fitted with only one component as was the case in *Kovàcs et al.* [136]. The small component representative of TiN has increased and represents 11.0% of the signal and the peak is fitted with a higher FWHM of 1.3 eV, indicating a broadening of the interface between the metallic Ti and the AlGaN substrate.

A new component appears at 4969.6 eV binding energy, corresponding to 15.4% of the peak area. Its chemical shift is 5.1 eV compared to the metallic peak found previously. Such high chemical shift has been observed by *Kovàcs et al.* [136] and *Leinen et al.* [137] and attributed to Al_2TiO_5. This peak could then be a TiAl alloy with incorporation of an electronegative element. In Fig. 71(a) and hereafter this component is labeled as $TiAl_{ox}$. However the only origin of oxygen is the initial surface native oxide but the corresponding amount of O is too small to be responsible for the formation of such species. Another possible source of electronegative element is the N_2 used during RTA at 600°C. However the chemical shift corresponding to TiAl alloy with N atoms is not compatible with the observed chemical shift. The most probable source of oxygen is an unintentional contamination during the RTA, but since we did not look for N or O in our experiment, the exact chemical environment of this particular species cannot be determined and will require further investigation (with use of laboratory source for example). The peaks characteristics are summarized in Tab.14(b).

4.4.2 Aluminum 1s core-level analysis

The high resolution Al 1s spectrum normalized to unit area is presented in Fig. 71(b). In contrast to Fig. 67(b), it presents a very small component of metallic Al of only 8.5%. Two other significant peaks appear. The one with a chemical shift toward lower binding energy of 1559.2 eV is consistent with the shift observed by *Kovàcs et al.* [136] for TiAl. This peak representing 15.4% of the peak area is fitted with a product between a Gaussian function (80%) and Lorentzian function (20%) with a FWHM of 0.9 eV.

The other new peak appear toward higher binding energy with an energy shift of 3.4 eV is representative of the formation of TiAl alloy with incorporation of electronegative elements. This peak is fitted with a product between a Gaussian function (80%) and Lorentzian function (20%) with a FWHM of 1.7 eV. It cannot be attributed to the Al_2TiO_5 because it is not consistent with the chemical shift of 3.9 eV assumed by the literature [136, 137]. The observed chemical shift of 3.4 eV in the measurement have also been observed by *Chang et al.* for an oxidation state of pure Al in UHV condition at room temperature [138] and also by *Olefjord et al.* [139]. As the Ti 1s spectrum shows a high intermixing between Ti and Al, this peak will be considered as representative of the $TiAl_{ox}$ species. The peaks characteristics are summarized in Tab.14(a).

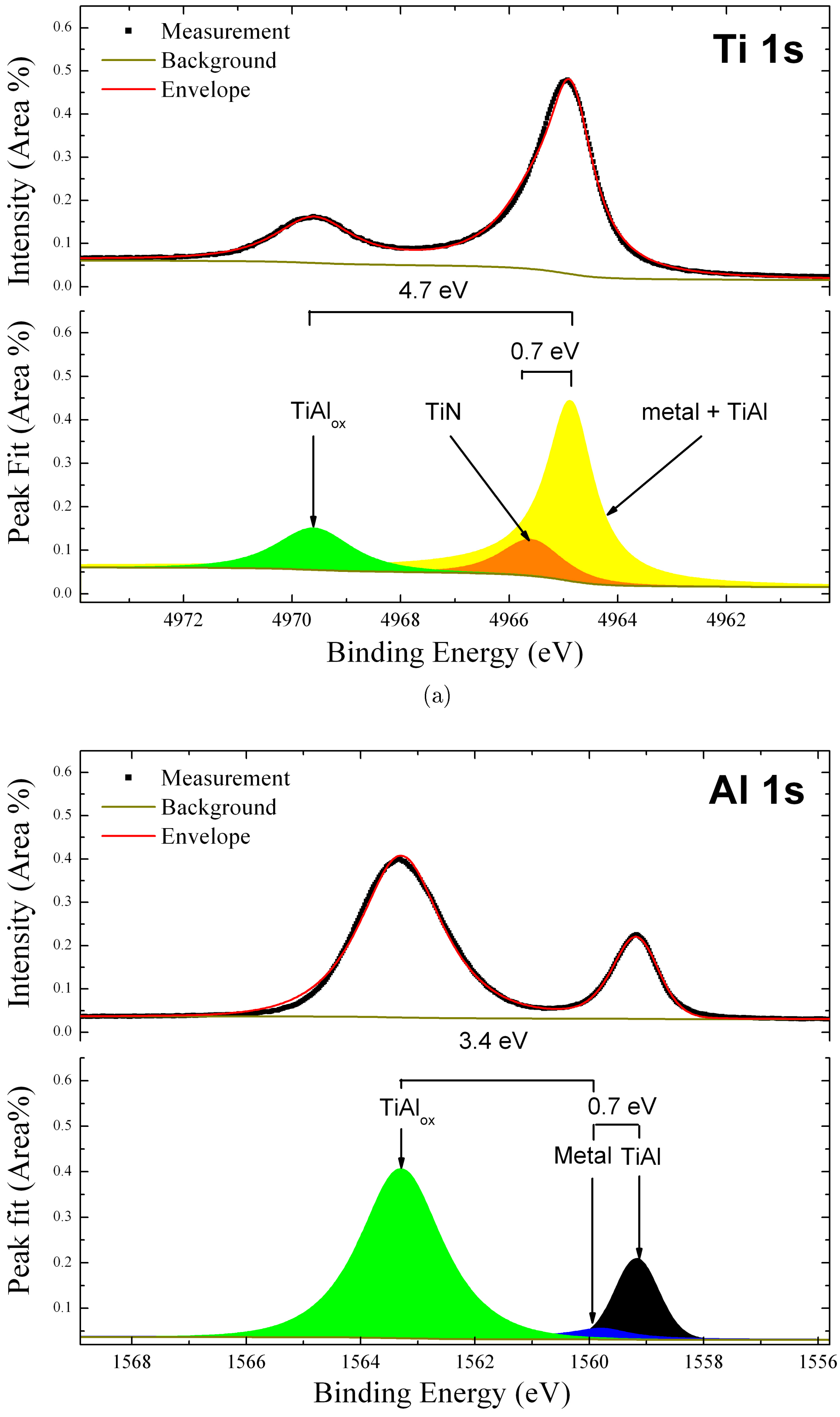

(a)

(b)

Figure 71: *High resolution spectra of (a) Ti 1s and (b) Al 1s measured at 8 keV photon energy for the 600°C sample. The spectra are normalized to unit area.*

4.4.3 Inelastic background analysis of Ti 1s and Ga 2s,2p

The drastic decrease of metallic Al component is confirmed by the Ti 1s inelastic background presented in Fig. 72(a): the strong oscillations corresponding to Al plasmon excitations near the no-loss peak seen in the unannealed sample (Fig. 68(b)) have decreased. As the Ti is still in metallic form, these oscillations arise from plasmon loss inside the Ti layer. As a result, the inelastic scattering cross section is chosen as a weighted averaging of the cross-section of TiO and the two parameters universal cross-section.

The result of the automated procedure on Ti 1s is showed in Fig. 72(a). It points to a lowest χ_{eff} found for a Ti layer located between 7.3 nm and 20.4 nm for top and bottom interface respectively. As can be seen in Fig. 72(b), the reproduction of the background for such a depth distribution is rather poor. As a manual trial and error process could not lead to a better matching between the measurement and the modelled background, this discrepancy cannot be imputed to an erroneous estimation made by the automated procedure. The discrepancy is attributed to the choice of the inelastic scattering cross-section: the high resolution spectra show intermixing of Ti and Al in two forms, a TiAl alloy and a TiAl oxidized. Therefore the most accurate inelastic cross-section describing the inelastic losses inside the sample would be an average of the TiAl cross section and the $\mathrm{TiAl_{ox}}$ cross section. As these cross sections are not implemented in the software, the use of TiO and the two parameters cross section is an approximation which implies a high uncertainty in the results of inelastic background analysis. It could explain the shrinking of the Ti layer compared to the unannealed sample.

The analysis of Ga 2s,2p inelastic background is shown in Fig. 73(a) and 73(b). The quality of the background analysis is very good over the entire energy range from 6550 to 6900 eV. The top interface is found to be located at 22 nm below the surface and a bottom interface deeper than 75 nm (probing depth limit of this peak). For the same reason as in the case of the unannealed sample, only the top interface location for Ga can be obtained from inelastic background analysis (8xIMFP = 76 nm, see Tab.12).

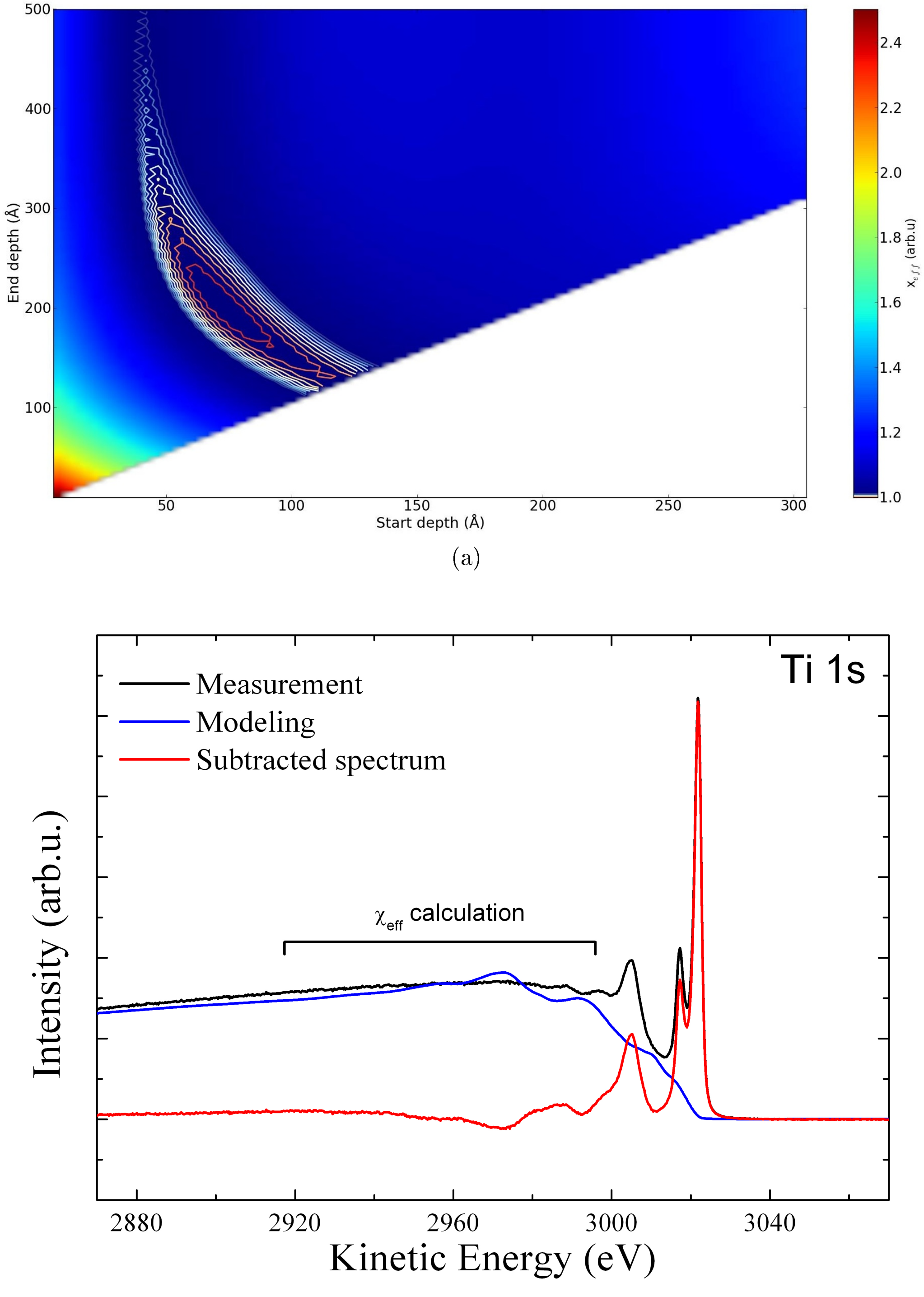

(a)

(b)

Figure 72: *(a) Result from automated treatment of the 600°C sample Ti 1s spectrum, showing a depth distribution with top interface located at 7.3 nm and a bottom interface located at 20.4 nm below the surface. The corresponding measurement (in black) and the corresponding modelled background (in blue) also with the subtracted spectrum (in red) are presented in (b) with the energy range used for calculation of* χ_{eff}.

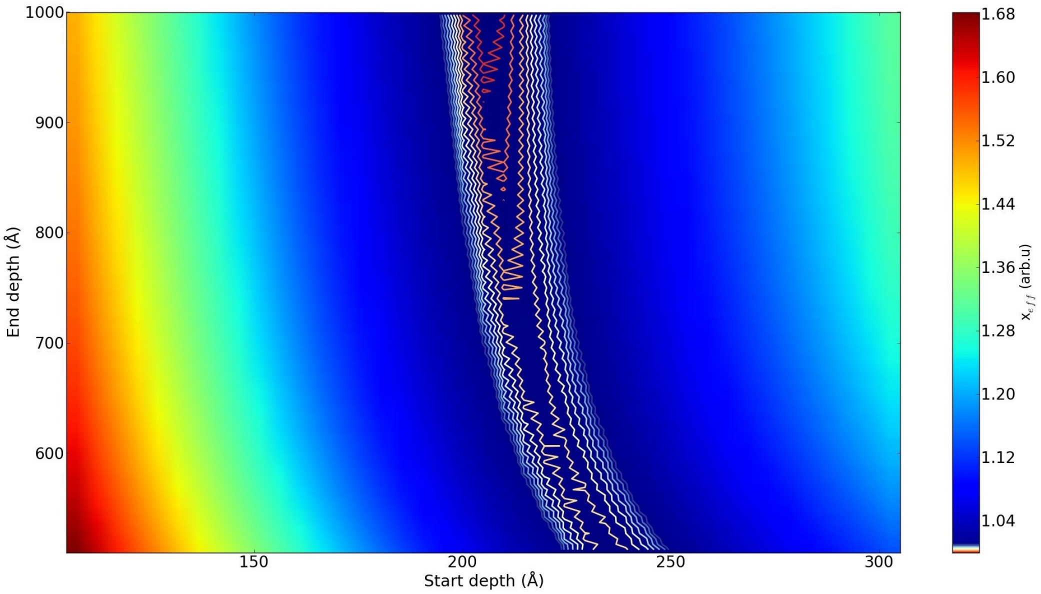

(a)

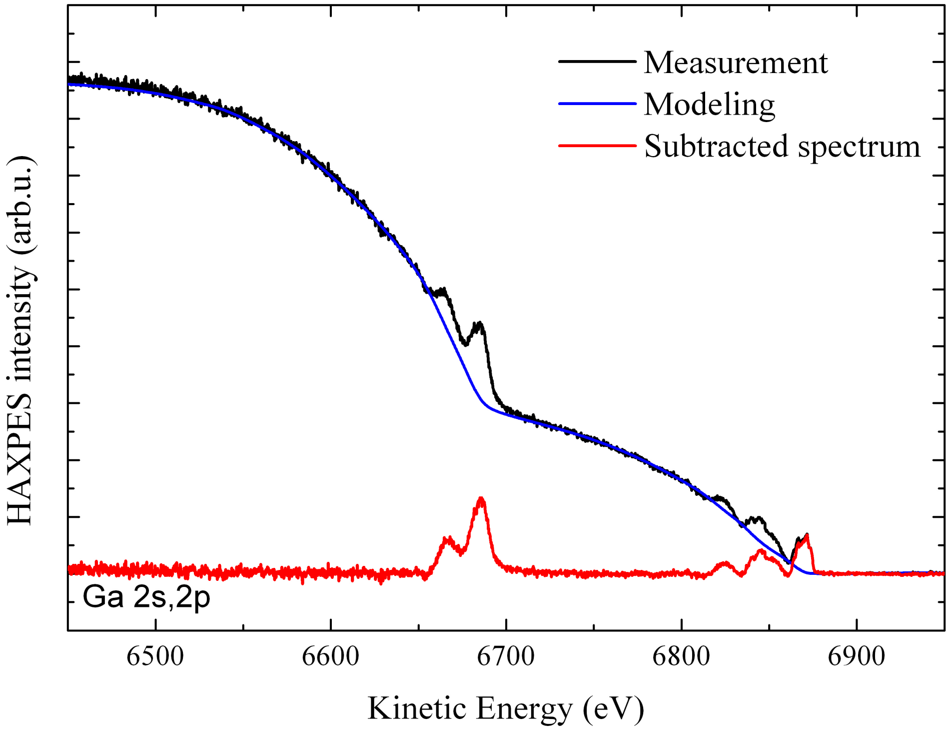

(b)

Figure 73: *(a) Result from automated treatment of the 600°C sample Ga 2s,2p spectrum, showing a depth distribution with top interface located at 22.0 nm and a bottom interface beyond detection limit. The corresponding measurement (in black) and the corresponding modelled background (in blue) also with the subtracted spectrum (in red) are presented in (b) with the energy range used for calculation of* χ_{eff}.

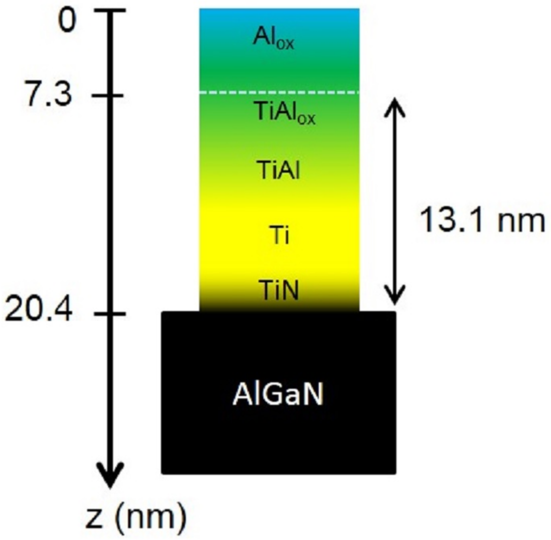

Figure 74: *Structure of the HEMT sample annealed at 600°C. The depths of the layer are extracted from the inelastic background analysis and the different layers from the core-level analysis.*

4.4.4 Structure of the sample deduced from the analysis

The combination of the high resolution spectra and inelastic background analysis depict a structure where the aluminum state is transformed from metallic (in the unannealed sample) to a mixture of aluminum compounds: metallic aluminum, TiAl alloy and TiAl alloy with incorporation of electronegative atoms. The TiAl is due to the enlargement of the Ti/Al interface as the inelastic background analysis showed a diffusion of Ti toward the surface.

It is not suitable to depict aluminum as separated layers with precise interface, it is more accurate to describe a global aluminum layer with composition variation: the TiAl close to the Ti layer, above the TiAl oxidized alloy and on top a layer both containing metallic aluminum and aluminum oxide.

Thermodynamics considerations predict the favoured compound at 600°C to be $TiAl_2$ species. However the observation of Ti_xAl_y alloys in photoemission has been made for $TiAl_3$ and Ti_3Al by *Mencer et al.* but with chemical shift < 1 eV, not compatible with the observed chemical shift > 3 eV. Therefore the $TiAl_{ox}$ peak is more likely to be like a $Ti_xAl_{1\text{-}x}O_y$.

The main source of N atoms is the AlGaN layer, which contributes to the TiN species observed in the Ti 1s spectrum. N migration is expected in the Ti layer, but as Ti remains metallic as demonstrated in the high resolution spectrum, the N atoms from the AlGaN layer does not diffuse toward the topmost Al layer. The increase of the TiN component shows the broadening of the interface between the Ti and the AlGaN layers. As the TiAl components are seen in both Ti 1s and Al 1s peak fitting, a TiAl compound is located at the interface between Ti and Al.

Assignment	Binding energy (eV)	Peak shape	FWHM (eV)	Area (%)
TiAl	1559.2	Gaussian 80% - Lorentzian 20%	0.9	17.4
Al metal	1559.8	Doniach-Sunjic α=0.12	1.2	8.3
$TiAl_{OX}$	1563.3	Gaussian 80% - Lorentzian 20%	1.5	74.2

(a)

Assignment	Binding energy (eV)	Peak shape	FWHM (eV)	Area (%)
Ti metal + TiAl	4964.9	Doniach-Sunjic α=0.05	1.0	73.6
TiN	4965.6	Gaussian 80% - Lorentzian 20%	1.3	11.0
$TiAl_{ox}$	4969.6	Gaussian 80% - Lorentzian 20%	1.6	15.4

(b)

Table 14: *Components used in the peak fitting procedure for Al 1s (a) and Ti 1s (b) of the sample annealed at 600°C.*

4.5 Results for the 900°C sample

4.5.1 Titanium 1s core-level analysis

This sample is the 600°C sample which is further annealed at 900°C for 60 s under N_2 atmosphere. The Ti 1s high resolution spectrum normalized to unit area is presented in Fig. 75(b). The main peak representing 78.5% of the peak area is representative of Ti-Al alloy with incorporation of electronegative element. It is fitted with the product between a Gaussian function (80%) and a Lorentzian function (20%) with a FWHM of 1.7 eV. Compared to the $TiAl_{ox}$ signal, the peak is shifted of 0.9 eV toward lower binding energy. It indicates a lower oxidation state of the alloy formed, therefore, this peak is attributed to TiAlN species. The fitting procedure also quantifies the TiN peak located at 4966.1 eV binding energy to represent 21.3% of the signal. The FWHM of the TiN has increased from 1.6 to 2.5 eV. It is the indication of a higher disorder of the TiN. The peaks characteristics are summarized in Tab.15(b).

4.5.2 Aluminum 1s core-level analysis

The Al 1s high resolution spectrum normalized to unit area and its decomposition are showed in Fig. 75(a). The spectrum is fitted with only one component located at 1561.8 eV binding energy with the product between a Gaussian function (80%) and a Lorentzian function (20%) with a FWHM of 1.4 eV. This peak is attributed to Ti-Al alloy with incorporation of electronegative element, but as the binding energy is lower than the one found for the 600°C sample, the alloy is in a lower oxidation state. For the same reason as previously (for Ti 1s), this peak is attributed to TiAlN. The peak characteristics are summarized in Tab.15(a).

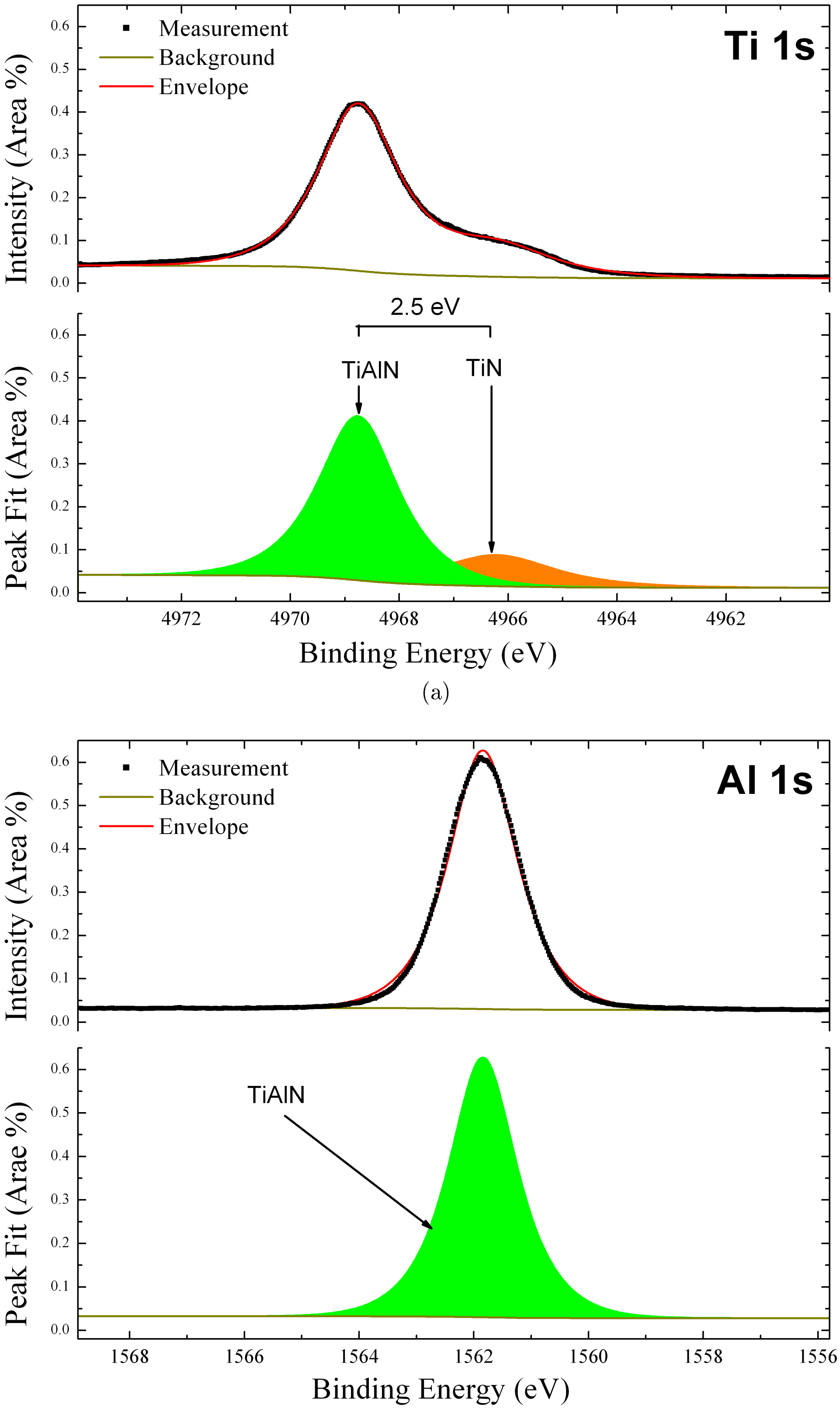

(a)

(b)

Figure 75: *High resolution spectra of Ti 1s (a) and (b) Al 1s measured at 8 keV photon energy for the 900°C sample. The spectra are normalized to unit area.*

4.5.3 Inelastic background analysis of Ti 1s and Ga 2s,2p

The inelastic background analysis was performed on Ti 1s and Ga 2s,2p spectra with use of the two-parameter universal cross-section as the high resolution spectra showed an almost total intermixing between Ti and Al. Fig. 76(a) shows the result of the automated procedure for the Ti 1s spectrum. The lowest χ_{eff} value points out two depth distributions reproducing the measurement: one with a top interface located at 1.5 nm below the surface and a bottom interface located at 42 nm and the other with top interface located at 6.8 nm and bottom interface located at 42 nm. In both cases the analysis shows that Ti has not reached the surface. The choice between these two depth profiles is discussed in the next section.

The Ga 2s,2p inelastic background analysis in Fig. 77(a) shows a top interface located at 32 nm below the surface. The background reproduction in Fig. 77(b) is almost perfect in the full energy range used for computing the error and even beyond.

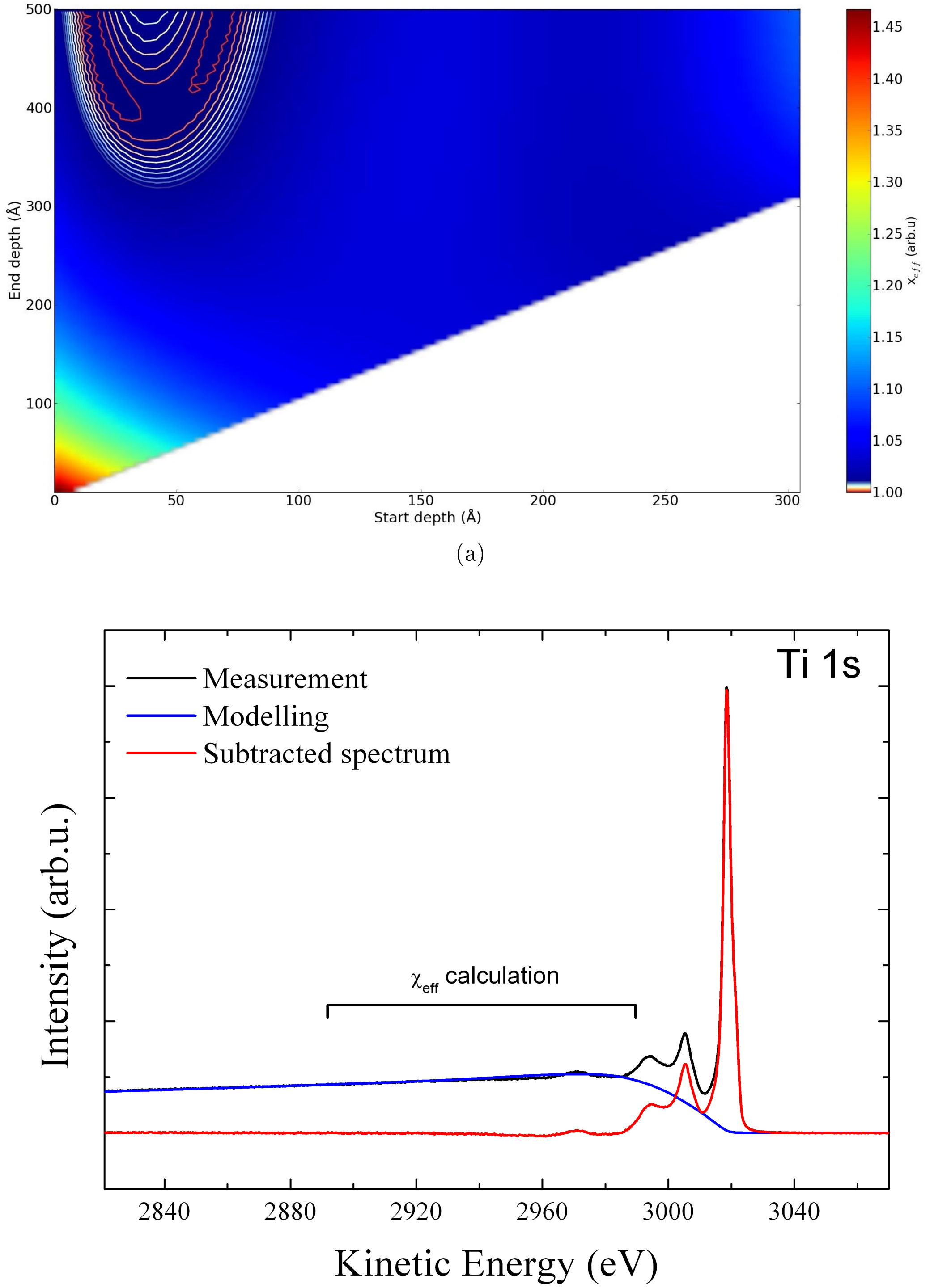

(a)

(b)

Figure 76: *(a) Result from automated treatment of the 900°C sample Ti 1s spectrum, showing a depth distribution with top interface located at 1.5 nm and a bottom interface located at 42 nm below the surface. The corresponding measurement (in black) and the corresponding modelled background (in blue) also with the subtracted spectrum (in red) are presented in (b) with the energy range used for calculation of* χ_{eff}.

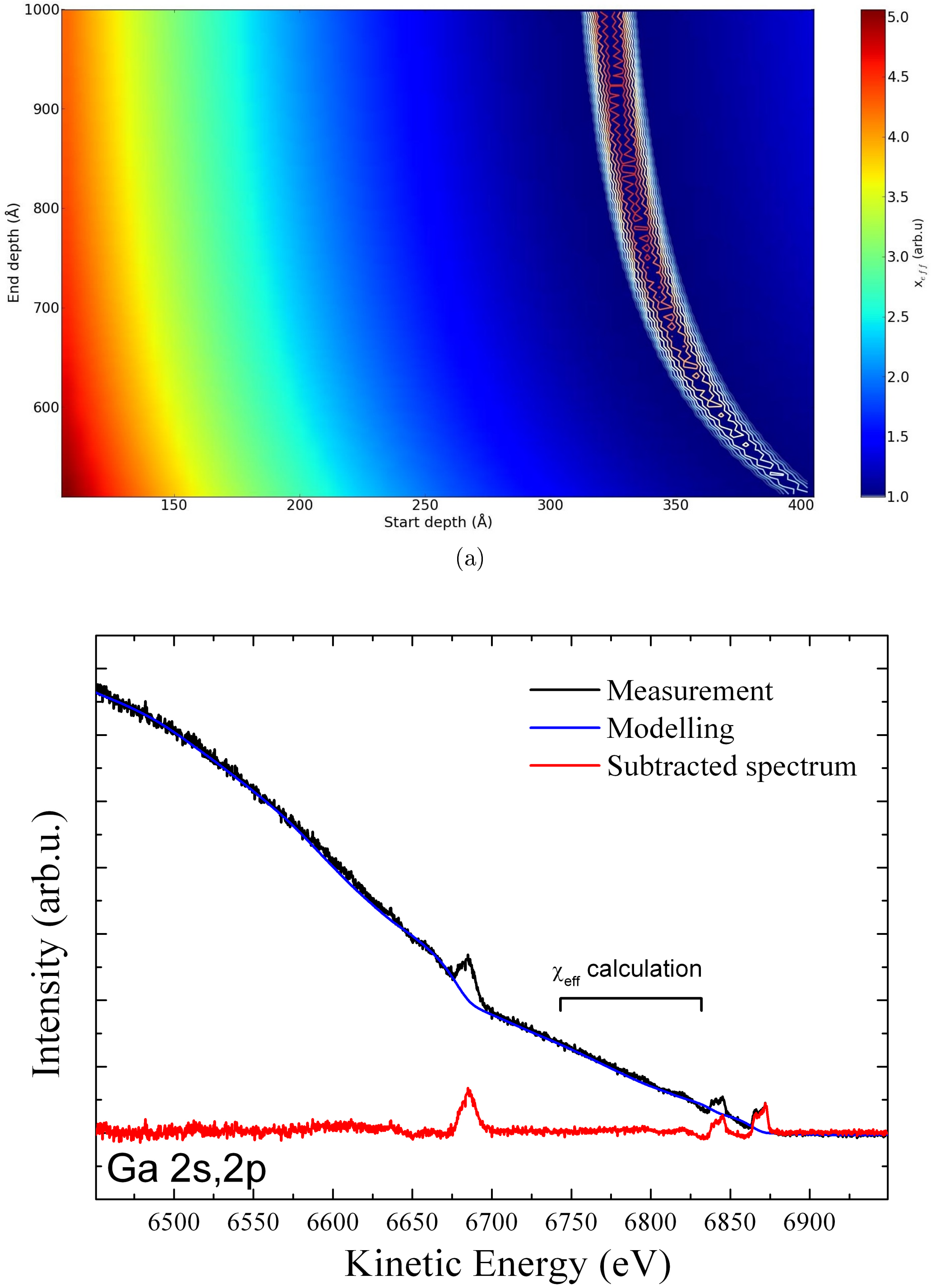

(a)

(b)

Figure 77: *(a) Result from automated treatment of the 900°C sample Ga 2s,2p spectrum, showing a depth distribution with top interface located at 25.0 nm and a bottom interface beyond detection limit. The corresponding measurement (in black) and the corresponding modelled background (in blue) also with the subtracted spectrum (in red) are presented in (b) with the energy range used for calculation of* χ_{eff}.

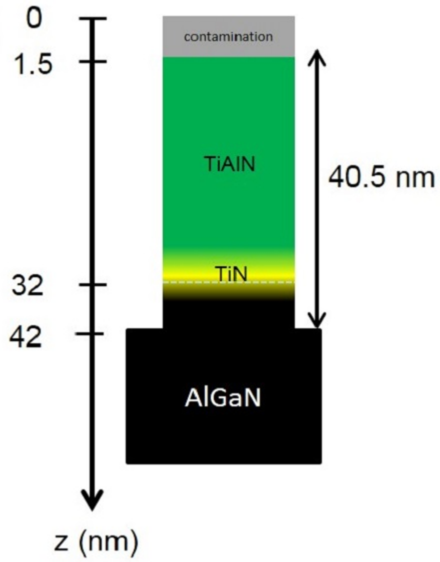

Figure 78: *Structure of the HEMT sample annealed at 600+900°C. The depths of the layer are extracted from the inelastic background analysis and the different layers from the core-level analysis.*

4.5.4 Structure of the sample deduced from the analysis

In summary, the inelastic background analysis shows the intermixing between Ti and Al, the Ti being located almost to the surface. The analysis of high resolution spectra depicts a sample formed essentially of an alloy of Ti and Al with additional electronegative element. The peak fitting of Ti 1s and Al 1s indicates the formation of a TiAlN alloy, different from the $TiAl_{ox}$ found for the 600°C sample.

The sample is considered to be a full intermixing of Ti and Al with incorporation N. A part of the Ti remains in TiN state and the inelastic background analysis shows an overlap between the two interfaces of Ga located at 32 nm below the surface and the bottom interface of Ti 42 nm below the surface. For the same reason as for the 600°C sample, the increase of the TiN component corresponds to the broadening of the interface between Ti and AlGaN. The background analysis has led to two top interface locations at 1.5 nm or 6.8 nm below the surface. However the depth distribution is more likely to be the one with top interface located at 1.5 nm for two reasons. First because the inelastic background analysis of the 600°C sample showed a top interface located at 7.3 nm, the inelastic background of the 900°C sample decreases compared to the 600°C sample, so the Ti in the 900°C is located closer to the surface. Second, the Al 1s has only one component, attributed to a TiAl alloy, and no Al oxide (which should be expected in the case of a Ti top interface at 7.3 nm). For these reasons, the surface is assumed to be covered by a 1.5 nm layer. In the absence of definite information, this surface layer is labelled as a contamination layer.

Assignment	Binding energy (eV)	Peak shape	FWHM (eV)	Area (%)
Al-Ti_{ox}	1561.8	Gaussian 80% - Lorentzian 20%	1.4	100

(a)

Assignment	Binding energy (eV)	Peak shape	FWHM (eV)	Area (%)
TiN	4966.2	Gaussian 80% - Lorentzian 20%	2.5	21.3
Al-Ti_{ox}	4968.7	Gaussian 80% - Lorentzian 20%	1.7	78.7

(b)

Table 15: *Components used in the peak fitting procedure for Al 1s (a) and Ti 1s (b) of the sample annealed at 600+900°C.*

4.6 Summary and discussion

The components determined by peak fitting of the high-resolution spectra are summarized in Tab.16 and their relative evolution after various annealing procedures are shown in Fig. 79. Results of inelastic background modeling are presented in Tab.17. The combination of these results provides an insight on the sample structure and allows to propose the reaction scheme shown in Fig. 82. The results are supported by the conclusion derived from the TEM images and EDX profiles shown in the following.

Attribution	Unannealed (%)	600°C (%)	900°C (%)
Ti metal	96.5	73.6*	0
TiN	3.5	11.0	21.3
Al-Ti_{ox}	0	15.4	78.7

(a)

Attribution	Unannealed (%)	600°C (%)	900°C (%)
TiAl	0	17.4	0
Al metal	87.9	8.3	0
Al_{ox}	12.1	0	0
Al-Ti_{ox}	0	74.2	100

(b)

Table 16: *Components area for all samples in percentage; (a) Ti 1s peak; (b) Al 1s peak.*The Ti metal component of the 600°C sample is representative of metallic Ti and stoichiometric Ti-Al alloy.*

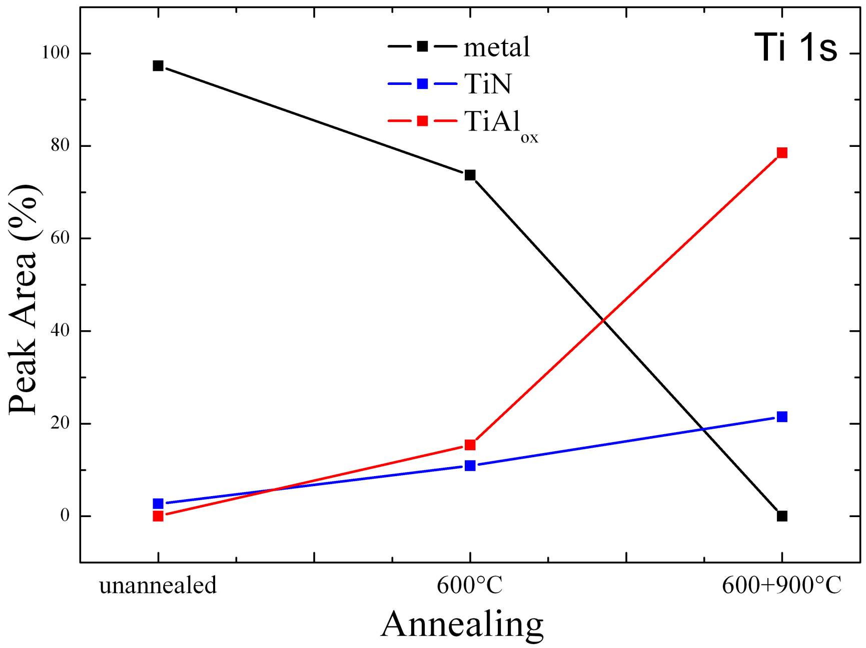

(a)

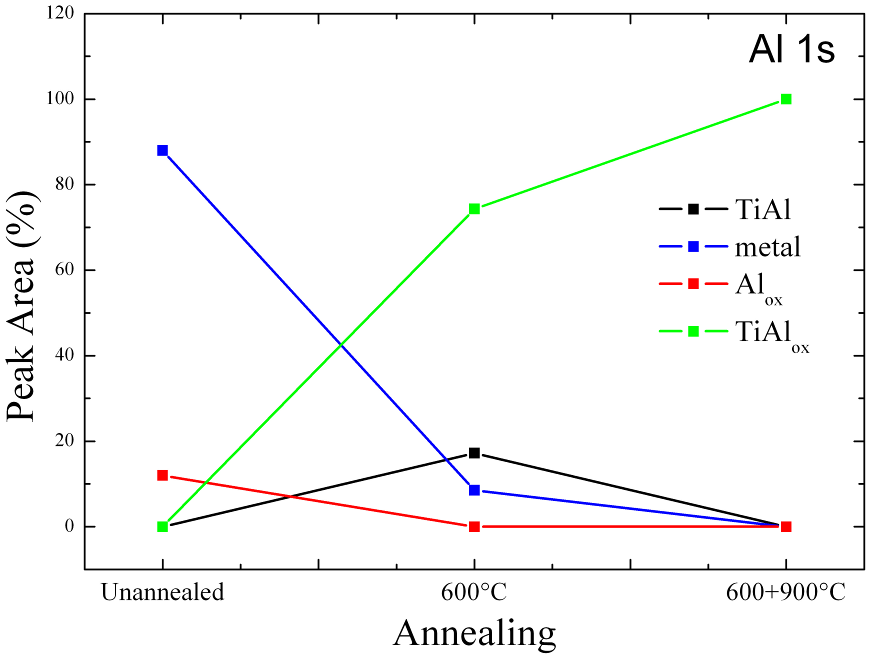

(b)

Figure 79: *Component evolution during annealing; (a) Ti 1s peak; (b) Al 1s peak.*

4.6.1 Comparison with TEM and EDX profiles

TEM and EDX profiles have been performed on similar samples with thickness increased by a factor 10 (Al layer of 100 nm and Ti layer of 150 nm) for the 600°C sample (Fig. 80) and the

900°C sample (Fig. 81). As the oxygen was not expected in the sample when the experiment was performed, only Ti, Al, Ga and N elements were analysed (and the W used for the sample preparation). The results cannot be directly compared to the samples studied here but can support the peak assignments in the peak fitting and the results of the depth distributions. There is no lateral resolution in HAXPES experiments performed here so the measurement is averaged by the size of the irradiated sample area seen by the analyzer, whereas the EDX profiles are representative of phenomena at the nm scale. Therefore, care must be taken in the comparison of the two results, as the scale and the sample preparation is very different in each case.

600°C sample Fig. 80(a) shows the TEM image of the 600°C sample with the Al represented in blue, the Ti presented in yellow and the N in red. The sample shows lateral inhomogeneities at the ~ 50 nm scale. This effect is important as the intermixing of Ti and Al is either total (on the left part) or partial. The encapsulation of the sample needed to prepare the sample for obtaining the TEM image has an impact on the sample surface. For this reason the EDX profile is measured at the arrow position of the TEM image, which corresponds to the mean location of the surface.

As the studied sample presents an increased thickness on both Ti and Al layers, the intermixing seen in the EDX profile of Fig. 80(b) at the Ti and AlGaN interface can be qualitatively compared to the results of the 600°C sample studied by photoemission. The Ga and N signals decrease abruptly at the exact location where the Al signal appear. Then theinterface of ~ 50 nm wide can be decomposed in two parts, one near the AlGaN layer where the Ti and Al concentrations are about 40 and 55% respectively, and a second part where the Al concentration increases and Ti concentration decreases. In both regions, the N atoms are in a non-negligible concentration. The major part of the sample consists in a $TiAl_3$ alloy, located between the substrate and the surface.

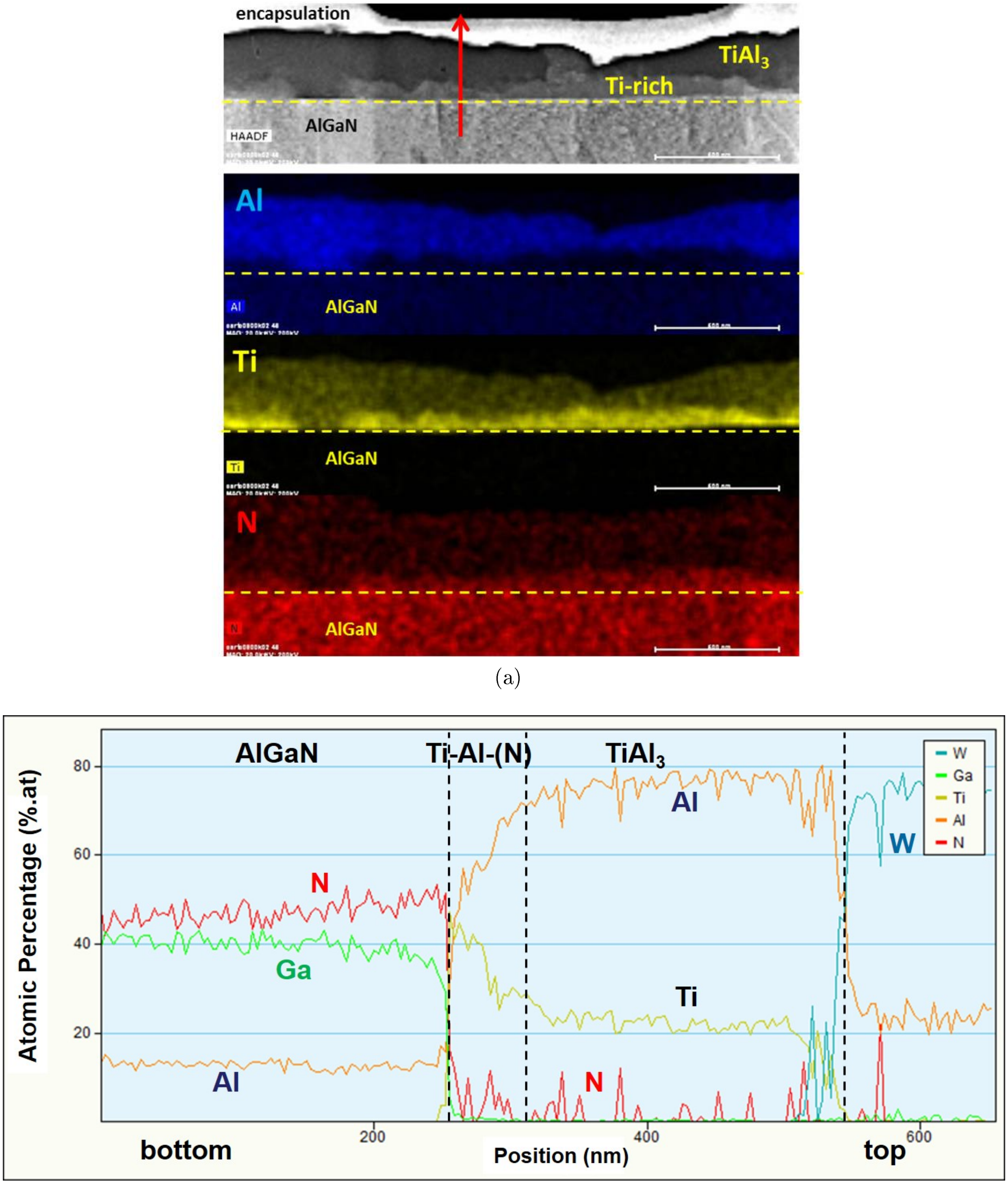

(a)

(b)

Figure 80: *TEM image (a) with scale bar of 500 nm. The EDX profile (b) is measured along the arrow in the top image for a sample annealed at 600°C.*

900°C sample Fig. 80(a) shows the TEM image of the 900°C sample with the Al represented in orange, the Ti presented in yellow and the N in red. The sample shows high lateral inhomogeneity, as the left part of the figure shows a high intensity of Al and the right part shows a higher intensity of Ti. The encapsulation of the sample has an effect on the roughness of the surface and on the surface composition. The blue circle points out this effect by showing a Ti-free surface which is not consistent with the high Ti concentration seen in the remainder surface. The EDX profile is measured at the arrow position of the TEM image which corresponds to the mean position of the lateral inhomogeneity.

The EDX profile of Fig. 81(b) is inverted compared to the Fig. 80(b) (the AlGaN layer is on the right part). The interface between the AlGaN and the Ti layer has narrowed compared to the 600°C sample and diffusion of Ga toward the surface is seen. The interface also shows a higher concentration of Ti at the interface with AlGaN and at the surface than the rest of the sample.

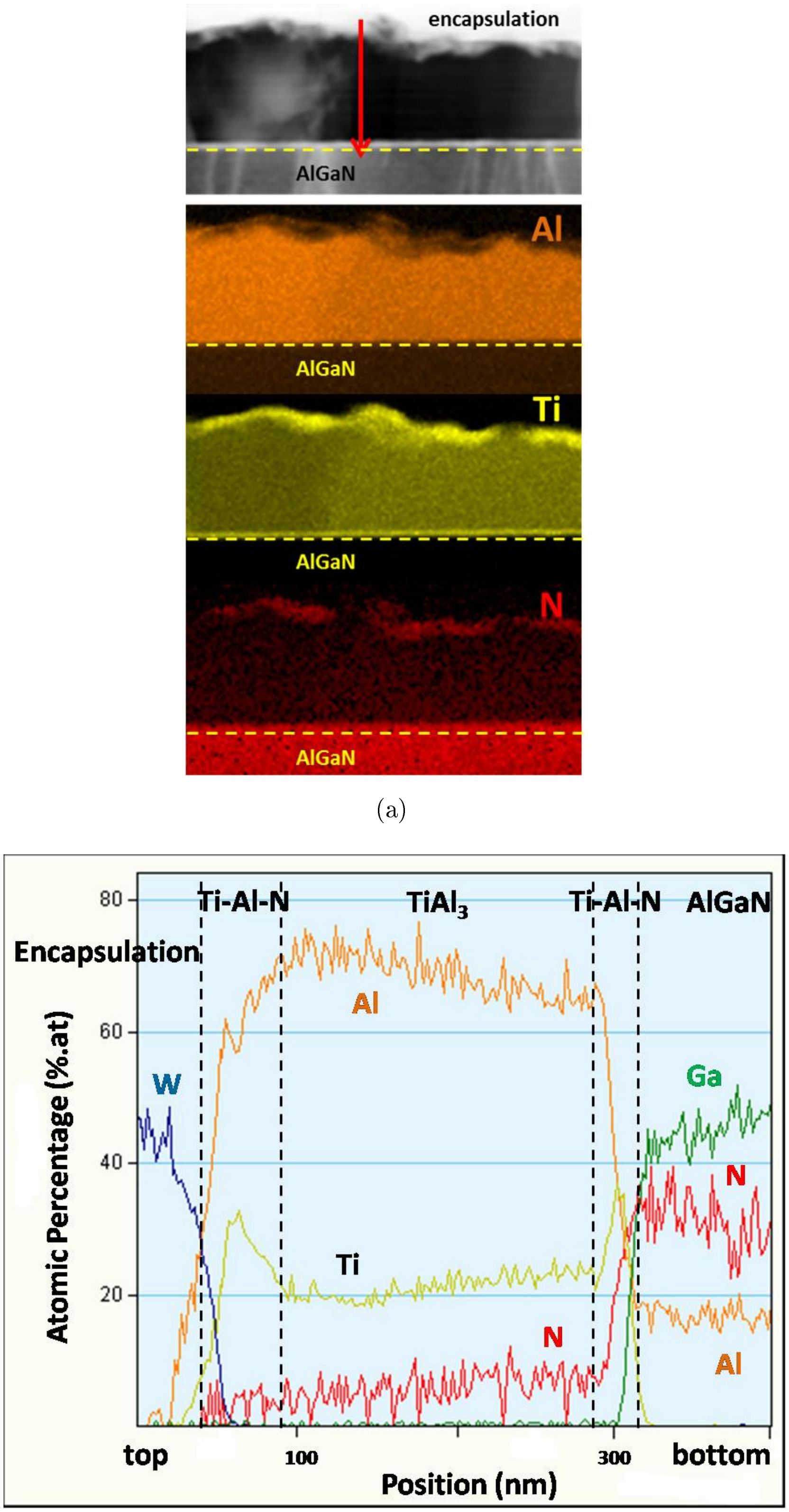

(a)

(b)

Figure 81: *(a) TEM image and EDX profile (b) measured along the arrow in the top image for a sample annealed at 600+900°C.*

4.6.2 Discussion

Case of the unannealed sample In the unannealed sample, most of the aluminum and the titanium are in metallic form. The high resolution spectra indicate an oxidation of the surface aluminum due to air exposure of the sample and a TiN component at the interface of the AlGaN and Ti layers. The inelastic background analysis shows a deposition of a 14.3 nm-thick Ti layer beneath Al as presented in Fig. 82(a). The structure obtained with combination of high resolution spectra and inelastic background analysis is presented in Fig. 82(a).

Case of the 600°C sample The annealing at 600°C induces diffusion of Ti into the Al layer according to the background analysis. The Al has decreased its metallic character but part of the Ti remains metallic. The intermixing between Ti and Al is seen through two components in Ti 1s and Al 1s high resolution spectra, corresponding to a TiAl alloy and an oxidized state of TiAl alloy. The increasing peak area of the TiN compound indicates a broadening of the interface between Ti and the AlGaN layer.

The TEM experiment shown in Fig. 80(a) confirms the N diffusion toward the surface and the presence of a broad interface between the Ti and the AlGaN layer. The EDX profile of Fig. 80(b) indicates that the majority of the sample is dominated by a homogeneous layer composed of around 25% of Ti and 75% of Al in atomic percentage. The EDX profile shows a complete intermixing of the two layers with an interface between AlGaN layer and a $TiAl_3$ layer formed which gives a $Ti_xAl_yN_z$ compound. These two experiments do not support the observation of the $TiAl_{ox}$ species found in the high resolution spectra previously studied, but they show presence of N in all the sample, which can be consistent with a chemical shift toward lower binding energy seen in Fig. 71. It is also possible that the annealing made at 600°C was made with residual O, explaining the high chemical shift observed. The structure obtained with combination of high resolution spectra and inelastic background analysis is presented in Fig. 82(b).

Case of the 900°C sample The inelastic background analysis showed that the Ti has diffused through the Al layer. High resolution spectra showed an almost complete intermixing of Ti and Al, with a gradient of concentration. The Ti atoms form a broad interfacial TiN layer with the AlGaN substrate which is representative of the broadening of the interface between Ti and the AlGaN layer. The analysis indicates that the surface does not contains Ti or Al.

These observations are supported by the TEM image and the corresponding EDX profile presented in Fig. 81, where part of the surface is composed by Ti (the red arrow in TEM image) and other part of the surface is composed by Al (blue circle in TEM image). As photoemission is performed here without any lateral resolution, the results of depth distribution are averaged. The top interface location of Ti at 1.5 nm (instead of 6.8 nm) below the surface is interpreted in

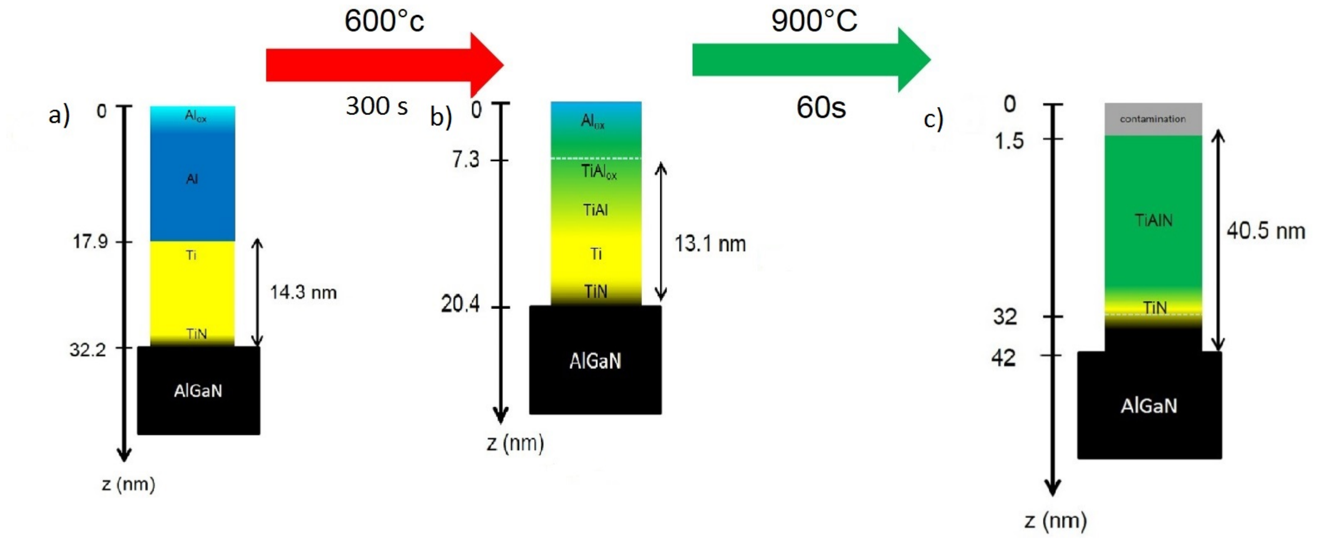

Figure 82: *Scheme of the HEMT structure obtained with high resolution spectra and inelastic background analysis. (a) Unannealed sample, (b) sample annealed at 600°C, (c) sample annealed at 600+900°C.*

this sense. The no observation of specific Al compound representative of this inhomogeneity in the high resolution spectrum is explained by the low surface sensitivity of the experiment.

The EDX profile of Fig. 81(b) also shows that the sample is homogeneous with an atomic percentage of Ti around 20% and Al around 70% which is in concordance with the high resolution results showing only one component in the fitting of Ti 1s and Al 1s. The profile shows an increasing amount of N atoms along the sample, corresponding to the observations made in the high resolution spectra of the TiAlN in the 900°C sample.

The structure obtained by combining high resolution spectra and inelastic background analysis is presented in Fig. 82(c).

Element	Ti			Ga
	Top interface (nm)	Bottom interface (nm)	Thickness (nm)	Top interface (nm)
Unannealed	17.9	32.2	14.3	25
600°C	7.3	20.4	13.1	22
600+900°C	1.5	42	40.5	32

Table 17: *Table of depth distribution profiles obtained.*

4.7 Conclusions of Chapter 4

In this Chapter, how the background analysis of HAXPES spectra could be used at the practical level in device technology has been highlighted.

A new method applied to the study of HEMT samples showing for the first time the **complementarity** between **high resolution** spectra unraveling the **chemical information on the first 3 IMFP** and the **inelastic background** analysis giving **depth distribution in the first 8 IMFP**. Results obtained for the chemical environment impacts the choice of the corresponding individual inelastic scattering cross sections because the effective inelastic scattering cross-section must be chosen as the best ones describing the sample. If the inelastic background analysis points to two different depth distributions, the observations made from high resolution analysis can support one depth distribution at the expense of the other. The use of averaging multiple individual cross-sections is a good approximation if the exact inelastic scattering cross section is not known.

The respective sensitivity of both high resolution and inelastic background analysis allows to **suggest a reaction scheme** for the various annealing situations investigated. It showed the diffusion of Ti and Al with incorporation of electronegative atoms and a broadening of the interface between Ti and the AlGaN layer. The Ti does not penetrate deeply in the AlGaN layer, which is a requirement for a good device performance.

5 Conclusion and perspective

This work exposed the first study of inelastic background analysis of HAXPES spectra and its potential to obtain elemental depth distribution of advanced technological devices.

Characterization of thin buried layers for micro- and nano-electronic is of prime importance for understanding properties of the operating devices. Among the various experimental techniques, X-rays PhotoEmission is widely used as it allows to obtain the chemical environment of an element without modification of the sample. The limiting factor of the XPS measurements is the probing depth which is not beyond 9 nm with laboratory sources and 35 nm with hard x-rays delivered by synchrotron radiation. Increasing the probed depth by analysis of the inelastic background allows to retrieve depth distribution of deeply buried layers up to 20 nm using soft-x-rays source and 35 nm using hard x-rays.

The difficulty of the background analysis of HAXPES spectra lies in the wide possibilities of locations for an element if there is no prior knowledge of the depth distribution. Moreover in the case of a deeply buried layer, the variation of the inelastic background for different depth distribution is very small, thus determination of the depth distribution by visual inspection is very difficult. A bot and an error estimation procedure can help to explore all the reasonable depth distributions which can lead to the observed spectra. In this direction, a semi-automated procedure has been implemented in order to determine the best matching between the measured and the simulated background.

5.1 Sensitivity to deeply buried monolayer

The third Chapter exposed the sensitivity of the HArd X-rays Photoemission Electron Spectroscopy (HAXPES) toward deeply buried layer with detection of a monolayer of lanthanum below electrodes of 20, 30 or 50 nm-thick. Background analysis on the measured spectra was successfully performed in the Tougaard's framework. Extensive analysis on the La $2p_{3/2}$ measurements showed various effects of the parameters:

- The photon energy must be chosen as a compromise between the two configurations: (i) A high photon energy where the probed depth is high but the signal/noise ratio is low; (ii) a low photon energy where the probed depth is low and the signal/noise ratio is high.
- The inelastic scattering cross-section plays a major role in the effectiveness of the inelastic background analysis. It must be representative of the sample and the photon energy.
- The inelastic mean free path (IMFP) has a low incidence on the inelastic back ground simulation. The uncertainty on the individual IMFPs does not affect the inelastic background analysis for more than 30% deviation.

- The electron detection angle uncertainty has no influence on the inelastic background analysis.

- The amount of substance (AOS) influences the inelastic background analusis which is more precise with an increasing AOS.

- The use of reference samples increases the reliability of the analysis because the inelastic cross section can be better determined.

5.2 Reliability - comparison with other techniques

Previously the methodology for finding the depth distribution corresponding to the inelastic background of the measurement by trial and error and eye inspection. To increase the reliability of the results, a semi-automated procedure has been set up with use of a bot and applying an empirical error formula. Several inelastic backgrounds modeling where showed in this work and they all present a good match between the measurement and the modelled background, ensuring a stable procedure which can be continued to be implemented.

The comparison of the results of inelastic background analysis with destructive techniques (TEM-EELS, APT) and invasive techniques (Auger depth profiling) showed the agreement on the results. This is of major importance as the photoemission experiment is a non destructive technique and allows to perform further mesurements on the sample, especially for electric characterization.

5.3 Limitations of background analysis of HAXPES spectra

Despite the effort made in this work, the determination of a depth distribution of an element present in two separated layers is still equivocal.

The experiments were performed with analysis of high binding energy core-levels with use of hard x-rays. In this condition the peaks are separated by a few hundred eV. Therefore two overlapping peaks (if they are separated by $<$120 eV) could not be studied.

5.4 Complementarity of core-level and background analysis

The study of the HEMT samples showed the complementarity between the study of the high resolution spectra of core-levels which unravels the chemical composition of the sample within the 3 first IMFP and the inelastic background analysis which unravels the depth distribution of an element within the 8 first IMFP. The chemical analysis indicates which inelastic scattering cross-section should be used while the depth distribution of the element obtained with the background analysis can give an insight of the location in the sample of the components determined with the high resolution spectra. This back and forth analysis provides a global description of the sample and allows to suggest a scheme for the various annealing presented.

5.5 Future trends

The optimized procedure (bot) proposed in this work allows to discriminate, in the case of the "buried layer" model, two different inelastic background shapes corresponding to depth distributions varying by less than 1 nm at burying depths larger than 20 nm. The procedure can be directly applied to XPS data treatment. However, the reliability of the error calculation needs to be further improved, for example by analyzing HAXPES simpler bilayer systems.

Such an automated procedure could have an important application in "real-time" processing of XPS data, as required for instance for in-line control in semiconductor industry. Besides in line control, one can also think about in-situ characterization of deposition or annealing processes of materials in a stack. The processing time is however too long for the moment to allow this: in the present version of the program, processing times of 50 min for a depth range of 0 to 300 nm and 0 to 500 nm for top and bottom interfaces (case of Ti 1s of the unannealed HEMT sample) has been achieved.

Working on the data processing time is also a prerequirement to be used in laterally resolved background analysis, as can be implemented in a photoelectron emission microscope (PEEM). In spectroscopic, energy-filtered XPEEM, one would have to consider the analysis of a series of inelastic background spectra generated within the microscope field-of-view, and ultimately at each image pixel, in order to obtain a map of the elemental depth distribution. The parallel treatment of these spectra would require a drastic reduction of the processing time, and maybe also, to apply noise reduction techniques. Such measurements are becoming possible in HAXPES with the recent HAXPEEM instrument [140, 141]. During this work, preliminary experiments were performed and the first results should be available soon, opening the way to microscopic analysis of deeply buried interfaces.

6 Appendices

Appendix I - Dipole approximation

In 1927, P. Auger observed that the intensity of the photoelectron emitted with use of unpolarized x-rays depends only on the angle between the incident photon and the emerging photoelectron [142].

The electric-dipole approximation assumes the electromagnetic field of the photon beam, $exp(ikr)$, expressed as a Taylor-series expansion $1 + ikr + ...$, can be truncated to unity [143]. This approximation is valid for UV and far UV photon ranges as the photoelectron velocities following UV photoemission are extremely small compared to the speed of the light (i.e. relativistic effect are negligible) and the wavelength of the UV light is much larger than the orbitals from which electrons are ejected [144].

For high energy regime with $h\nu \geq 5$ keV, the breakdown of the dipole approximation becomes complete and therefore require the use of a full Taylor-series expansion. This phenomenon was predicted and observed decades ago [145, 146], only recent description valid for HAXPES experiments will be detailed here.

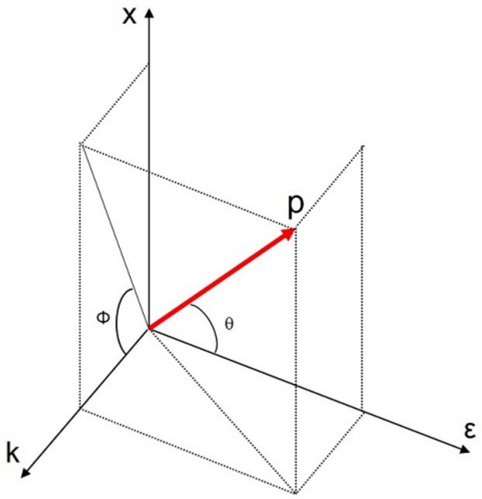

Figure 83: *Geometry describing the photoelectron angular-distribution measurement using linearly polarized light. The polar angle ϑ is measured between the photon polarization vector ϵ and the momentum vector $\vec{p}$ of the photoelectron. The azimuthal angle Φ is defined by the photon propagation vector k and the projection of p into the x-z plane.*

Effects and limitations of the dipole approximation

The electric-dipole approximation leads to the expression of the differential photoionization cross-section for linearly polarized light as described by *Cooper et al.* [147]:

$$\frac{d\sigma_i}{d\Omega} = \frac{\sigma_i}{4\pi}\left[1 + \beta P_2(\cos\theta)\right] \tag{81}$$

where $P_2(\cos\theta) = \frac{1}{2}(3\cos^2\theta - 1)$ with θ defined in Fig.83 as the angle between the momentum vector of the ejected electron and the polarization vector of the incident light, β is a parameter describing the angular distribution of the photoelectron. For unpolarized radiation, the expression of the photoionization cross-section is modified as:

$$\frac{d\sigma_i}{d\Omega} = \frac{\sigma_i}{4\pi}\left[1 - \frac{1}{2}\beta P_2(\cos\theta)\right] \tag{82}$$

with ϑ the angle between the momentum vector of the ejected electron and the propagation vector of the incident light.

For an experiment with $\theta \simeq 54.7°$, so-called magic angle, one obtain $P_2(cos\theta) = 0$. It is then possible to determine the relative photoionization cross-section σ_i (which is also angular dependent). The parameter β depends on the quantum number l, ranging from -1 to 2 given by [147]:

$$\beta = \frac{l(l-1)\sigma_{l-1}^2 + (l+1)(l+2)\sigma_{l+1}^2 - 6l(l+1)\sigma_{l+1}\sigma_{l-1}cos(\delta_{l+1} - \delta_{l-1})}{3(2l+1)\left[l\sigma_{l-1}^2 + (l+1)\sigma_{l+1}^2\right]} \tag{83}$$

with

$$\sigma_{l\pm1} = \int_0^\infty R_{n,l}rR_{kl\pm1}dr \tag{84}$$

the dipole radical matrix element.

This approximation is widely used in the solid photoemission community. However it was shown that with use of unpolarized Mg and Al K_α x-ray, deviation from dipolar angular distribution can be observed and attributed to the influence of retardation or phonon-momentum transfer . This work have been followed by extensive theoretical effort, mainly using the Independent Particle Approximation (IPA) which showed the dependance of non-dipole effects with atomic number and the orbital angular momentum of the photoemitted electron. For example, experiments on Ne 2s and 2p valence photoionization for $0.25\,keV \leq h\nu \leq 1.2\,keV$ showed the limit of the dipole approximation [148] and for specific interference between different-parity autoionization resonances, Martin et al. observed non-dipole effects $\leq 0.5\%$ [149].

First order corrections

For soft x-rays experiments, the first order corrections to the dipole approximation is usually sufficient for the photon momentum. The correction is based on non-dipole effects in a perturbation theory framework [10] where the truncature of the electromagnetic field happens in the second term: $exp(ikr) = 1 + ikr$. Two new angular parameters δ and γ and the azimuthal angle ϕ relative to the photoelectron propagation axis (see Fig.83) are introduced. The differential cross section of

Eq.81 then becomes:

$$\frac{d\sigma_i}{d\Omega} = \frac{\sigma_i}{4\pi}\left[1 + \beta P_2(\cos\theta) + \left[\delta + \gamma\cos^2\theta\right]\sin\theta\cos\phi\right] \tag{85}$$

for linearly polarized light. For unpolarized or circularly polarized light the Eq.82 becomes:

$$\frac{d\sigma_i}{d\Omega} = \frac{\sigma_i}{4\pi}\left[1 - \beta P_2(\cos\Theta) + \left[\delta + \frac{\gamma}{2}\sin^2\theta\right]\cos\theta\right] \tag{86}$$

These first order corrections are valid for HAXPES experiments [44].

Second order correction

The second order correction is used with $exp(ikr) = 1 + ikr - \frac{1}{2}(kr)^2$. Then the expression of Eq.85 becomes [150]:

$$\frac{d\sigma_i}{d\Omega} = \frac{\sigma_i}{4\pi}\left[1 + (\beta + \Delta\beta)P_2(\cos\theta) + \left[\delta + \gamma\cos^2\theta\right]\sin\theta\cos\phi\right] + \eta P_2\cos 2\phi + \mu\cos 2\phi + \xi(1+\cos 2\phi)P_4(\cos\theta) \tag{87}$$

where four new angular-distribution parameters $\Delta\beta, \eta, \mu\, and\, \xi$ are introduced. However $\Delta\beta$ is not experimentally easily distinguishable from the first order correction parameter β and the relationship $\xi = -\eta - \mu$ guarantees only two new independent parameters can be experimentally measured.

Appendix II - Synchrotron radiation

Synchrotron radiation is the electrical field emitted from charged particles (electrons or positrons). A synchrotron machine is decomposed in three parts: the linear accelerator which produces the electrons and accelerates them; a booster, where electrons become relativistic and a storage ring where electrons are maintained at constant velocity and orbit as can be seen in fig.84. The appendix details SOLEIL synchrotron setup, where the storage ring injection is continuous, on opposite of the ESRF where injection is non-continuous.

In order to perform experiments in a synchotron facility, the operator, qualified as a user, must fill a form which is called a proposal. The proposal is unique and follow a template available online on sychrotron's website. It consists in a small text describing the user experience in previous synchotron experiments and a detailed description of the experiment needed.

The proposal is examined by a scientific committee which attributes beamtime. The scientist in charge of the beamline work out the planning with the users.

For every project is attributed a beamline scientist called local contact, whom prepare the beamtime with the user and helps seting up the beamline to delivers specific photons with defined energy.

This appendix presents a table of the HAXPES beamlines used in this thesis and additional beamlines from the German synchrotron DESY, the English synchrotron Diamond and the Japanese SPRing8.

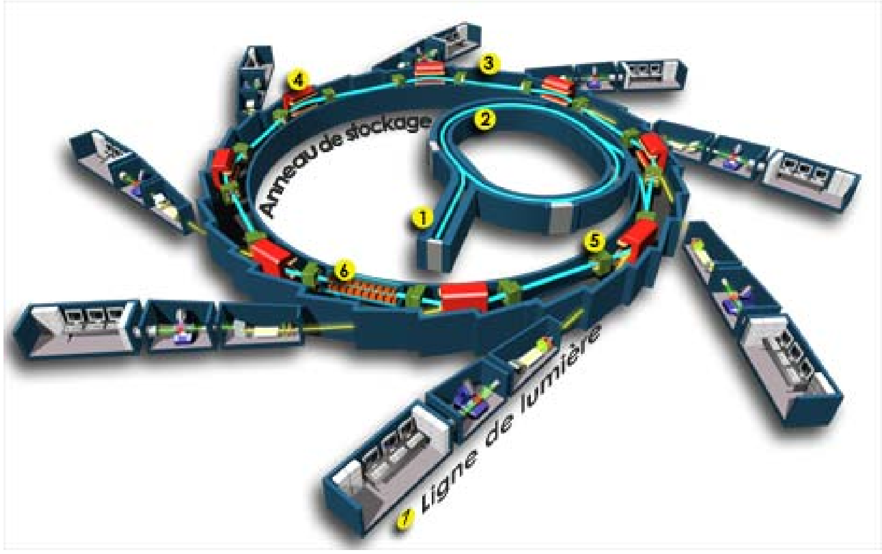

Figure 84: *Scheme of a synchrotron facility. (1) LINAC, (2) Booster, (3) storage ring, (4-5-6) wigglers, (6) insertion device, (7) beamline.*

Linear accelerator

The linear accelerator (Linac) produces electrons thanks to an electron gun: a tungsten filament is heated and produces electrons. They are accelerated with a wehnelt at 90 kV. They pass through a "grouper" in order to have a velocity near c and form bunches, their energy is then of 15 MeV. They achieve their path in the linac in two linear acceleration devices, with electromagnetic waves of 3000 MHz to reach energy of 100 MeV. They form bunches of 300 ns with a 3 Hz frequency and enter in the booster with a ratio of 0.3. The others are lost.

Booster

The booster is a ring of 157 m perimeter. Due to an electric field, electrons gain energy from 100 MeV to 2.75 GeV in a period of 166 ms. Magnetic field of dipoles inside the booster changes from 0,027 T when they electrons enter from the linac and 0.74 T when they reach the energy of 2.75 GeV and are ready to enter in the storage ring. They enter in the storage ring in a transfer section of 42 m with 3 dipoles and 7 quadrupoles with an efficiency of 0.7.

Storage ring

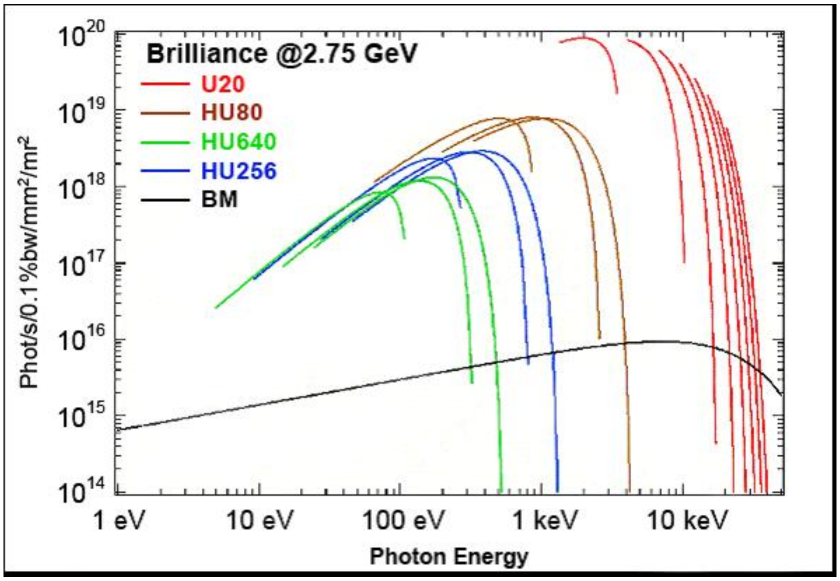

Figure 85: *Source brilliance as a function of photon energy for different insertion devices in SOLEIL synchrotron. From [151].*

The storage ring (of perimeter 354 m) is the part where relativistic electrons must be kept at constant velocity and orbit to produce stable synchrotron radiation for the experiments. In 3rd generation sources, the photon beams are produced by insertion devices placed in the straight sections between the bending magnets. A storage ring is then constituted of curved and straight magnetic lenses. Since the circulating electrons must be pumped continuously to balance the radiation losses they must arrive with a well-defined phase at the acceleration electrodes. For this reason they can only circulate in bunches. Every bunch is used to provide synchrotron radiation. The significant quantity is the stored current, which can reach several 100 mA, circulating for many hours in the storage ring. Eventually, as more and more electron gets lost, the electron beam dies out and the storage ring must be refilled. Typically the widths of bunches are a few picoseconds (13 ps for SOLEIL) and the circulation time is in the order of microseconds (1.181 μs in SOLEIL). Each time that the electron bunch trajectory is deflected in the storage ring by the bending magnet or going through an insertion device, synchrotron radiation is emitted in the forward direction. SOLEIL operates in the top-up mode providing practically constant beam current in the storage ring: the beam losses are compensated by frequent injections into the storage ring. This procedure overcomes lifetime limitations and keeps a constant photon flux for a thermal equilibrium at the beamline. The beam current is thereby kept constant at 400 mA. We immediately see the impact of insertion device between bending magnet (BM) and undulators (color lines) in fig.85 where the brilliance is around 10^{15}-10^{20} phot/0,1%bw/mm^2/mr^2, for comparison, x-ray tubes have a brightness of 10^9 phot/0,1%bw/mm^2/mr^2 (which is already of the same order of magnitude as the sun).

Insertion devices are the only part of beamline inside the storage ring. The wiggler produce an oscillation in the trajectory of the electrons in the storage ring as can be seen in fig.86

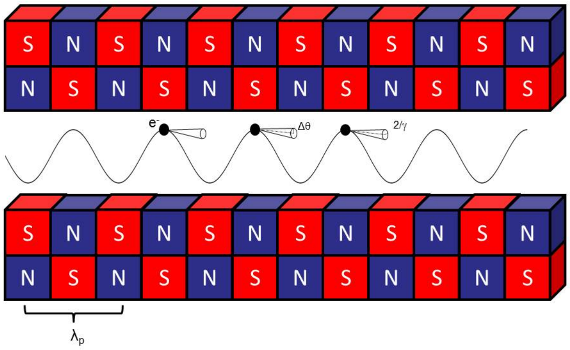

Figure 86: *Wiggler scheme*

. Radiation is emitted in various points and results in a beam of N-fold intensity (N is the number of consecutive magnets). Since N is large, the wiggler operates as an undulator. The beam intensity is then proportional to N^2. The total emitted power for highly relativistic particle is:

$$P = \frac{e^2 c_0 (\beta\gamma)^4}{6\pi R^2 \varepsilon_0} = \frac{e^2 (\beta\gamma)^4}{6\pi m_0 c_0^7 R^2 \varepsilon_0} \tag{88}$$

With $\beta = \frac{\nu}{c_0}$, $\gamma = \frac{1}{\sqrt{1-\beta^2}}$ and $\varepsilon = \gamma m_0 c_0^2$ and R is the radius of the bending magnet seen in fig.87

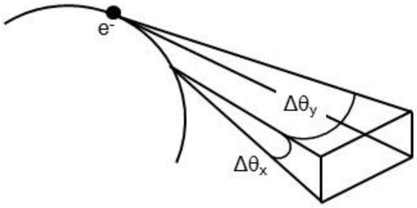

Figure 87: *Scheme of a bending Magnet*

. We can see that total energy is proportional to the 4th power of the energy particle ε. Emission pattern for relativistic particle is highly oriented due to Doppler effect and the photons are polarized in the acceleration plane. The half width at half maximum is then:

$$\Delta\theta = \frac{1}{\gamma} = \frac{m_0 c_0}{\varepsilon} \tag{89}$$

The brilliance of the source, defined as the photon flux per solid angle and per area is

$$L = \frac{F}{(\Delta\theta_y \Delta y)(\Delta\theta_x \Delta z)} \tag{90}$$

In an undulator, electrons pass through several magnets, resulting in coherent interaction (the undulator is built this way). In its reference frame, electrons see the spatial period of the undulator λp/γ. It is then its undulating period, giving the same period for the emitted radiation. With respect to the Doppler effect in the laboratory frame this period is then divided by a factor 2γ. The fundamental wavelength λ can be modified by changing the magnetic field B (in our case this modification is obtained by mechanically changing the gap between the magnetic elements):

$$\lambda \cong \frac{\lambda_p/2\gamma^2}{1+bB^2} \tag{91}$$

Where b is a parameter of the undulator. The bandwidth of the emitted beam is then given by:

$$\frac{\Delta\lambda}{\lambda} = N - 1 \tag{92}$$

Where N is the number of magnetic dipoles, then the angular spread is given by:

$$\Delta\theta = \frac{1}{\gamma\sqrt{N}} \tag{93}$$

Beamlines

The Tab.18 shows some beamlines and their features. All beamlines are operational except ID32 which was closed for user operation on 5 December 2011 and I09 which is not open to the users yet.

Synchrotron	ESRF		SOLEIL	DESY	SPring8	DIAMOND
Beamline	ID32*	BM25	GALAXIES	P09	BL47XU	I09
Location	Grenoble, FRANCE		Saclay, FRANCE	Hamburg, GERMANY	JAPAN	Harwell, ENGLAND
Photon energy range	2-25 keV	6-35 keV	2.3-12 keV	2.7-24 keV	5.2-37.7 keV	2.1-18 keV
Electron energy range	4-15 keV	6-12 keV	2.3-12 keV	4-12 keV	6-10 keV	2.3-12 keV
Analyzer	SPECS PHOIBOS 225 HV	HV CSA	SCIENTA EW4000	SPECS Phoibos 225HV	VG Scienta R4000	VG Scienta EW4000
Insertion device type	Undulator	Bending magnet	Undulator	Undulator	Undulator	Undulator
Type of experiment	HAXPES	HAXPES	HAXPES	HAXPES	HAXPES	HAXPES-XSW
Other setup on the beamline	XSW-XRD	HRPD-XAS	RIXS	RSD	µCT	XPS-XPD

Table 18: *Table of HAXPES beamline worldwide.*ID32 is no longer in operation.*

Appendix III - Commercial XPS and HAXPES apparatus

This appendix presents some commercial apparatus for XPS and HAXPES measurements. The list is not exhaustive and presents only apparatus designed to perform “classical” experiment, observing chemical shifts. The laboratory apparatus is composed by the buyer with choice in sources and detector, depending on its need to perform several experiments.

- ARXPS, where the acceptance angle of the anlyser is very wide, allowing to measure spectrum from different take off angle at the same time.
- Near Ambiant pressure (NAP) which is a developping field. in this case, the apparatus allow to have a significvant presuure in the ordre of mbar near the sample by differential pumping.
- ARPES in synchotron facilites where the $k_{//}$ component of the photoelectron is conserved, allow to obtain band mapping of the sample.

The tables summarize technical informations for analyzers from the websites of the 3 main manufacturers: SPECS [152], VGScienta [153] and FOCUS Gmbh [154] are separated in two tables. Tab.19(a) presents experimental apparatus for HAXPES measurement and Tab.19(b) presents the same specificity for XPS apparatus sumamrizing general informations, especially the energy detection limit and the energy resolution.

The laboratory sources for XPS are generally Al K_α, Mg K_α.

The HAXPES sources are generally radiation sources but Zr K_α, Ag K_α can also be used. SPECS has the possibility to buy laboratory hard x-rays source based on Cr K_α and Cu K_α which emits photons of 5417 eV and 8055 eV respectively but to our knowledge, no publication were made with these sources.

Name (manufacturer)	PHOIBOS 225 HV (SPECS)	PHOIBOS 150 HV (SPECS)	R4000 (VGScienta)	EW4000 (VGScienta)	HV CSA (FOCUS GmbH)
Type of experiment	HAXPES	HAXPES	XPS - HAXPES	UPS -HAXPES	XPS-HAXPES
Type of Analyser	HSA	HSA	HSA	HSA	CSA
Mean radius	225 mm	150 mm	200 mm	200 mm	300 mm
Energy detection limit	15 keV	7 keV	5 eV - 10 keV	12 keV	1 eV - 15 keV
Energy resolution in HAXPES	<15 meV	<10 meV	<100 meV	<100 meV	<100 meV
Entrance slits number	8	8	9	9	6

(a)

Name (manufacturer)	PHOIBOS 150 (SPECS)	PHOIBOS 100 (SPECS)	R3000 (VGScienta)	R4000 (VGScienta)	CSA 200 (FOCUS GmbH)
Type of experiment			UPS-XPS	UPS - XPS	
Type of Analyser	HSA	HSA	HSA	HSA	CSA
Mean radius	150 mm	100 mm	135 mm	200 mm	200 mm
Energy detection limit			0.5 - 1500 eV	0.5 - 1500 eV	0 - 3200 eV
Energy resolution in XPS	<1 meV	<1 meV	3.0 meV	1.8 meV	<10 meV
Entrance slits number	8	8	6	9	3

(b)

Table 19: *Table of commercial HAXPES (a) and XPS (b) apparatus and their principal features.*

Appendix IV- State of the art for depth profiling methods

In microelectronics, the characterization techniques have to be sensitive to ultra-thin layers, even to monolayers, sometimes buried under rather thick overlayers. Characterization techniques capable of analyzing such deeply buried thin layers can be roughly classified into three major categories depending on their impact on the sample: destructive techniques, invasive and non-invasive techniques.

The destructive techniques require sample preparation. This is not trivial because the sample can be modified during preparation. For example, to perform a TEM experiment, one of the most commonly used techniques, the sample must be made in form of a thin lamina. It must be cut by Focused Ion Beam (FIB) and then polished to reduce roughness [155].

The invasive techniques are the ones that may modify the sample during the analysis without necessarily requiring complex sample preparation. Most of these techniques employ ion beam as a probe. Cycles of small sputtering before non-destructive surface analysis can also be classified as invasive.

Non-invasive techniques are techniques that do not (or only slightly) modify the sample.

Destructive Methods

Transmission Electron Microscopy - Electron Energy Loss Spectroscopy (TEM-EELS)

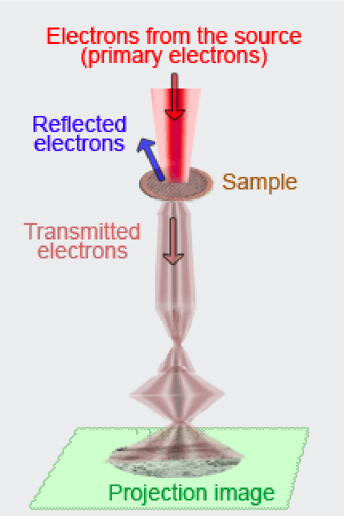

Figure 88: *Scheme of Transmission electron microscope.*

Electron microscopy is a widely used technique as it presents a sub-nanometric resolution. The impinging electron beam of nanometric size can be measured after transmission through the sample (“bright field”) or after diffraction (dark field”). It implies the use of a micrometric thick sample, generally shaped with a FIB. The results are analyzed thanks to a diffraction image which can be converted to a real image via Fourier transform[156, 157, 158]. The measurement of electron energy loss (EELS) allowing to obtain depth distribution along the sample surface is proportional to Z, therefore the distinction of two juxtaposed elements of close atomic number can be difficult or even impossible without modeling. These techniques can give results on the chemical state, the depth distribution, the optical and magnetic properties, the structural defects and strain. The detection limit is of 1 10^{19}at/cm^{3}and the ultimate spatial resolution of a TEM is of 0.2 nm. This resolution is mainly limited by the sample preparation.

Atom Probe Tomography (APT)

Atom Probe Tomography (APT) is an analytical technique for studying materials at the nanoscale. It enables the generation of a three dimensional elemental map, from which local composition measurement can be extracted. Initially used only for metallic specimens [159], the introduction of a pulsed laser [160] in recent years has made possible the analysis of semiconductors and even insulators. APT is based on the field evaporation effect requiring the sample to be prepared in the

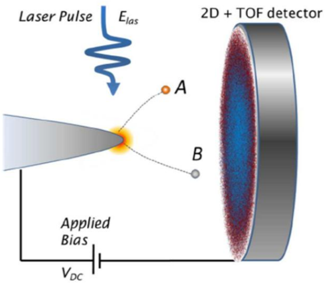

Figure 89: *Schematic diagram of an Atom Probe Tomography experiment.*

form of a needle of radius <50 nm, using a Focused Ion Beam (FIB). This tip is submitted to a high electric voltage (V∼1-15 kV) leading a high electrical field at the sample surface (E∼V/R, R is the tip radius at the apex) as can be seen in Fig.89. The atoms at the surface of the tip are ionized, accelerated by the high electric field and finally detected by a spatial and time resolved detector. A pulse voltage or laser allows the chemical identification of ions by time of flight (TOF) mass spectrometry. More precisely, the ion TOF from the tip to the detector is proportional to the mass to charge (m/n) ratios. Reconstruction of the evaporated sample is obtained using a projection algorithm taking into account the sequence and nature of detected ions as well as their position [114]. In ideal conditions, depth resolution can be better than 0.2 nm and lateral resolution better than 0.5 nm [161].

Invasive depth profiling methods

Elemental depth profiling can be done by combining sputtering with surface-sensitive techniques such as X-ray Photoelectron Spectroscopy (XPS) or Auger Electron Spectroscopy (AES). As the photoemission was described in the previous section in detail, the depth profiling using sputtering will be illustrated with Auger electron Spectroscopy. The Time of flight Secondary ions Mass Spectroscopy will be explained as it employs two ions beams.

Auger Electron Spectroscopy

Auger Electron Spectroscopy uses an electron focused beam as a source and collects electrons emitted via an Auger process as a function of their kinetic energy. The Auger process is a deexcitation process where a hole in the subshell K allows a transition from the electron of subshell L toward the K subshell. The corresponding energy is given to an electron of subshell M which is ejected from the sample. As the energy of K, L and M subshells are fixed the resulting kinetic energy of the emitted Auger electron is fixed. The efficiency of the Auger deexcitation process decreases with increasing atomic number [162]. For this reason, elements with atomic number > 50 are rarely

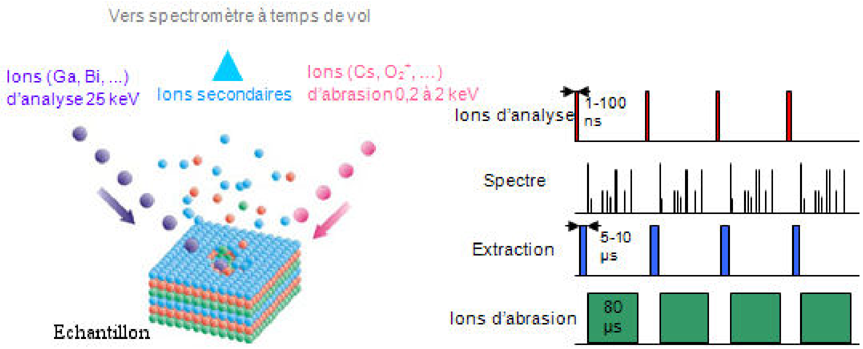

Figure 90: *ToF SIMS principles. On the left the pink ions are the sputtering ion beam, whereas the purple are the analysis ion beam. The right panel shows successive sequences of sputtering (green), extracting (blue) and analysis (red). The resulting spectrum (in black) is obtained. Moreover, it is possible to obtain ionic image with a surface scan and combining the depth profiling with imaging, permits to visualize a 3D render.*

studied by AES because acquisition time becomes rather long. The ultimate depth resolution is 0.2 nm and the detection limit is of 1 10^{19}at/cm^3.

Time of Flight Secondary Ions Mass spectroscopy (ToF-SIMS)

This technique allows obtaining elemental and molecular composition by analyzing secondary ions emitted when the sample is bombarded with a primary ion beam as shown in Fig.90. To obtain the depth profile, a second ion beam is used to sputter the surface step by step. The emitted ions are analyzed in a time of flight mass spectrometer, so all elements and their isotopes can be detected. The molecular ions emitted correspond to molecules in the sample matrix, so that not only depth distribution is obtained but also stereochemistry for organic compounds. The spot size is usually around a few µm^{2}and the ToF-SIMS can be used as a microscope with lateral resolution around 100 nm and ultimate depth resolution of 0.5 nm. The primary ion beam has an energy from a few hundred eV to a few keV (typically 25 keV for analysis beam) and can be made of various ions, the most usual being $Bi_n{}^+$, Cs^+, $O_2{}^+$, Au^+ and $C_{60}{}^+$. As the kinetic energy of the ionized compounds is fixed by the extraction voltage, the time needed for the ions to reach the detector inside the analyzer is proportional to the square root of mass/charge. The primary ion beam has a pulse of a few ns, which allows to measure precisely the time of flight of the ions. The quantification can be performed only with use of reference samples.

Non invasive optical methods

The invasive techniques do not , or very slightly modify the sample. They involve photons as probe source and techniques presented here rely on the photon detection (transmitted or emitted).

Ellipsometry

Ellipsometry is an optical non-destructive characterization technique based on the change in the polarization state of an electromagnetic wave after reflexion on the surface of a sample [163]. The ellipsometry principle is described in figure 91. The apparatus is composed of a light source (generally between 1 and 10 eV), a polarization state generator (PSG), a polarization state analyzer (PSA) and a detector [164]. The PSG determines a specific state polarization to the light impinging the sample, generally linearly polarized. The reflected beam after interaction with the sample is analyzed by the PSA. In the case of a monochromatic linearly polarized light, the electrical field of the incident beam is $\overrightarrow{E} = \overrightarrow{E_0}e^{i(\omega-\overrightarrow{k}.\overrightarrow{r})}$and the same expression is used for , the electrical field reflected by the sample. These two waves can be decomposed in two orthogonal directions, one perpendicular to the incident plane (s wave represented in green in the figure) and the other parallel to this plane (p wave represented in purple in the figure). The p and s vibrations reflect on the sample without reciprocal interaction and the corresponding reflexion coefficients $\mathrm{r_p}$ and $\mathrm{r_s}$ are written as:

$$r_p = \frac{E'_p}{E_p}\ r_s = \frac{E'_s}{E_s} \tag{94}$$

The p and s polarizations show different changes in amplitude and phase upon light reflection causing the reflected light to become elliptically polarized. By measuring different reflected intensities, ellipsometry allows the reflexion coefficients ratio for the p and s waves to be calculated. This complex number is expressed as:

$$\rho(\theta, \lambda) \equiv \frac{r_p}{r_s} \equiv tan\psi e^{i\Delta} \tag{95}$$

The parameters tan ψ and Δ are respectively the amplitude and phase variations between the p and s waves of the electric field. To obtain the measurement of the unknown properties of the analyzed sample (refractive index and thicknesses of the layers), a mathematical model can provide theoretical values for ψ and Δ [165]. These values are compared to the experimental data and adjusted through an iterative process. The quality of the obtained values are evaluated by minimization of the mean squared error χ^2 representing the difference between the experimental data and the calculated values. Nowadays ellipsometry is a widely used technique for measurements of refractive indices n and extinction coefficient k of all types of materials due to its non-destructive character and extreme sensitivity to the surface and ultra-thin layers (<1 nm) [166]. The depth resolution is of 0.5 nm and the probed depth up to a few µm depending on the absorption of the material.

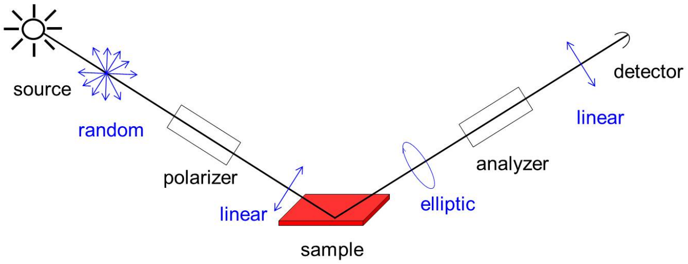

Figure 91: *Scheme of an ellipsometer experimental apparatus. The elements appear in black whereas the light polarization is in blue.*

Specular X-Ray Reflectivity (XRR)

Specular X-ray Reflectivity (XRR) [167] is a non-destructive technique used to precisely determine the thickness, roughness and electronic density of thin films, surfaces or multilayers. XRR is performed by measuring the intensity of an x-ray beam reflected specularly from the surface as function of the grazing incident angle. Typically, the incident and exit angles values are of about few degrees. Specular reflectivity means that the incident and exit angles of the x-ray beam are equal. This allows one to determine the electron density profile perpendicular to the surface over a range spanning approximately 1 to few hundred of nm below the surface [168]. XRR can be equally performed on amorphous, polycrystalline or liquid materials since it is only sensitive to the electronic contrast between materials. The amplitudes of the transmitted and reflected waves can be determined by the conditions for continuity of the waves at the interface, resulting in the so-called Fresnel equations. Close to the critical angle, correction from refraction must be also applied according to Snell's law:

$$n_1 cos(\theta_1) = n_2 cos(\theta_2) \tag{96}$$

as depicted in Fig.92. For a given ϑ_1, called the critical angle, ϑ_2 is equal to zero, and according to the above equation, the critical angle is directly related to the coefficient n_2 of the irradiated material (considering that n_1 is equal to 1 for air). The precise measurement of this critical angle can thus give access to the electronic density of an individual layer [169]. Below the critical angle, the beam is almost fully reflected. Above the critical angle, the intensity decreases rapidly and this decay can be related to the roughness of the surface. When a film of different electron density to the substrate is present, partial reflection occurs at both the top and bottom interfaces. Interference occurs between the waves, resulting in interference fringes as the optical path difference between them is changed by varying the incidence angle. The fringes are popularly known as Kiessig fringes, after their discoverer. The condition for constructive interference is that the path difference must be an integral number of wavelengths. These Kiessig fringes periods can thus be used to extract the film thickness if the thickness is between 1 and 1000 nm [170]. The XRR experiment is not restricted in sort of sample as long as their surface is flat.

experiment	TEM-EELS	APT	Auger depth profiling	ToF-SIMS	Ellipsometry	XRR	XPS
Analyzable element	conductors	conductors and insulators	Z≤50	all types	all types	all except H	all except H and noble elements
Primary source	electrons (100-500 keV)	laser	electrons (1-10 keV)	Ions (around 25 keV)	Photons (1-10 eV)	x-rays (1.5 keV)	x-rays (1487 eV)
Analysis	transmitted electrons	emitted ions	emitted electrons	emitted ions	reflected photon	reflected photon	emitted electrons
Detector	EDS	PSD	MCD	ToF	Photomultiplicator	Scintillator	MCD
Sensitivity	1.10^{19}at.cm^{-3}	1.10^{18}at.cm^{-3}	1.10^{19}at.cm^{-3}	1.10^{12}at.cm^{-3}	1.10^{15}at.cm^{-3}	1% at.	5.10^{18}at.cm^{-3}
Depth resolution	0.2 nm	0.3	0.2 nm	0.5 nm	0.5 nm	3 nm	0.1 nm
Depth probe		length of the tip	3 -5 nm	0.5 nm	100 µm	10 µm	6-8 nm
Information	Imaging, cristalline structure, thickness	3D imaging, chemical composition, concentration, thickness	Imaging, chemical composition, concentration, thickness	3D imaging, chemical composition, concentration	optical constant, thickness, interface roughness	Thickness, interface roughness	Thickness, chemical composition

Table 20: *Experimental techniques and their principal features.*

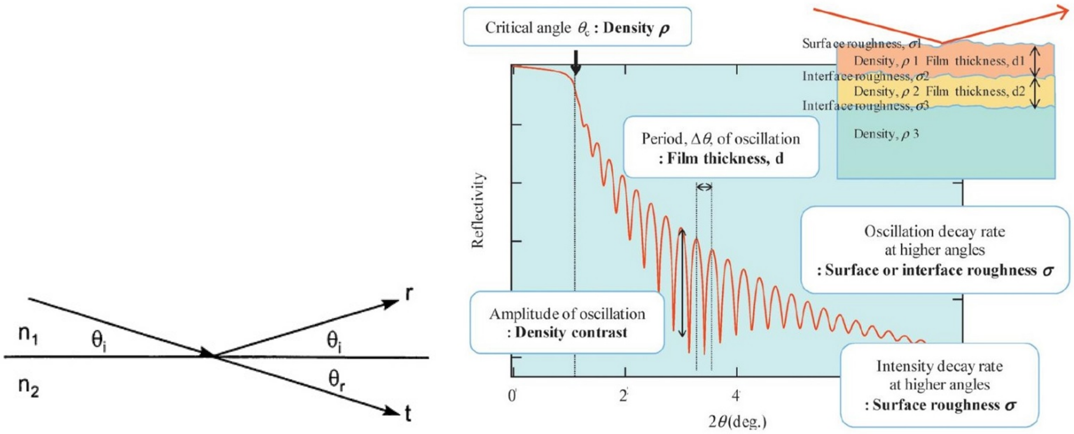

(a) (b)

Figure 92: *(a) Reflection and transmission at an interface, r is the reflected ray and t the transmitted ray. (b) Typical spectrum measured by XRR and the physical information contained within, from [171].*

Appendix V: TLM structures

The samples studied in the thesis are full sheet samples; they are deposited in large area to avoid any border effect. They cannot be used to measure DC characteristics, neither I-V curves, but are representative of the physical processes which will occur in the real device. The thicknesses of the metal layers are reduced compared to the thicknesses in the functional device but are the same as the one used to measure DC characteristics.

The electrical characterizations were performed on samples deposited with the same conditions but on patterned Transfer Length Method (TLM) structures as shown in Fig.93.

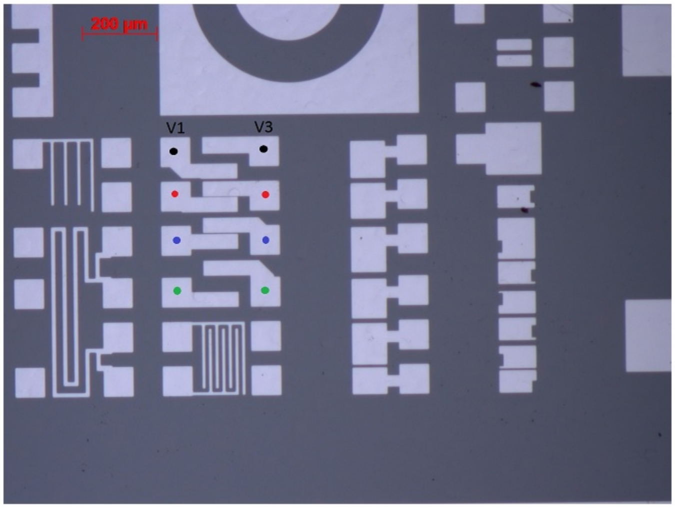

Figure 93: *Picture of the TLM structure taken with an optical microscope. V1 and V3 are the points for electric characterization.*

The measurement was performed with contact between two points V1 and V3 as presented in Fig.93. The resulting Resistivity is measured with different distances between V1 and V3 as plotted in Fig.94(b) where the y-intercept gives the resistivity. As expected the unannealed sample and the sample annealed at 600°C do not form electric contact and therefore cannot be used to obtain I-V curves.

The sample annealed at 900°C presents a good response as can be seen in Fig.94(a) where the I-V curves shows an ohmic contact and the corresponding resistivity R_C is found to be 3.7 (±0.8) Ω.mm. For these reasons the research was oriented toward this sample. The aim of the study is to find the chemical composition difference between the samples which is believed to be responsible for the quality of the contact formation. The study of the unannealed sample will be used as a control step and the 600°C sample will be seen as an intermediate state before the contact formation expecetd in the 900°C samples.

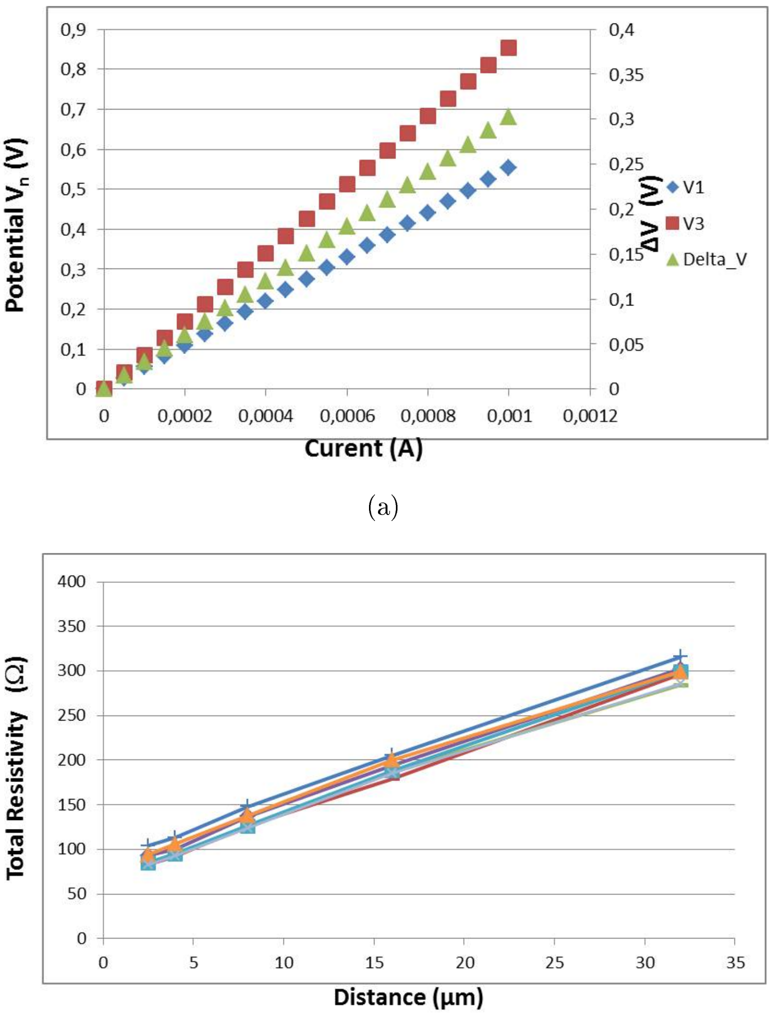

(a)

(b)

Figure 94: *(a) I-V curve and (b)* R_c*=f(l) for the sample annealed at 900°C.*

References

[1] H. Hertz. Ueber einen einfluss des ultravioletten lichtes auf die electrische entladung. *Annalen der Physiks*, 267(8):983–1000, 1887.

[2] A. Einstein. Über einen die erzeugung und verwandlung des lichtes betreffenden heuristischen gesichtspunkt. *Annalen der Physiks*, 322(6):132–148, 1905.

[3] Kai Siegbahn. Electron spectroscopy for chemical analysis. *Philosophical Transactions of the Royal Society of London A*, pages 33–57, 1970.

[4] C.S. Fadley. X-ray photoelectron spectroscopy: Progress and perspectives. *Journal of Electron Spectroscopy and Related Phenomena*, 178-179:2 – 32, 2010. Trends in X-ray Photoelectron Spectroscopy of solids (theory, techniques and applications).

[5] W.F. Egelhoff Jr. Core-level binding-energy shifts at surfaces and in solids. *Surface Science Reports*, 6(6-8):253 – 415, 1987.

[6] C. S. Fadley, S. B. M. Hagström, J. M. Hollander, M. P. Klein, and D. A. Shirley. Chemical bonding information from photoelectron spectroscopy. *Science*, 157(3796):1571–1573, 1967.

[7] E. Sokolowski, C. Nordling, and K. Siegbahn. Chemical shift effect in inner electronic levels of cu due to oxidation. *Phys. Rev.*, 110:776–776, May 1958.

[8] C. N. Berglund and W. E. Spicer. Photoemission studies of copper and silver: Theory. *Phys. Rev.*, 136:A1030–A1044, Nov 1964.

[9] S. Hüfner. *Photoelectron spectroscopy - Principles and applications.* Spinger, 2003.

[10] J. W. Cooper. Photoelectron-angular-distribution parameters for rare-gas subshells. *Phys. Rev. A*, 47:1841–1851, Mar 1993.

[11] M. B. Trzhaskovskaya, V. I. Nefedov, and V. G. Yarzhemsky. Photoelectron angular distribution parameters for elements z=1 to z=54 in the photoelectron energy range 100-5000 ev. *Atomic Data and Nuclear Data Tables*, 77(1):97–159, 2001.

[12] M. B. Trzhaskovskaya, V. I. Nefedov, and V. G. Yarzhemsky. Photoelectron angular distribution parameters for elements z=55 to z=100 in the photoelectron energy range 100-5000 ev. *Atomic Data and Nuclear Data Tables*, 82(2):257–311, 2002.

[13] M. B. Trzhaskovskaya, V. K. Nikulin, V. I. Nefedov, and V. G. Yarzhemsky. Non-dipole second order parameters of the photoelectron angular distribution for elements z=1-100 in the photoelectron energy range 5-10kev. *Atomic Data and Nuclear Data Tables*, 92(2):245–304, 2006.

[14] Iso 181115:2001, surface chemical analysis - vocabulary, international organisation for standardisation, geneva, 2001 (iso18115:2001/amd 1:2006; iso18115:2001/amd2:2007)c.

[15] S. Tanuma, C. J. Powell, and D. R. Penn. Calculations of electron inelastic mean free paths. v. data for 14 organic compounds over the 50-2000 ev range. *Surface and Interface Analysis*, 21(3):165–176, 1994.

[16] Giancarlo Panaccione and Keisuke Kobayashi. Hard x-ray photoemission spectroscopy: Variable depth analysis of bulk, surface and interface electronic properties. *Surface Science*, 606(3-4):125–129, 2012.

[17] C.J. Powell, A. Jablonski, S. Tanuma, and D.R. Penn. Effects of elastic and inelastic electron scattering on quantitative surface analyses by {AES} and {XPS}. *Journal of Electron Spectroscopy and Related Phenomena*, 68:605 – 616, 1994.

[18] M. P. Seah. Quantitative auger electron spectroscopy: Via the energy spectrum or the differential? *Surface and Interface Analysis*, 1(3):86–90, 1979.

[19] C. J. Powell and A. Jablonski. Progress in quantitative surface analysis by x-ray photoelectron spectroscopy: Current status and perspectives. *Journal of Electron Spectroscopy and Related Phenomena*, 178-179:331–346, 2010.

[20] A. Jablonski C.J Powell. Nist electron effective-attenuation-length datadata, version 1.1 standard reference data program database, 2003.

[21] A. Jablonski. Database of correction parameters for the elastic scattering effects in xps. *Surface and Interface Analysis*, 23(1):29–37, 1995.

[22] S. Thiess, C. Kunz, B. C. C. Cowie, T. L. Lee, M. Renier, and J. Zegenhagen. Hard x-ray photoelectron spectroscopy from 5-14.5 kev. *Solid State Communications*, 132(9):589–594, 2004.

[23] M. A. Reshchikov, M. Foussekis, and A. A. Baski. Surface photovoltage in undoped n-type gan. *Journal of Applied Physics*, 107(11):–, 2010.

[24] L. Kronik and Y. Shapira. Surface photovoltage phenomena: theory, experiment, and applications. *Surface Science Reports*, 37(1-5):1 – 206, 1999.

[25] D. R. Penn. Role of intrinsic plasmons in conduction-band x-ray photoemission from solids. *Physical Review Letters*, 40(9):568–571, 1978. PRL.

[26] S. Tougaard. Background removal in x-ray photoelectron spectroscopy: Relative importance of intrinsic and extrinsic processes. *Physical Review B*, 34(10):6779–6783, 1986. PRB.

[27] L. Hedin, J. Michiels, and J. Inglesfield. Transition from the adiabatic to the sudden limit in core-electron photoemission. *Phys. Rev. B*, 58:15565–15582, Dec 1998.

[28] T. Fujikawa, M. Kazama, and H. Shinotsuka. Theoretical study of plasmon losses in core-level photoemission spectra. *e-Journal of Surface Science and Nanotechnology*, 6:263–268, 2008.

[29] R. Ritchie. Plasma losses by fast electrons in thin films. *Phys. Rev.*, 106:874–881, Jun 1957.

[30] K. Siegbahn, C. Nordling, A. Fahlman, R. Nordberg, S.-E. Karlsson, and I. Lindgren. Esca atomic, molecular and solid state structure studied by means of electron spectroscopy. *Almqvist and Wiksell AB, Stockholm*, 1967.

[31] S. Doniach W. Spicer I. Lindau, P. Pianetta. X-ray photoemission spectroscopy. *Nature*, 250:214, 1974.

[32] K. Siegbahn. Preface to hard x-ray photo electron spectroscopy (haxpes). *Nuclear Instruments and Methods in Physics Research Section A: Accelerators, Spectrometers, Detectors and Associated Equipment*, 547(1):1–7, 2005.

[33] W. Drube. Preface. *Journal of Electron Spectroscopy and Related Phenomena*, 190, Part B:125–126, 2013.

[34] K. Kobayashi. Hard x-ray photoemission spectroscopy. *Nuclear Instruments and Methods in Physics Research Section A: Accelerators, Spectrometers, Detectors and Associated Equipment*, 601(1-2):32–47, 2009.

[35] L. Kövér. X-ray photoelectron spectroscopy using hard x-rays. *Journal of Electron Spectroscopy and Related Phenomena*, 178-179:241–257, 2010.

[36] T. Fujikawa, R. Suzuki, and L. Kövér. Theory of recoil effects of elastically scattered electrons and of photoelectrons. *Journal of Electron Spectroscopy and Related Phenomena*, 151(3):170–177, 2006.

[37] T. Fujikawa, H. Arai, R. Suzuki, H. Shinotsuka, L. Kövér, and N. Ueno. Recoil effects in high-energy photoemission beyond single-site approximation. *Journal of Electron Spectroscopy and Related Phenomena*, 162(3):146–157, 2008.

[38] Y. Takata, Y. Kayanuma, M. Yabashi, K. Tamasaku, Y. Nishino, D. Miwa, Y. Harada, K. Horiba, S. Shin, S. Tanaka, E. Ikenaga, K. Kobayashi, Y. Senba, H. Ohashi, and T. Ishikawa. Recoil effects of photoelectrons in a solid. *Physical Review B*, 75(23):233404, 2007. PRB.

[39] S. Tanuma, C. J. Powell, and D. R. Penn. Calculations of electron inelastic mean free paths. ix. data for 41 elemental solids over the 50 ev to 30 kev range. *Surface and Interface Analysis*, 43(3):689–713, 2011.

[40] C.J. Powell A. Jablonski, F. Salvat. Nist electron elastic-scattering-cross-section database, version 1.1 standard reference data program database 64, 2003.

[41] A. Jablonski and C. J. Powell. Practical expressions for the mean escape depth, the information depth, and the effective attenuation length in auger-electron spectroscopy and x-ray photoelectron spectroscopy. *Journal of Vacuum Science & Technology A*, 27(2):253–261, 2009.

[42] M. Sacchi, F. Offi, P. Torelli, A. Fondacaro, C. Spezzani, M. Cautero, G. Cautero, S. Huotari, M. Grioni, R. Delaunay, M. Fabrizioli, G. Vanko, G. Monaco, G. Paolicelli, G. Stefani, and G. Panaccione. Quantifying the effective attenuation length in high-energy photoemission experiments. *Physical Review B*, 71(15):155117, 2005. PRB.

[43] E. Stern and R. Ferrell. Surface plasma oscillations of a degenerate electron gas. *Phys. Rev.*, 120:130–136, Oct 1960.

[44] M. Novák, N. Pauly, and A. Dubus. Polarization and dipole effects in hard x-ray photoelectron spectroscopy. *Journal of Electron Spectroscopy and Related Phenomena*, 185(1-2):4–12, 2012.

[45] M. Kobata, I. Pis, H. Iwai, H. Yamazui, H. Takahashi, M. Suzuki, H. Matsuda, H. Daimon, and K. Kobayashi. Development of the hard-x-ray angle resolved x-ray photoemission spectrometer for laboratory use. *Analytical Sciences*, 26(2):227–232, 2010.

[46] M. Kobata, I. Pis, H. Nohira, H. Iwai, and K. Kobayashi. Application of cr k x-ray photoelectron spectroscopy system to overlayer thickness determination. *Surface and Interface Analysis*, 43(13):1632–1635, 2011.

[47] K. Kobayashi, M. Kobata, and H. Iwai. Development of a laboratory system hard x-ray photoelectron spectroscopy and its applications. *Journal of Electron Spectroscopy and Related Phenomena*, 190, Part B:210 – 221, 2013. Recent advances in Hard X-ray Photoelectron Spectroscopy (HAXPES).

[48] D. Briggs and J. T. Grant, editors. *Surface Analysis*. IMPublications, 2003.

[49] S. Tougaard. Accuracy of the non-destructive surface nanostructure quantification technique based on analysis of the xps or aes peak shape. *Surface and Interface Analysis*, 26(4):249–269, 1998.

[50] P. Sigmund. Theory of sputtering. i. sputtering yield of amorphous and polycrystalline targets. *Phys. Rev.*, 184:383–416, Aug 1969.

[51] J. Erlewin and S. Hofmann. *Thin Solid Films*, 69:L39, 1980.

[52] V. Naundorf and C. Abromeit. Limits of depth resolution for sputter sectioning: Moments of tracer depth distribution. *Nuclear Instruments and Methods in Physics Research Section B: Beam Interactions with Materials and Atoms*, 43(4):513 – 519, 1989.

[53] B. V. King and I. S. T. Tsong. A model for atomic mixing and preferential sputtering effects in sims depth profiling. *Journal of Vacuum Science & Technology A*, 2(4):1443–1447, 1984.

[54] J. D. Geller and N. Veisfeld. Depth resolution improvements using specimen rotation during depth profiling. *Surface and Interface Analysis*, 14(1-2):95–98, 1989.

[55] I. Yamada, J. Matsuo, N. Toyoda, and A. Kirkpatrick. Materials processing by gas cluster ion beams. *Materials Science and Engineering: R: Reports*, 34(6):231 – 295, 2001.

[56] S. Hofmann. Sputter depth profile analysis of interfaces. *Reports on Progress in Physics*, 61(7):827, 1998.

[57] G. Kupris, H. Roessler, G. Ecke, and S. Hofmann. Interpretation of sputter depth profiles by mixing simulations. *Fresenius' Journal of Analytical Chemistry*, 353(3-4):307–310, 1995.

[58] P.S. Ho and J.E. Lewis. Deconvolution method for composition profiling by auger sputtering technique. *Surface Science*, 55(1):335 – 348, 1976.

[59] S. Hofmann. Depth resolution in sputter profiling. *Applied physics*, 13(2):205–207, 1977.

[60] R.W. Paynter and M. Rondeau. Comparison of regularization methods for the inversion of {ARXPS} data. *Journal of Electron Spectroscopy and Related Phenomena*, 184(1-2):43 – 51, 2011.

[61] S Doniach and M Sunjic. Many-electron singularity in x-ray photoemission and x-ray line spectra from metals. *Journal of Physics C: Solid State Physics*, 3(2):285, 1970.

[62] P. J. Cumpson. Angle-resolved xps and aes: Depth-resolution limits and a general comparison of properties of depth-profile reconstruction methods. *Journal of Electron Spectroscopy and Related Phenomena*, 73(1):25–52, 1995.

[63] P. J. Cumpson. Angle-resolved xps depth-profiling strategies. *Applied Surface Science*, 144-145:16 – 20, 1999.

[64] W. Weaver C.E. Shannon. *The mathematical Theory of Communication*. University of Illinois Press, Urbana, Illinois, 1949.

[65] S.F. Gull and J. Skilling. Maximum entropy method in image processing. *Communications, Radar and Signal Processing, IEE Proceedings F*, 131(6):646–659, October 1984.

[66] S.F. Gull. *Maximum Entropy and Bayesian Methods*. Conference Proceeding Cambridge, 45-52 Kluwer, Dordrecht, 1989.

[67] G. C. Smith and A. K. Livesey. Maximum entropy: A new approach to non-destructive deconvolution of depth profiles from angle-dependent xps. *Surface and Interface Analysis*, 19(1-12):175–180, 1992.

[68] S. Tougaard and C. Jansson. Comparison of validity and consistency of methods for quantitative xps peak analysis. *Surface and Interface Analysis*, 20(13):1013–1046, 1993.

[69] A. Herrera-Gomez, M. Bravo-Sanchez, O. Ceballos-Sanchez, and M. O. Vazquez-Lepe. Practical methods for background subtraction in photoemission spectra. *Surface and Interface Analysis*, 46(10-11):897–905, 2014.

[70] O. Ceballos-Sanchez, A. Sanchez-Martinez, M. O. Vazquez-Lepe, T. Duong, R. Arroyave, F. Espinosa-Magaña, and A. Herrera-Gomez. Mass transport and thermal stability of tin/al2o3/ingaas nanofilms. *Journal of Applied Physics*, 112(5):–, 2012.

[71] A. Herrera-Gomez, M. Bravo-Sanchez, F.S. Aguirre-Tostado, and M.O. Vazquez-Lepe. The slope-background for the near-peak regimen of photoemission spectra. *Journal of Electron Spectroscopy and Related Phenomena*, 189:76 – 80, 2013.

[72] rdataa.com/aanalyzer.

[73] C. Weiland, J. Krajewski, R. Opila, V. Pallem, C. Dussarrat, and J. C. Woicik. Nondestructive compositional depth profiling using variable-kinetic energy hard x-ray photoelectron spectroscopy and maximum entropy regularization. *Surface and Interface Analysis*, 46(6):407–417, 2014.

[74] J.R. Rubio-Zuazo, E. Martinez, P. Batude, L. Clavelier, A. Chabli, and G. R. Castro. Probing buried interfaces on ge-based metal gate/high-k stacks by hard x-ray photoelectron spectroscopy. *Applied Surface Science*, 257(7):3007–3013, 2011.

[75] J.R. Rubio-Zuazo and G. R. Castro. Information depth determination for hard x-ray photoelectron spectroscopy up to 15 kev photoelectron kinetic energy. *Surface and Interface Analysis*, 40(11):1438–1443, 2008.

[76] J.R Rubio-Zuazo and G R Castro. Non-destructive compositional depth profile analysis by hard x-ray photoelectron spectroscopy. *Journal of Physics: Conference Series*, 100(1):012042, 2008.

[77] J.R. Rubio-Zuazo, P. Ferrer, and G. R. Castro. Non-destructive compositional depth profile in the tens-of-nanometer scale. *Journal of Electron Spectroscopy and Related Phenomena*, 180(1-3):27–33, 2010.

[78] S. Tougaard. Surface nanostructure determination by x-ray photoemission spectroscopy peak shape analysis. *Journal of Vacuum Science & Technology A: Vacuum, Surfaces, and Films*, 14(3):1415–1423, 1996.

[79] S. Tougaard. Deconvolution of loss features from electron spectra. *Surface Science*, 139(1):208 – 218, 1984.

[80] L. Landau. *Journal Physics (Moscow)*, 8:201, 1944.

[81] S. Tougaard and H. S. Hansen. Non-destructive depth profiling through quantitative analysis of surface electron spectra. *Surface and Interface Analysis*, 14(11):730–738, 1989.

[82] S. Tougaard and I. Chorkendorff. Differential inelastic electron scattering cross sections from experimental reflection electron-energy-loss spectra: Application to background removal in electron spectroscopy. *Phys. Rev. B*, 35:6570–6577, May 1987.

[83] S. Tougaard and J. Kraaer. Inelastic-electron-scattering cross sections for si, cu, ag, au, ti, fe, and pd. *Phys. Rev. B*, 43:1651–1661, Jan 1991.

[84] S. Tougaard. Low energy inelastic electron scattering properties of noble and transition metals. *Solid State Communications*, 61(9):547 – 549, 1987.

[85] S. Tougaard. Universality classes of inelastic electron scattering cross-sections. *Surface and Interface Analysis*, 25(3):137–154, 1997.

[86] T.S. Lassen, S. Tougaard, and A. Jablonski. Practical correction procedures for elastic electron scattering effects in arxps. *Surface Science*, 481(1-3):150 – 162, 2001.

[87] S. Tougaard. Energy loss in xps: Fundamental processes and applications for quantification, non-destructive depth profiling and 3d imaging. *Journal of Electron Spectroscopy and Related Phenomena*, 178-179:128–153, 2010.

[88] S. Tougaard and B. Jørgensen. Inelastic background intensities in xps spectra. *Surface Science*, 143(2-3):482 – 494, 1984.

[89] S. Tougaard. "quases: Software package for quantitative xps/aes of surface nanostructures by peak shape analysis" ver 5.3 (2011) see: www.quases.com, 2011.

[90] D. A. Shirley. High-resolution x-ray photoemission spectrum of the valence bands of gold. *Physical Review B*, 5(12):4709–4714, 1972. PRB.

[91] J. Végh. The shirley background revised. *Journal of Electron Spectroscopy and Related Phenomena*, 151(3):159–164, 2006.

[92] J; Végh. The shirley-equivalent electron inelastic scattering cross-section function. *Surface Science*, 563(1-3):183–190, 2004.

[93] C. J. Powell and J. M. Conny. Evaluation of uncertainties in x-ray photoelectron spectroscopy intensities associated with different methods and procedures for background subtraction. i. spectra for monochromatic al x-ray. *Surface and Interface Analysis*, 41(4):269–294, 2009.

[94] W. Smekal, W. S. M. Werner, and C. J. Powell. Simulation of electron spectra for surface analysis (sessa): a novel software tool for quantitative auger-electron spectroscopy and x-ray photoelectron spectroscopy. *Surface and Interface Analysis*, 37(11):1059–1067, 2005.

[95] W. Smekal W.S.M. Werner and C.J. Powell. Nist database for the simulation of electron spectra for surface analysis, sdr 100, version1.3, 2011.

[96] W. S. M. Werner. Simulation of electron spectra for surface analysis using the partial-intensity approach (pia). *Surface and Interface Analysis*, 37(11):846–860, 2005.

[97] W. S. M. Werner. Electron transport in solids for quantitative surface analysis. *Surface and Interface Analysis*, 31(3):141–176, 2001.

[98] W. S. M. Werner. Electron transport for spectrum analysis and experiment design. *Journal of Electron Spectroscopy and Related Phenomena*, 178-179:154–177, 2010.

[99] C. J. Tung, Y. F. Chen, C. M. Kwei, and T. L. Chou. Differential cross sections for plasmon excitations and reflected electron-energy-loss spectra. *Phys. Rev. B*, 49:16684–16693, Jun 1994.

[100] W. S. M. Werner. Obtaining quantitative information on surface excitations from reflection electron energy-loss spectroscopy (reels). *Surface and Interface Analysis*, 35(4):347–353, 2003.

[101] W.S.M. Werner, T. Cabela, J. Zemek, and P. Jiricek. On line shape analysis in x-ray photoelectron spectroscopy. *Surface Science*, 470(3):325 – 336, 2001.

[102] K.M. Case and P.F. Zweifel. *Linear Transport Theory.* Addison-Wesley, 1999.

[103] W. S. M.c Werner. Trajectory reversal approach for electron backscattering from solid surfaces. *Phys. Rev. B*, 71:115415, Mar 2005.

[104] A. Jablonski C.J Powell. Nist inelastic-mean-free-path datadata, version 1.1 standard reference data program datadata 71, 2000.

[105] W. S. M. Werner, W. Smekal, T. Hisch, J. Himmelsbach, and C. J. Powell. Simulation of electron spectra for surface analysis (sessa)for quantitative interpretation of (hard) x-ray photoelectron spectra(haxpes). *Journal of Electron Spectroscopy and Related Phenomena*, 190, Part B:137–143, 2013.

[106] M.M. Atalla and D. Kahng. Ire solid-state devices research conference. 1960.

[107] D. A Muller, T. Sorsch, S. Moccio, F.H. Baumann, K. Evans-Lutterodt, and G. Timp. The electronic structure at the atomic scale of ultrathin gate oxides. *Nature*, 399:758–761, 1999.

[108] G. D. Wilk, R. M. Wallace, and J. M. Anthony. High-k gate dielectrics: Current status and materials properties considerations. *Journal of Applied Physics*, 89(10):5243–5275, 2001.

[109] H. Wong and Y.C. Cheng. On the nitridation-induced enhancement and degradation of {MOSFET} characteristics. *Solid-State Electronics*, 33(8):1107 – 1109, 1990.

[110] I. De, D. Johri, A. Srivastava, and C.M. Osburn. Impact of gate workfunction on device performance at the 50 nm technology node. *Solid-State Electronics*, 44(6):1077 – 1080, 2000.

[111] J. Zegenhagen, B. Detlefs, T.L. Lee, S. Thiess, H. Isern, L. Petit, L. André, J. Roy, Y. Mi, and I. Joumard. X-ray standing waves and hard x-ray photoelectron spectroscopy at the insertion device beamline id32. *Journal of Electron Spectroscopy and Related Phenomena*, 178-179:258–267, 2010.

[112] J.R. Rubio-Zuazo and G.R. Castro. Hard x-ray photoelectron spectroscopy (haxpes) at spline, the spanish beamline at the esrf. *Nuclear Instruments and Methods in Physics Research Section A: Accelerators, Spectrometers, Detectors and Associated Equipment*, 547(1):64 – 72, 2005. Proceedings of the Workshop on Hard X-ray Photoelectron Spectroscopy {HAXPES}.

[113] D. Céolin, J. M. Ablett, D. Prieur, T. Moreno, J. P. Rueff, T. Marchenko, L. Journel, R. Guillemin, B. Pilette, T. Marin, and M. Simon. Hard x-ray photoelectron spectroscopy on the galaxies beamline at the soleil synchrotron. *Journal of Electron Spectroscopy and Related Phenomena*, 190, Part B:188–192, 2013.

[114] F. Vurpillot, M. Gruber, G. Da Costa, I. Martin, L. Renaud, and A. Bostel. Pragmatic reconstruction methods in atom probe tomography. *Ultramicroscopy*, 111(8):1286 – 1294, 2011.

[115] O. C. Hellman, J. A. Vandenbroucke, J. Rusing, D. Isheim, and D. N. Seidman. Analysis of three-dimensional atom-probe data by the proximity histogram. *Microscopy and Microanalysis*, 6:437–444, 9 2000.

[116] G. Hollinger and F. J. Himpsel. Oxygen chemisorption and oxide formation on si(111) and si(100) surfaces. *Journal of Vacuum Science & Technology A*, 1(2):640–645, 1983.

[117] S. Tanuma, C. J. Powell, and D. R. Penn. Calculation of electron inelastic mean free paths (imfps) vii. reliability of the tpp-2m imfp predictive equation. *Surface and Interface Analysis*, 35(3):268–275, 2003.

[118] F. Offi, W. S. M. Werner, M. Sacchi, P. Torelli, M. Cautero, G. Cautero, A. Fondacaro, S. Huotari, G. Monaco, G. Paolicelli, W. Smekal, G. Stefani, and G. Panaccione. Comparison of hard and soft x-ray photoelectron spectra of silicon. *Physical Review B*, 76(8):085422, 2007. PRB.

[119] M. Asif Khan, J. N. Kuznia, J. M. Van Hove, N. Pan, and J. Carter. Observation of a two-dimensional electron gas in low pressure metalorganic chemical vapor deposited gan-alxgax-n heterojunctions. *Applied Physics Letters*, 60(24):3027–3029, 1992.

[120] M. Asif Khan, A. Bhattarai, J. N. Kuznia, and D. T. Olson. High electron mobility transistor based on a gan-alxgaxn heterojunction. *Applied Physics Letters*, 63(9):1214–1215, 1993.

[121] Y.F. Wu, B.P. Keller, S. Keller, D. Kapolnek, S.P. DenBaars, and U.K. Mishra. Measured microwave power performance of algan/gan modfet. *Electron Device Letters, IEEE*, 17(9):455–457, Sept 1996.

[122] B.M. Green, K.K. Chu, E.M. Chumbes, J.A. Smart, J.R. Shealy, and Lester F. Eastman. The effect of surface passivation on the microwave characteristics of undoped algan/gan hemts. *Electron Device Letters, IEEE*, 21(6):268–270, June 2000.

[123] J R Shealy, V Kaper, V Tilak, T Prunty, J A Smart, B Green, and L F Eastman. An algan/gan high-electron-mobility transistor with an aln sub-buffer layer. *Journal of Physics: Condensed Matter*, 14(13):3499, 2002.

[124] Y. Ando, Y. Okamoto, H. Miyamoto, T. Nakayama, T. Inoue, and M. Kuzuhara. 10-w/mm algan-gan hfet with a field modulating plate. *Electron Device Letters, IEEE*, 24(5):289–291, 2003.

[125] Y. F Wu, A Saxler, M. Moore, R.P. Smith, S.T. Sheppard, P.M. Chavarkar, T. Wisleder, U.K. Mishra, and P. Parikh. 30-w/mm gan hemts by field plate optimization. *Electron Device Letters, IEEE*, 25(3):117–119, March 2004.

[126] R. Gaska, J. W. Yang, A. Osinsky, Q. Chen, M. Asif Khan, A. O. Orlov, G. L. Snider, and M. S. Shur. Electron transport in algan/gan heterostructures grown on 6h-sic substrates. *Applied Physics Letters*, 72(6):707–709, 1998.

[127] U. K. Mishra, L. Shen, T.E. Kazior, and Y.F. Wu. Gan-based rf power devices and amplifiers. *Proceedings of the IEEE*, 96(2):287–305, Feb 2008.

[128] K. Yates and R. H. West. Monochromatized ag l-alpha x-rays as a source for higher energy xps. *Surface and Interface Analysis*, 5(4):133–138, 1983.

[129] J. Bearden and A. Burr. Reevaluation of x-ray atomic energy levels. *Rev. Mod. Phys.*, 39:125–142, Jan 1967.

[130] C. D. Wagner. X-ray photoelectron spectroscopy with x-ray photons of higher energy. *Journal of Vacuum Science and Technology*, 15(2):518–523, 1978.

[131] J. E. Castle, L. B. Hazell, and R. D. Whitehead. X-ray photoelectron spectroscopy using si k-alpha radiation. *Journal of Electron Spectroscopy and Related Phenomena*, 9(2):247–250, 1976.

[132] A. R. Chourasia and D. R. Chopra. X-ray photoelectron study of tin. *Surface Science Spectra*, 1(2):233–237, 1992.

[133] A.R. Chourasia and D.R. Chopra. X-ray photoelectron study of tin/sio2 and tin/si interfaces. *Thin Solid Films*, 266(2):298 – 301, 1995.

[134] M.V. Kuznetsov, J.F. Zhuravlev, V.A. Zhilyaev, and V.A. Gubanov. Xps study of the nitrides, oxides and oxynitrides of titanium. *Journal of Electron Spectroscopy and Related Phenomena*, 58(1-2):1 – 9, 1992.

[135] B. J. Burrow, A. E. Morgan, and R. C. Ellwanger. A correlation of auger electron spectroscopy, x-ray photoelectron spectroscopy, and rutherford backscattering spectrometry measurements on sputter-deposited titanium nitride thin films. *Journal of Vacuum Science & Technology A*, 4(6):2463–2469, 1986.

[136] K. Kovacs, I. V. Perczel, V. K. Josepovits, G. Kiss, F. Réti, and P. Deak. In situ surface analytical investigation of the thermal oxidation of ti-al intermetallics up to 1000°c. *Applied Surface Science*, 200(1-4):185–195, 2002.

[137] D. Leinen, A. Fernandez, J. P. Espinos, J. P. Holgado, and A. R. Gonzalez-Elipe. An xps study of the mixing effects induced by ion bombardment in composite oxides. *Applied Surface Science*, 68(4):453–459, 1993.

[138] S. L. Chang, J. W. Anderegg, and P. A. Thiel. Surface oxidation of an al-pd-mn quasicrystal, characterized by x-ray photoelectron spectroscopy. *Journal of Non-Crystalline Solids*, 195(1-2):95–101, 1996.

[139] I. Olefjord, H. J. Mathieu, and P. Marcus. Intercomparison of surface analysis of thin aluminium oxide films. *Surface and Interface Analysis*, 15(11):681–692, 1990.

[140] C. Wiemann, M. Patt, S. Cramm, M. Escher, M. Merkel, A. Gloskovskii, S. Thiess, W. Drube, and C. M. Schneider. Probing buried layers by photoelectron spectromicroscopy with hard x-ray excitation. *Applied Physics Letters*, 100(22):–, 2012.

[141] M. Patt, C. Wiemann, N. Weber, M. Escher, A. Gloskovskii, W. Drube, M. Merkel, and C. M. Schneider. Bulk sensitive hard x-ray photoemission electron microscopy. *Review of Scientific Instruments*, 85(11):–, 2014.

[142] P. Auger F. Perrin. Etude eexperimental des directions d'émission des photoélectrons. *Jornal de Physique et Radium*, 8:85–92, 1927.

[143] H. A. Bethe E. E. Salpeter. *Quantum Mechanics of One- and Two-electron Atoms.* Springer, Berlin, 1957.

[144] D. W. Lindle and O. Hemmers. Breakdown of the dipole approximation in soft-x-ray photoemission. *Journal of Electron Spectroscopy and Related Phenomena*, 100(1-3):297 – 311, 1999.

[145] F. Sauter. *Ann. Phys. (Leipzig)*, 9:217, 1931.

[146] F. Sauter. *Ann. Phys. (Leipzig)*, 11:454, 1931.

[147] J. Cooper and R. N. Zare. Angular distribution of photoelectrons. *The Journal of Chemical Physics*, 48(2):942–943, 1968.

[148] O Hemmers, G Fisher, P Glans, D L Hansen, H Wang, S B Whitfield, R Wehlitz, J C Levin, I A Sellin, R C C Perera, E W B Dias, H S Chakraborty, P C Deshmukh, S T Manson, and D W Lindle. Beyond the dipole approximation: angular-distribution effects in valence photoemission. *Journal of Physics B: Atomic, Molecular and Optical Physics*, 30(21):L727, 1997.

[149] N. L. S. Martin, D. B. Thompson, R. P. Bauman, C. D. Caldwell, M. O. Krause, S. P. Frigo, and M. Wilson. Electric-dipole quadrupole interference of overlapping autoionizing levels in photoelectron energy spectra. *Phys. Rev. Lett.*, 81:1199–1202, Aug 1998.

[150] A. Derevianko, O. Hemmers, S. Oblad, P. Glans, H. Wang, S. B. Whitfield, R. Wehlitz, I. A. Sellin, W. R. Johnson, and D. W. Lindle. Electric-octupole and pure-electric-quadrupole effects in soft-x-ray photoemission. *Phys. Rev. Lett.*, 84:2116–2119, Mar 2000.

[151] http://www.synchrotron soleil.fr/.

[152] http://www.specs.de.

[153] http://www.vgscienta.com/.

[154] http://www.focus-gmbh.com/.

[155] M.W Phaneuf. Applications of focused ion beam microscopy to materials science specimens. *Micron*, 30(3):277 – 288, 1999.

[156] S. A. Müller, U. Aebi, and A. Engel. What transmission electron microscopes can visualize now and in the future. *Journal of Structural Biology*, Journal of Structural Biology(3):235–245, 2008.

[157] V. Everts, A. Niehof, W. Tigchelaar-Gutter, and W. Beertsen. Transmission electron microscopy of bone. In Miep H. Helfrich and Stuart H. Ralston, editors, *Bone Research Protocols*, volume 816 of *Methods in Molecular Biology*, pages 351–363. Humana Press, 2012.

[158] P.A. Midgley and M. Weyland. 3d electron microscopy in the physical sciences: the development of z-contrast and eftem tomography. *Ultramicroscopy*, 96(3-4):413 – 431, 2003. Proceedings of the International Workshop on Strategies and Advances in Atomic Level Spectroscopy and Analysis.

[159] A. Sarrau J. M. Deconihout B. Menand A. Blavette, D. Bostel. An atom probe for three-dimensional tomography. *Nature*, 363(6428):432–435, 1993.

[160] B. Gault, F. Vurpillot, A. Vella, M. Gilbert, A. Menand, D. Blavette, and B. Deconihout. Design of a femtosecond laser assisted tomographic atom probe. *Review of Scientific Instruments*, 77(4), 2006.

[161] M. K. Miller. *Atom Probe Tomography.* Kluwer Academic/Plenum, 2000.

[162] M. O. Krause. Atomic radiative and radiationless yields for k and l shells. *Journal of Physical and Chemical Reference Data*, 8(2):307–327, 1979.

[163] H. Fujiwara. *Spectroscopic Ellipsometry: Principles and Applications.* Wiley, 2007.

[164] W. McGahan H.G. Tompkins. *Spectroscopic Ellipsometry and reflectometry.* Wiley & Sons, 1999.

[165] R. M. Azzam and N. M. Bashara. *Ellipsometry and polarized light.* North-Holland, 1977.

[166] Y. J. Cho, N. V. Nguyen, C. A. Richter, J. R. Ehrstein, B. H. Lee, and J.C. Lee. Spectroscopic ellipsometry characterization of high-k dielectric hfo2 thin films and the high-temperature annealing effects on their optical properties. *Applied Physics Letters*, 80(7):1249–1251, 2002.

[167] D. K. Bowen and B. K. Tanner. Characterization of engineering surfaces by grazing-incidence x-ray reflectivity. *Nanotechnology*, 4(4):175, 1993.

[168] E. Chason and T. M. Mayer. Thin film and surface characterization by specular x-ray reflectivity. *Critical Reviews in Solid State and Materials Sciences*, 22(1):1–67, 1997.

[169] A; van der Lee. Grazing incidence specular reflectivity: theory, experiment, and applications. *Solid State Sciences*, 2(2):257 – 278, 2000.

[170] A. van der Lee, S. Roualdes, R. Berjoan, and J. Durand. Mass density determination of thin organosilicon films by x-ray reflectometry. *Applied Surface Science*, 173(1-2):115 – 121, 2001.

[171] M. Yasaka. X-ray thin film measurement techniques v. x-ray reflectivity measurement. *Rigaku Journal*, 26(2):c, 2010.